Diverse Charge Tunneling in Hybrid Quantum Confined Systems

Han, L.

DOI
10.4233/uuid:be41d4fb-c5ec-4967-a418-a6e7dc9c63c1

Publication date
2025

Document Version
Final published version

Citation (APA)
Han, L. (2025). *Diverse Charge Tunneling in Hybrid Quantum Confined Systems*. [Dissertation (TU Delft), Delft University of Technology]. https://doi.org/10.4233/uuid:be41d4fb-c5ec-4967-a418-a6e7dc9c63c1

DIVERSE CHARGE TUNNELING IN HYBRID QUANTUM CONFINED SYSTEMS

Diverse charge tunneling in hybrid quantum confined systems

Dissertation

for the purpose of obtaining the degree of doctor
at Delft University of Technology
by the authority of the Rector Magnificus prof. dr. ir. T.H.J.J. van der Hagen,
chair of the Board for Doctorates,
to be defended publicly on Tuesday 6 May 2025 at 15:00 pm.

by

Lin Han

Master of Science in Physics (Applied and Engineering Physics),
Technische Universität München (TUM), Germany,
born in Shijiazhuang, Hebei, China.

This dissertation has been approved by the promotor(s).

Composition of the doctoral committee:

Rector Magnificus,	chairperson
Prof. dr. ir. L. P. Kouwenhoven	Delft University of Technology, promotor
Dr. S. Goswami	Delft University of Technology, copromotor
Independent members:	
Prof. dr. Y. M. Blanter	Delft University of Technology
Prof. dr. L. DiCarlo	Delft University of Technology
Dr. C. K. Andersen	Delft University of Technology
Prof. dr. J. M. van Ruitenbeek	Leiden University
Prof. dr. Y. V. Nazarov	Delft University of Technology, reserve member

Keywords: quantum dot, hybrid semiconductor–superconductor, nanowire, dispersive gate sensing, quantum capacitance, topological qubit readout

Printed by: www.proefschriftenprinten.nl

ISBN 000-00-0000-000-0

An electronic version of this dissertation is available at
http://repository.tudelft.nl/.

Contents

SUMMARY

Quantum mechanics opens exciting avenues for technological advancements, particularly in quantum computation, enabling the solution of complex problems that classical computers struggle to address. However, the implementation of quantum bits (qubits) faces significant challenges due to unwanted disturbances. Previous theoretical work suggests that developing topological qubits could alleviate concerns about the complexities of error correction, as their robust topological protection promises fault tolerance.

This thesis focuses on the progress made toward constructing such Majorana-based qubits using nanowire-based hybrid superconducting-semiconductor quantum dot systems. It specifically investigates the application of dispersive gate sensing in these systems, emphasizing the characterization of diverse charge tunneling events and the understanding of forthcoming parity readout signals for potential topological qubits in their simplified forms. Through a combination of chip design, fabrication, cryogenic measurements at base temperatures, data analysis, and theoretical simulations, our findings have emerged.

The main idea of this thesis is to separate the two interfering paths required for qubit readout and to understand each path individually. One path connects two quantum dots through a semiconductor reference arm, while the other connects them via a superconducting island. Key achievements include the implementation of dispersive gate sensing on normal dots within dot-island systems, revealing charge tunneling processes and demonstrating the efficacy of this technique for investigating subgap excitations. Our work extends to characterizing spin-orbit field orientations in InSb nanowire-based double quantum dots, emphasizing that dispersive gate sensing is an effective tool for situations where transport measurements are not feasible. Additionally, novel methods for measuring capacitance in micro- and nanoscale devices using RF resonators have been validated, showcasing sensitivity suitable for both room temperature and cryogenic applications. The latest developments return to the exploration of one of the core segments of topological qubits, focusing on charge tunneling processes in a hybrid dot-island-dot system, and highlighting the tunability between elastic cotunneling and cross-Andreev reflection.

The findings presented in this thesis not only contribute to the understanding of hybrid quantum systems but also pave the way for future research in topological quantum computing, emphasizing the potential of dispersive gate sensing in advancing the field.

Samenvatting

De kwantummechanica opent spannende mogelijkheden voor technologische vooruitgang, met name in de kwantumcomputatie, waardoor complexe problemen kunnen worden opgelost die klassieke computers moeilijk kunnen aanpakken. De implementatie van quantum bits (qubits) staat echter voor aanzienlijke uitdagingen door ongewenste verstoringen. Eerdere theoretische werken suggereren dat de ontwikkeling van topologische qubits de zorgen over de complexiteit van foutcorrectie zou kunnen verlichten, omdat hun robuuste topologische bescherming fouttolerantie belooft.

Dit proefschrift richt zich op de voortgang die is geboekt bij het construeren van dergelijke Majorana-gebaseerde qubits met behulp van nanodraad-gebaseerde hybride supergeleidende-semiconductordot-systemen. Het onderzoekt specifiek de toepassing van dispersieve poortdetectie in deze systemen, met de nadruk op de karakterisering van diverse ladings tunnelingprocessen en het begrijpen van de komende pariteit lees signalen voor potentiële topologische qubits in hun vereenvoudigde vormen. Door een combinatie van chipontwerp, fabricage, cryogene metingen bij basistemperaturen, data-analyse en theoretische simulaties zijn onze bevindingen naar voren gekomen.

Het belangrijkste idee van dit proefschrift is om de twee interfererende paden die nodig zijn voor qubit-leesprocessen te scheiden en elk pad afzonderlijk te begrijpen. Het ene pad verbindt twee quantum dots via een semiconductorreferentiearm, terwijl het andere hen verbindt via een supergeleidende eiland. Belangrijke prestaties omvatten de implementatie van dispersieve poortdetectie op normale dots binnen dot-eiland systemen, waarbij ladings tunnelingprocessen worden onthuld en de effectiviteit van deze techniek voor het onderzoeken van subgap-excitatie wordt aangetoond. Ons werk breidt zich uit naar de karakterisering van spin-orbit veldoriëntaties in InSb nanodraad-gebaseerde dubbele quantum dots, waarbij wordt benadrukt dat dispersieve poortdetectie een effectieve tool is voor situaties waarin transportmetingen niet haalbaar zijn. Daarnaast zijn nieuwe methoden voor het meten van capaciteit in micro- en nanoschaal apparaten met behulp van RF-resonatoren gevalideerd, wat een gevoeligheid toont die geschikt is voor zowel kamertemperatuur als cryogene toepassingen. De laatste ontwikkelingen keren terug naar de verkenning van een van de kernsegmenten van topologische qubits, met de nadruk op ladings tunnelingprocessen in een hybride dot-eiland-dot systeem, en benadrukken de afstelbaarheid tussen elastische cotunneling en cross-Andreev reflectie.

De bevindingen gepresenteerd in dit proefschrift dragen niet alleen bij aan het begrip van hybride kwantumsystemen, maar effenen ook de weg voor toekomstig onderzoek in topologische kwantumcomputing, waarbij het potentieel van dispersieve poortdetectie wordt benadrukt in de vooruitgang van het vakgebied.

1

INTRODUCTION

1

1.1. QUANTUM COMPUTATION

At the beginning of the 20th century, it was discovered that the old classical physics theories could no longer adequately describe microscopic systems. At that time, "a dark cloud in the sky" was used to describe the confusion that experiments such as blackbody radiation and the photoelectric effect brought to the physics community [1]. As the German physicist Max Planck introduced the concept of energy dispersion in his explanation of black body radiation, Albert Einstein realized that quantization is a fundamental physical property and could explained the photoelectric effect accordingly [2, 3]. Since then, the microscopic world under the dark cloud became clear, and quantum mechanics was born. It updated people's understanding of the microscopic material structure and its interaction, and has been developed to the present.

In the same period of time, the proposal of Turing's computing model opened the era of computing with virtual machines instead of human beings [4]. The subsequent invention of the semiconductor transistor made the hardware level of the computer enter the fast lane of development [5, 6]. During the next half century, as stated by Moore's Law, the number of transistors that can be accommodated on an integrated circuit will double approximately every two years [7]. However, when the scale of nano-components shrinks, quantum effects in microscopic systems begin to interfere with the normal operation of computers, and classical computers will eventually reach their limits. To extend the limits of conventional computers, researchers have turned to computing devices based on quantum mechanics, and thereby the field of quantum computation emerges [8].

Quantum computing is to perform fast parallel computing by replacing digital bits with quantum bits (named as qubits) by making use of the quantum properties superposition and coherence. At this point the encoding of qubits is realized in different quantum systems, including electronic spins in quantum dots [9], trapped ions in electromagnetic fields [10, 11, 12], nitrogen-vacancy centers in diamonds [13, 14], and transmons in superconducting circuits [15, 16]. However, the quantum computing systems is still not commercially available, but more confined to laboratories because there are still many technical challenges in building large-scale quantum computers. According to physicist David DiVincenzo's five requirements for a practical quantum computer, the scalability of qubits, and the problem of controlling and eliminating decoherence are crucial to be solved, and have always been the focus of academic efforts to optimize [17].

1.2. TOPOLOGICAL ROADMAPS

At the end of the 20th century, in order to solve the problem of quantum decoherence that is inevitable in every quantum system, Alexei Kitaev mathematically proposed a topological quantum computing scheme. In three-dimensional space, particles can only be fermions or bosons according to their different statistical properties. While in two-dimensional space, Bose-Einstein statistics and Fermi-Dirac statistics are no longer applicable, thus people proposed the definition of anyon. Anyon is a kind of quasiparticle that is imagined and extended from the particle exchange property. For two anyons that make an exchange in space, their wave functions may have an arbitrary phase, or even their degenerate ground state changes [18]. This exchange results in braiding of the worldline of the anyons, which has nothing to do with the paths but simply depends on the topology of the braid. Such braiding operations are therefore far more resistant to the interference caused by the external environment. Since the non-integer degrees of freedom brought by a non-Abelian anyon (a type of anyon) can be used to store quantum information or perform quantum calculations, its topological protection is theoretically resistant to quantum decoherence and errors. Once quantum materials supporting non-Abelian anyons are manufactured and scalable quantum device structures are designed, we could solve the scalability and coherence problems of quantum computers from origination.

Time back to the year of 1937, Ettore Majorana hypothesized a kind of Majorana particle, sometimes named as Majorana fermion, to be its own antiparticle [19]. The interest in Majorana fermions emerged initially in the study of high energy and particle physics, but not yet proved in nature. Even so, it aroused strong interest in the field of condensed matter physics in early 21st centry when it is proposed to be realized as a Bogoliubov quasiparticle in superconducting materials. Such quasiparticles are exactly one type of non-Abelian anyons, and are often called Majorana zero modes[1].

Certain key components are required to achieve Majorana zero modes. These include superconductivity, which provides the pairing potential crucial for the formation of Majorana zero modes, and strong spin-orbit coupling, which facilitates the creation of topological states conducive to Majorana zero modes. An applied magnetic field breaks the time-reversal symmetry, driving the system into a topological phase where Majorana zero modes can emerge. Low dimensionality, precise chemical potential tuning and controlled isolation of Majorana zero modes are also essential to ensure the stability and distinct properties of Majorana zero modes.

Since the last decade, researchers in laboratories have been aiming to realize Majorana zero modes at the two ends of a one-dimensional topological superconductor, by covering a semiconductor nanowire with a thin layer of conventional superconductor [20, 21, 22, 23, 24]. Possibly limited by the progress of advanced materials and fabrication techniques, robust Majorana zero modes with topological protection is hard to be established. Meanwhile, a less constrained type called the poor man's Majorana[2] and a fundamental model of Majorana zero modes called the Kitaev chain[3] have also been explored with rewarding outcomes [25, 26, 27, 28, 29, 30, 31, 32, 33, 34].

1.3. MAJORANA BASED QUBITS

Concurrent with advancements in condensed matter physics on establishing and probing the robustness of Majorana zero modes, there is ongoing research into designing readable topological qubits. A promising geometry of several Majorana-based qubit prototypes is the Majorana box qubit, the core component of which is a floating[4] supercon-

[1] The name of zero modes originates from a topologically protected degeneracy of the ground state. That is, in a system with 2N Majorana zero modes (described by operators γ_i, with i =1,...,2N), the ground state is 2N-fold degenerate and it costs zero energy from one ground state to another.

[2] We refer to them as "poor man's Majorana (zero modes)" because they lack topological protection, but they exhibit similar properties to Majorana zero modes formed in topological superconductors.

[3] A toy model proposed by Kitaev shows that the Majorana zero modes can arise at the ends of a spinless p-wave superconducting chain.

[4] Floating means that the charge is conserved within the system. There is no charge transfer between the system and the environment.

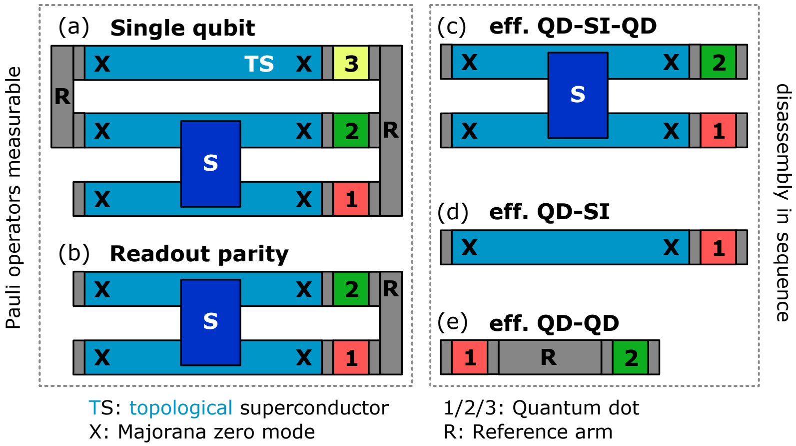

Figure 1.1: **Majorana box qubit and its sequential disassembly.** **(a)** Single Majorana box qubit for readout of all Pauli operators and full one-qubit control. **(b)** Interferometor that allowing parity readout of one pair of Majorana zero modes near quantum dot 1 and 2, equivalent to measure one Pauli operator σ_z. **(c)** By removing the reference arm, the structure effectively becomes a dot-island-dot system, leaving only one path for the charges to tunnel compared to (b). **(d)** Removing quantum dot 2 results in an effective dot-island system. **(e)** The other path for the charges to tunnel, as in (b). This is effectively a double quantum dot.

ducting island [35]. Such a floating island consists of two parallel topological superconducting segments, denoted TS in Fig. 1.1(a-b), coupled by a superconducting link, which could be a conventional s-wave superconductor. Together, they form a floating island of identical charging energy. Note that this finite charging energy should be large enough to avoid destruction of the computational basis by quasiparticle poisoning.

The Majorana box qubit states can be readout using quantum dots with interferometrical measurements, the simplest version of which is shown in Fig. 1.1 (b). We see two paths for electron tunneling between the two quantum dots, one through the reference arm (denoted as R) as in Fig. 1.1 (e), and the other through the topological island as in Fig. 1.1 (c). The information of the qubit, namely the parity of a pair of Majorana zero modes, either even or odd, is contained in the effective charge tunneling strength between two quantum dots. With a magnetic flux applied perpendicular to the plane, the phase difference between the two paths can be tuned to make the measurable tunneling strength of two parities as distinguishable as possible. In this situation, the Majorana box qubit state readout is practically equivalent to tunnel coupling readout between the quantum dots.

Conventional transport measurements, are no longer good candidates for qubit readout after the characterization of the existence of robust Majorana zero modes. Taking into account the preferred high speed of the qubit measurement and the simplicity of the design for further scalability, we started to employ dispersive gate sensing technique with RF reflectometry. This technique is also the focus of the entire thesis.

In the following chapters, we present the initial steps in the use of dispersive gate sensing towards the first functional Majorana box qubit with full qubit control. Disassembling the design sequentially, for each material type we first measured the charge tunneling strengths between two quantum dots (Fig. 1.1 (e)), considering the reference arm as part of the barrier gates, to ensure that dispersive gate sensing works. The charge tunneling events between a quantum dot and a superconducting island are then studied, in a structure similar to Fig. 1.1 (d). This is an intermediate step towards understanding charge tunneling between two quantum dots via the island, as in Fig. 1.1 (c). Regarding the future, the parity readout of a pair of Majorana zero modes is applicable with the interferometer (Fig. 1.1 (b)), and finally a single qubit readout with three Pauli operators can be obtained (Fig. 1.1 (a)).

1.4. CHAPTERS OVERVIEW

The experimental results contained in this thesis are packaged as follows.

CHAPTER 2

describes all the core elements within the hybrid systems we study, including single and double quantum dots, spin-orbit interactions that dominate InSb and InAs materials, superconductivity, and superconducting islands. It also introduces the principles of dispersive gate sensing, covering aspects from the circuit side to quantum capacitance, and explains the reflection coefficient model that we utilize.

CHAPTER 3

covers the design and fabrication procedures of the InAs and InSb nanowire-based devices, the availability of charge sensors in addition to the functionality of gate sensing, the measurement setup, and the sanity checks performed during the preparation of cryogenic measurements.

CHAPTER 4: (EFF. QD-SI)

shows how charge tunneling occurs between a semiconductor quantum dot and a superconducting island in an open or floating system. It also demonstrates the ability of dispersive gate sensing to probe a subgap state in the island through a quantum dot.

CHAPTER 5: (EFF. QD-QD)

talks about the dispersive gate sensing applied to a double quantum dot. In the absence of an external field, the sensing signal allows the total charge occupancy to be identified. It also finds that the orientation of the spin-orbit field can be extracted, while it changes significantly between charge transitions and is typically neither perpendicular to the nanowire nor aligned with the chip plane.

CHAPTER 6: APPLICATIONS

exhibits many applications of RF reflectometry in semiconductor quantum devices, including compressibility measurements. It predicts sensitivity and updates the resonator model for analyzing capacitances and losses measured by dispersive gate sensing.

CHAPTER 7: (EFF. QD-SI-QD)

discusses the signal of elastic cotunneling and crossed Andreev reflections in a floating dot-island-dot device, by tuning the charging energy of the middle superconducting island. We quantitatively analyzed the value of diverse charge tunneling strengths and realized the extracted dissipations from the resonator provided additional dimension in understanding the system.

CHAPTER 8
summarizes the experimental results in a timeline. It also suggests several advanced fabrication techniques that can aid in more complex device design, as well as upcoming experiments that can be conducted based on the current understanding of dispersive gate sensing, particularly in relation to hybrid systems for Majorana-based qubit readout.

BIBLIOGRAPHY

[1] Lord Kelvin. I. nineteenth century clouds over the dynamical theory of heat and light. *The London, Edinburgh, and Dublin Philosophical Magazine and Journal of Science*, 2(7):1–40, 1901.

[2] Max Planck. The theory of heat radiation. *Entropie*, 144(190):164, 1900.

[3] Albert Einstein. Concerning an heuristic point of view toward the emission and transformation of light. *American Journal of Physics*, 33(5):367, 1965.

[4] Alonzo Church. Am turing. on computable numbers, with an application to the entscheidungs problcm. proceedings of the london mathematical society, 2 s. vol. 42 (1936–1937), pp. 230–265. *The Journal of Symbolic Logic*, 2(1):42–43, 1937.

[5] Julius E Lilienfeld. Electric current control mechanism. *Canadian patent CA*, 272437(19):07, 1927.

[6] Oskar Heil. Improvements in or relating to electrical amplifiers and other control arrangements and devices. *British Patent*, 439(457):10–14, 1935.

[7] Gordon E Moore. Cramming more components onto integrated circuits. *Proceedings of the IEEE*, 86(1):82–85, 1998.

[8] Richard P Feynman. Simulating physics with computers. In *Feynman and computation*, pages 133–153. CRC Press, 2018.

[9] Guido Burkard, Thaddeus D Ladd, Andrew Pan, John M Nichol, and Jason R Petta. Semiconductor spin qubits. *Reviews of Modern Physics*, 95(2):025003, 2023.

[10] Colin D Bruzewicz, John Chiaverini, Robert McConnell, and Jeremy M Sage. Trapped-ion quantum computing: Progress and challenges. *Applied Physics Reviews*, 6(2), 2019.

[11] Raghavendra Srinivas, SC Burd, HM Knaack, RT Sutherland, Alex Kwiatkowski, Scott Glancy, Emanuel Knill, DJ Wineland, Dietrich Leibfried, Andrew C Wilson, et al. High-fidelity laser-free universal control of trapped ion qubits. *Nature*, 597(7875):209–213, 2021.

[12] Kenneth R Brown, John Chiaverini, Jeremy M Sage, and Hartmut Häffner. Materials challenges for trapped-ion quantum computers. *Nature Reviews Materials*, 6(10):892–905, 2021.

[13] Sébastien Pezzagna and Jan Meijer. Quantum computer based on color centers in diamond. *Applied Physics Reviews*, 8(1), 2021.

[14] Mohamed H Abobeih, Yu Wang, John Randall, SJH Loenen, Christina E Bradley, Matthew Markham, Daniel J Twitchen, Barbara M Terhal, and Tim H Taminiau. Fault-tolerant operation of a logical qubit in a diamond quantum processor. *Nature*, 606(7916):884–889, 2022.

[15] Morten Kjaergaard, Mollie E Schwartz, Jochen Braumüller, Philip Krantz, Joel I-J Wang, Simon Gustavsson, and William D Oliver. Superconducting qubits: Current state of play. *Annual Review of Condensed Matter Physics*, 11:369–395, 2020.

[16] Irfan Siddiqi. Engineering high-coherence superconducting qubits. *Nature Reviews Materials*, 6(10):875–891, 2021.

[17] David P DiVincenzo. The physical implementation of quantum computation. *Fortschritte der Physik: Progress of Physics*, 48(9-11):771–783, 2000.

[18] A Yu Kitaev. Fault-tolerant quantum computation by anyons. *Annals of physics*, 303(1):2–30, 2003.

[19] Ettore Majorana. A symmetric theory of electrons and positrons. *Scientific Papers of Ettore Majorana: A New Expanded Edition*, pages 113–128, 2020.

[20] V Mourik, K Zuo, SM Frolov, SR Plissard, EP Bakkers, and LP Kouwenhoven. Signatures of majorana fermions in hybrid superconductor-semiconductor nanowire devices. *Science (New York, NY)*, 336(6084):1003–1007, 2012.

[21] Sven Marian Albrecht, Andrew P Higginbotham, Morten Madsen, Ferdinand Kuemmeth, Thomas Sand Jespersen, Jesper Nygård, Peter Krogstrup, and CM Marcus. Exponential protection of zero modes in majorana islands. *Nature*, 531(7593):206–209, 2016.

[22] MT Deng, S Vaitiekėnas, M Leijnse, and P Krogstrup. Majorana bound state in a coupled quantum-dot hybrid-nanowire system. *Science*, 354(6319):1557–1562, 2016.

[23] Roman M Lutchyn, Erik PAM Bakkers, Leo P Kouwenhoven, Peter Krogstrup, Charles M Marcus, and Yuval Oreg. Majorana zero modes in superconductor–semiconductor heterostructures. *Nature Reviews Materials*, 3(5):52–68, 2018.

[24] Elsa Prada, Pablo San-Jose, Michiel WA de Moor, Attila Geresdi, Eduardo JH Lee, Jelena Klinovaja, Daniel Loss, Jesper Nygård, Ramón Aguado, and Leo P Kouwenhoven. From andreev to majorana bound states in hybrid superconductor–semiconductor nanowires. *Nature Reviews Physics*, 2(10):575–594, 2020.

[25] A Yu Kitaev. Unpaired majorana fermions in quantum wires. *Physics-uspekhi*, 44(10S):131, 2001.

[26] Martin Leijnse and Karsten Flensberg. Parity qubits and poor man's majorana bound states in double quantum dots. *Physical Review B*, 86(13):134528, 2012.

[27] Guanzhong Wang, Tom Dvir, Grzegorz P Mazur, Chun-Xiao Liu, Nick van Loo, Sebastiaan LD Ten Haaf, Alberto Bordin, Sasa Gazibegovic, Ghada Badawy, Erik PAM Bakkers, et al. Singlet and triplet cooper pair splitting in hybrid superconducting nanowires. *Nature*, 612(7940):448–453, 2022.

[28] Tom Dvir, Guanzhong Wang, Nick van Loo, Chun-Xiao Liu, Grzegorz P Mazur, Alberto Bordin, Sebastiaan LD Ten Haaf, Ji-Yin Wang, David van Driel, Francesco Zatelli, et al. Realization of a minimal kitaev chain in coupled quantum dots. *Nature*, 614(7948):445–450, 2023.

[29] Alberto Bordin, Guanzhong Wang, Chun-Xiao Liu, Sebastiaan LD Ten Haaf, Nick Van Loo, Grzegorz P Mazur, Di Xu, David Van Driel, Francesco Zatelli, Sasa Gazibegovic, et al. Tunable crossed andreev reflection and elastic cotunneling in hybrid nanowires. *Physical Review X*, 13(3):031031, 2023.

[30] Francesco Zatelli, David van Driel, Di Xu, Guanzhong Wang, Chun-Xiao Liu, Alberto Bordin, Bart Roovers, Grzegorz P Mazur, Nick van Loo, Jan Cornelis Wolff, et al. Robust poor man's majorana zero modes using yu-shiba-rusinov states. *arXiv preprint arXiv:2311.03193*, 2023.

[31] Rubén Seoane Souto and Ramón Aguado. Subgap states in semiconductor-superconductor devices for quantum technologies: Andreev qubits and minimal majorana chains. *arXiv preprint arXiv:2404.06592*, 2024.

[32] Alberto Bordin, Xiang Li, David Van Driel, Jan Cornelis Wolff, Qingzhen Wang, Sebastiaan LD Ten Haaf, Guanzhong Wang, Nick Van Loo, Leo P Kouwenhoven, and Tom Dvir. Crossed andreev reflection and elastic cotunneling in three quantum dots coupled by superconductors. *Physical review letters*, 132(5):056602, 2024.

[33] Alberto Bordin, Chun-Xiao Liu, Tom Dvir, Francesco Zatelli, Sebastiaan LD ten Haaf, David van Driel, Guanzhong Wang, Nick van Loo, Thomas van Caekenberghe, Jan Cornelis Wolff, et al. Signatures of majorana protection in a three-site kitaev chain. *arXiv preprint arXiv:2402.19382*, 2024.

[34] Athanasios Tsintzis, Rubén Seoane Souto, Karsten Flensberg, Jeroen Danon, and Martin Leijnse. Majorana qubits and non-abelian physics in quantum dot–based minimal kitaev chains. *PRX Quantum*, 5(1):010323, 2024.

[35] Stephan Plugge, Asbjørn Rasmussen, Reinhold Egger, and Karsten Flensberg. Majorana box qubits. *New Journal of Physics*, 19(1):012001, 2017.

2

THEORY

2

2.1. COMPONENT 1: SEMICONDUCTOR

Quantum dots (QDs) are nanoscale structures that confine the motion of charge carriers in all three dimensions. This confinement occurs when the size of a QD is relatively small compared to the de Broglie wavelength[1] of the charge carrier [1, 2], resulting in the emergence of discrete energy levels similar to those in natural atoms. QDs are thus often referred to as artificial atoms, while with their energy levels tunable. In semiconductor nanowires, QDs can be precisely defined and linked through an electrically adjustable potential profile. The electrochemical potential of each QD can be controlled by gate electrodes [3, 4].

In recent decades, there has been a notable emphasis on research into QDs, with a focus on their applications in the field of quantum computing. For instance, they have played a significant role in the development and measurement of spin qubits [5, 6, 7]. As previously stated in Chapter. 1, they have also been proposed as the core component in reading out Majorana-based topological qubits. This section provides an overview of single and double QDs.

2.1.1. SINGLE DOTS

A single QD can be well described by the constant interaction model [8, 9], as depicted in Fig. 2.1(a). The model relies on two fundamental assumptions. First, the Coulomb interactions of a charge carrier within the QD with all other charges, whether within the QD or from the external environment, are quantified by a constant capacitance (C_0). The value of C_0 is determined by the sum of the capacitances between the QD and the source (C_S), the drain (C_D), and the gate (C_G), which is expressed as $C_0 = C_\mathrm{S} + C_\mathrm{D} + C_\mathrm{G}$. Second, the discrete energy levels, whose energies are designated by E_n[2], are not influenced by the number of electrons N or the mutual interactions between the electrons on the QD. The total energy $U(N)$ of the QD in its ground state is thus given by the following expression:

$$U(N) = \frac{[-|e|(N-N_0) + \sum_{i=S,D,G} C_i V_i]^2}{2C_0} + \sum_{n=1}^{N} E_n, \tag{2.1}$$

where e is the elementary charge, while N_0 denotes the net electron charge number in the absence of gate voltages. The term V_i refers to the voltage applied to the corresponding electrode.

The minimal energy required to place the Nth electron into the QD is the electrochemical potential $\mu(N)$, defined as:

$$\mu(N) = U(N) - U(N-1) = 2\left(N - N_0 - \frac{1}{2}\right)E_\mathrm{C} - \frac{2E_\mathrm{C}\sum_{i=S,D,G} C_i V_i}{|e|} + E_N, \tag{2.2}$$

with the charging energy of a single electron on the QD given by $E_\mathrm{C} = e^2/2C_0$. The ground state energy spacing of such QDs can be expressed by the addition energy

$$E_\mathrm{add} = \mu(N+1) - \mu(N) = 2E_\mathrm{C} + (E_{N+1} - E_N), \tag{2.3}$$

[1] The de Broglie wavelength $\lambda = h/p$ is defined as the wavelength associated with any moving particle. It reflects the wave-particle duality of matter and can be calculated by dividing Planck's constant h by the momentum of the particle p.

[2] The variable n in E_n ranges from 1 to N, and represents the charge number index of the discrete energy levels within the QD.

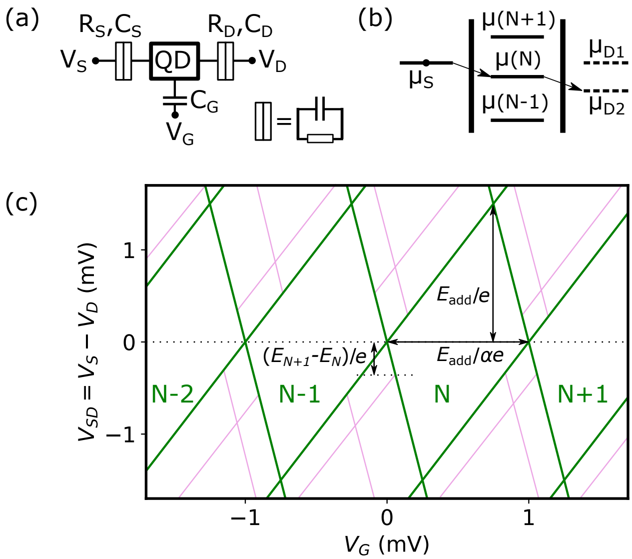

Figure 2.1: **Single quantum dot (QD). (a)** The equivalent circuit model of a single QD involves connections to the source (V_S) and drain (V_D) reservoirs through tunnel barriers. These barriers are represented in the model as a resistor $R_\mathrm{S(D)}$ in parallel with a capacitor $C_\mathrm{S(D)}$. The gate voltage V_G is capacitively coupled to the QD through a capacitor C_G to adjust its electrochemical potential, thereby regulating the facilitation of charge transport at specific bias voltages. **(b)** The schematic of charge tunneling between the reservoirs through a QD. At zero bias, where $\mu_\mathrm{S} = \mu_\mathrm{D1}$, the transport is blockaded when the electrochemical potential μ of the QD is misaligned with the Fermi level of the reservoir. At a finite bias, where $\mu_\mathrm{S} > \mu_N > \mu_\mathrm{D2}$, the single charge state begins facilitating the transport of charges through the QD. **(c)** By sweeping the voltages across multiple charge transitions, the Coulomb blockade regions manifest on the bias voltage V_SD versus V_G map as Coulomb diamonds. The addition energy E_add and the lever arm α are indicated in relation to the width and height of the Coulomb diamonds. The transport through excited states is represented by pink lines. The energy spacing $(E_{N+1} - E_N)$ can be determined by analyzing the height of their intersection with the boundary of the Coulomb diamonds.

which relates to both E_C and the energy spacing $(E_{N+1} - E_N)$ between two discrete energy levels. As a consequence of the finite E_add, the tunneling of charge carriers can be suppressed at low temperatures, which gives rise to a phenomenon known as Coulomb blockade. See Fig. 2.1(b) for the case when $\mu(N) < \mu_\mathrm{S} = \mu_\mathrm{D1} < \mu(N+1)$ [10]. The Coulomb blockade can be overcome by tuning the gate voltage V_G, to achieve $\mu(N) = \mu_\mathrm{S} = \mu_\mathrm{D1}$. Additionally, the bias voltage $V_\mathrm{SD} = V_\mathrm{S} - V_\mathrm{D}$ needs to be adjusted to a value that guarantees the bias window between V_S and V_D covers more than one energy level of the QD. Fig. 2.1(b) illustrates an example where $\mu_\mathrm{S} > \mu(N) > \mu_\mathrm{D2}$.

Characterizing the conductance through the QD in relation to the gate voltage V_G and the bias voltage V_SD yields Coulomb diamonds [11], as illustrated in Fig. 2.1(c). The charge transport is impeded by the emergence of Coulomb blockade within these diamonds, leading to a fixed charge number for the QD for each Coulomb diamond. In the absence of a bias, the conductance through the QD is non-zero only at the junction points where two adjacent Coulomb diamonds intersect. These junction points occur when the electrochemical potential of the QD ground state (μ_N) precisely aligns with the Fermi level of the source and drain. Moving along the V_G axis, the charge number in adjacent Coulomb diamonds increments by one. Occasionally, at high bias voltage V_{SD}, transport processes involving excited states, such as $\mu(N+1)$ in Fig. 2.1(b), can emerge outside the blockade regions, running parallel to the edges of the Coulomb diamonds associated with ground state transport. The distance from these charge transitions to the edge of the Coulomb diamonds provides direct insights into level spacings based on the corresponding $-|e|V_{SD}$ values, as labeled in Fig. 2.1(c). Furthermore, the height of a Coulomb diamond provides a direct measure of E_{add}. The ratio of height to width in each Coulomb diamond represents the lever arm of the gate, which is defined as $\alpha = C_G/C_0$.

2.1.2. DOUBLE DOTS

By applying the same model and assumptions as those used for the single QDs, we can derive the equivalent circuit for two QDs in series, with its schematic illustrated in Fig. 2.2(a). In this double quantum dot (DQD) configuration, the tunnel barrier between the two QDs is represented by a mutual capacitance C_M in parallel with a resistance R_M. The value of C_M reflects the capacitive coupling between the two QDs, enabling charge transitions between them and regulating the interdot tunneling strength t_C.

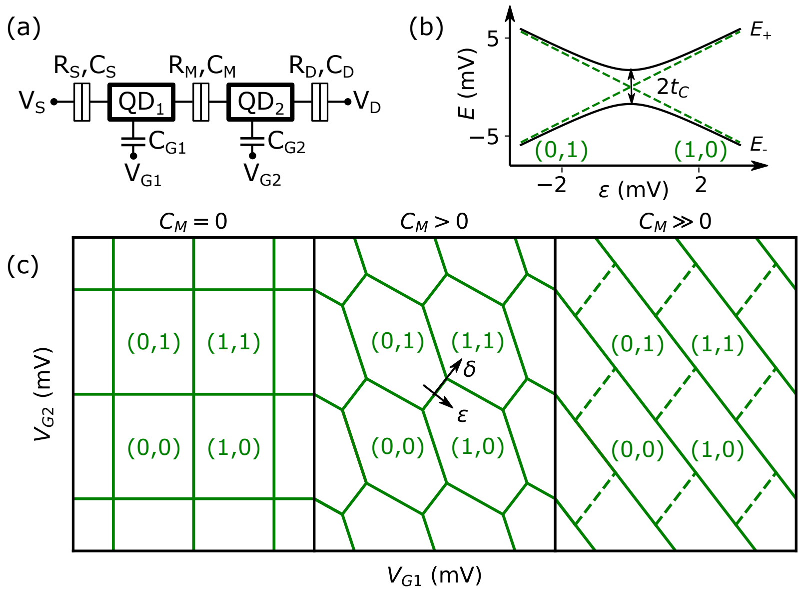

Figure 2.2: **Double quantum dot (DQD). (a)** The equivalent circuit model of a DQD system, in which the two QDs are coupled in series. **(b)** The hybridization spectrum of the two charge states (N_1+1, N_2) and (N_1, N_2+1) arises from interdot coupling t_C. **(c)** The charge stability diagrams that depict the equilibrium electron numbers corresponding to (N_1, N_2) in the gate space defined by V_{G1} and V_{G2}, as the mutual capacitance C_M is varied. Here, $N_{1(2)}$ represents the charge number of QD 1(2). When $C_M = 0$, the two QDs are completely decoupled. The horizontal and vertical lines indicate the gate settings at which the number of electrons in the ground state changes. When C_M is finite, interdot transitions appear, making the charge numbers in two QDs interdependent. When C_M is large enough, the two QDs are not distinguishable, such that the system is equivalent to a single QD that is gated by both V_{G1} and V_{G2}.

We consider the scenario where QDs 1 and 2 are occupied by $N_{1(2)}$ charges respectively, with an extra charge tunneling within the DQD. With a significant tunneling strength t_C, the charge carrier is more likely to tunnel coherently, facilitating the formation of molecular-like structures within the DQD with covalent-like bonds. Due to the hybridization of the two charge states $(N_1+1,\ N_2)$ and $(N_1,\ N_2+1)$, the bonding state exhibits a lower energy level than the antibonding state. Fig. 2.2(b) plots the energy spectrum where the hybridization takes place. Here, the difference between the electrochemical potentials of the two relevant charge states is defined as the detuning ε, which can be expressed as $\varepsilon = \mu_1(N_1+1, N_2) - \mu_2(N_1, N_2+1)$. The axis orthogonal to detuning is defined as δ. In the single-charge regime, the effective Hamiltonian of a DQD system with finite t_C can be written using Pauli matrices σ_i $(i = x, y, z)$, following:

$$H_{\mathrm{DQD}} = -\frac{t_C}{2}\sigma_x - \frac{\varepsilon}{2}\sigma_z. \tag{2.4}$$

The eigenenergies for the bonding state (E_-) and the anti-bonding state (E_+) are

$$E_\pm = \pm\frac{1}{2}\sqrt{\varepsilon^2 + t_C^2}, \tag{2.5}$$

with their energy difference $E_+ - E_- = 2t_C$ at zero detuning, which is also shown in Fig. 2.2(b).

Similar to the scenario of a single QD, the gate voltages V_{G1} and V_{G2} control the electrochemical potential of QD 1 and 2, respectively. A charge stability diagram (CSD) depicts the equilibrium charge configurations based on the two gate voltages, serving as a starting point for experimental manipulations of spin or charge. As illustrated in Fig. 2.2(c), the solid green lines indicate transitions between distinct charge states, differing by a single charge movement either within the DQD or between one QD and the reservoir. As the interdot capacitance C_M approaches zero, the interdot transitions become obstructed, resulting in a CSD composed of intersecting vertical and horizontal lines. The charge number of each dot is affected only by the corresponding gate voltage, for accepting or releasing a charge from or to the reservoir. As the interdot capacitance, C_M, increases, each intersecting point in the CSD splits into two trijunctions, forming a honeycomb-like pattern where each charge state resides in a hexagonal region. Trijunctions occur when three charge states are energetically degenerate, indicating that the two QD states are in resonance with each other and also with the reservoirs. The charge transitions between the two QDs are illustrated as diagonal line segments. When a sufficiently large C_M is in place, the two QDs are effectively treated as a single entity, with both V_{G1} and V_{G2} adjusting its energy. In this scenario, charge states with the same total charge number merge, while the anti-diagonal transition lines indicate that the system exchanges charge with the reservoir.

2.1.3. SPIN-ORBIT INTERACTION

In the context of atomic physics, spin-orbit interaction (SOI) refers to the interaction between the spin of an electron and its motion, which gives rise to shifts in the energy levels of the electron. Electrons moving in an electric field **E** experience the influence of an effective magnetic field **B**, typically perpendicular to **E** and the velocities **v**, given by

$\mathbf{B} = \mathbf{v} \times \mathbf{E}/c^2$. Originating from a nonrelativistic approximation of the relativistic Dirac equation, the Hamiltonian of the SOI can be formulated as [4]:

$$H_{\mathrm{SO}} = -\frac{\hbar}{4m_0^2c^2}\sigma \cdot \mathbf{p} \times (\nabla V_0), \tag{2.6}$$

with $\hbar$ the reduced Planck's constant, m_0 the free electron mass, c the speed of light. Here, the vector $\sigma = (\sigma_{\mathbf{x}}, \sigma_{\mathbf{y}}, \sigma_{\mathbf{z}})$ corresponds to the Pauli spin matrices, while $\mathbf{p}$ signifies the momentum operator. The term V_0 denotes the Coulomb potential of the nucleus, where the electric field produced by the charged atoms within the lattice is given by the equation $\mathbf{E} = -\nabla V_0$. The dependence of H_{SOI} on the gradient of V_0 implies that an increase in the nuclear charge results in a corresponding enhancement of the SOI effect. Eq. 2.6 also allows us to ascertain that the spin of an electron rotates independently of its velocity, but is determined solely by the distance traversed[3]. The quantity spin-orbit length l_{SO} describes the distance associated with a π rotation of the spin.

Generally in semiconductors, the Kramers degeneracy[4] of states obeys the principle of spatial inversion symmetry of the crystal lattice, and the time reversal symmetry at zero magnetic field [12]. Both of the two symmetries transforms the wavevector $\mathbf{k}$ of an electron into $-\mathbf{k}$, namely $E_\uparrow(\mathbf{k}) = E_\uparrow(-\mathbf{k})$, while the latter inverts the orientation of the spin, follows $E_\uparrow(\mathbf{k}) = E_\downarrow(-\mathbf{k})$. Under the effect of both, we get $E_\uparrow(\mathbf{k}) = E_\downarrow(\mathbf{k})$ that implies spin degeneracy. By applying finite external magnetic field, we can break the time reversal symmetry, and lift the degeneracy of opposite spin by the Zeeman energy. The breaking of inversion symmetries results in the emergence of Dresselhaus and Rashba contributions to the SOI Hamiltonian. These contributions can be attributed to the violation of bulk inversion symmetry and structure inversion symmetry, respectively.

Starting from two-dimensional electron gas, the Dresseulhaus term is characterized by Dresselhaus coefficient β_D that is relevant to the band structure parameters of the material and the thickness of the electron gas in the growth direction. The Rashba term, described by its coefficient α_{r}, is dependent on the applied $\mathbf{E}$ along the growth direction. Therefore, the hamiltonian of the two-dimensional electron gas is given as

$$H^{2D} = H_0 + \alpha_{\mathrm{r}} \cdot (k_x\sigma_y - k_y\sigma_x) + \beta_D \cdot (k_x\sigma_x - k_y\sigma_y), \tag{2.7}$$

where H_0 is the energy of the electron in the absence of SOI. The Dresselhaus and Rashba contributions to the SOI are independent of each other and collectively alter the dispersion relation $E(\mathbf{k})$, and can vary depending on the material structures. As a result, it is possible that SOI is anisotropic.

For the nanowire that of interest in this thesis, InSb and InAs are both with significant effects of SOI compared to other commonly-used materials. The Rashba SOI is dominant in InAs, rendering it an optimal platform for investigating the Rashba effect. In contrast, both effects are of comparably large in InSb. This thesis considers solely the Rashba

[3]The greater the velocity of the electron, the more rapidly its spin rotates, and the greater the distance traversed. Ultimately, the rotation angle is determined exclusively by the distance and the strength of the spin-orbit interaction.

[4]The Kramer degeneracy refers to the degeneracy that occurs in quantum systems where each energy level is at least doubly degenearate due to the conservation of time-reversal symmetry. It ensures that for every energy eigenstate with energy $\mathbf{E}$, there exists another degenerate state with the same energy but with opposite spin.

component of the InSb nanowire, as the Dresselhaus term is deemed to be negligible when the electron is moving along the [111] crystal orientation in a zinc-blende crystal, which corresponds to the direction along which the nanowires are grown [13]. Therefore in one-dimentional nanowire, the hamiltonian stated in Eq. 2.7 is simplified to

$$H^{1D} = H_0 + \alpha_\mathrm{r} \cdot k_x \sigma_y. \tag{2.8}$$

The spin-orbit length for Rashba SOI is $l_\mathrm{SO} = \hbar^2 / m_e \alpha_\mathrm{r}$, with m_e as the effective mass of the electron. For zero-dimentional QDs, consider the length scale of which is smaller than l_SO, the electron spin states hardly rotate its spin affected by SOI [9]. There the SOI can be treated as a perturbation to the energy levels in QD [14]. In multi QD systems defined on nanowires, the prohibited transition between two charge states that contain both different orbital and different spin is supported by SOI.

2.2. COMPONENT 2: SUPERCONDUCTOR

Superconductors are materials that exhibit zero resistance and the exclusion of magnetic field lines under specific low-temperature conditions [15]. Analogous to the principles used in constructing semiconductor QDs, we define nanoscale structures made from superconducting materials as "superconducting islands". A superconducting island can be created by depositing superconducting materials onto a segment of a semiconductor nanowire [16]. The charging energy of the superconducting island can be elevated using electrical barrier gates, while the electrochemical potential of any subgap states can be fine-tuned with gate electrodes.

The application of superconductors has also been widely extended into the field of quantum computing, including the use of Josephson junctions in constructing superconducting qubits [17, 18]. In the pursuit of Majorana-based topological qubits, superconducting islands play an even more crucial role, as they are expected to host Majorana modes under ideal conditions [19]. This section will explain superconductivity and the characteristics of superconducting islands.

2.2.1. SUPERCONDUCTIVITY

Superconductivity encompasses a collection of macroscopic effects that has a rich history spanning the past century, starting from the early days of experimentalists working with liquefied helium. The journey began with the observation that the electrical resistance of several metals drops to zero below their critical temperature T_C, leading to the discovery of Meissner effect, where the magnetic field is excluded from entering a superconductor [20]. The phenomena of perfect conductivity and diamagnetism were initially explained by the London equations, which aimed to establish the relationship between the microscopic electric and magnetic fields [21]. However, the London equations had limitations in terms of both quantitative and certain qualitative predictions. Subsequently, the Ginzburg-Landau theory introduced a complex pseudo-wavefunction that describes the superconducting electrons based on the general Landau theory of phase transitions, thereby providing a more effective tool for phenomenological explanations of the macroscopic nature of superconducting states [22]. It went beyond the scope of the London equations in adding the variation of the number density of superconducting electrons. After a decade, it is proved to be a limiting form of the microscopic Bardeen–Cooper–Schrieffer (BCS) theory, that valid near the critical temperature [23].

The widely recognized BCS theory has revolutionized our understanding of superconductors and established a framework for calculating microscopic parameters. This theory shows that even a weak attraction, such as the electron-phonon interaction, can overcome Coulomb repulsion, leading to the formation of bound pairs of electrons. These paired electrons, known as Cooper pairs, have equal and opposite momentum and spin. Cooper pairs are classified as bosons and can undergo Bose–Einstein condensation at the Fermi energy [24], resulting in the emergence of an energy gap on the order of kT_C between the ground state and quasi-particle excitations (see Fig. 2.3(a)).

Using second quantization, the original formulation of BCS theory begins with the effective pairing Hamiltonian:

$$H_{\mathrm{BCS}} = \underbrace{\sum_{\mathbf{k}\sigma} \epsilon_{\mathbf{k}} c^{\dagger}_{\mathbf{k}\sigma} c_{\mathbf{k}\sigma}}_{H_{\mathrm{kinetic}}} + \underbrace{\sum_{\mathbf{kk'}} V_{\mathbf{kk'}} c^{\dagger}_{\mathbf{k}\uparrow} c^{\dagger}_{\text{-}\mathbf{k}\downarrow} c_{\text{-}\mathbf{k'}\downarrow} c_{\mathbf{k'}\uparrow}}_{H_{\mathrm{pair}}}, \tag{2.9}$$

where $c^{\dagger}_{\mathbf{k}\sigma}$ and $c_{\mathbf{k}\sigma}$ corresponds to the electron creation and annihilation operator, respectively, with $\mathbf{k}$ denoting momentum and σ denoting spin. The electron number operator $c^{\dagger}_{\mathbf{k},\sigma} c_{\mathbf{k},\sigma}$ reflects the occupancy of the state with momentum $\mathbf{k}$ and spin σ, thus the first term of the Hamiltonian H_{kinetic} accounts for the kinetic energies of all electrons $\epsilon_{\mathbf{k}}$ relative to the Fermi level. The second term of the Hamiltonian describes the primary interaction between Cooper pairs, with $V_{\mathbf{kk'}}$ representing the effective interaction between the states $(\mathbf{k}\uparrow, -\mathbf{k}\downarrow)$ and $(\mathbf{k'}\uparrow, -\mathbf{k'}\downarrow)$.

By applying a mean field approximation to the BCS Hamiltonian and disregarding any minor fluctuations in the term $b^{\dagger}_{\mathbf{k}} \equiv \langle c^{\dagger}_{\mathbf{k}\uparrow} c^{\dagger}_{-\mathbf{k}\downarrow}\rangle$, which defines the average number of Cooper pairs, the Hamiltonian in Eq. 2.9 can be refomulated as:

$$H_{\mathrm{BCS,mean}} = \sum_{\mathbf{k}\sigma} \epsilon_{\mathbf{k}} c^{\dagger}_{\mathbf{k}\sigma} c_{\mathbf{k}\sigma} - \sum_{\mathbf{k}} (\Delta_{\mathbf{k}} c^{\dagger}_{\mathbf{k}\uparrow} c^{\dagger}_{-\mathbf{k}\downarrow} + \Delta^{*}_{\mathbf{k}} c_{-\mathbf{k}\downarrow} c_{\mathbf{k}\uparrow} - \Delta_{\mathbf{k}} b^{\dagger}_{\mathbf{k}}). \tag{2.10}$$

There, the electron pairing term $\Delta_{\mathbf{k}} \equiv -\sum_{\mathbf{k'}} V_{\mathbf{kk'}} \langle c_{\text{-}\mathbf{k'}\downarrow} c_{\mathbf{k'}\uparrow}\rangle$ gives the superconducting gap in the energy spectrum.

The complete Hamiltonian in Eq. 2.10 can be diagonalized through the implementation of a Bogoliubov transformation, providing the stationary solutions to the corresponding Schrödinger equation [25]. The transformation introduces genuinely fermionic operators $\gamma_{\mathbf{k}}$ that is typically written as:

$$\begin{aligned} c_{\mathbf{k}\uparrow} &= u^{*}_{\mathbf{k}} \gamma_{\mathbf{k}0} + v_{\mathbf{k}} \gamma^{\dagger}_{\mathbf{k}1} \\ c^{\dagger}_{-\mathbf{k}\downarrow} &= -v^{*}_{\mathbf{k}} \gamma_{\mathbf{k}0} + u_{\mathbf{k}} \gamma^{\dagger}_{\mathbf{k}1}. \end{aligned} \tag{2.11}$$

The operator $\gamma_{\mathbf{k}0}$ corresponds to either annihilating an electron with $\mathbf{k}$ and spin up, or creating an electron with $-\mathbf{k}$ and spin down. Both the two cases brings about a decrease of the system momentum by $\mathbf{k}$, while similarly, the operator $\gamma^{\dagger}_{\mathbf{k}1}$ is responsible for increasing the system momentum by $-\mathbf{k}$. The numerical coefficients $u_{\mathbf{k}}$ and $v_{\mathbf{k}}$ satisfing

$$|v_{\mathbf{k}}|^2 = 1 - |u_{\mathbf{k}}|^2 = \frac{1}{2}(1 - \frac{\epsilon_{\mathbf{k}}}{E_{\mathbf{k}}}) \tag{2.12}$$

are electron- and hole-like coherence factors, respectively. The excitation energy of a quasi-particle with momentum $\hbar\mathbf{k}$ is given by $E_\mathbf{k} = (\epsilon_\mathbf{k}^2 + |\Delta_\mathbf{k}|^2)^{1/2}$. In the new basis, the BCS Hamiltonian can be rewritten as

$$H_{\rm BCS} = \sum_\mathbf{k}(\epsilon_\mathbf{k} - E_\mathbf{k} + \Delta_\mathbf{k} b_\mathbf{k}^*) + \sum_\mathbf{k} E_\mathbf{k}(\gamma_{\mathbf{k}0}^\dagger \gamma_{\mathbf{k}0} + \gamma_{\mathbf{k}1}^\dagger \gamma_{\mathbf{k}1}). \tag{2.13}$$

The first sum is a constant value corresponding to the ground state energy of quasi-particles, signifying the condensation energy of Cooper pairs. The second term accounts for the additional energy beyond the ground state, expressed in terms of number operators $\gamma_\mathbf{k}^\dagger\gamma_\mathbf{k}$, where the fermionic operator $\gamma_\mathbf{k}$ here describes the elementary quasi-particle excitation of the system. These quasi-particles are commonly referred to as Bogoliubov quasi-particles. By inverting Eq. 2.11, we find:

$$\begin{aligned}\gamma_{\mathbf{k}0}^\dagger &= u_\mathbf{k} c_{\mathbf{k}\uparrow}^\dagger - v_\mathbf{k} c_{\text{-}\mathbf{k}\downarrow}\\ \gamma_{\mathbf{k}1}^\dagger &= u_\mathbf{k} c_{\text{-}\mathbf{k}\downarrow}^\dagger + v_\mathbf{k} c_{\mathbf{k}\uparrow},\end{aligned} \tag{2.14}$$

meaning that the quasi-particle locating far above (below) the Fermi level is more electron- (hole-) like.

It should be noted that the condensation of Cooper pairs in BCS theory differs from the condensation of pure bosonic particles. This distinction arises primarily because the spatial extension of a Cooper pair is quite large, leading to significant overlap with one another in real space. The average distance between two electrons in a Cooper pair is on the order of the coherence length, defined by $\xi = 2\hbar v_{\rm F}/\pi\Delta$, where $v_{\rm F}$ is the Fermi velocity and Δ is the superconducting gap.

The quasi-particle excitations in a superconductor are denoted as $\gamma_\mathbf{k}^\dagger$, being analogous to the representation of electrons in a typical metal as $c_\mathbf{k}^\dagger$. The density of quasi-particle states $N(E)$ can be calculated via $N(E)dE = n(\varepsilon)d\varepsilon$, with $n(\varepsilon)$ refer to the density of normal electron states at energy ε. Since the relevant energy scale is close to the Fermi energy, we take $n(\varepsilon) = n_0$ as a constant. Then below the superconducting gap, namely for $E < \Delta$, $N(E)$ is zero, while for $E > \Delta$, $N(E) = n_0 E/\sqrt{E^2 - \Delta^2}$, result in a coherence peak at $E = \Delta$, as the filled region in Fig. 2.3(a) shows. Sometimes the superconducting gap is not "hard" enough to follow the above energy distribution, but obtains quasiparticle excitations, an example of a subgap state with energy E_0 is also marked in Fig. 2.3(a). The Majorana bound state of great interest is the special case when such subgap state has E_0 pinned to zero. Here and later, E_0 can also generally denoting the lowest energy state within the superconductor, it equals to Δ when subgap states are absent.

2.2.2. SUPERCONDUCTING ISLANDS

We obtain a superconducting island when a normal QD mentioned in Sec. 2.1.1 is made of superconductor. The above BCS theory suggests that the ground state energy of such an island is determined by the parity of the charge number, rather than the charge number itself. Assume finite E_0 with the island initially occupied by an even number of charges, adding an extra electron to the island requires additional E_0 to reach the quasi-particle excitation energy, while adding two extra electrons to the island requires no energy because they form a Cooper pair sticking to the Fermi level. This lead to the so-

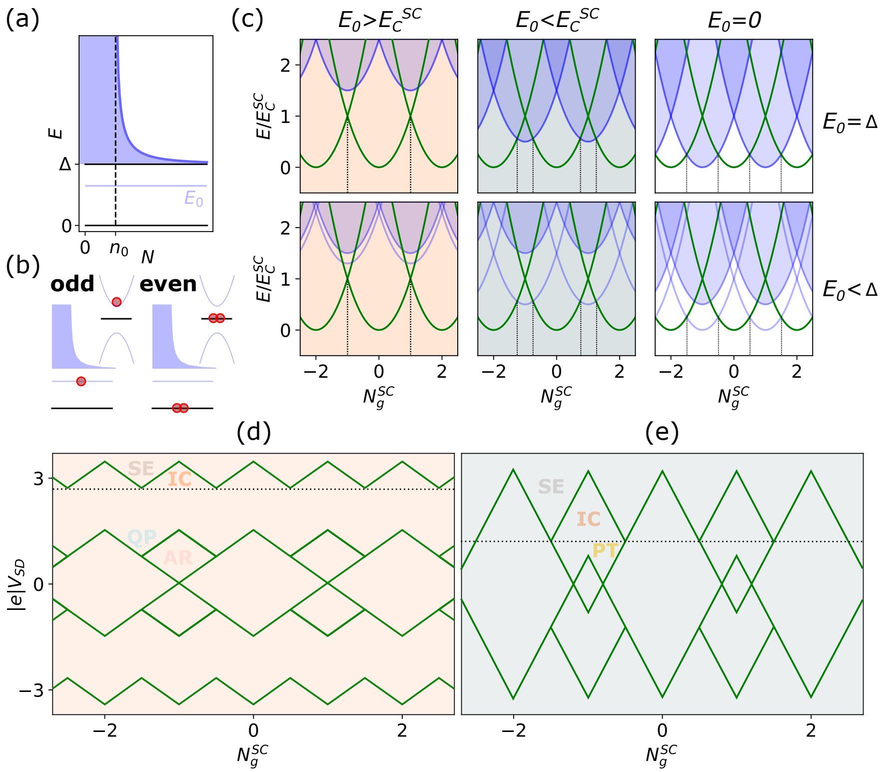

Figure 2.3: **Single superconducting island.** **(a)** Density of states in superconductors. When $E < \Delta$, all states below the gap in a normal metal are shifted to higher energy levels above the gap in a superconducting state, unless the gap is "soft" and there exist subgap states. We expect a sharp increase in state density just above $E = \Delta$, and $N(E) \approx n_0$ when $E \gg \Delta$, meaning it get close to the density of electron states for a normal metal. **(b)** A schematic showing the different cases when odd or even electrons stay in a superconducting island. **(c)** The energy dispersions of a single superconducting island, exhibiting the parity effect. The top(bottom) row corresponds to the island with(without) subgap states. The left column represents when $E_0 > E_C^{SC}$, there we obtain a 2e-periodic ground state with only Cooper pairs allowed to transfer. The middle column represents when $E_0 < E_C^{SC}$, there the even or odd charge states can be distinguished from the iterating spacing of the ground state. The right column represents when $E_0 = 0$, there we obtain a 1e-periodic ground state with single quasiparticles tunneling permitted. The Coulomb diamonds for a superconducting island with transport regimes, **(d)** for $E_0 > E_C^{SC}$, and **(e)** for $E_0 < E_C^{SC}$. The black dashed lines marks the energy equals to 2Δ. For the sake of simplicity, processes involving three or more electrons are neglected.

called parity effect. Figure 2.3(b) schematically compares the cases of an superconducting island occupied by an odd versus an even number of charges.

Figure 2.3(c) presents a series of energy parabolas that clearly illustrate the circuit energy E of a superconducting island as a function of the gate charge, assuming no bias voltage is applied. For each possible number of charges in the island N_g^{SC}, there is a shifted parabola in energy that reaches its minimum at N_g^{SC}. The green and purple parabola represent the energy diagram for even and odd charge states respectively. The lowest segments of such crossing parabolas correlate with the ground state energy occurring at different discrete N_g^{SC}, while the boundaries between different N_g^{SC} are indicated by vertical dashed lines in Fig. 2.3(c). The top and bottom row of subplots in Fig. 2.3(c) are differ in the absence or presence of a subgap state, but are identical regarding to the ground state energy. The three columns of subplots are differ in the range of the lowest energy state E_0. Specifically, we notice a 1e(2e)-periodicity of the charging energy when $E_0 = 0 (E_0 > E_C^{SC})$, and an iteration of charging energy for even and odd charge numbers when $E_0 < E_C^{SC}$. The resulting Coulomb diamonds are presented in Fig. 2.3(d-e).

When $E_0 > E_C^{SC}$, the sequential charge tunneling inside the diamonds is prevented by Coulomb blockades, similar to a normal QD, but with the diamonds higher and twice as wide[5]. Another difference is at zero-bias degeneracy points, the switching between charge states occurs by means of Cooper pair tunneling, that do not have to create a quasiparticle on entering the island. Around such degeneracy points allows Andreev reflection (AR), where the electron is reflected from the island as a hole. Unlike the elastic Andreev reflection, here the electron and hole energies must be differed by the charging energy of the island E_C^{SC}. When the bias exceeds the boundary of the Andreev reflection region, quasiparticles are allowed to enter the island, quenching the two-electron transport current and forming the region of quasiparticle poisoning (QP). Other low-voltage process such as the co-tunneling of three electrons are omitted in Fig. 2.3(d) for simplicity, partly because the rather small rate of the process prohibits experimental observation. With sufficiently high bias up to $|e|V_{SD} > 2\Delta$, inelastic cotunneling (IC) can happen as single quasiparticle tunneling becomes dominant. This process produces four quasiparticles, including one in each normal metal contact and two in the island. A single-electron transfer (SE) region appears in a bias voltage above all other transport regimes, where quasiparticles in the island can reach higher excited states.

When $E_0 < E_C^{SC}$, there are similar transport regimes as with $E_0 > E_C^{SC}$ at high bias although with different shapes. When the bias is less than 2Δ, we notice that the Coulomb blockade regimes for even numbers of charges are larger than those for odd numbers. Near the degeneracy points between the charge states with even and odd number of electrons, the island holds single-charge transfer process that we note as parity tunneling (PT). The occurrence of these various charge tunneling events serves to exemplify the elegance of a hybrid semiconductor-superconductor system.

2.3. COMPONENT 3: DISPERSIVE GATE SENSING

Fast readout is essential for studying dynamic phenomena in quantum devices, enabling experiments that surpass time-averaged measurements, such as the conventional transport measurements [26, 27, 4]. As an example of fast readout, radio frequency (RF) reflectometry can rapidly detect changes in impedance over very short timescales [28]. This method involves sending RF signals into a system and analyzing the reflected signals to gather information about the properties of the circuit components.

Dispersive gate sensing is one of the specific applications of this RF technique, which makes use of gate voltage modulation to manipulate the energy levels of QDs [29, 30, 31]. This leads to a dispersive shift in the resonant frequency of microwave resonators. By monitoring this frequency shift, we gain insight into the charge state of QDs, enabling

[5]Doubling the charge unit e results in the addition energy E_{add} increasing fourfold.

non-invasive readout and control of quantum states at each single-electron level. This method is essential for advancing quantum computing technologies and is being developed for possible topological or spin qubits in the last decade [32, 33]. At the operational level, gate sensing requires careful consideration during the design process, however, it can simplify the design of quantum systems compared to other popular method[6]. The core of this thesis is based on the capacitance measurements using RF reflectometry and dispersive gate sensing.

2.3.1. CIRCUIT AND IMPEDANCE

Traditional transport measurements operate in DC circuits, where resistance R controls current flow I via Ohm's law ($V = IR$). In high frequency circuits, the interplay of resistance and reactance cannot be ignored, thus the impedance Z takes precedence and represents their combined effect. The system to be measured in high frequency circuits, together with the tank circuit, acts as a load on the transmission line and presents a total impedance Z_{load} (see Fig. 2.4(a)). When the value of Z_{load} differs from the characteristic

[6]Charge sensing requires an additional quantum segment to be capacitively coupled to the area of interest, while transport measurements need metal contacts. In contrast, gate sensing imposes no additional requirements on the quantum system being measured.

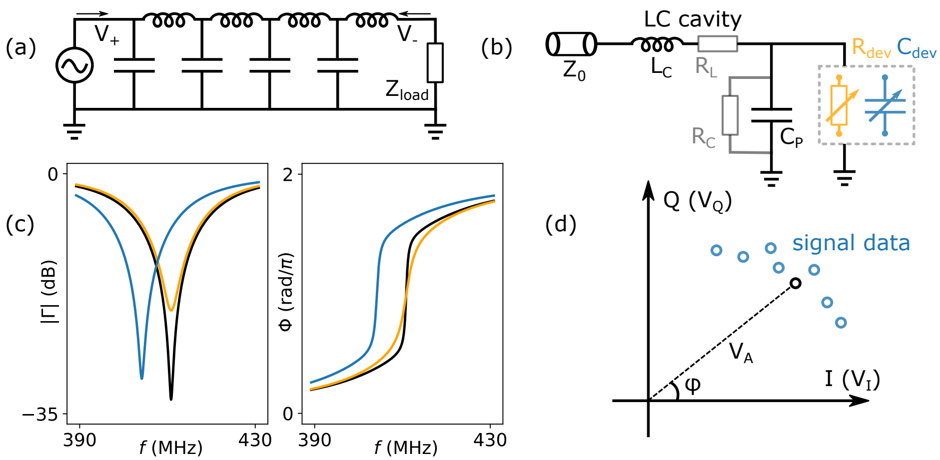

Figure 2.4: **Impedance and reflections.** **(a)** Schematic of an equivalent lumped element circuit. The output signal V_+ comes from the high frequency generator, is transmitted through the line and results in a reflected portion V_- when it reaches the load. **(b)** Schematic of a reflectometry circuit used to measure a variable resistor or a variable capacitor. The device to be measured is inserted into an LC cavity consisting of an inductor and a capacitance C_P to match the characteristic impedance Z_0 of the line. The resistance R_L models ohmic losses in the inductor, and R_C models the dielectric losses in the capacitor. Ideally for good matching network, R_L is at its maximum and R_C at its minimum. **(c)** The magnitude and phase spectrum of the reflection coefficient $|\Gamma|$ for a bare resonator couple to a resistor $R_0 = 60$ kΩ (black), comparing with the case when it couples to additional resistive device (orange) or a reactive device (blue). The resonator has a inductance of 500 nH, with $R_L = 20$ Ω, $R_C = 100$ MΩ, $C_P = 0.3$ pF. The resistance introduced by the resistive device $R_{\text{dev}} = 20$ kΩ, while the capacitance introduced by the reactive device $C_{\text{dev}} = 10$ fF.

impedance $Z_0 = 50\ \Omega$ of commercial coaxial cables[7], the impedance mismatch causes part of the signal to be reflected back. The reflection coefficient $\Gamma(\omega)$ of the incident signal is then defined with the angular frequency ω as follows

$$\Gamma(\omega) = \frac{V_-(x=0,\omega)}{V_+(x=0,\omega)} = \frac{Z_{\text{load}}(\omega) - Z_0}{Z_{\text{load}}(\omega) + Z_0}. \tag{2.15}$$

There V_+ (V_-) is describing the signal voltage propagating in the positive (negative) direction, and $x = 0$ marks the location along the cable. Close to its resonance, a resonator can be effectively represented by an equivalent LCR circuit consisting of an inductor L, a capacitor C and a resistor connected in series, giving the impedance

$$Z_{\text{load}}(\omega) = j\omega L + \frac{1}{j\omega C} + R. \tag{2.16}$$

The resonant frequency $f_\text{r} = 1/2\pi\sqrt{LC}$ is therefore derived with $f = \omega/2\pi$. Such resonance causes a dip in the amplitude of $|\Gamma|$, which is usually described in unit of decibels with the transformation $|\Gamma|_\text{dB} = 20\log_{10}(|\Gamma|)$. The corresponding phase spectrum $\Phi = \arg(\Gamma)$.

A quantum device to be measured can be considered as an element embedded in a circuit in Fig. 2.4(b). The circuit schematic assumes a resistor R_L in series with the matching inductor L_C and a resistor R_C in parallel with the parasitic capacitor C_P. Depending on how the device responds to electrical currents and voltages, the element can be either a resistor R_dev or a capacitor C_dev, corresponding to a resistive or reactive device respectively. The orange curve in Fig. 2.4(c) shows the effect of a resistive device on the signal reflection, in this case changing the depth of the dip in $|\Gamma|$, but keeping f_r the same. A reactive device, on the other hand, changes the capacitance or inductance, which ultimately affects f_r and shifts $\Phi(f)$ horizontally. The change in resonant frequency is measurable when the quantum device functions as a variable capacitor C_dev, as demonstrated in the experiments included in this thesis:

$$\Delta f = f_\text{r}' - f_\text{r}^0 = \frac{1}{2\pi}\left[\frac{1}{\sqrt{L_\text{C}(C_\text{P} + C_\text{dev}')}} - \frac{1}{\sqrt{L_\text{C}(C_\text{P} + C_\text{dev}^0)}}\right]. \tag{2.17}$$

Here, f_r' and C_dev' denote the signal data measured at specific gate voltages of interest, while f_r^0 and C_dev^0 are associated with the Coulomb blockade regime.

These resonance dips have an inverse Lorentzian shape, with their bandwidth BW as the full width at half maximum of the reflected power. Alternatively, it can be expressed as being approximately -3 dB from the top when plotted in logarithmic units. The bandwidth is determined by the rate at which energy is lost from the resonator and includes both internal losses (such as dissipation) and external losses (such as radiation to the transmission line). A dimensionless parameter Q called the quality factor is therefore defined as the ratio of the resonant frequency to its bandwidth to describe the efficiency of

[7]The $Z_0 = 50\ \Omega$ characteristic impedance of coaxial cables balances power handling and signal loss, making it optimal for most RF and microwave applications. This value is widely accepted as a standard for RF equipment.

energy storage and dissipation in the resonant system. The corresponding internal quality factor Q_{in}, external quality factor Q_{ex}, and the total quality factor $Q_{\mathrm{tot}} = (Q_{\mathrm{in}}^{-1} + Q_{\mathrm{ex}}^{-1})^{-1}$ describing their combination are respectively:

2

$$Q_{\mathrm{in}} = \frac{1}{R}\sqrt{\frac{L}{C}} = \frac{2\pi f_{\mathrm{r}} L}{R}, \quad Q_{\mathrm{ex}} = \frac{1}{Z_0}\sqrt{\frac{L}{C}} = \frac{2\pi f_{\mathrm{r}} L}{Z_0}, \quad Q_{\mathrm{tot}} = \frac{1}{R+Z_0}\sqrt{\frac{L}{C}}. \tag{2.18}$$

A large Q_{tot} is desirable for fast readout measurements to maximize the sensitivity of relevant circuit parameters, while simultaneously limiting the bandwidth $BW = f_{\mathrm{r}}/Q_{\mathrm{tot}}$ and resulting in a sharper resonance dip in Fig. 2.4 (c). Of the two components, Q_{in} reflects the internal losses within the resonator, while Q_{ex} considers losses associated with external components connected to the resonator. Therefore, for the applied fitting models in Sec. 2.3.3, we assume that Q_{ex} is constant and only Q_{in} varies under the influence of the quantum device. One standard way of representing a periodic signal is in terms of amplitude A and phase φ, expressed as $V(t) = V_A \cos(\omega t + \varphi)$. Another way is to define a pair of the in-phase component $V_I = V_A \cos(\varphi)$ and the out-of-phase quadrature component $V_Q = V_A \sin(\varphi)$, so that the signals can be generated on the IQ plane for analysis, as in Fig.2.4(d).

2.3.2. PARAMETRIC CAPACITANCE

In the previous Sec. 2.3.1 we explained the basics of the high frequency circuit and the reflection technique, which is well suited to the study of charge dynamic phenomena. Practically, implementing RF reflectometry for charge sensors such as single electron transistors or quantum point contacts is equivalent to integrating a resistive device into a matching network (as shown in Fig. 2.4(b)). However, one of the disadvantages of using indirect charge sensors is that they increase the complexity of the geometry. This complexity is alleviated by measuring dispersive signals arising from quantum capacitance C_{q}, which can be directly detected using the existing gates designed for multiple purposes[8].

Quantum capacitance measures electronic properties in quantum systems, especially in the context of low-dimensional systems where the density of states is low. It is a correction to the capacitance that associated with the density of electronic states and plays a crucial role in determining charge dynamics. Let C_{geom} represent the geometrical capacitance formed by a metallic electrode and a mesoscopic conductor separated by a dielectric layer. When a voltage ΔV_{G} is applied to the electrode, it induces changes in both the electrostatic ($\Delta V_{\mathrm{es}} = e\Delta N/C_{\mathrm{geom}}$, with ΔN being the charge number difference) and chemical potential ($\Delta V_{\mathrm{cp}} = \Delta\mu/e$, with μ being the chemical potential). The total capacitance of the sample C_{dev} is then composed by C_{geom} in series with quantum capacitance C_{q}:

$$C_{\mathrm{dev}}^{-1} = \frac{\Delta V_{\mathrm{G}}}{e\Delta N} = \frac{\Delta V_{\mathrm{es}} + \Delta V_{\mathrm{cp}}}{e\Delta N} = \frac{1}{C_{\mathrm{geom}}} + \frac{1}{e^2}\frac{d\mu}{dN} = C_{\mathrm{geom}}^{-1} + C_{\mathrm{q}}^{-1}. \tag{2.19}$$

For devices with negligible level spacing, the value of C_{q} is infinite and $C_{\mathrm{dev}} = C_{\mathrm{geom}}$. Note this expression of $C_{\mathrm{q}} = e^2 \frac{dN}{d\mu}$ refers to the definition of electron compressibility $K =$

[8]For example, for tuning the chemical potential of a quantum dot.

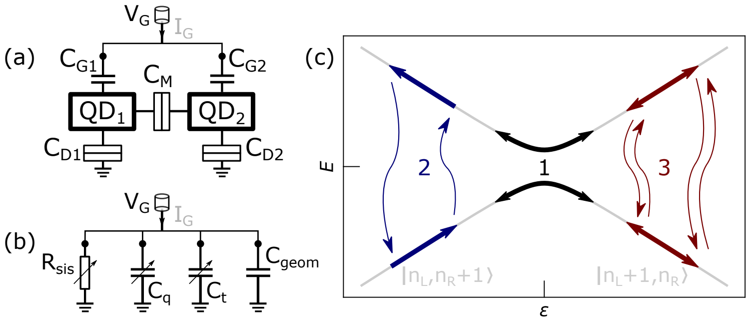

Figure 2.5: **Equivalent circuit for a DQD and the relevant physical processes.** **(a)** The DC version of equivalent circuit for a DQD seen from the gate electrode. **(b)** The AC version of the equivalent circuit for a DQD, including the quantum capacitance C_q, the tunneling capacitance C_t and the Sisyphus resistance R_{sis}. **(c)** The ground state energy and the excited state energy of the DQD as a function of the detuning. The arrows overlapping such energy states indicate the effects caused of an RF voltage source. The wiggly lines with arrows pointing down and up indicate phonon emission and absorption processes respectively. The sets of arrows labelled with numbers and different colors represent the origin of (1) C_q, (2) both R_{sis} and C_t, (3) pure C_t.

$\frac{1}{N^2}\frac{dN}{d\mu}$ [34]. It is sometimes called electron compressibility at finite temperature, and the strict definition quantum capacitance is used at absolute zero temperature to represent the capacitance behaviour resulting solely from quantum effects. The application of the same technique to the measurement of electron compressibility is shown in Chapter. **??**.

For DQD weakly coupled to the reservoirs, as shown in Fig. 2.5, the capacitance term instead consists of a parametric capacitance C_{pm} in parallel to C_{geom}. The latter contains components from two distinctive origin: the pure quantum capacitance C_q and the tunneling capacitance C_t. Consider a small amplitude gate voltage $V_G = \delta V_G \sin(\omega t)$ that drives the system. The equivalent circuit illustrated in Fig. 2.5(a) provides the relevant parameters, including the gate capacitances C_{Gi}, the capacitance to ground C_{Di}, and the mutual capacitance C_M, where i is the index of the quantum dots. The gate current I_G is defined in relation to the total net charges of Q_i in QD_i, as indicated in the left-most part of Eq. 2.20. With the excitation frequency much smaller than the DQD charge transfer frequency $\omega \ll t_C/\hbar$, the equivalent impedance of the DQD can be described as $Z_{eq} = V_G/I_G$.

To get the analytical form of Z_{eq}, we define the gate coupling factors $\alpha_i = C_{Gi}/(C_{Gi} + C_M + C_{Di})$ and the charge occupation probability in QD_i as P_i. The total charge of the system is $Q_1 + Q_2 = \sum_i \alpha_i (C_{Di} V_G + eP_i)$, and for interdot transitions the charge occupations follow $dP_2/dt = -dP_1/dt$. The total I_G in the weak coupling limit $C_M \ll C_{Gi} + C_{Di}$ can then be expressed as

$$I_G = \frac{d(Q_1+Q_2)}{dt} = \sum_i \alpha_i \left(C_{Di}\frac{dV_G}{dt} + e\frac{dP_i}{dt}\right) = (C_{geom} + C_{pm})\frac{dV_G}{dt}, \tag{2.20}$$

where $C_{geom} = \sum_i \alpha_i C_{Di}$, the parametric capacitance $C_{pm} = (e\alpha')^2 dP_r/d\varepsilon$ with $\alpha' = \alpha_2 - \alpha_1$, and detuning $\varepsilon = \mu_2 - \mu_1 = e\alpha'\Delta V_G$. There P_r denotes the charge occupancy for the readout dot[9], in some literature are marked as $\langle N \rangle$ [35]. The expression of C_{pm} refers to

[9]The quantum dot that coupled to the resonator.

2

changes in charge occupancy resulting from time-dependent variations in detuning.

In order to distinguish the physical mechanisms leading to charge redistribution, we start from the Hamiltonian of a DQD as referenced in Eq. 2.4, which yields the eigenenergies $E_\pm = \pm(\varepsilon^2 + t_C^2)^{1/2}/2$. The energy difference is given by $\Delta E = E_+ - E_-$. The probability in the readout dot charge basis P_r

$$P_r = P_r^- P_- + P_r^+ P_+ = \frac{1}{2}[1 + \frac{\varepsilon}{\Delta E}\chi] \tag{2.21}$$

then includes $P_r^\pm = (1 \mp \varepsilon/\Delta E)/2$ and $P_\pm$ as the probabilities in the ground and excited state energy basis. The term $\chi = P_- - P_+$ denotes the polarization of the system in the energy basis. In the context of a two-level quantum system, χ is the Boltzmann factor associated with the energy difference between the two levels (denoted as ΔE) at a given temperature, representing the probability of the upper level being occupied due to thermal effects.

With the system driven by $\varepsilon(t) = \varepsilon_0 + \delta\varepsilon \sin(\omega t)$ and with ε_0 the zero detuning, we assume the excitation rate $\omega \ll t_C^2/\hbar\delta\varepsilon$ being low to avoid Landau-Zener transitions. Expanding the parametric part in Eq. 2.20 under this condition, we have

$$C_{pm} = (e\alpha')^2 \frac{dP_r}{d\varepsilon} = \frac{(e\alpha')^2}{2}[\frac{\partial^2 E_+}{\partial \varepsilon^2}\chi + \frac{\varepsilon}{\Delta E}\frac{\partial \chi}{\partial \varepsilon}]. \tag{2.22}$$

Its first term links to the strict description of C_q in QDs and coincides with the electron compressibility at $T = 0$ K (see Fig. 2.5(c) process 1). The second term links to irreversible redistribution processes leading to Sisyphus dissipation and also to an additional source of capacitance, named as tunneling capacitance C_t (see Fig. 2.5(c) process 2 and 3). These two terms therefore indicate two different ways of changing the probability distribution of an electron in the DQD. As Fig. 2.5(c) points out, the first way is via adiabatic charge tunneling that is illustrated in process 1, while the second is via irreversible phonon absorption and emission that depicted in process 2 and 3, associated with the derivative of χ.

To further break down the expression of C_{pm}, it is necessary to calculate the changes in χ. From the Bose-Einstein distribution, which describes the statistics of particles with integer spin such as the phonon, we obtain the phonon occupation number $n_p = 1/[\exp(\Delta E/k_B T) - 1]$ that gives the probability of occupying a phonon state with energy ΔE [36]. The phonon absorption rate $\gamma_+ = \gamma_C n_p$ is then proportional to n_p, with γ_C a constant relates to the coupling strength between the phonon and the system. The phonon emission rate $\gamma_- = \gamma_C(1 + n_p)$ is similarly proportional to $(1 + n_p)$, as one additional phonon is introduced into the system during the emission. For a two-level system, $\delta\chi$ can be calculated by solving the master equation (i.e. $\dot{P}_- = -\gamma_+ P_- + \gamma_- P_+$ and $\dot{P}_+ = \gamma_+ P_- - \gamma_- P_+$) to first order approximation in $\delta\varepsilon/t_C$. With $\gamma_{tot} = \gamma_+ + \gamma_-$ being the characteristic relaxation rate of the system, and η essentially represents the difference between the rates of change of $\gamma_\pm$ with respect to the gate charge at equilibrium, we obtain

$$\delta\chi = \frac{-2\eta\delta\varepsilon}{\omega^2 + \gamma_{tot}^2}[\gamma_{tot}\sin(\omega t) - \omega\cos(\omega t)]. \tag{2.23}$$

There $\Delta E_0 = \Delta E(\varepsilon = \varepsilon_0)$. Ultimately, by averaging over a complete cycle of the RF signal after inserting the full form of Eq. 2.22, we conclude

$$
\begin{aligned}
I_{\mathrm{G}} = & \underbrace{\sum_i \alpha_i C_{Si}}_{C_{\mathrm{geom}}} \frac{dV_{\mathrm{G}}}{dt} + \underbrace{\frac{(e\alpha')^2}{2} \frac{t_{\mathrm{C}}^2}{(\Delta E_0)^3} \tanh(\frac{\Delta E_0}{2k_B T})}_{C_{\mathrm{q}}} \frac{dV_{\mathrm{G}}}{dt} \\
& + \underbrace{\frac{(e\alpha')^2}{2} \frac{1}{2k_B T} (\frac{\epsilon_0}{\Delta E_0})^2 \frac{\gamma_{\mathrm{tot}}^2}{\omega^2 + \gamma_{\mathrm{tot}}^2} \cosh^{-2}(\frac{\Delta E_0}{2k_B T})}_{C_{\mathrm{t}}} \frac{dV_{\mathrm{G}}}{dt} \\
& + \underbrace{\frac{4R_K}{\alpha'^2} \frac{k_B T}{h\gamma_{\mathrm{tot}}} (\frac{\omega^2 + \gamma_{\mathrm{tot}}^2}{\omega^2}) \cosh^2(\frac{\Delta E_0}{2k_B T})}_{R_{\mathrm{sis}}} V_{\mathrm{G}} \\
= & \underbrace{(C_{\mathrm{geom}} + C_{\mathrm{q}} + C_t)}_{C_{\mathrm{dev}}} \frac{dV_{\mathrm{G}}}{dt} + R_{\mathrm{sis}} V_{\mathrm{G}}.
\end{aligned}
\tag{2.24}
$$

This expression now gives the form of the equivalent impedance Z_{eq}, where the coefficients in the component proportional to dV_{G}/dt represent capacitances, while the one coefficient in the component proportional to V_{G} represent a conductance. Since C_{dev} is added up by the reactive terms C_{geom}, C_{q} and C_{t}, the capacitances are in parallel with each other, as shown in Fig. 2.5(b). It simultaneously shows that the Sisyphus resistance R_{sis} is also modelled in parallel with C_{dev}, as both components contribute to the overall behaviour of the system and share a part of the current I_{G} in Eq. 2.24.

2.3.3. REFLECTION COEFFICIENT

A better understanding of the quantum system with dispersive gate sensing requires appropriate fitting models to accurately convert the reflected signal into physical quantities, such as quantum capacitances. More specifically, since the resonance dips do not always directly correspond to the resonant frequency of the resonator f_{r}, it is not possible to determine the frequency shift solely from the movement of the resonance dips along the frequency axis. Instead, we fit the curve of measured reflection coefficient S_{11}[10] within a finite frequency range around f_{r} on the complex plane of S_{11}, as the described IQ plot in Sec. 2.3.1. Here the S_{ij} represents the power received at port i relative to the power input to port j. During the fitting analysis, except for Q_{in} and the resonant frequency for each data points f_{r}', all other parameters are supposed to be fixed to the values that are extracted in Coulomb blockade regime, for instance, the Q_{ex}. The goal therefore becomes to find the expression of the complex S_{11} value as a function of Q_{in} and f_{r}, with other parameters such as Q_{ex} as a given constant.

In this thesis, we mainly adopt the model that originally derived to obtain the transmission coefficient S_{21} for resonators coupled to a coplanar waveguide, and then extend it to a corresponding reflection mode to get the reflection coefficient S_{11} that we ought

[10] For a two-port network, S_{11} and Γ are equivalent, meaning that S_{11} can be considered a particular case of the reflection coefficient Γ that we mentioned before.

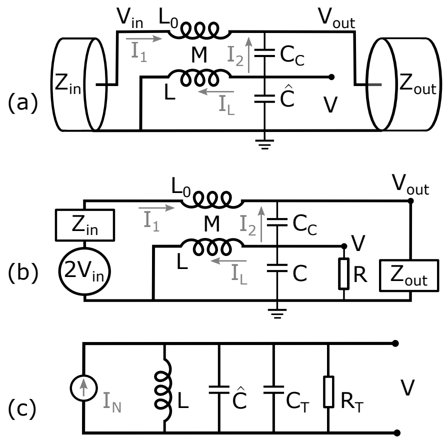

Figure 2.6: **Measurement setups on transmission lines with its equivalent circuits. (a)** A schematic illustrates the setup for measuring resonators, incorporating both inductive and capacitive coupling. The setup also includes transmission lines with mismatched characteristics. **(b)** The equivalent circuit with the complex capacitance $\hat{C}$ in (a) is separated into a capacitive part (C) and a resistive part ($1/\omega R$). **(c)** The Norton equivalent circuit for (b), with V denoting the voltage across the capacitor. This diagram helps with getting the expression of Norton equivalent conductance G_N and current I_N.

to measure. Starting with the derivation of a matched transmission line coupled to a resonator, we model the circuit as in Fig. 2.6(a) but with $Z_\mathrm{in} = Z_\mathrm{out} = Z_0$. The resonator consists of the inductor L and the capacitor $\hat{C}$, where $\hat{C}$ is a complex term whose imaginary part $1/\omega R$ takes into account the dielectric losses. V_in and V_out are the input and output voltage amplitudes, and we thereby define $S_{21} \equiv V_\mathrm{out}/V_\mathrm{in}$. Assume the transmission lines are perfectly coupled with Z_0 and $L_0 \ll C_\mathrm{C} Z_0^2$ is small, Fig. 2.6(a) can be redrawn as Fig. 2.6(b) at low loss case, namely $1/\omega R = \mathrm{Im}\{\hat{C}\} \ll \mathrm{Re}\{\hat{C}\} = C$. The Kirchhoff's equation set for the circuit in Fig. 2.6(b) can then be written as

$$\begin{aligned} 2V_\mathrm{in} - V_\mathrm{out} &= I_1(Z_0 + i\omega L_0) - i\omega M I_\mathrm{L} \\ V_\mathrm{out} &= (I_1 + I_2) Z_0 \\ V = V_\mathrm{out} + \frac{I_2}{i\omega C_\mathrm{C}} &= i\omega L I_\mathrm{L} - i\omega M I_1 = -\frac{I_2 + I_\mathrm{L}}{i\omega \hat{C}}, \end{aligned} \tag{2.25}$$

giving the expression for the transmission S_{21} as a function of V, with some approximations including $\omega C \ll 1/Z_0$ and $\{\omega L_0, \omega M^2/L\} \ll Z_0$:

$$S_{21} = \frac{V_\mathrm{out}}{V_\mathrm{in}} = 1 + \frac{V}{2V_\mathrm{in}}\left(\frac{M}{L} + Z_0 i\omega C_\mathrm{C}\right). \tag{2.26}$$

The reformulated version of Eq. 2.25 after eliminating V_out

$$\Big[\frac{1}{i\omega L} + i\omega\hat{C} + \underbrace{\frac{i\omega C_\mathrm{C}}{i\omega C_\mathrm{C} Z_0 + 1} + \frac{1}{2Z_0}\Big(\frac{M}{L} - \frac{i\omega C_\mathrm{C} Z_0}{1 + i\omega C_\mathrm{C} Z_0}\Big)^2}_{G_\mathrm{N}}\Big] V = \underbrace{-\frac{V_\mathrm{in}}{Z_0}\Big(\frac{M}{L} - \frac{i\omega C_\mathrm{C} Z_0}{1 + i\omega C_\mathrm{C} Z_0}\Big)}_{I_\mathrm{N}} \tag{2.27}$$

takes the form of a Norton equivalent circuit (see Fig. 2.6(c)) [37], whose current I_N and conductance G_N follows

$$(\frac{1}{i\omega L} + i\omega\hat{C} + G_N)V = I_N. \tag{2.28}$$

Since the extracted G_N term is complex, we separate its real and imaginary part by defining $\mathrm{Re}\{G_N\} \equiv 1/R_T$, $\mathrm{Im}\{G_N\} \equiv \omega C_T$, together with $1/R_{\mathrm{eff}} \equiv 1/R + 1/R_T$, $Q_{\mathrm{tot}} \equiv R_{\mathrm{eff}}\omega_0(C+C_T)$ and $\omega_0 = 1/\sqrt{L(C+C_T)}$. There the terms C_T and R_T are depicted in Fig. 2.6(c), and $\omega = 2\pi f'_r$ with $\omega_0 = 2\pi f^0_r$. Expanding the expression of G_N around the small values M/L and retaining the lowest order non-negligible terms, there is

$$S_{21} = 1 - \frac{R_{\mathrm{eff}} R_T^{-1}}{1 + 2iQ_{\mathrm{tot}}\frac{\omega-\omega_0}{\omega_0}} = 1 - \frac{Q_{\mathrm{tot}} Q_{\mathrm{ex}}^{-1}}{1 + 2iQ_{\mathrm{tot}}\frac{\omega-\omega_0}{\omega_0}} \tag{2.29}$$

which shows a basic conformal form of a coupling situation giving rise to S_{21} with Lorentzian line shape controlled by the parameters Q_{tot}, Q_{ex} and ω_0. In the ideal case discussed above, the resonance dip marks the resonant frequency.

However, when $Z_{\mathrm{in}} \neq Z_{\mathrm{out}} \neq Z_0$, the non-ideal experimental setups shown in Fig. 2.6(a) can lead to asymmetry in the resonance line shape. In this non-ideal case, Eq. 2.26 must replace the Z_0 term with $Z'_{\mathrm{in}} \equiv Z_{\mathrm{in}} + i\omega L_0 - i\omega M^2/L$, and in the following, the whole S_{21} expression omits a dropable multiplicative factor $(1+\hat{\epsilon}) \equiv 2/[1 + (i\omega C_C + 1/Z_{\mathrm{out}})Z'_{\mathrm{in}}]$, which can compensate for an attenuation of the signal. Unlike the ideal case, which considers only the second-order expansion of M/L and $\omega C_C Z_{\mathrm{out}}$ in the left part of Eq. 2.29, the mismatched case employs the diameter correction method [38] to expand up to third order. Therefore, we can rewrite S_{21} as follows:

$$S_{21} = 1 - \frac{(G_D + R_T^{-1})R_{\mathrm{eff}}}{1 + 2iQ_{\mathrm{tot}}\frac{\omega-\omega_0}{\omega_0}} = 1 - \frac{Q_{\mathrm{tot}} \hat{Q}_{\mathrm{ext}}^{-1}}{1 + 2iQ_{\mathrm{tot}}\frac{\omega-\omega_0}{\omega_0}}, \tag{2.30}$$

where we define

$$G_D \equiv -\frac{I_N}{2V_{\mathrm{in}}}(\frac{M}{L} + Z'_{\mathrm{in}} i\omega C_C) - \frac{1}{R_T} \tag{2.31}$$

which is purely imaginary and introduces the asymmetry in the line shape. Or in other words, G_D induces a rotation of the resonance circle relative to an off-resonance point.

The right part of Eq. 2.30 is the starting point for understanding the measurements in reflection mode. Typically, the RF reflectometry is realized by directly measuring the reflected signal from a resonator shunted to ground. While measuring the quantum effects in a dilution fridge, the input line is normally heavily attenuated in order for thermalization and noise reduction. Therefore, directional coupler is used to route the reflected signal back out of the fridge along an amplified output line. The measurement of S_{11} is converted to a two-port S_{21} measurement, thus we are able to apply fittings with

$$S_{11} = 1 - \frac{2Q_{\mathrm{tot}}|Q_{\mathrm{ex}}^{-1}|}{1 + 2iQ_{\mathrm{tot}}\frac{\omega-\omega_0}{\omega_0}} e^{i\phi}, \tag{2.32}$$

where the terms $\hat{Q}_{\mathrm{ext}}^{-1}$ is represented in terms of its magnitude and phase ϕ.

2

BIBLIOGRAPHY

[1] Louis De Broglie. The wave nature of the electron. *Nobel lecture*, 12:244–256, 1929.

[2] Tapash Chakraborty. Quantum dots: A survey of the properties of artificial atoms. 1999.

[3] Mikael T Björk, Claes Thelander, Adam E Hansen, Linus E Jensen, Magnus W Larsson, L Reine Wallenberg, and Lars Samuelson. Few-electron quantum dots in nanowires. *Nano Letters*, 4(9):1621–1625, 2004.

[4] Thomas Ihn. *Semiconductor Nanostructures: Quantum states and electronic transport*. OUP Oxford, 2009.

[5] Dimitrie Culcer, Łukasz Cywiński, Qiuzi Li, Xuedong Hu, and S Das Sarma. Quantum dot spin qubits in silicon: Multivalley physics. *Physical Review B—Condensed Matter and Materials Physics*, 82(15):155312, 2010.

[6] Erika Kawakami, Pasquale Scarlino, Daniel R Ward, FR Braakman, DE Savage, MG Lagally, Mark Friesen, Susan N Coppersmith, Mark A Eriksson, and LMK Vandersypen. Electrical control of a long-lived spin qubit in a si/sige quantum dot. *Nature nanotechnology*, 9(9):666–670, 2014.

[7] Jun Yoneda, Kenta Takeda, Tomohiro Otsuka, Takashi Nakajima, Matthieu R Delbecq, Giles Allison, Takumu Honda, Tetsuo Kodera, Shunri Oda, Yusuke Hoshi, et al. A quantum-dot spin qubit with coherence limited by charge noise and fidelity higher than 99.9%. *Nature nanotechnology*, 13(2):102–106, 2018.

[8] Leo P Kouwenhoven, DG Austing, and Seigo Tarucha. Few-electron quantum dots. *Reports on progress in physics*, 64(6):701, 2001.

[9] Ronald Hanson, Leo P Kouwenhoven, Jason R Petta, Seigo Tarucha, and Lieven MK Vandersypen. Spins in few-electron quantum dots. *Reviews of modern physics*, 79(4):1217–1265, 2007.

[10] Leo P Kouwenhoven, Charles M Marcus, Paul L McEuen, Seigo Tarucha, Robert M Westervelt, and Ned S Wingreen. Electron transport in quantum dots. *Mesoscopic electron transport*, pages 105–214, 1997.

[11] S Tarucha, T Honda, DG Austing, Y Tokura, K Muraki, TH Oosterkamp, JW Janssen, and LP Kouwenhoven. Electronic states in quantum dot atoms and molecules. *Physica E: low-dimensional systems and nanostructures*, 3(1-3):112–120, 1998.

[12] Jeroen SW Lamb and John AG Roberts. Time-reversal symmetry in dynamical systems: a survey. *Physica D: Nonlinear Phenomena*, 112(1-2):1–39, 1998.

[13] R Winkler, S Papadakis, E De Poortere, and M Shayegan. *Spin-orbit coupling in two-dimensional electron and hole systems*, volume 41. Springer, 2003.

[14] Lucjan Jacak, Jurij Krasnyj, and Arkadiusz Wójs. Spin-orbit interaction in the quantum dot. *Physica B: Condensed Matter*, 229(3-4):279–293, 1997.

[15] Michael Tinkham. *Introduction to superconductivity*, volume 1. Courier Corporation, 2004.

[16] P Krogstrup, NLB Ziino, W Chang, SM Albrecht, MH Madsen, Erik Johnson, Jesper Nygård, Charles M Marcus, and TS Jespersen. Epitaxy of semiconductor–superconductor nanowires. *Nature materials*, 14(4):400–406, 2015.

[17] BRIAN D Josephson. The discovery of tunnelling supercurrents. *Reviews of Modern Physics*, 46(2):251, 1974.

[18] Frank Arute, Kunal Arya, Ryan Babbush, Dave Bacon, Joseph C Bardin, Rami Barends, Rupak Biswas, Sergio Boixo, Fernando GSL Brandao, David A Buell, et al. Quantum supremacy using a programmable superconducting processor. *Nature*, 574(7779):505–510, 2019.

[19] Liang Fu and Charles L Kane. Superconducting proximity effect and majorana fermions<? format?> at the surface of a topological insulator. *Physical review letters*, 100(9):096407, 2008.

[20] John Bardeen. Theory of the meissner effect in superconductors. *Physical Review*, 97(6):1724, 1955.

[21] Fritz London and Heinz London. The electromagnetic equations of the supraconductor. *Proceedings of the Royal Society of London. Series A-Mathematical and Physical Sciences*, 149(866):71–88, 1935.

[22] Igor S Aranson and Lorenz Kramer. The world of the complex ginzburg-landau equation. *Reviews of modern physics*, 74(1):99, 2002.

[23] John Bardeen, Leon N Cooper, and John Robert Schrieffer. Theory of superconductivity. *Physical review*, 108(5):1175, 1957.

[24] Richard A Ogg Jr. Bose-einstein condensation of trapped electron pairs. phase separation and superconductivity of metal-ammonia solutions. *Physical Review*, 69(5-6):243, 1946.

[25] Nikolay N Bogoljubov, Vladimir Veniaminovic Tolmachov, and DV Širkov. A new method in the theory of superconductivity. *Fortschritte der physik*, 6(11-12):605–682, 1958.

[26] CWJ Beenakker and Henk van Houten. Quantum transport in semiconductor nanostructures. In *Solid state physics*, volume 44, pages 1–228. Elsevier, 1991.

[27] Yuli V Nazarov and Yaroslav M Blanter. *Quantum transport: introduction to nanoscience*. Cambridge university press, 2009.

[28] H Huebl, RP Starrett, DR McCamey, AJ Ferguson, and Laurens Henry Willems van Beveren. Electrically detected magnetic resonance using radio-frequency reflectometry. *Review of Scientific Instruments*, 80(11), 2009.

[29] JI Colless, AC Mahoney, JM Hornibrook, AC Doherty, H Lu, AC Gossard, and DJ Reilly. Dispersive readout of a few-electron double quantum dot with fast rf gate sensors. *Physical review letters*, 110(4):046805, 2013.

[30] JM Hornibrook, JI Colless, AC Mahoney, XG Croot, S Blanvillain, H Lu, AC Gossard, and DJ Reilly. Frequency multiplexing for readout of spin qubits. *Applied Physics Letters*, 104(10), 2014.

[31] Imtiaz Ahmed, James A Haigh, Simon Schaal, Sylvain Barraud, Yi Zhu, Chang-min Lee, Mario Amado, Jason WA Robinson, Alessandro Rossi, John JL Morton, et al. Radio-frequency capacitive gate-based sensing. *Physical Review Applied*, 10(1):014018, 2018.

[32] Damaz De Jong, Jasper Van Veen, Luca Binci, Amrita Singh, Peter Krogstrup, Leo P Kouwenhoven, Wolfgang Pfaff, and John D Watson. Rapid detection of coherent tunneling in an in as nanowire quantum dot through dispersive gate sensing. *Physical Review Applied*, 11(4):044061, 2019.

[33] Guoji Zheng, Nodar Samkharadze, Marc L Noordam, Nima Kalhor, Delphine Brousse, Amir Sammak, Giordano Scappucci, and Lieven MK Vandersypen. Rapid gate-based spin read-out in silicon using an on-chip resonator. *Nature nanotechnology*, 14(8):742–746, 2019.

[34] Joseph A Sulpizio. *Quantum Transport in One-Dimensional Nanostructures*. Stanford University, 2011.

[35] M Fernando Gonzalez-Zalba, Sergey N Shevchenko, Sylvain Barraud, J Robert Johansson, Andrew J Ferguson, Franco Nori, and Andreas C Betz. Gate-sensing coherent charge oscillations in a silicon field-effect transistor. *Nano letters*, 16(3):1614–1619, 2016.

[36] Yuji Ijiri and Herbert A Simon. Some distributions associated with bose-einstein statistics. *Proceedings of the national academy of sciences*, 72(5):1654–1657, 1975.

[37] Edward Lawry Norton. Design of finite networks for uniform frequency characteristic. *Bell Labs, Murray Hill, NJ, USA, Tech. Rep, TM26-0-1860*, 1926.

[38] MS Khalil, MJA Stoutimore, FC Wellstood, and KD Osborn. An analysis method for asymmetric resonator transmission applied to superconducting devices. *Journal of Applied Physics*, 111(5):054510, 2012.

3

METHOD

3

3.1. TOWARDS FUNCTIONAL DEVICES

Producing hybrid semiconductor-superconductor devices requires relatively complicated nanofabrication procedures. This section describes the necessary steps and possible difficulties when working in cleanrooms and laboratories.

3.1.1. NANOWIRES AND GROWTH CHIPS

Two main types of nanowires are used in this thesis: partially superconductor-covered InAs nanowires and stemless InSb nanowires. They are both good candidates to hold hybrid systems but need different treatments. The tilted scanning electron micrographs (SEM) of the growth chips of the above-mentioned nanowires are presented in Fig. 3.1. The fabrication of a device then begins with the precise transfer of several nanowires onto a pre-fabricated sample chip.

INAS NANOWIRE

In Copenhagen, Peter Krogstrup's group uses a two-step molecular beam epitaxy (MBE) process to grow InAs/Al nanowires [1]. Those bare <0001>B InAs nanowires are grown on [111]B InAs substrates and have {$1\bar{1}00$} side facets, with their width of 80-120 nm and length of 5-10 μm. Subsequently, around 8-10 nm aluminum shell is grown with the substrate orientation fixed in the same vacuum period, to cover the bare InAs nanowire on two of the six facets. The high quality of the thin shell and the uniform InAs/Al interface promise a hard induced gap close to that of bulk aluminium. In this thesis, InAs nanowires are combined with Al etching, which allows us to define semiconductor quantum dots and normal contacts.

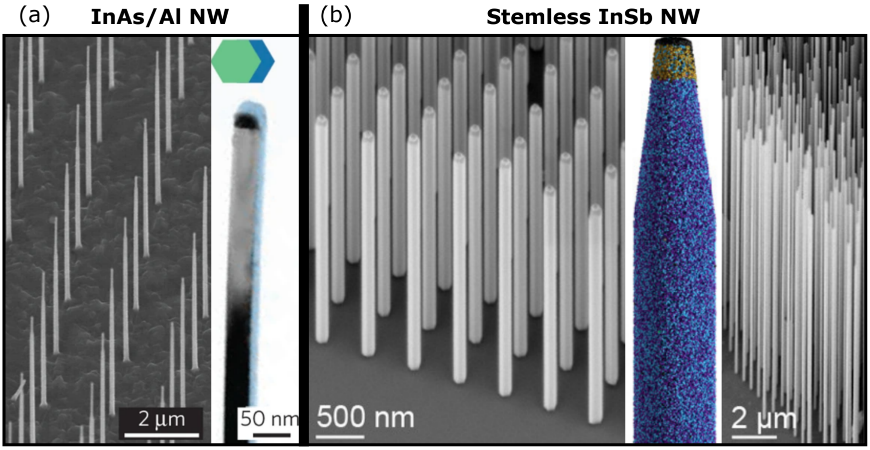

Figure 3.1: **Nanowire (NW) growth chips.** Tilted SEM images illustrating the nanowire growth chips, depicting InAs/Al nanowires with Al covering two facets in **(a)**, and bare InSb nanowires in **(b)**. Figures are adopted from Ref. [1, 2]

INSB NANOWIRE

The InSb nanowires are grown by metal organic vapour phase epitaxy (MOVPE) using the selective-area vapour liquid solid (SA-VLS) growth principle, in Erik Bakkers' group in Eindhoven [2]. Such InSb nanowires are grown directly on an Si_xN_y masked InSb (111)B substrate with gold as a catalyst, without the need of a foreign nanowire stem. This leads to the nanowires extending along [111] direction obtaining smooth {110} side facets, with their typical diameter in the range of 130-190 nm, and especially long lengths up to 10 μm. They obtain low temperature electron mobility of 4.4×10^4 $cm^2/(Vs)$ in average. In this thesis, the treatment with InSb nanowires aims to adapt to the applications of a shadow-wall lithography technique, which promises a better quality of the hybrid interfaces [3, 4].

3.1.2. SUBSTRATE FABRICATION AND SAMPLE CHIPS

The sample chips are taken from 4-inches intrinsic silicon wafers covered by 20 nm LPCVD-deposited SiN_x, which aim to decrease the parasitic capacitance during reflectometry measurements. With each fresh Si/SiN_x wafer, we draw and apply precise metal markers first, some of which serve as localized references for subsequent electron beam lithography (EBL), while others serve as dicing markers. Due to the limited space available for holding chips on our printed circuit board (PCB), we then dice the wafer into 6.7 mm×6.7 mm pieces (see Fig. 3.2(a)), and thus obtaining plenty sample chips in storage.

As mentioned above, we start the fabrication steps from these tiny sample chips to avoid possible damage to the devices during dicing. Next, to avoid too much treatment of the nanowires, which would degrade their quality, we perform several pre-fabrication steps prior to nanowire deposition. There are some variations in the pre-fabrication processes for the two types of nanowires:

SUBSTRATES FOR INAS NANOWIRES

For devices relying on InAs/Al nanowires, we transfer the nanowires to the sample chip immediately after cleaning the chip. The wet cleaning process always involves a 10 minutes ultrasonic bath with acetone, followed by a 1 minute rinse with IPA. This step can remove the leftover of photoresist (AZ9260) that applied during dicing. The delicate transfer process is then carried out using a nanowire manipulator machine (Fig. 3.2(b)), where a needle controlled by a mechanical system is picking up a single nanowire from the growth chip (Fig. 3.2(c): left) and then depositing it onto a sample chip (Fig. 3.2(c): middle) in its nanowire deposition region (Fig. 3.2(a) version A). To facilitate the design of top gate patterns using microscope images, it is preferable to keep the nanowire away from fine markers.

PRE-FABRICATIONS ON INSB NANOWIRES

For devices relying on InSb nanowires, the nanowire transfer becomes a relatively late-stage procedure. The sample chips differ from those used for InAs/Al nanowires in that an additional layer of about 17 nm of tungsten is sputtered onto the surface (by a vacuum magnetron sputtering machine: Alliance Concept AC450). After the wet cleaning process, we spin-coat and bake the sample chip with negative e-beam resist (primer AR300-80, followed by AR-N7500.08) and then apply EBL to define the pattern of bottom gates (done by a e-beam pattern generator: EBPG 5200). Developer AR300-47 is then used to develop the exposed areas, after which the sample chip is re-baked for 1 minute at 128 °C. The tungsten layer is then etched with SF6 gas at 20 °C (using an inductively coupled plasma etcher: Plasmalab system 100), leaving the tungsten gate patterns on the chip. This is followed by a lift-off process to remove the e-beam resist by immersing the chips in AR600-71 liquid for over 4 hours, and we clean the chip by rinsing it in water for 2 minutes. Note that Teflon tweezers are essential for this step to avoid contaminating the samples. Oxygen plasma is then applied to the sample chip for 10 minutes to further remove any residual e-beam resists (this is done using a semi-automatic plasma asher: PVA Tepla 300). Next, another round of EBL is employed to define the pattern of gate pads, this time using positive e-beam resist PMMA 950-A6 to spin-coat and bake. We opted for a different e-beam resist for this step, as it is a simpler process using PMMA, and also because we tolerate larger discrepancies and require less precision for the gate pads. We then develop the PMMA layer on the chip, sputter on a new layer of tungsten, lift-off the PMMA by acetone at 50 °C, and finally obtain sample chips with the complete pattern of bottom gates. The pre-fabrication process is completed with a thin layer of AlO_x deposited on the top surface of the chip (using an atomic layer deposition system: Oxford FlexAL) to act as a dielectric layer. The sample chip is then ready for nanowire transfer as in Fig. 3.2(c: right).

UPDATE SAMPLE CHIPS

Obviously, the deposition of InSb nanowires is more tricky than that of InAs/Al nanowires because a nanowire has to be placed exactly on top of the bottom gates, which is only a super thin stripe under the microscope. If the nanowire is placed incorrectly, we can gently push the nanowire with the needle, but it is possible to bend the nanowire and introduce unknown disorders in semiconductor, or even break the nearby fine gates, or penetrate the dielectric layer. It is therefore important to design the device and chip intelligently to increase the yield. Fig. 3.2(a) shows two versions of the sample chips used in this thesis.

The original design is Version A, which has the device region and the resonator region placed in each half of the sample chip. In the device region, there are three separate areas in the center defined by fine-markers (see the gold markers in Fig.3.2(c): middle), each of which is intended to hold a device, with its contact and gate pads extending to the boundary of the device region. This design has the advantage of easy and fast drawing of the contact and gate patterns, but the disadvantage of wasted space on the sample chip. There is also a much greater chance of damage to the device during the fabrication process, as the metal paths to the bonding pads are long and narrow.

The updated design is Version B, which has one dose test region and two device regions, with the resonator region later covering the less promising device region. As there are no pre-defined areas with fine-markers, we have the freedom to place the device as densely as possible. And by placing the bonding pads as close to the device as possible, we reduce the risk of losing a working device due to accidental dirt, scratches or misplaced nanowires. The maximum number of devices on a sample chip is mainly limited by the size of the bonding pads, which cannot be further minimized. The resonator region is not specifically designed in Version B, because the resonator chip can choose to cover any area with inactive devices, leaving enough space for working devices. The craziest design we ever tried was to glue two resonator chips onto a sample chip with 20 devices, there each resonator chip has two devices bonded to it. The aim of the dose test

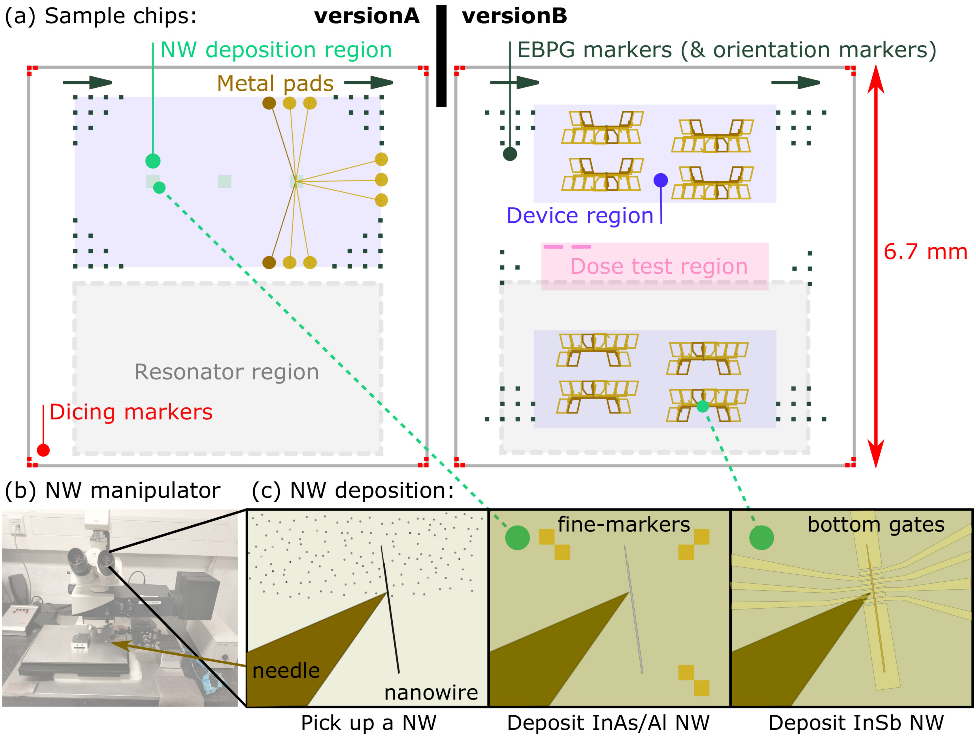

Figure 3.2: **Design of sample chips and nanowires deposition.** **(a)** There are two versions of diced sample chips: Version A has one device region, which can hold three devices, and one resonator region, which is ready to attach an off-chip resonator. Version B has two device regions, each capable of accommodating many devices, and a region for dose test, maximising the use of a single chip. The device region with fewer operating units can be selected as the resonator region later. **(b)** Transferring nanowires from a growth chip to a pre-fabricated sample chip is facilitated by a nanowire manipulator machine. The three microscope images on the right showcase the process: the needle picking up a nanowire from the nanowire forest on the growth chip (left); the needle depositing the InAs/Al nanowire in the center of the marked region, identified by fine EBPG markers (middle); the needle depositing the InSb nanowire on the previously placed bottom gates (right).

region is to obtain as much information as possible about the dose parameters of the e-beam in a single fabrication run, and to obtain the first working device as early as possible. Typically, we do some dose testing of fine structures (e.g. bottom gates) on another spare chip, i.e. we run different dose values to draw the same fine structure, develop, deposit metals and take SEM images to check where the correct range of dose value is, and then start applying the value to a real device chip. Apart from taking up too much time, this arrangement can still lead to failures when preparing a sample chip, as once this value is applied around the nanowire, unexpected overexposure or other problems can occur. Instead, we do the first EBL process to directly draw the pattern on few of the real devices (e.g. choose two over twenty devices in the device regime) with a guessed value of dose, and in the same time draw many identical patterns with different dose in the dose test region. If the dose is correct, we get a promising device that we can cool down in a fridge and the fabrication process is complete. If the dose value is incorrect, we sacrifice only two devices, but we gain enough information about the correct dose range. And in particular, by comparing the pattern with the same dose in the device region and in the dose test region, we know a more precise range of dose values. This fabrication arrangement, with the sample chip designed as Version B, has saved an average of two weeks and at least half the amount of Si wafers in obtaining an available sample.

3.1.3. ALUMINUM ETCHING

Once the InAs/Al nanowires have been deposited on the sample chip, the most important step to be followed is to etch the aluminium shell to form superconducting islands. Using EBL with PMMA as the e-beam resist, we define the etch mask on each nanowire and then rinse the sample chip shortly in Transene-D or MF-321 liquid to remove the aluminium in certain sections.

TRANSENE-D

Transene-D is initially used as the aluminium etchant, as it has a controllable etching rate, offers high resolution with minimal undercutting, and do not harm to the Si/SiN$_x$ substrate. One downside of using Transene-D is that it slowly but unavoidablly etch the InAs nanowire, which may introduces disorders to the semiconductor. Fig. 3.3(a) shows an example of partially etched InAs/Al nanowire with 10 nm thick aluminium shell under Transene-D. There the aluminium bulges are obvious with sharp edges, leaving the etched area clean. Another downside comes from the very sensitive etching rate to the temperature and the required quick procedures. Namely for the optimized recipe, the Transene-D is heated in a water bath to 48.2 °C for strictly 10 seconds, followed by multiple rinses in water for 3 seconds, 5 seconds, 5 seconds and 15 seconds respectively to dilute the concentration of Transene-D and stop the etching process. The first two rinses must be relatively short, and the transfer between liquid must be quick to ensure rapid dilution.

MF-321

MF-321 is a photoresist developer that can also be a good candidate for etching aluminium. Compared to Transene-D, MF-321 is not aggressive to the InAs nanowire itself,

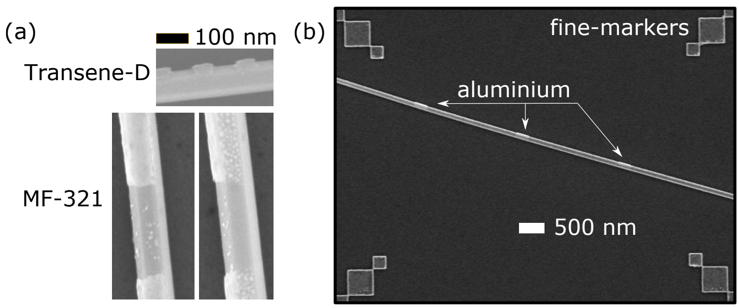

Figure 3.3: **Aluminium etching.** **(a)** SEM images of aluminium etching results using either Transene-D or MF-321. **(b)** SEM image of a nanowire that has undergone aluminium etching, leaving three aluminium sections behind.

has a lower etch rate and can be applied at room temperature, making the process easier to handle. The average etching time with MF-321 is 70 seconds, followed by slightly longer rinses in water for 5 seconds, 10 seconds, 30 seconds, and 30 seconds. A disadvantage of using MF-321 is that, due to the gentle etching, droplets of AlO_x are always left on the surface of the nanowire. Fig. 3.3(a) also shows two examples of etched InAs/Al nanowire with 6 nm thick aluminium shell under MF-321, where the droplets are randomly distributed on the InAs surface, no matter how good the aluminium shell quality is. The edges of the aluminium bulges are also not sharply defined, suggesting another disadvantage, namely over-etching of the aluminium under the etch mask. It is not negligible or avoidable, but can be minimised by using a resist adhesion promoter hexamethyldisilizane (HMDS), prior to spin-coating PMMA 950-A4.

The resulting aluminium sections left to define the superconducting islands are shown in Fig. 3.3(b), such SEM images need to be taken to adjust the presumed position of the contact lead patterns and the wrapped gate patterns (done by Hitachi ultra-high resolution FE-SEM S-4800). As SEM imaging is detrimental to aluminium quality and the dielectric layer, we use low power for the focused beam (typically 5 kV) and try to take only one picture within 3 seconds before moving the beam away.

3.1.4. CHARGE SENSOR

In addition to gate sensing, charge sensing is also planned to be employed to provide compensating information on charge transfer. This decision influenced the design of the devices, although the charge sensing results are not included in the main chapters of this thesis. The charge sensor consists of a single quantum dot as the sensing dot, and a metal bridge gate connecting the sensing dot to the segment to be sensed. To reduce the complexity, the sensing dot in this thesis is defined on the same nanowire, and it is connected to one of the normal quantum dots to detect its charge occupation. The metal bridge gate is preferred to be short to ensure large capacitive coupling. Here we present the fabrication and basic characterisation of such charge sensors.

BASED ON INAS NANOWIRES

For InAs/Al nanowire based devices, the process of defining the charge sensor becomes the final step to complete the fabrication. Prior to this step, the aluminium sections are left by aluminium etching, followed by one round of EBL process and metal evaporation process (see details in Sec. 3.1.5). The thin AlO_x dielectric layer of 7-10 nm then covers the entire sample chip, upon which we can deposit the wrapped top gates in the same way as we deposit contact leads.

In order to get decent wrapped gates, it is essential to obtain the correct recipe for the EBL process, including the selection of e-beam resist, the spin-coating speed, precise baking time, reasonable e-beam step size, and the optimized dose parameter. Fig. 3.4(a) illustrates the significant effects of an incorrect dose on the gate patterns. It provides an example of underdosing, where the metal pieces are easily removed during the lift-off process, and an example of overdosing, where the gate patterns are compressed together. Worse scenarios can occur when the pattern is applied to a nanowire, such as the metal bridge fusing with the nearest plunger gate.

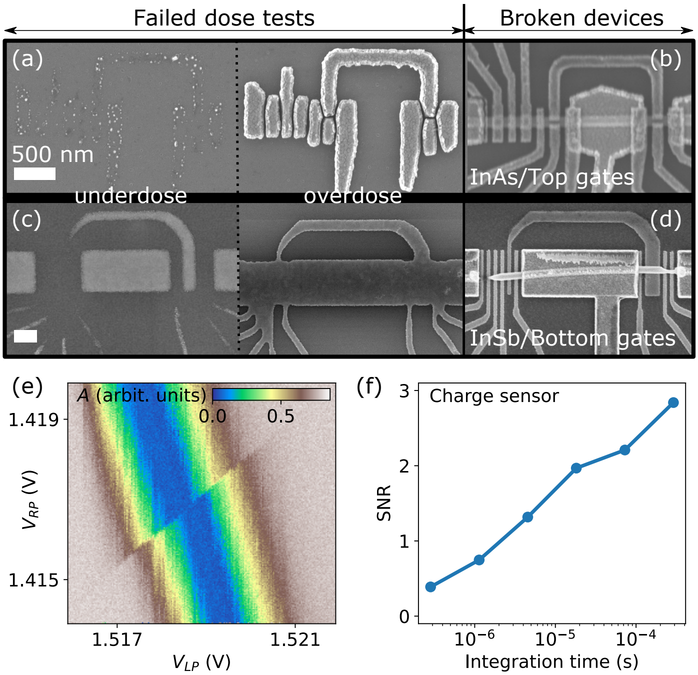

Figure 3.4: **Fabrication and characterization of gates and charge sensors.** **(a)** Left: Dose testing of Ti/Au wrapped top gates for InAs/Al nanowire based devices. Right: A broken device due to a lift-off problem caused by too much overlap of the gate patterns with respect to the contact leads, which has a similar consequence to the devices with horizontal misalignment. **(b)** Left: Dose testing of tungsten bottom gates for InSb nanowire based devices. Right: A broken device due to improper argon ion milling and electrostatic discharge (ESD) problem. **(c)** Charge sensing signal of a floating bottom gated double quantum dot (DQD) device based on InSb nanowire, with the gate patterns designed as (a). The Coulomb peak of the sensing dot is visibly shifted along the diagonal due to the charge occupation variations of the connected quantum dot. **(d)** The value of SNR of the bottom gated charge sensor with respect to the experimental integration time in log scale.

Another difficulty in obtaining such a working device is to ensure the wrapped gates are precisely aligned with the aluminium island profile and the nanowire position. Otherwise, the horizontally misaligned gates, which are supposed to tune the charge transfer rates between the superconducting island and another normal quantum dot, end up tuning the chemical potential of the superconducting island itself. In addition, if the shifted wrapped gates result in too little overlap with the nanowire on one side, the barrier gate pattern can be completely lifted by the thick contact lead and lost control of the nanowire. As shown in Fig. 3.4(b), if the leftmost barrier gate has more overlap with the left contact lead, the metal piece of the gate can be washed away during the lift-off process. However, the particular device in Fig. 3.4(b) is not failing because of misalignment, but because of poor design of the gate patterns, which are intended to overlap more with the contact leads to avoid forming additional quantum dots at the edges. The vertical misalignment of the bottom gates can ruin the charge sensor, as the metal bridge should physically overlap the nanowire but not completely cover it, leaving enough space for the plunger gate to tune the chemical potential from the other side of the nanowire.

Fig. 3.4(b) meanwhile shows a good example with no vertical misalignment.

BASED ON INSB NANOWIRES

For InSb nanowire based devices, the charge sensor is prepared in advance of the dielectric layer and nanowire deposition. As briefly mentioned in Sec. 3.1.2, the superfine bottom gates are no longer achieved by metal evaporation but are made by etching the sputtered tungsten onto the top surface of the sample chip.

An optimised recipe for the EBL process is also crucial for this etching step, including the precise bake time (187 °C for the primer AR300-80, and 87.5 °C for the resist AR-N7500.08) and the dose parameter, as mentioned above for the preparation of the wrapped gates. Fig. 3.4(c) shows the unfavourable appearance of the tungsten bottom gates from the dose tests. At lower doses, the supposed patterns are largely etched away, while at higher doses the patterns of individual gates are indistinguishable. The spacing between the finger gates, as well as the width of each finger gate, will affect the output, so the dose parameter must be adjusted for different gate sizes. In general, the wider the finger gates and the greater the spacing between the finger gates, the wider the range of dose parameters suitable for obtaining reasonable bottom gates.

Fig. 3.4(b) shows a complete device with satisfactory bottom gates but broken nanowire. The refined version of this device is evaluated in Chapter 5. The charge sensing signal of one functional device with identical design is shown in Fig. 3.4(e), with the corresponding SNR of various measurement integration time summarized in Fig. 3.4(f). The results indicate a relatively high SNR of the charge sensor, up to 1 within the integration time of a few microseconds.

With a thin dielectric layer of AlO_x sandwiched between the nanowire and the bottom gates, the lever arm for these bottom gates typically averages about 0.3, which is less than the 0.8 observed for the optimized wrapped top gates. Given that the nanowire is transferred onto the gate patterns afterward, there is a potential risk of damaging the dielectric layer with the needle, particularly when it becomes necessary to manipulate the nanowire using the needle. Since the nanowire with aluminium does not favour high temperatures, we sacrifice the quality of the dielectric layer by depositing AlO_x at rather low temperatures (105 °C). This value can be freely increased up to 300 °C for bottom-gated devices with a temporary absence of nanowires. The choice to use bottom gates is partly aimed at collaborating with the development of shadow wall lithography, which can improve the performance of the aluminium shell and allow complicated device architectures [3, 4, 5]. The related details will be discussed in Chapter 8.

3.1.5. OHMIC CONTACT

We use the same EBL and metal evaporation process to form the normal contact leads for devices based on either InAs/Al or InSb nanowires. The complete EBL process, employing pre-baked positive e-beam resist PMMA and a developer mixture of MIBK/IPA (mixed at a 1:3 ratio), provides opening windows on the sample chip for contact lead patterns. The sample chip is then placed upside down in the vacuum chamber for metal evaporation (using an electron beam heating evaporator: Temescal FC2000 or AJA QT).

ARGON MILLING

Since there is an unavoidable oxidized layer on the surface of the nanowire, we first apply argon ion milling in vacuum. The goal is to form ohmic contacts by aggressively removing such a layer, which can introduce Schottky barriers at the metal-semiconductor interface. The argon ion milling parameters must be carefully selected and will vary from machine to machine, and in some cases it is necessary to introduce several short milling pauses of a few seconds each. Otherwise, as shown in Fig. 3.4(d), this step has the potential to destroy the semiconductor nanowire and make it more susceptible to electrostatic discharge (ESD) problems.

METAL DEPOSITION

Next, we heat the crucibles containing the metals to deposit $\approx$ 10 nm of titanium and 130-150 nm of gold (Ti/Au) on the sample chips. The titanium layer helps the metal to adhere well to the chip and the nanowire, while its thickness, together with the gold layer, should be in proximity to the diameter of the nanowire. Too thick leads are a waste of metal and can increase lift-off difficulties and interfere with the deposition of the nearby gate pattern for top gate devices. On the other hand, too thin leads can cause discontinuity in the metal piece. A similar consideration of metal thickness applies to the fabrication of wrapped gates (mentioned above in Sec. 3.1.4), where thick gates are undesirable for lift-off and thin gates can break the gates or at least reduce the lever arm we gain from their wrapped shape.

To finalize the fabrication of contact leads, the sample chips are rinsed in acetone at 50 °C for lift-off. This also marks the final step in the process of obtaining complete InSb nanowire-based devices.

3.1.6. POST-FABRICATION AND RESONATOR CHIPS

Dispersive gate sensing in this thesis is accomplished through an on-chip approach to frequency multiplexing (MUX), enabling the simultaneous readout of devices. The MUX resonator chips, sourced from David Reilly's group in Sydney [6], are securely stored in our lab, featuring photoresist covering on their surface. All that is required is to wash off the photoresist with 10 miniutes bath in acetone at room temperature, while ensuring that the chips are not flipped upside down. Fig. 3.5(a) shows a picture of one part of a cleaned MUX chip, the sophisticated patterns of which is fabricated from one or two layers of low-loss superconducting niobium film via photolithography. The patterns include the bonding pads of an RF line and several DC lines, capacitors and spiral inductors, with the expected inductance value (from 40 nH to 310 nH) labelled near the bonding pads on the other side.

A test on probe station is then conducted after taking the promising sample chip and the cleaned resonator chip from the cleanroom. We use a beeper box or any instrument work as a ohmmeter connecting to the probe station, and use two probing needles to touch a pair of bonding pads. The purpose is to check that the nanowire of the target devices are conducting and to ensure that there are no short circuits formed by the gates. Meanwhile, we check the MUX resonator chip to confirm that the resistance of each DC loop is between 20-110 kΩ, so that the spiral inductor does not break.

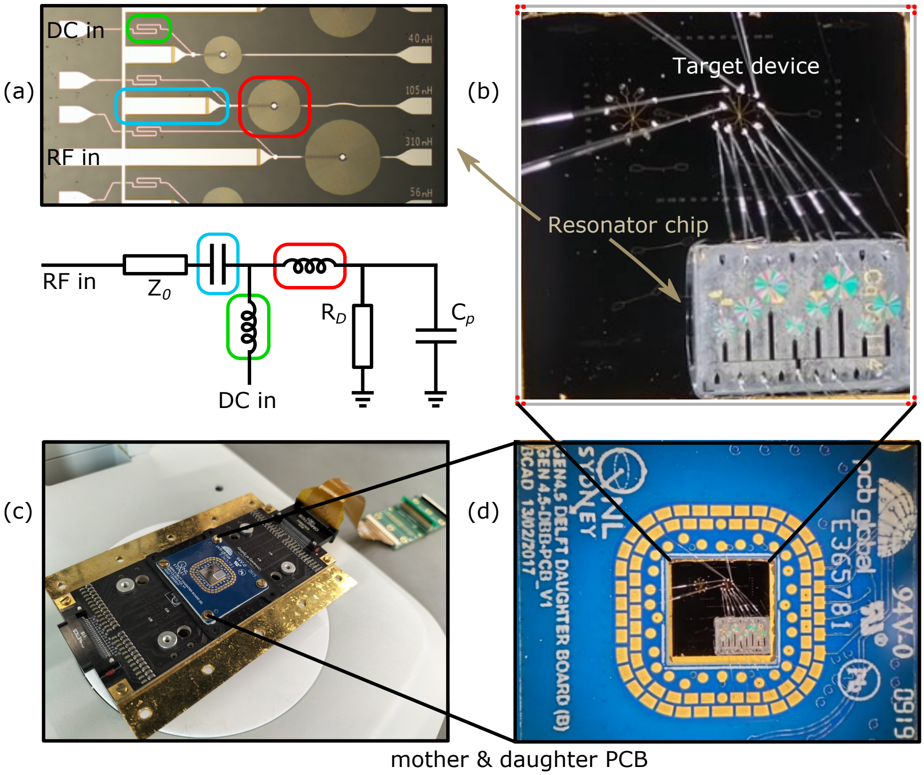

Figure 3.5: **Prepare the sample chip for cryogenic measurements.** **(a)** The photo of a section of the MUX resonator chip fabricated on a sapphire substrate using superconducting niobium (top), and the corresponding circuit (bottom). The frequency multiplexing is achieved by the different inductances, labelled on the right side of the MUX resistor chip. **(b)** The resonator chip is glued on the sample chip, with the target device connected by bonding wires. **(c)** The daughter board is screwed to the mother board. After covering the daughter board with a cotton cap, the sample chip is ready to be loaded into the probe for electrical measurements. **(d)** The sample chip is glued on a daughter PCB, whose metal pads are connected to both the resonator chip and the device by aluminium bonding wires.

The MUX resonator chips can then be glued to the sample chip using a small amount of PMMA, as shown in Fig. 3.5(b), and the sample chip can then be similarly glued to a daughter PCB, as shown in Fig. 3.5(d). A pause of at least half an hour is required to allow the PMMA to dry and the chips to stick together firmly. Without this pause, the chip could slip or fall off during bonding or loading.

Finally, we make connections between the target device, the MUX resonator chip and the daughter PCB by aluminium bonding wires. To stabilize the position of the bonding pads, the daughter PCB is fastened onto the fixed mother PCB designated for cryogenic measurements. As with the MUX resonator chips, both the mother PCB and the replaceable daughter PCB are contributed by David Reilly's group and accommodate 96/102 DC lines and 8/32 RF lines. The bonding process is then achieved with the support of a conductive holder underneath, as illustrated in Fig. 3.5(c). The bonding machine (FS-

Bondtec 5630) has a camera and a microscope for checking the bonding positions, and the bonding parameters such as power or loop heights are programmable before each move. As the MUX resonator chip is much taller than other bonding pads, we always start with the bondings from the resonator chip to the target device or to the daughter PCB.

3.2. MEASUREMENT SETUP

3

The previous section outlined the steps to obtaining a working device, but success is still not guaranteed. In this section we list the room temperature measurements required to assess the availability of the target sample, and the setups for performing cryogenic measurements.

3.2.1. PRELIMINARY MEASUREMENTS

ENSURE CONDUCTANCE

From probing, to bonding, and to loading the sample chip onto the probe of a dilution fridge (see Sec. 3.2.2), it is important to keep your hands grounded to prevent damage from ESD. As the example mentioned in Fig. 3.4(d) of Sec. 3.1.4, the ESD can cause the nanowire to explode when there is a sudden flow of charge at the interface of two materials. Sometimes the spark created by the two different electrostatic potentials can penetrate the dielectric layer, causing short circuits from the gates to ground or burning the nanowire and fine metal structures. In practice, after taking the finished sample chip out of the clean room, we always store it in an antistatic bag and never touch it with metal tweezers. While screwing the daughter PCB onto the mother PCB and during the bonding process, we stand on an antistatic mat (sometimes with shoes off) and wear a grounding wrist strip.

Given the potential risk of such an ESD problem damaging the device, before lowering the probe into the bellows and starting the vacuum, we unground the device and repeat measurements similar to the probe station test. Here we need to confirm that the nanowire is still conductive, with a resistance of around 100 kΩ, and the gates to ground are open. If the target device passes the test, we re-ground the device and continue the cooling process.

When the probe has cooled down to the base temperature, we unground the device and run this test one last time, but in more detail. Firstly, we measure the leakage current by setting the absolute gate voltages to 5 V and expect to get several tens of pA for functional gates. The nanowire may not be conductive when all gates are set to zero, we secondly sweep all the gates together from a finite negative value to a positive value to open the nanowire, and measure the conductance simultaneously using lock-in amplifier. Fixing all the gates to the value when the conductance is high and close to saturation, we thirdly pinch off each gate separately to know the hysteresis effect of each gate (see Fig. 3.6(b) as an example).

ENSURE REFLECTOMETRY

For the MUX resonator chip, we measure the reflectometry signal in the frequency range between 200 MHz and 800 MHz (see Fig. 3.6(a)). Ideally, there should be noticeable dips in amplitude at the resonance frequency of each resonator. Fig. 3.6(c) shows the example

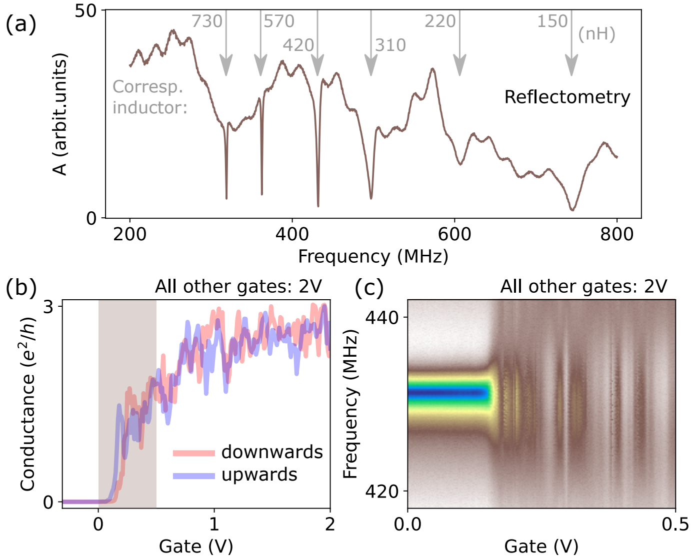

Figure 3.6: **Basic characterization prior to measurements.** **(a)** Reflectometry test result when six resonators on the MUX resonator chip are bonded to the target device. The corresponding inductor of each resonator is labelled above. It shows that the higher inductance gives a lower resonance frequency and a sharper dip in the amplitude signal. Those resonances at higher frequency range can be identified by comparing two results with different gate settings. **(b)** The conductance measured by lock-in amplifer when sweeping one single gate from 2 V to -0.3 V (red) and from -0.3 V to 2 V (blue). It indicates the nanowire can be opened with all gates set to 2 V and reaches the conductance of about 3 e^2/h, and the sweeping gate has limited hysteresis while pinching off the conductance successfully. **(c)** The conductance pinch-off of the same gate as the shadowed area in (b) can be detected by a resonator coupled to the contact lead, where the open wire significantly changes the reflectometry signal. It suggests that rf conductance measurements can replace transport measurements for characterisation.

of pinching off the nanowire with the contact lead coupled to the resonator with 420 nH spiral inductance, suggesting how transport measurements can be replaced by using rf techniques. As long as the target device has negligible leakage current, relatively high conductivity that can be pinched off with accessible gate settings, and gates with limited hysteresis, we could consider the device sufficient to use for further measurements.

3.2.2. CRYOGENIC HARDWARE AND CIRCUITS

The measurements in this thesis are taken in a dilution fridge at its base temperature close to 30 mK. Such a fridge uses a mixture of two isotopes of helium, ^{3}He and ^{4}He, which have boiling points of 3.2 K and 4.2 K respectively at one atmosphere pressure. The phase diagram of their mixture, however, tells the absolute zero temperature is theoretically reachable either for pure ^{3}He or for system stays in dilute ^{4}He rich phase with ^{3}He component less than 6%. The dilution fridge, as its name signals, uses the latter principle for cooling, which is made possible by the large amount of heat demanded while pumping ^{3}He into its dilute phase. Fig. 3.7 (a-4) shows the embedded large metallic plates of a dilution fridge after removing its shield, each plate holds a different temperature stage

3

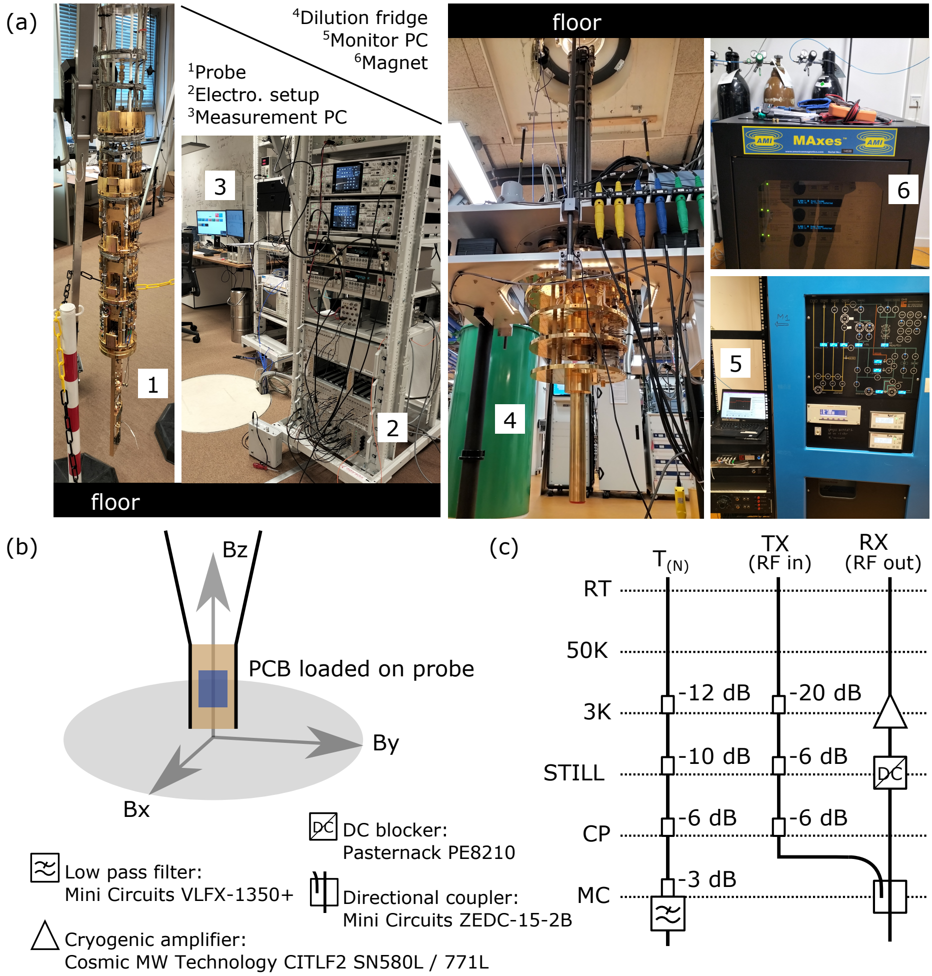

Figure 3.7: **Measurement setup, dilution fridge, and experimental circuit.** **(a)** The relevant experimental equipment is located separately on two floors. The sample chip is mounted to the probe on the top floor (#1) and loaded through a hole (#4) into the bellows lifted from the bottom floor. On the measurement computer (#3), we take measurements at room temperature with the electrical setup (#2) to check that the nanowire is conductive and that the gates are not shorted to ground or to each other. When the pressure of the probe is low enough with the help of an air compressor, the probe is lowered into the fridge and we then start the condensation process via the control panel (#5). The current source for the vector magnets in XYZ directions (#6) remain at zero throughout the loading process. **(b)** The orientation of the sample chip with respect to the components of the external magnetic field applied by the vector magnet. Ideally, the orientation of B_z is in the plane of the sample chip. **(c)** The reflectometry circuit with corrected attenuations. The metallic plates separating the different temperature stages are marked by horizontal dashed lines from top to bottom in the following order: room temperature (RT), 50K and 3K stages, still, cold plate (CP) and mixing chamber (MC). The corresponding electronic products are marked alongside.

that can be measured by a temperature sensor. The helium mixture is initially precooled by a pulse tube to 50 K and then to about 3 K, after which the ^{4}He component becomes liquid. The temperature is then further reduced through the dilution unit, which consists of the still, the cold plate and the mixing chamber, where the phase boundary is located to allow ultra-low temperatures. The device placed at the bottom of the probe (see Fig. 3.7 (a-1)) can then be measured in a continuous millikelvin environment. In our lab, the operation of a Leiden dilution fridge can be realized by pressing the buttons on its control panel, or via the monitor computer, as Fig. 3.7 (a-5) presents.

The loaded device, bonded to the mother PCB, is placed vertically and surrounded by the vector magnet, as Fig. 3.7 (b) marked out. The external magnetic field in three orthogonal axes is supplied by three separate instruments. It can reach up to 6 T along the B_z orientation and up to 1 T along the B_x and B_y orientations. The magnitude of the external magnetic field in this thesis is rather low, so this arrangement leaves enough freedom in the orientation of the nanowires placed on the sample chip.

The equivalent circuit in our Leiden Cryogenics cryostat is depicted in Fig. 3.7 (c). Each DC line is used to set the an individual gate voltage, and a low pass filter is used at the base temperature to stabilize the value before it input to the device. The attenuators are placed for noise reduction, and to avoid the introduced noise from the attenuators themselves, the attenuators are distributed over many temperature stages. This logic applies to both the DC lines and the RF line. As for the RF line, the use of a directional coupler separates the input and output signals, and routes the reflected signal to pass through a DC blocker and be amplified before being collected by room temperature instruments.

Fig. 3.7 (a) overall shows how the room temperature measuring equipments and the cryogenic hardwares are distributed in our lab. The upper floor houses the raised probe, awaiting the mounting of a PCB with a sample chip, the electronic setups and the measurement computer, which controls the operation of all the instruments via a Jupyter notebook. The lower floor houses the dilution fridge, the vector magnet, and the monitor computer that keeps track of the temperature and pressure of the sensors embedded in the fridge. The probe can be lowered into the fridge through a hole between the two floors, through which the cables can also reduce their lengths.

3.2.3. ROOM TEMPERATURE ELECTRONICS

LOW FREQUENCY

The DC characterization measurements, which are still part of the preliminary tests, are performed by different instruments. One option is the locally designed modules known as the IVVI-DAC rack from the Raymond Schouten group [7]. It contains a summing module with 16 digital-to-analogue converters (DACs) that are connected to the target device, either providing voltages through the gates or introducing bias current through the contact leads. The voltage range it supply is between -2 V and +2 V. The IVVI-DAC rack is battery powered to isolate the measurement electronics from any 50 Hz noise arising from unintentional ground loops. The measurement PC in Fig.3.7 (a-3) can only communicate with them through an optical link. Another option is to use an adopted 64-channel precision DAC unit named MDAC, which has a enlargen voltage range between -5 V and +5 V. MDAC uses a power supply unit (PSU) that are connected together with a MDAC power cable, the grounds of both MDAC and PSU are connected internally after passing through a power filter. Using voltage amplifiers or I/V converters, the signal can be amplified and measured with a digital multimeter or using lock-in techniques in the range of 50-100 Hz. An arbitrary waveform generator (AWG) is a plus when there is need to apply an designed waveform.

HIGH FREQUENCY

The RF reflectometry measurements can be based on a number of options such as an adopted multi-frequency integrated data acquisition system (MIDAS), an ultra-high frequency dual channel lock-in amplifier (UHFLI) or a virtual network analyser (VNA). The MIDAS generates multiple RF frequencies through a single DAC to the fridge. It then demodulates and processes the return signals through its analogue-to-digital conversion (ADC) port to provide reflection coefficient data on all channels simultaneously and in real time. With MIDAS we can acquire data in single shot or distributed acquisition modes. The UHFLI is suitable because it can read signals from DC to 600 MHz, covering the frequency range of the MUX chip resonators with the top four inductances (see Fig.3.6 (a)). The VNA is generally used to measure reflection coefficients, while in this thesis it is only briefly used for single channel characterisation without multiplexing.

BIBLIOGRAPHY

[1] P Krogstrup, NLB Ziino, W Chang, SM Albrecht, MH Madsen, Erik Johnson, Jesper Nygård, Charles M Marcus, and TS Jespersen. Epitaxy of semiconductor–superconductor nanowires. *Nature materials*, 14(4):400–406, 2015.

[2] Ghada Badawy, Sasa Gazibegovic, Francesco Borsoi, Sebastian Heedt, Chien-An Wang, Sebastian Koelling, Marcel A Verheijen, Leo P Kouwenhoven, and Erik PAM Bakkers. High mobility stemless insb nanowires. *Nano letters*, 19(6):3575–3582, 2019.

[3] Sebastian Heedt, Marina Quintero-Pérez, Francesco Borsoi, Alexandra Fursina, Nick van Loo, Grzegorz P Mazur, Michał P Nowak, Mark Ammerlaan, Kongyi Li, Svetlana Korneychuk, et al. Shadow-wall lithography of ballistic superconductor–semiconductor quantum devices. *Nature Communications*, 12(1):4914, 2021.

[4] Francesco Borsoi, Grzegorz P Mazur, Nick van Loo, Michał P Nowak, Léo Bourdet, Kongyi Li, Svetlana Korneychuk, Alexandra Fursina, Ji-Yin Wang, Vukan Levajac, et al. Single-shot fabrication of semiconducting–superconducting nanowire devices. *Advanced Functional Materials*, 31(34):2102388, 2021.

[5] GP Mazur, N van Loo, D van Driel, J-Y Wang, G Badawy, S Gazibegovic, EPA Bakkers, and LP Kouwenhoven. The gate-tunable josephson diode. *arXiv preprint arXiv:2211.14283*, 2022.

[6] JM Hornibrook, JI Colless, AC Mahoney, XG Croot, S Blanvillain, H Lu, AC Gossard, and DJ Reilly. Frequency multiplexing for readout of spin qubits. *Applied Physics Letters*, 104(10), 2014.

[7] Raymond Schouten group. Qt designed instrumentation - ivvi rack page.

4

Revealing charge-tunneling processes between a quantum dot and a superconducting island through gate sensing

We report the detection and identification of charge-tunneling processes between a quantum dot and a superconducting island through radio-frequency gate sensing. We are able to resolve spin-dependent quasiparticle tunneling as well as two-particle tunneling involving Cooper-pairs. The sensor allows us to characterize the superconductor excitation spectrum, enabling us to access subgap states without transport. Our results provide crucial guidance for future dispersive parity measurements of Majorana modes, which can be realized by detecting the parity-dependent tunneling between dots and islands.

This chapter is based on J. van Veen, D. de Jong, L. Han, C. Prosko, P. Krogstrup, J. D. Watson L. P. Kouwenhoven, and W. Pfaff, Revealing charge-tunneling processes between a quantum dot and a superconducting island through gate sensing, published (2019).

4.1. INTRODUCTION

Quantum dots coupled to superconductors can give rise to novel physical phenomena such as π and ϕ_0-junctions [1, 2, 3], Cooper-pair splitting [4, 5], and Yu-Shiba-Rusinov (YSR) states [6, 7]. These phenomena arise because the single-electron states of the dot hybridize with the more complicated many-particle states of the superconductor. Recently, such hybrid systems have gained interest in the context of Majorana zero modes (MZMs) where the quantum dot (QD) can, for example, be used as a spectrometer [8]. Moreover, projective parity measurements can be achieved by coupling a QD to a pair of MZMs, which are located on a superconducting island (SC) [9, 10], enabling topologically protected quantum computation. These projective measurements rely on the parity-dependent hybridization between a single dot level and the MZMs [11, 12]. Therefore, unambiguous detection of coherent tunneling between a QD and the superconducting island is needed to implement this readout.

Dispersive gate sensing provides direct access to the charge hybridization between weakly coupled dots or islands. More precisely, coherent tunneling within these structures can impart a frequency shift on a resonant circuit that can be observed on short time scales with high accuracy. In this way, experiments have revealed coherent charge hybridization between superconductors [13, 14, 15] and in semiconductor double quantum dots [16, 17, 18]. Moreover, capacitive RF sensing has been used to study charging of QDs connected to normal- and superconducting reservoirs [19, 20]. However, while dispersive readout presents an excellent opportunity to study charge-tunneling between QDs and superconducting islands, it has not been employed yet in such hybrid systems.

In this chapter, we report detection and identification of charge-tunneling processes between a QD and a superconducting island through RF sensing via an *LC* resonator connected to the gate of the QD. From observations of the resonator response, supported by numerical simulations of the system, we find that the nature of the tunneling depends crucially on the ordering of the relevant energy scales of the SC. When the smallest scale is the energy of the lowest single-particle state, the QD and SC can exchange quasiparticles, giving rise to a characteristic “even-odd” effect. Conversely, when the charging energy of the SC is lowest, we detect signatures of Cooper-pairs tunneling out of the SC. Depending on the tunneling amplitude, this results in either $1e$-charging of the QD, with the other electron leaving into a reservoir, or $2e$-charging of the QD via coherent Cooper-pair tunneling. We can re-enable the tunneling to the single-particle states by operating the device in a floating regime where the total number of charges in the two systems is conserved.

A schematic of our experiment is shown in Fig. 1a. Two charge islands are formed in an InAs nanowire with an epitaxially grown Al-shell. A superconducting island is defined by removing the Al outside a 1.2 μm segment with wet-etching. Tunneling barriers are implemented with gates, insulated from the wire by 10 nm AlO_x. They are used to define the QD and SC; and to control the various tunneling rates. Large-lever arm top gates (“plungers”) on both QD and SC can be used to tune the chemical potentials. The dot plunger is connected to an off-chip, superconducting resonator [21]. We use its response near the resonance frequency to probe the charge tunneling on and off the dot. We have fabricated two of these devices, and measured them separately at temperatures of $T \approx$ 20 mK in a dilution refrigerator.

The relevant energy scales in our devices can be obtained from Coulomb blockade measurements: Figure 1b shows Coulomb diamonds of the superconducting island alone, measured through conductance. The diamonds of device A display a clear even-odd pattern, indicating that the energy of the lowest odd-parity state, E_0, is smaller than the charging energy of the superconducting island, E_C^S (Fig. 1c) [22, 23, 24]. For this device, we estimate $E_0 = 72\ \mu$eV and $E_C^S = 112\ \mu$eV from the extent of the diamonds. Conversely, the charging of the superconducting island of device B is $2e$-periodic, indicating that $E_0 > E_C^S$ [25, 23]; here, we estimate $E_0 \approx 90\ \mu$eV and $E_C^S \approx 70\ \mu$eV. While in an ideal BCS superconductor E_0 is equal to the superconducting gap Δ, current measurements on device A (Supplemental Material) and the negative differential conductance observed

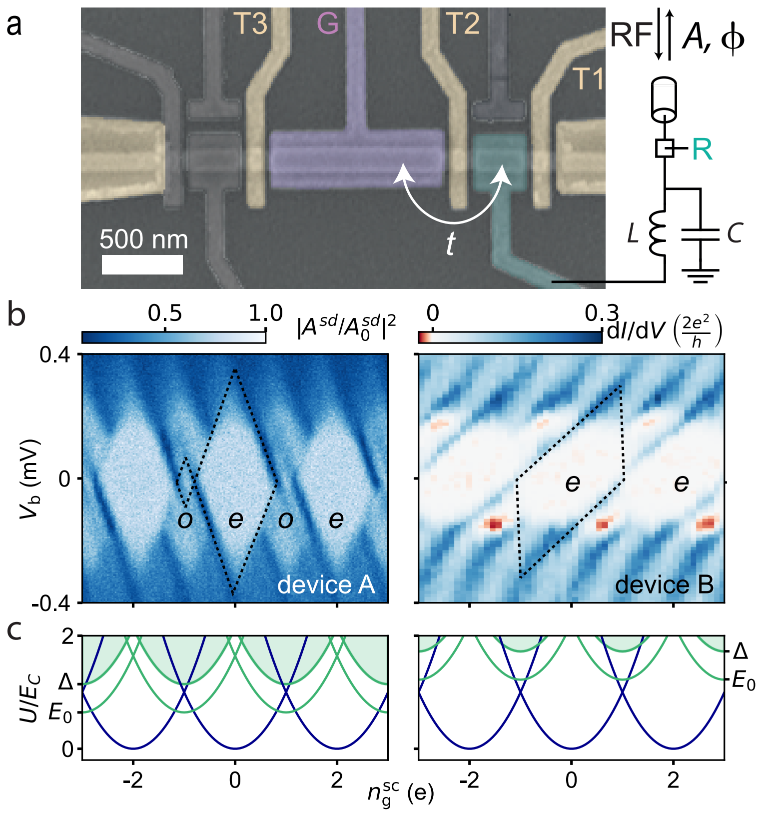

Figure 4.1: **Experimental setup and sample characterization. a** False-colored electron micrograph of a nominally equivalent hybrid double dot. The plunger gate of the QD (island) is colored cyan (purple). A *LC* resonator is capacitively coupled via the gate of the QD. Its phase ϕ and amplitude A response are monitored at a constant probe frequency. **b** Coulomb blockade measurement of the SC. Left: for device A measured using RF reflectometry off the source (circuit not shown in **a**). The even-odd pattern indicates that $E_0 < E_C^S$. Right: for device B measured using standard lockin techniques. The doubling of the period at low bias V_b illustrates that $E_0 > E_C^S$. **c** Energy dispersion of the superconducting island for device A (left) and device B (right). The even (odd) energy levels are shown in darkblue (green). The odd parity sector consists of a discrete subgap state at E_0 and a continuum of states above Δ.

in device B indicate the presence of subgap states [9]. In both devices, the charging energy of the dot, $E_{\mathrm{C}}^{\mathrm{QD}} \approx 200-300\ \mu$eV, is the largest energy scale in the system, and the typical QD level spacing exceeds the thermal energy (Supplemental Material).

4.2. RESULTS

4.2.1. SPIN-DEPENDENT TUNNELING

In the following, we investigate the change in resonator response when charges are able to tunnel between the QD and SC at zero bias, beginning with device A. To this end, we form a hybrid double dot by tuning the gates T1 and T2 close to pinch-off, and T3 into pinch-off. Figures 2a,b show the resonator response as a function of the two plunger gates in the weakly coupled regime. Both the amplitude- and phase response display the charge stability diagram (CSD) of the hybrid double dot, which shows a clear $1e$ pattern along the QD gate, and an even-odd pattern along the SC gate; this is again a manifestation of $E_0 < E_{\mathrm{C}}^{\mathrm{S}}$, and the CSD shape can be readily reproduced by computing the charge ground states of the system (Supplemental Material).

4

We focus on the interdot transitions, highlighted in Figs. 2a-c, where we observe a strong amplitude and phase response on all charge degeneracy points. Interestingly, we see a strong difference in the resonator response across interdot transitions with a different parity of the total particle number, indicating a difference between the coupling between the involved states [26]. Two scenarios can lead to such a different coupling: One, an asymmetric electron- and hole coupling to the quasiparticle state in the SC [24]; and second, a difference in the available spin states for the different transitions [27].

We find that the latter situation can qualitatively describe the asymmetry in our data. To see this, we label the states according to their pairing; for the SC states as even/odd, and for the states in the QD as singlet/doublet: $|e/o, S/D\rangle$. We can differentiate couplings between two sets of states; $|e, D\rangle$ to $|o, S\rangle$ and $|e, S\rangle$ to $|o, D\rangle$. The coupling is different for these two sets, because they involve a different number of states. Only one spin channel contributes to the coupling between $|e, D\rangle$ and $|o, S\rangle$, while both spins of a Cooper-pair can couple to the QD doublet for the transition between $|e, S\rangle$ and $|o, D\rangle$ [27]. The "checkerboard"-like pattern in the CSD that results from this mechanism is in agreement with our data. This effect has originally been predicted for a double quantum dot and is thus not restricted to the QD-SC system [27]. The asymmetry from the electron or hole tunneling would result in a different pattern in the CSD; we thus conclude that the features observed in the data are most likely explained by the number of available spin states in the hybrid double dot.

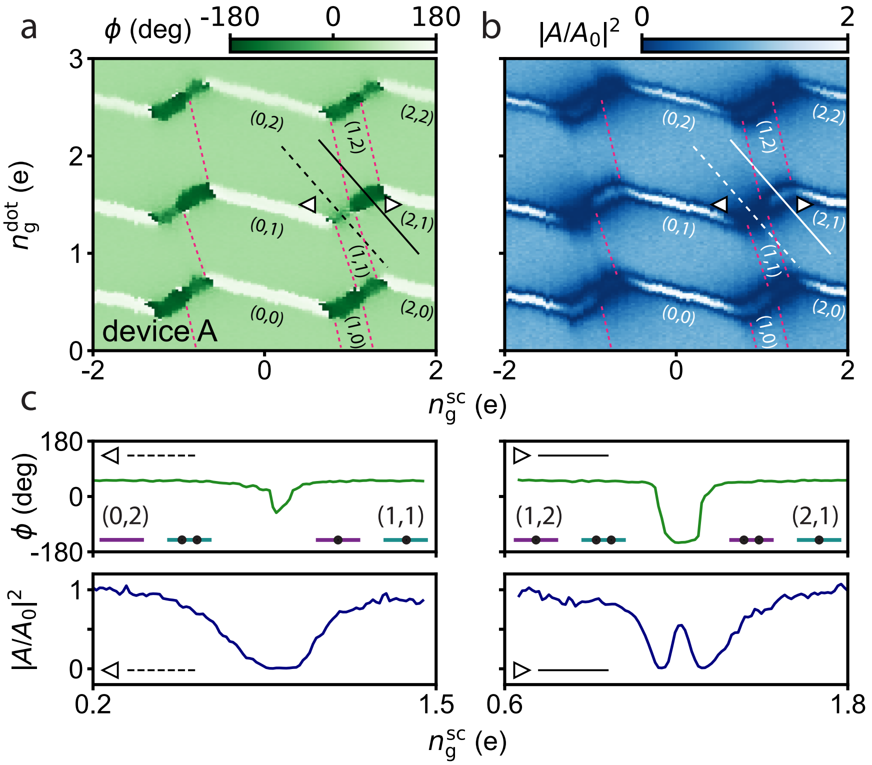

Figure 4.2: **Spin-dependent tunneling between a QD and a SC. a** and **b** Charge stability diagram of device A measured in phase **a** and amplitude **b**. The charge states are labeled with $\left(n^{\mathrm{SC}}, n^{\mathrm{QD}}\right)$ with respect to the state (N, M) with N and M even. Dashed pink lines: expected locations of the lead-island transitions. **c** Linecuts of the phase (green) and amplitude (blue) along the interdot transitions. The linecut crosses the states (0,2) and (1,1) in the left panel (dashed line) and (1,2) and (2,1) in the right panel (continuous line). A pronounced different resonator response is observed for the two transitions. For the $\left|e(\text{ven}), S(\text{inglet})\right\rangle$ to $|o(\text{dd}), D(\text{oublet})\rangle$ transition between (0,2) and (1,1) (left panel), both spin channels are available, while only one spin channel contributes to the $|o,S\rangle$ to $|e,D\rangle$ transition between (1,2) and (2,1) (right panel).

4.2.2. COOPER-PAIR TUNNELING

For device B, the situation changes significantly. The energy ordering $E_0 > E_C^S$ implies that quasiparticle states are not accessible (Fig. 1c). We form a hybrid double dot by tuning T1, T2, and T3 close to pinchoff. The CSD for a weak QD-SC coupling is shown in Fig. 3a. The diagram is $2e$-periodic in the SC gate, indicating that the island is charged via Andreev reflections from the lead. The QD is again $1e$-periodic. To model the measured CSDs, we compute the charge ground state by diagonalizing an effective Hamiltonian of the system that includes charging effects, the superconducting gap in the island, and coupling terms (Supplemental Material). This model, with the energy scales extracted from the Coulomb blockade measurements and an adjustable tunneling amplitude (rightmost panel in Fig. 3a), describes the observed CSD well.

4

The different gate charge periodicity for the QD and SC leads to interdot transitions that change the total charge of the dot-island system. This implies that a reservoir must be involved in the corresponding charge-transfer process. The observed resonator signal, with a linecut shown in Fig. 3b, results from tunneling on and off the QD, and thus should not contain information of SC-lead coupling [26]. A possible candidate for the precise underlying process that gives rise to our data is crossed Andreev reflection (CAR) [4, 5]. There, a hole from the QD is converted to an electron in the lead, consistent with the charge states involved in the experiment. This process is exponentially suppressed in the length of the island $\exp(-L/\pi\xi)$, where ξ is the superconducting coherence length [28]. Still, with $L = 1.2\ \mu$m and assuming a coherence length of $\xi \sim 260$ nm [10] this remains a plausible scenario.

Interestingly, increasing the tunnel coupling allows for bringing the system into a regime where a particle-conserving interdot transition emerges. The CSD in a more strongly coupled regime, together with a simulation of the charge ground states is shown in Fig. 3c. In this regime, we assume an induced gap in the quantum dot, consistent with earlier studies in the context of YSR states [7]. Here, we observe that the regions with odd charge number in the QD shrink, while the regions with an even number of QD charges connect, resulting in an even-odd pattern in both gates. Now, the interdot transition shows a purely dispersive signal (Fig. 3d): we observe only a small phase shift, without any amplitude response; this is indicative of a coherent transition. We can thus conclude that this transition is caused by coherent Cooper-pair transfer between the dot and the island, resulting in an anti-crossing in the energy spectrum.

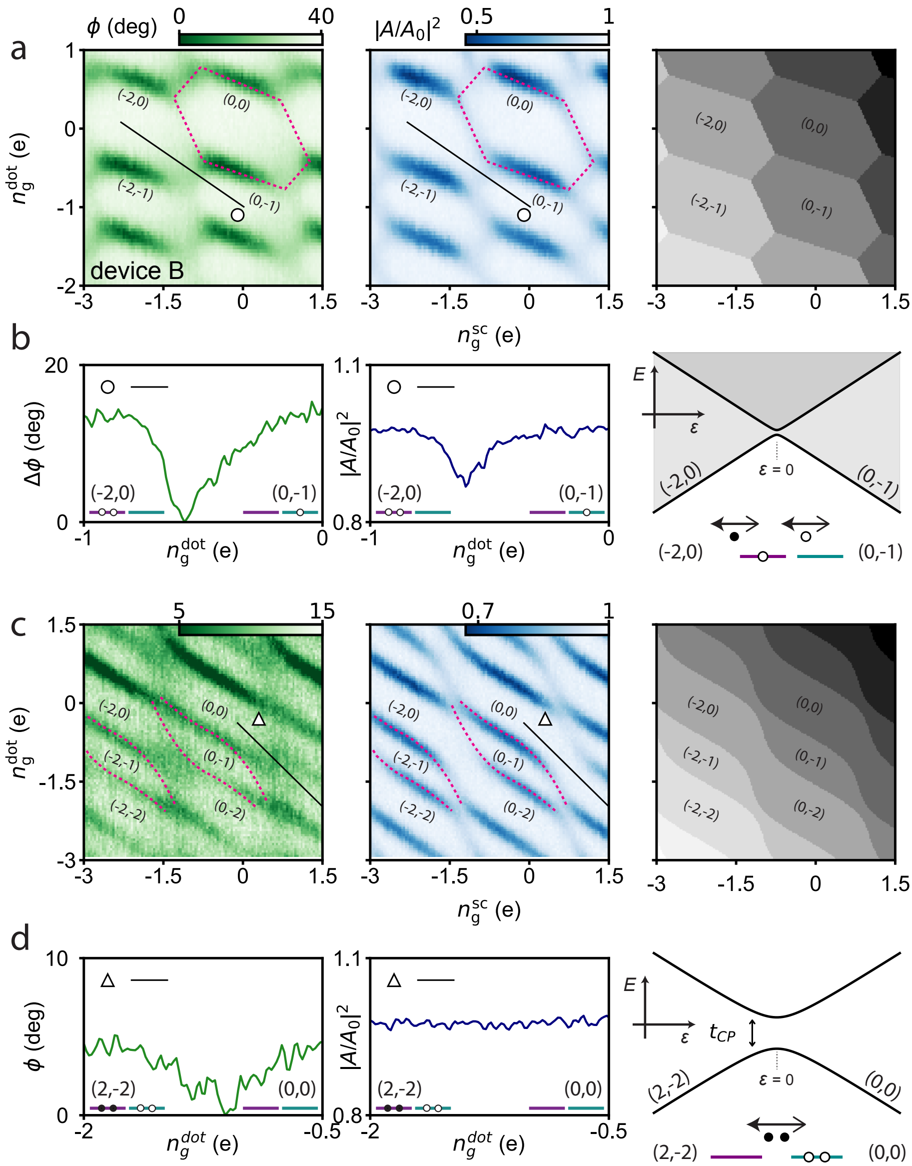

Figure 4.3: **Cooper-pair tunneling in a hybrid double dot.** **a** Charge stability diagram measured in phase (left) and amplitude (middle) along with a simulation of the charge ground state (right) in the weakly coupled regime. The charge states are labeled with $\left(n^{\mathrm{SC}}, n^{\mathrm{QD}}\right)$ with respect to the state (N, M) with N even. Dashed pink lines: locations of the transitions from the (0,0) state as a guide to the eye. The gray scale in the simulation indicates the sum of the charge in the combined system. **b** Linecuts of the phase (green) and amplitude (blue) along the (-2,0) to (0,-1) interdot transition. This transition involves a reservoir with a continuous spectrum, indicated by the shaded region above the lowest available energy state. The schematic shows how these states couple via crossed Andreev reflection. **c** Same as in **a** for the strongly coupled regime. Dashed pink lines: locations of the lead transitions from the (-2,-1) and (0,-1) states as a guide to the eye. **d** Linecuts of the phase (green) and amplitude (blue) along the (2,-2) to (0,0) interdot transition. These states couple via coherent Cooper-pair tunneling. All data is measured in device B.

4.2.3. Floating regime

As we have seen, the main difference between the two devices is that the odd states of the SC can not be directly accessed in the regime $E_0 > E_C^S$. This changes in absence of lead reservoirs because quasiparticles that tunnel from the QD onto the SC are confined to the system [15]. The additional energy associated with decharging the QD makes Cooper-pair tunneling energetically unfavorable when $E_0 < E_C^S + E_C^{QD}$. We realize this situation experimentally in device B by closing the outer tunnel barriers, through gates T1 and T3. The resulting CSD and corresponding calculation of the ground state transitions are shown in Figs. 4a,b. It can readily be seen that no transitions to a reservoir take place, and the even-odd pattern is indicative of the alternating occupation of even and odd states of the SC.

4

Importantly, even though SC and QD are now galvanically isolated from the environment, the gate sensor still allows us to study the quasiparticle states in the SC. To establish this further, we study the evolution of the even-odd spacing as a function of temperature (Fig. 4c). This spacing is a measure for the free energy difference of the SC. In particular, the temperature evolution of the free energy difference can be used to identify and characterize subgap states [29]; for proximitized nanowires, this has earlier been studied in transport [9]. The extracted free energy difference $F_o - F_e$ as a function of temperature is shown in Fig. 4d. A fit to the model from Ref. [9] yields a gap of $\Delta = 220\ \mu$eV a subgap state energy of $E_0 = 106\ \mu$eV, and an Al volume of $V = 2.9 \times 10^5$ nm^3, consistent with the dimensions of the island. We note that the slightly larger energy of the subgap state is consistent with the more negative plunger gate voltage for this measurement [30]. The excellent quality of the fit corroborates our initial assessment of the presence of a subgap state (Fig. 1b). This result shows clearly that the resonator response of the QD gate sensor can be used to characterize states of the SC, even when leads for transport experiments are not available.

4.3. Conclusions

In summary, we have performed dispersive gate sensing on a quantum dot that can exchange particles with a superconducting island. Analysis of the resonator response has allowed us to directly detect and identify the charge-tunneling processes that take place between the dot and the superconductor. We have found that single- or multi-particle tunneling processes take place, depending on the dominating energy scales of the hybrid double dot. In particular, our data shows that gate sensing provides an excellent tool for studying subgap excitations, even in situations where an absence of leads prohibits transport studies. Going forward, the ability to detect the coherent tunneling into subgap states will be crucial for the realization and operation of Majorana qubits based on proximitized nanowires [12, 11]. Our results thus set the stage for the implementation of quantum measurements of topological qubits.

4.4. Supplemental Material

4.4.1. Additional Coulomb diamond measurements

In this section, we present additional Coulomb blockade measurement of the quantum dots (QD) in Fig. 4.5, and the superconducting island (SC) of device A in Fig. 4.6.

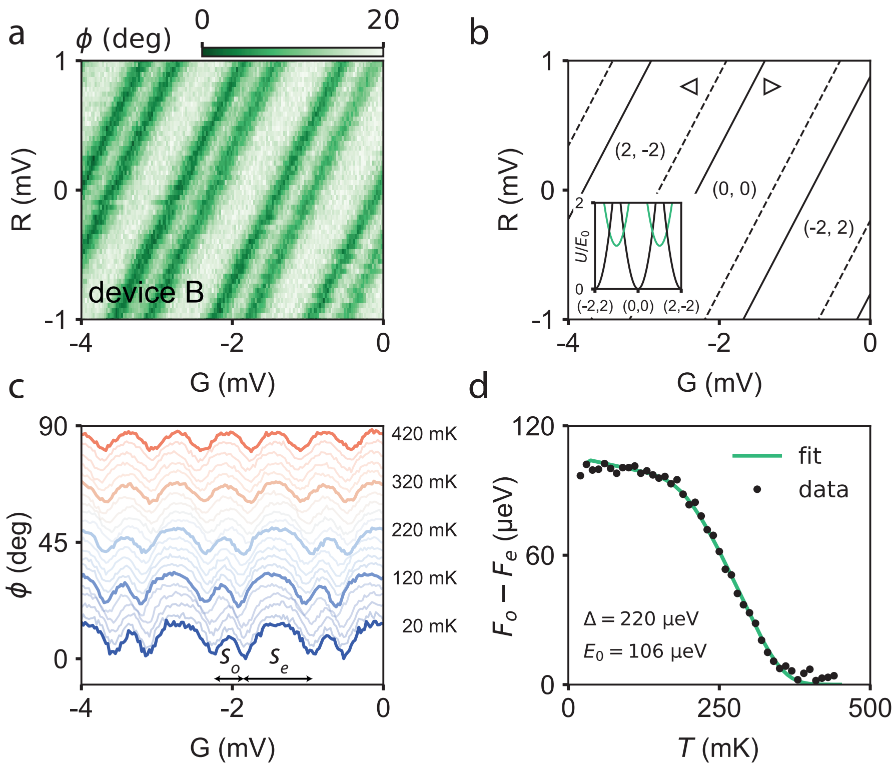

Figure 4.4: **Re-enabling of single-particle tunneling in the floating regime a** Charge stability diagram measured in phase in device B. The anti-diagonal lines indicate that the total charge in the system is conserved. **b** The calculated positions of the transitions in good agreement with the measured stability diagram. Inset: energy spectrum with the even states in black and the odd states in green showing that the even-odd pattern is caused by the parity effect even though $E_0 > E_C^S$. **c** Temperature dependence of the even-odd pattern. **d** The evolution of the free energy difference with temperature. The free energy difference is extracted from the even-odd pattern via $F_o - F_e = (S_e - S_o)\, e\alpha/4$ with $\alpha = 0.9$ the lever arm of G, and e the elementary electron charge.

From the Coulomb diamonds in Fig. 4.5, we extract the QD charging energy and estimate the typical level spacing of the dot. We find that the charging energy is the largest energy scale for both QD-SC systems. Moreover, the level spacing, δ, exceeds the thermal energy for both QDs, and it fluctuates with the charge occupation in the QD.

Figure 4.6 shows Coulomb diamonds for the SC of device A obtained via current measurements at the same gate settings as the diamond scan shown in Fig. 1b of the main text. The data in presented in the main text is measured using RF reflectometry from the source of the QD-SC system. The conductance shown here drops back to zero when V_b increase above the height of the small odd diamond. This indicates that for the odd charge states the current is carried by a discrete, subgap state. In contrast, if the current is carried by a continuum of states, the conductance would remain constant.

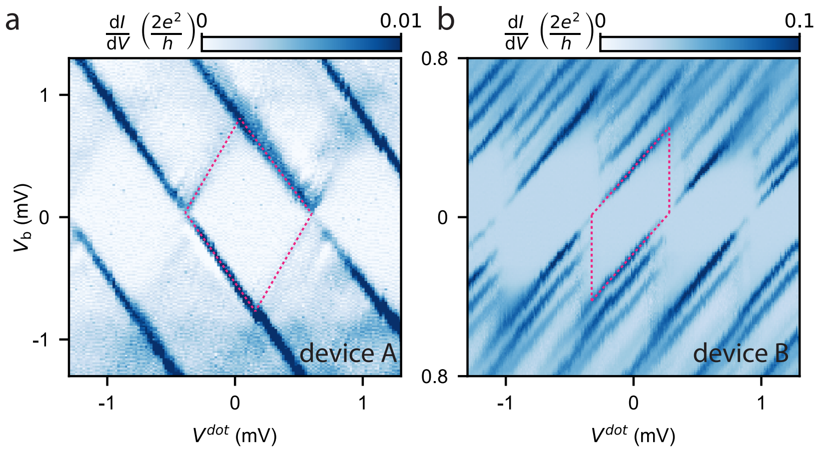

Figure 4.5: **Coulomb blockade measurements on the quantum dots.** **a** For device A, the conductance is calculated from the numerical derivative of the measured current. We extract $E_C^{\mathrm{QD}} \approx 300\ \mu$eV, $\delta = 50-150\ \mu$eV, and $\alpha^{\mathrm{QD}} = 0.8$. **b** For device B, we obtain $E_C^{\mathrm{QD}} \approx 200\ \mu$eV, $\delta = 100-170\ \mu$eV, and $\alpha^{\mathrm{QD}} = 0.72$.

4.4.2. SIMULATION OF THE CHARGE STABILITY DIAGRAMS

In this section, we discuss the phenomenological model used to simulate the charge stability diagrams shown in Fig. 3 of the main text. We start with the Hamiltonian of the QD-SC system

$$H = H_C + H_{\mathrm{BCS}} + H_T, \tag{4.1}$$

where H_C describes the charging energy of the combined system, H_{BCS} the superconductivity on the island and the induced superconductivity in the dot, and H_T the coupling between the two systems. Note that we neglect the level spacing in both systems.

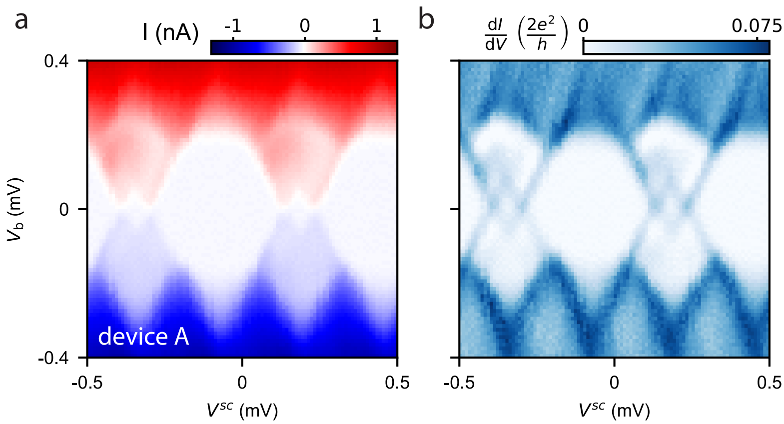

Figure 4.6: **Coulomb blockade measurements of the superconducting island in device A.** Left panel: current data, right panel: differential conductance obtained by taking the numerical derivative of the current data.

For the superconducting island, this is justified since its estimated level spacing is on the order of several mK. However, for the QD, where $\delta \approx 100\,\mu$eV, this is a large simplification. We model the charging term by $H_C = H_C^{\mathrm{QD}} + H_C^{\mathrm{SC}} + H_{C_m}$

$$H_C^{\mathrm{i}} = \sum_{n^i} E_C^i \left(n^i - n_g^i\right)^2 \tag{4.2}$$

$$H_{C_m} = \sum_{n^{\mathrm{SC}}, n^{\mathrm{QD}}} E_{C_m} \left(n^{\mathrm{SC}} - n_g^{\mathrm{SC}}\right)\left(n^{\mathrm{QD}} - n_g^{\mathrm{QD}}\right) \tag{4.3}$$

where $i = \mathrm{QD}, \mathrm{SC}$ labels the system; E_C^i is the charging energy, n_g^i the gate charge, and n^i labels the charge state.

We approximate the BCS Hamiltonian by assuming that only the lowest single particle state with energy E_0 is relevant

$$H_{\mathrm{BCS}} \approx \begin{cases} 0 & n^i \text{ is even} \\ E_0^i & n^i \text{ is odd.} \end{cases} \tag{4.4}$$

Note that $E_0 = \Delta$ in case there are no subgap states present on the SC. Usually, $E_0^{\mathrm{QD}} = 0$, we included this term to be able to model induced superconducting correlations in the quantum dot when the QD-SC coupling is strong.

Lastly, for the tunneling Hamiltonian, we include both $1e$ and $2e$ charge-transfer processes: $H_T = H_T^{1e} + H_T^{2e}$ with

$$H_T^{1e} = \sum_{n^{\mathrm{SC}}, n^{\mathrm{QD}}} t_{1e} \left|n^{\mathrm{SC}} - 1\right\rangle\left\langle n^{\mathrm{QD}} + 1\right| + \mathrm{h.c.} \tag{4.5}$$

$$H_T^{2e} = \sum_{n^{\mathrm{SC}}, n^{\mathrm{QD}}} t_{2e} \left|n^{\mathrm{SC}} - 2\right\rangle\left\langle n^{\mathrm{QD}} + 2\right| + \mathrm{h.c.}, \tag{4.6}$$

where t_{1e} (t_{2e}) is the tunneling amplitude for the $1e$ ($2e$) process.

To simulate the charge stability diagrams, we construct a Hamiltonian based of a finite number of charge states $\left|n^{\mathrm{SC}}, n^{\mathrm{QD}}\right\rangle = |-4,-4\rangle, |-4,-3\rangle, \ldots, |4,4\rangle$, using Kwant [**?**], and numerically solve for its eigenvalues and eigenvectors. We use the eigenvectors to calculate the charge expectation value of the total system which we compare to the data.

ADDITIONAL INFORMATION SIMULATIONS

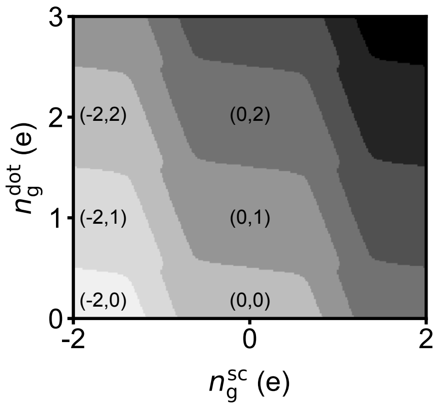

Figure 4.7: **Simulation of the charge stability diagram of Fig. 2 of the main text.** The gray scale indicates the total charge in the hybrid double dot.

Table 4.1: **Overview of the parameters used in the simulations.** All values are in μeV.

Simulation	E_C^{SC}	E_C^{QD}	E_{C_m}	E_0^{SC}	E_0^{dot}	t_{1e}	t_{2e}
Fig. 3a	72	230	50	88	0	9	0
Fig. 3c	72	230	60	88	18	176	308
Fig. 4.7	112	500	50	72	0	35	0

BIBLIOGRAPHY

[1] S. De Franceschi, L. P. Kouwenhoven, C. Schönenberger, and W. Wernsdorfer. Hybrid superconductor–quantum dot devices. *Nature Nanotechnology*, 5(10):703, 2010.

[2] J. A. Van Dam, Y. V. Nazarov, E. P. A. M. Bakkers, S. De Franceschi, and L. P. Kouwenhoven. Supercurrent reversal in quantum dots. *Nature*, 442(7103):667, 2006.

[3] D. B. Szombati, S. Nadj-Perge, D. Car, S. R. Plissard, E. P. A. M. Bakkers, and L. P. Kouwenhoven. Josephson ϕ_0-junction in nanowire quantum dots. *Nature Physics*, 12(6):568, 2016.

[4] L. Hofstetter, S. Csonka, J. Nygård, and C. Schönenberger. Cooper pair splitter realized in a two-quantum-dot Y-junction. *Nature*, 461(7266):960, 2009.

[5] L. G. Herrmann, F. Portier, P. Roche, A. Levy Yeyati, T. Kontos, and C. Strunk. Carbon nanotubes as Cooper-pair beam splitters. *Physical review letters*, 104(2):026801, 2010.

[6] D. C. Ralph, C. T. Black, and M. Tinkham. Spectroscopic measurements of discrete electronic states in single metal particles. *Physical review letters*, 74(16):3241, 1995.

[7] E. J. H. Lee, X. Jiang, M. Houzet, R. Aguado, C. M. Lieber, and S. De Franceschi. Spin-resolved Andreev levels and parity crossings in hybrid superconductor–semiconductor nanostructures. *Nature nanotechnology*, 9(1):79, 2014.

[8] M. T. Deng, S. Vaitiekenas, E. B. Hansen, J. Danon, M. Leijnse, K. Flensberg, J. Nygård, P. Krogstrup, and C. M. Marcus. Majorana bound state in a coupled quantum-dot hybrid-nanowire system. *Science*, 354(6319):1557–1562, 2016.

[9] A. P. Higginbotham, S. M. Albrecht, G. Kiršanskas, W. Chang, F. Kuemmeth, P. Krogstrup, T. S. Jespersen, J. Nygård, K. Flensberg, and C. M. Marcus. Parity lifetime of bound states in a proximitized semiconductor nanowire. *Nature Phys.*, 11(12):1017, 2015.

[10] S. M. Albrecht, A. P. Higginbotham, M. Madsen, F. Kuemmeth, T. S. Jespersen, J. Nygård, P. Krogstrup, and C. M. Marcus. Exponential protection of zero modes in Majorana islands. *Nature*, 531(7593):206, 2016.

[11] S. Plugge, A. Rasmussen, R. Egger, and K. Flensberg. Majorana box qubits. *New Journal of Physics*, 19(1):012001, 2017.

[12] T. Karzig, C. Knapp, R. M. Lutchyn, P. Bonderson, M. B. Hastings, C. Nayak, J. Alicea, K. Flensberg, S. Plugge, Y. Oreg, C. M. Marcus, and M. H. Freedman. Scalable designs for quasiparticle-poisoning-protected topological quantum computation with Majorana zero modes. *Physical Review B*, 95(23):235305, 2017.

[13] A. Wallraff, D. I. Schuster, A. Blais, L. Frunzio, R-. S. Huang, J. Majer, S. Kumar, S. M. Girvin, and R. J. Schoelkopf. Strong coupling of a single photon to a superconducting qubit using circuit quantum electrodynamics. *Nature*, 431(7005):162, 2004.

[14] T. Duty, G. Johansson, K. Bladh, D. Gunnarsson, C. Wilson, and P. Delsing. Observation of quantum capacitance in the Cooper-pair transistor. *Physical review letters*, 95(20):206807, 2005.

[15] A. A. Esmail, A. J. Ferguson, and N. J. Lambert. Cooper pair tunnelling and quasiparticle poisoning in a galvanically isolated superconducting double dot. *Applied Physics Letters*, 111(25):252602, 2017.

[16] K. D. Petersson, L. W. McFaul, M. D. Schroer, M. Jung, J. M. Taylor, A. A. Houck, and J. R. Petta. Circuit quantum electrodynamics with a spin qubit. *Nature*, 490(7420):380, 2012.

[17] T. Frey, P. J. Leek, M. Beck, A. Blais, T. Ihn, K. Ensslin, and A. Wallraff. Dipole coupling of a double quantum dot to a microwave resonator. *Physical Review Letters*, 108(4):046807, 2012.

[18] J. I. Colless, A. C. Mahoney, J. M. Hornibrook, A. C. Doherty, H. Lu, A. C. Gossard, and D. J. Reilly. Dispersive readout of a few-electron double quantum dot with fast rf gate sensors. *Physical review letters*, 110(4):046805, 2013.

[19] M. F. Gonzalez-Zalba, S. Barraud, A. J. Ferguson, and A. C. Betz. Probing the limits of gate-based charge sensing. *Nature communications*, 6:6084, 2015.

[20] L. E. Bruhat, J. J. Viennot, M. C. Dartiailh, M. M. Desjardins, T. Kontos, and A. Cottet. Cavity photons as a probe for charge relaxation resistance and photon emission in a quantum dot coupled to normal and superconducting continua. *Physical Review X*, 6(2):021014, 2016.

[21] J. M. Hornibrook, J. I. Colless, A. C. Mahoney, X. G. Croot, S. Blanvillain, H. Lu, A. C. Gossard, and D. J. Reilly. Frequency multiplexing for readout of spin qubits. *Applied Physics Letters*, 104(10):103108, 2014.

[22] D. V. Averin and Y. V. Nazarov. Single-electron charging of a superconducting island. *Physical review letters*, 69(13):1993, 1992.

[23] B. Van Heck, R. M. Lutchyn, and L. I. Glazman. Conductance of a proximitized nanowire in the Coulomb blockade regime. *Physical Review B*, 93(23):235431, 2016.

[24] E. B. Hansen, J. Danon, and K. Flensberg. Probing electron-hole components of subgap states in Coulomb blockaded Majorana islands. *Physical Review B*, 97(4):041411, 2018.

[25] F. W. J. Hekking, L. I. Glazman, K. A. Matveev, and R. I. Shekhter. Coulomb blockade of two-electron tunneling. *Physical review letters*, 70(26):4138, 1993.

[26] M. Esterli, R. M. Otxoa, and M. F. Gonzalez-Zalba. Small-signal equivalent circuit for double quantum dots at low-frequencies. *arXiv preprint arXiv:1812.06056*, 2018.

[27] A. Cottet, C. Mora, and T. Kontos. Mesoscopic admittance of a double quantum dot. *Physical Review B*, 83(12):121311, 2011.

[28] M. Leijnse and K. Flensberg. Coupling spin qubits via superconductors. *Physical review letters*, 111(6):060501, 2013.

[29] P. Lafarge, P. Joyez, D. Esteve, C. Urbina, and M. H. Devoret. Measurement of the even-odd free-energy difference of an isolated superconductor. *Physical review letters*, 70(7):994, 1993.

[30] A. E. Antipov, A. Bargerbos, G. W. Winkler, B. Bauer, E. Rossi, and R. M. Lutchyn. Effects of gate-induced electric fields on semiconductor Majorana nanowires. *Phys. Rev. X*, 8:031041, Aug 2018.

5

Variable and orbital-dependent spin-orbit field orientations in a InSb double quantum dot characterized via dispersive gate sensing

Utilizing dispersive gate sensing (DGS), we investigate the spin-orbit field ($\vec{B}_{SO}$) orientation in a manyelectron double quantum dot (DQD) defined in an InSb nanowire. While characterizing the interdot tunnel couplings, we find the measured dispersive signal depends on the electron-charge occupancy, as well as on the amplitude and orientation of the external magnetic field. The dispersive signal is mostly insensitive to the external field orientation when a DQD is occupied by a total odd number of electrons. For a DQD occupied by a total even number of electrons, the dispersive signal is reduced when the finite external magnetic field aligns with the effective $\vec{B}_{SO}$ orientation. This fact enables the identification of $\vec{B}_{SO}$ orientations for different DQD electron occupancies. The $\vec{B}_{SO}$ orientation varies drastically between charge transitions, and is generally neither perpendicular to the nanowire nor in the chip plane. Moreover, $\vec{B}_{SO}$ is similar for pairs of transitions involving the same valence orbital, and varies between such pairs. Our work demonstrates the practicality of DGS in characterizing spin-orbit interactions in quantum dot systems, without requiring any current flow through the device.

This chapter is based on L. Han, M. Chan, D. de Jong, C. Prosko, G. Badawy, S. Gazibegovic, E. P. Bakkers, L. P. Kouwenhoven, F. K. Malinowski, and W. Pfaff, Variable and orbital-dependent spin-orbit field orientations in a InSb double quantum dot characterized via dispersive gate sensing, published (2023).

5.1. INTRODUCTION

A spinful charge carrier moving in an electromagnetic field may experience a coupling between its spin and momentum degree of freedom, namely spin-orbit interaction (SOI). The SOI allows spin manipulation with electric fields in semiconductor platforms, such that it enables electric dipole spin resonance [1, 2, 3, 4], spin-cavity couplings [5, 6, 7, 8], while it also enhances effects detrimental to spin-based quantum information processing: relaxation and decoherence [9, 10]. For many cases, SOI can be described as an effective spin-orbit field ($\vec{B}_{SO}$) acting on the charge carriers. Notably, $\vec{B}_{SO}$ associated with the Rashba SOI is perpendicular to both the electric field $\vec{E}$ and the carrier momentum $\vec{p}$, following $\vec{B}_{SO} \propto \vec{E} \times \vec{p}$ [11, 12]. In ideal nanowire systems, carriers are confined in a one-dimensional path, which forces their momentum $\vec{p}$ to be along the nanowire. With the application of bottom electrostatic gates, the assumed electric field $\vec{E}$ is perpendicular to the substrate surface. Accordingly, the $\vec{B}_{SO}$ orientation is expected and has been experimentally proved to be not only in-plane of the chip, but also nearly perpendicular to a bottom-gated nanowire [12, 13]. Despite the electrostatic confinement, this conclusion is further found to hold for electron tunneling in few-electron double quantum dots (DQD), even when the center-to-center distance between the dots is small with respect to typical spin-orbit lengths [14, 15, 16]. Knowing the $\vec{B}_{SO}$ orientation in such nanowires is particularly important for semiconductor-superconductor hybrid systems that aim to realize Majorana zero modes, as setting the external magnetic field perpendicular to $\vec{B}_{SO}$ is a precondition to open a topological gap [17].

5

The conventional way to characterize SOI is associated with tunneling between quantum dots, which employs bias voltages across a DQD segment and measurements of spin blockade leakage current [18, 19, 14, 20]. However, scalable qubit devices [21, 22] may favor characterization methods that do not require transport measurements. Here, we explore dispersive gate sensing (DGS) [23, 8, 24, 25, 26, 27, 28] to characterize SOI, especially the $\vec{B}_{SO}$ orientation. Our protocol does not employ transport measurements, is compatible with fast data acquisition in rastering schemes [29, 25], and is promising for the integration of qubit characterization and readout capabilities [30, 31].

5.2. METHOD

In this section, we present the fabrication details of the device and the principal of the measurements (Sec. 5.2.1). At zero magnetic field, the measured charge diagram via DGS helps on charge parity recognition, and its result is evidenced by the data under finite external magnetic field (Sec. 5.2.2). The conversion of measured reflection coefficients to quantum capacitance C_q follows (Sec. 5.2.3), which is the basis of identifying spin-orbit field orientations for even total parity.

5.2.1. DEVICE AND MEASUREMENT APPROACH

The device under study is depicted in Fig. 5.1(a). An InSb nanowire is placed on top of prefabricated bottom finger gates. The barrier gates confine the electrons and control the tunnel coupling within the DQD and to the leads, while the plunger gates LP (RP) tune the chemical potential of the left (right) dot. The nanowire is grown along [111] direction, such that the Rashba SOI is expected to be dominant [14, 13, 32] To implement

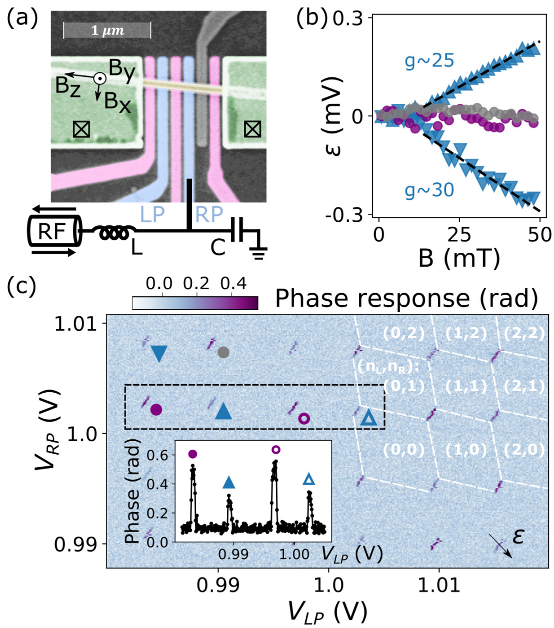

Figure 5.1: (a) False-colored SEM image of the device and the circuit schematics for DGS. The barrier and plunger gates are indicated in pink and blue respectively, while the metallic leads are indicated in green. The grey gate is electrostatically floating (unused in this work). (b) Charge stability diagram of the DQD at zero magnetic field. The inset shows the maximum phase response in the V_{LP} range marked by the dashed black rectangle. (c) The position of four neighboring ICTs along detuning axis, as a function of external field pointing in an arbitrary direction. Markers in (b) indicate the relative charge occupancy of the ICTs, although they do not correspond to the same ICTs as in (c).

DGS, the RP gate is coupled to an off-chip superconducting spiral-inductor resonator, with resonance frequency $f_0 \approx 318.4$ MHz and nominal inductance $L = 730$ nH [33].

At interdot charge transitions (ICTs), where the chemical potential for an electron residing in the left and the right dot are equal, the hybridization of electron wave functions between the two dots leads to an additional quantum capacitance C_q loading the resonator, which is observable as a shift of f_0 [34, 35, 23, 25]. While fixing the probing frequency f_p and detecting the reflected signal from the resonator, f_0 is translated into a change of reflection coefficient, thus to the amplitude and phase response. We fit the measured reflection coefficient with an analytical resonator model to extract f_0 and C_q (see Sec. 5.2.3). All measurements were performed in a dilution refrigerator at a base temperature $T \approx 30$ mK.

5.2.2. RECOGNITION OF CHARGE PARITY

In Fig. 5.1(b), the charge stability diagram (CSD) of the DQD is mapped by measuring the reflected phase response versus gate voltages V_{LP} and V_{RP}. It reveals a grid of ICTs with the lead-to-dot transitions hardly visible (marked by white lines), since the outer barrier gates are nearly pinched off. Along V_{LP} and V_{RP} axes, both the spacings between the

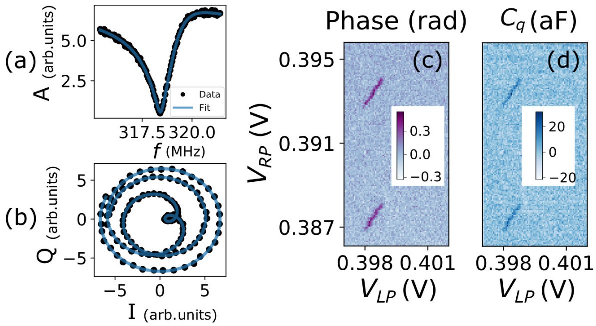

Figure 5.2: (a) The magnitude of the reflection signal as a function of probing frequency, as an example of the reference data. The black dots represents the raw data, while the blue curve shows the fitting result. (b) Parametric plot of the resonator reflection measurement in I-Q plane, and the corresponding fit result. (c) The reflected phase signal of the entire CSD. (d) The corresponding color maps of C_q values.

ICTs and the measured phase shifts at the ICTs tend to alternate between smaller and larger values (inset of Fig. 5.1(b)). As loading every other additional electron requires compensating for the level spacing on top of the charging energy, the smaller spacings along V_{LP} (V_{RP}) are associated with having an odd number of electrons in the left (right) dot [36]. Furthermore, an ICT corresponding to a total odd number of electrons in the DQD exhibit a larger phase shift, since the spin degeneracy of having total even charges leads to a reduction of the maximum of C_q [4, 37, 26].

The identification of the total charge parity in the DQD is additionally verified by applying an external magnetic field $\vec{B}$ (Fig. 5.1(c)) [38]. For four neighboring ICTs, their positions along the detuning axis are measured as a function of $\vec{B}$, with detuning $\varepsilon :=$ $[(V_{LP} - V_{LP,\varepsilon=0}) - (V_{RP} - V_{RP,\varepsilon=0})]/2$. We observe shifts only for the ICTs with a total even occupancy, consistent with Zeeman effect. Fits to the data for even-occupied ICTs in a region exhibiting a linear shift in magnetic field [4] yield the effective g-factors of approximately 25 and 30. Based on these observations, the parity of the electron numbers in the DQD is indicated with labels (n_L, n_R), with $n_{L(R)}$ indicating the excess number of electrons with respect to an even number of electrons (N_L, N_R) on the left (right) dot (also indicated in Fig. 5.1(b)). The number of electrons in each dot is estimated to be in the range of 70 to 150 electrons, considering the plunger gate voltages, pinch off voltages, and the spacing between ICTs.

5.2.3. EXTRACTION OF QUANTUM CAPACITANCE

Quantum capacitance C_q is extracted by calculating the changes of the capacitive load on the resonator from its bare value C_{cb}, as this results in a resonance frequency shift Δf that is directly obtainable from measurements [25]:

$$C_q = C - C_{cb} = \frac{1}{(2\pi)^2 (f_{cb} + \Delta f)^2 L} - \frac{1}{(2\pi)^2 f_{cb}^2 L}. \tag{5.1}$$

Here, C is the effective capacitance being measured, L is fixed to be 730 nH. C_{cb} and f_{cb} are the capacitance and resonance frequency at Coulomb blockade, respectively. According to this equation, the values of f_{cb} and Δf are required to get C_q.

The measurement of C_q at given gate settings under a certain external magnetic field consists of two steps. In the first step, we fix the gate settings near the ICT that we aim to study, and measure the frequency dependence of the reflection coefficient S_{11} around the resonance frequency f_0 (e.g. Fig. 5.2(a)). The measurement result is regarded as a reference data.

Considering the hanger geometry of the coupled resonator, we fit the measured S_{11} with the resonator model inspired by Khalil et al. [39], where they derive the transmission coefficient S_{21} of the hanger resonator. At probing frequency f_p, the measured S_{11} differs from S_{21} by a factor of 2 to convert from transmission to reflection:

$$S_{11} = 1 - \frac{2e^{i\Phi}\frac{Q}{Q_e}}{1+2iQ\frac{f_p - f_0}{f_0}}. \tag{5.2}$$

Here, $Q = 1/(1/Q_i + 1/Q_e)$ is the total quality factor, with $Q_{i(e)}$ being the internal (external) quality factor [26, 40]. The asymmetry of reflection is captured by the phenomenological phase term $e^{i\Phi}$, while is originated from the impedance mismatch as in Ref. [39]. Therefore, we obtain the value of f_0 for that particular gate setting, and the corresponding parameters of the resonator, including $Q_{i(e)}$, and phase factor Φ. With this approach, the values of quality factors are not accurately defined, but the influence on analysis is negligible when they are fixed in our case. Fig. 5.2(a,b) show an example of the fitting results compared to the raw data in both amplitude response and in I-Q plane. In the second step, we fix the probing frequency to f_p, and measure the CSD that completely encompasses the target ICT (see Fig. 5.2(c)).

We assume all resonator parameters collected from the reference data to be fixed within the gate voltage space of that CSD, except for C_q that changes the resonance frequency by Δf. As the probing frequency f_p is known, for each pixel i in the CSD (eg. in Fig. 5.2(c)), we convert all the measured S_{11}^i into different resonance frequencies f_0^i, according to the resonator model in Eq. (5.2) with the fitted resonator parameters. The value of f_{cb} is defined as a mean value of the resonance frequency f_0^i away from any ICT. This means that the resonance frequency shifts Δf^i are defined relative to f_{cb}. Finally, with Eq. (5.1), the values of C_q^i in the scanned gate voltage space are extracted, as shown in Fig. 5.2(d)).

5.3. IDENTIFICATION OF SPIN-ORBIT FIELD ORIENTATION

Having identified the total charge parity of the ICTs, we characterize the $\vec{B}_{SO}$ field orientation for an even-occupied ICT. We apply an external magnetic field with fixed amplitude $|\vec{B}| = 30$ mT. $C_{q,max}$ which denotes the maximum values of C_q at the ICT is extracted as a function of the field orientation in spherical coordinates φ and θ (Fig. 5.3(a)). Fig. 5.3 (d) and (e) display the obtained data in range $0° \le \theta \le 90°$, and $90° \le \theta \le 180°$, respectively. There are two regions at which $C_{q,max}$ is strongly suppressed. They lie at opposite directions in the spherical coordinates, neither perpendicular to the nanowire, nor in plane of the substrate. We interpret the centers of the suppression regions as corresponding to the directions parallel and anti-parallel to $\vec{B}_{SO}$. Energy diagrams of the DQD are presented in Fig. 5.3(b,c). Due to different total spin, the lowest singlet state $|S(2,0)\rangle$

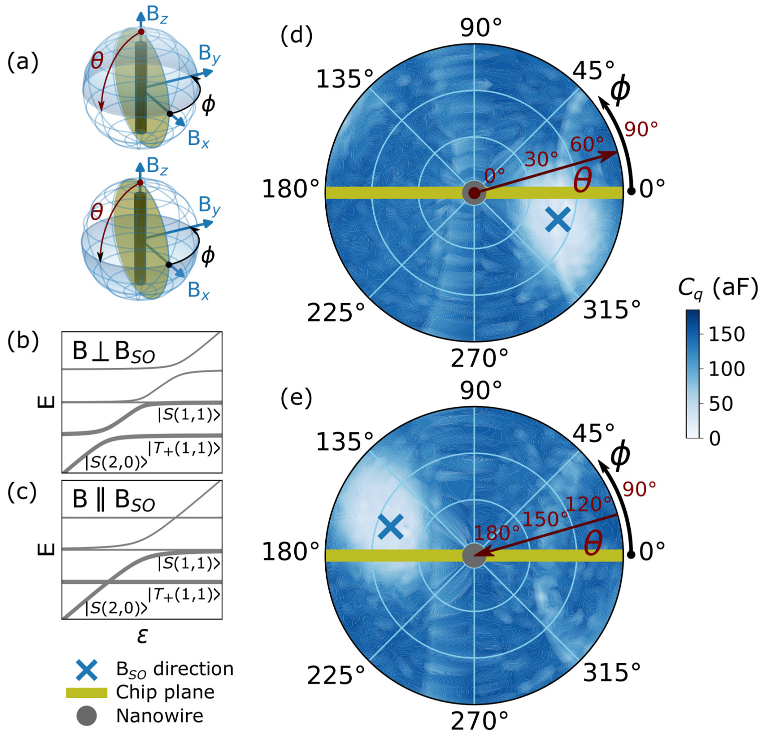

Figure 5.3: (a) Illustration of spherical coordinates with respect to the nanowire and the substrate. The top and bottom panel correspond to (d) and (e) respectively. (b-c) Schematic energy diagrams of a DQD for (b) $\vec{B} \perp \vec{B}_{SO}$ and (c) $\vec{B} \parallel \vec{B}_{SO}$. The (avoided) crossing between the two lowest states are highlighted. $C_{q,max} = 0$ when they cross, due to the flat shape of $|T_+(1,1)\rangle$. (d-e) The extracted $C_{q,max}$ values plotted on an external magnetic field angle map. Polar projection of the map is shown in (d) when $0° \leq \theta \leq 90°$, and (e) when $90° \leq \theta \leq 180°$. The blue crosses mark the characterized $\pm\vec{B}_{SO}$ orientations, which is the center of the region where $C_{q,max}$ is suppressed.

and triplet state $|T_+(1,1)\rangle$ only couple if electron spin flips during tunneling are allowed. This coupling arises only when $\vec{B}$ is not aligned with $\vec{B}_{SO}$ (Fig. 5.3(b)), resulting in finite curvature of the ground state energy at the ICT, and thus finite $C_{q,max}$. When $\vec{B} \parallel \vec{B}_{SO}$, the two states do not couple (Fig. 5.3(c)), therefore $C_{q,max}$ is suppressed because of the flat energy dispersion of $|T_+(1,1)\rangle$ state [4, 41, 42].

The observation that $\vec{B}_{SO}$ is neither perpendicular to the nanowire nor in-plane of the chip can be attributed to several reasons. First, the complicated gate structure is likely to create a nonuniform potential, making the local electric fields deviate significantly from the out-of-plane direction. Second, staying in many-electron regime brings more complexity, as the overlap between the wave functions of the two dots may not spatially coincide with the direction of the nanowire. Consequently, the momentum associated with electron tunneling is not necessarily along the nanowire. Third, although not dominant, a finite contribution of Dresselhaus SOI may also exist, so that spin mod-

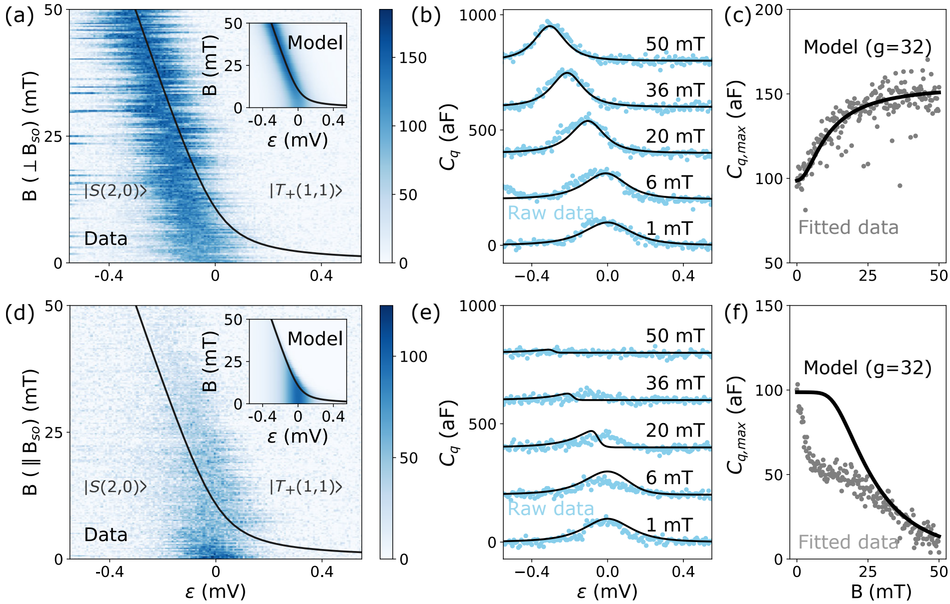

Figure 5.4: Evolution of the ICT in external magnetic field $\vec{B}$ for (a-c) $\vec{B} \perp \vec{B}_{SO}$, and (d-f) $\vec{B} \parallel \vec{B}_{SO}$. (a,d) C_q as a function of $\vec{B}$ and ε. The inset presents the numerical simulation. Black curves in both the main figure and the inset indicate the degeneracy point between $|S(2,0)\rangle$ and $|T_+(1,1)\rangle$. (b,e) Line cuts of (a,d) for several magnitudes of $\vec{B}$. For clarity, they are separated in the C_q axis by 200 aF. Black curves come from the simulation. (c,f) $C_{q,max}$ as a function of $\vec{B}$. Grey dots are extracted from a phenomenological Gaussian fit of the data. Black curves indicate the $C_{q,max}$ taken from the insets of (a,d).

ulations in the cross-sectional plane contribute to the offset angle with respect to the chip plane [43].

5.4. EXTERNAL FIELD DEPENDENCE OF QUANTUM CAPACITANCE

Next, we study the evolution of C_q at the same ICT, as a function of $\vec{B}$ and ε. While increasing the amplitude of $\vec{B} \perp \vec{B}_{SO}$, we find a nearly linear shift of the C_q maximum along detuning axis (Fig. 5.4(a,b)). This is accompanied by a gradual increase of $C_{q,max}$ value (Fig. 5.4(c)), starting at about 100 aF when $\vec{B}$ is zero, and saturating near 150 aF for $\vec{B}$ above 25 mT. In contrast, $C_{q,max}$ is suppressed (Fig. 5.4(d-f)) for $\vec{B} \parallel \vec{B}_{SO}$, since $\vec{B}_{SO}$ no longer introduces singlet-triplet coupling in this orientation. Along $\vec{B_{SO}}$, the suppression occurs in two distinct steps (see Fig. 5.4(f)). Initially, $C_{q,max}$ drops rapidly from 100 aF for low $\vec{B}$, and starts saturating near the value of 50 aF with $\vec{B}$ above ~10 mT. Then, $C_{q,max}$ starts dropping even further at about 25 mT. In the limited measurement range, $C_{q,max}$ appears to be trending towards zero.

To understand the capacitative response of the ICT in magnetic field, we employ a two-site Hubbard model (see Appendix) [44]. The SOI in our model is phenomenologically described as an effective field which can point in an arbitrary direction in space, namely both Rashba and Dresselhaus SOI are taken into consideration. The model includes the spin precessing tunneling matrix element t_p as part of total tunneling strength t_{tot}. The term t_p depends on the SOI strength and modulates spin-flip together with the angle between $\vec{B}$ and $\vec{B}_{SO}$. The individual cuts at $B = 0$ and $B = 50$ mT for $\vec{B} \perp \vec{B}_{SO}$ are used to estimate $t_{tot} = 20$ μeV and $t_p = 18$ μeV, by fitting the analytical expressions of C_q in Appendix. For simplicity, we assume isotropic g-factors $g = 32$ being equal in both dots, with the value taken from linear shifts of charge transitions in Fig. 5.4(a). The effective lever arm of the gate attached to the resonator is $\alpha = 0.26$, according to the ratio between the height and width of a Coulomb diamond, and an estimated crosstalk between the gates of 20%. The electron temperature in the model is set to 30 mK, based on a Coulomb blockade thermometry measurement performed before this experiment. The simulated results are illustrated in the insets of Fig. 5.4(a,d), and in black in Fig. 5.4(b,c,e,f). For $\vec{B} \perp \vec{B}_{SO}$, we find an excellent agreement with the data in a full range of magnetic fields, with no free parameters. In contrast, for $\vec{B} \parallel \vec{B}_{SO}$, the simulated shift of the ICT along detuning axis is greater than observed when $\vec{B}$ is below 25 mT. Furthermore, the model does not qualitatively capture the two-stage suppression of $C_{q,max}$ when $\vec{B}$ increases (Fig. 5.4(f)).

We identify two elements in our model potentially responsible for the discrepancy. First, we consider possible g-factor non-uniformity and anisotropy [14, 45, 46]. In particular, a smaller g-factor for $\vec{B} \parallel \vec{B}_{SO}$ can reduce the shift in detuning of the ICT in Fig. 5.4(d), and eventually increase $\vec{B}$ at which the predicted suppression of $C_{q,max}$ occurs. Second, when $\vec{B} \parallel \vec{B}_{SO}$, spin relaxation rates mediated by hyperfine and SOI are hindered [47, 48]. As a consequence, Pauli spin blockade traps the system in one of the excited states which do not contribute to $C_{q,max}$. We hypothesize that unaccounted Pauli spin blockade is responsible for the suppression of the $C_{q,max}$ in range of 0-25 mT. Meanwhile, the $C_{q,max}$ suppression above 25 mT is consistent with our model, except it occurs at higher field due to an overestimated g-factor. This can be identified from comparing the C_q peaks of model and data in Fig. 5.4(e).

5.5. VARIATIONS OF SPIN-ORBIT FIELD ORIENTATION

After analyzing an individual ICT, we look into the $\vec{B}_{SO}$ orientation of clusters of ICTs. Specifically, in the gate voltage space along V_{LP} and V_{RP}, we study 4-by-4 array of neighboring ICTs (see Fig. 5.5(a-p)), and exhibit them in the same order as in the CSD in Fig. 5.1(c). We rotate $\vec{B}$ with fixed amplitude of 50 mT while measuring $C_{q,max}$ for those neighboring ICTs, where for odd-occupied ICTs, the extracted $C_{q,max}$ is independent of the $\vec{B}$ orientation. On the contrary, the majority of even-occupied ICTs show a fairly well defined direction in which $C_{q,max}$ is suppressed, indicating the orientation of $\vec{B}_{SO}$. A few of the ICTs reveal a $C_{q,max}$ suppression in a peculiar pattern with no clear preferred direction (e.g. Fig. 5.5(a,f)), which will be discussed later.

Fig. 5.5(q) summarizes all of the extracted $\vec{B}_{SO}$ orientations, including some cases where we tune the barrier and plunger gates by a large amount. The crosses with the same color indicate pairs of ICTs of the same valence orbital. For three such ICT pairs, the corresponding maps of extracted $C_{q,max}$ with colored crosses are presented in Fig. 5.5(a-p). Blue squares in (q) indicate the ICTs for which the other ICT from a pair is not measured. Because of the inversion symmetry shown in Fig. 5.3(d-e), only the measurements

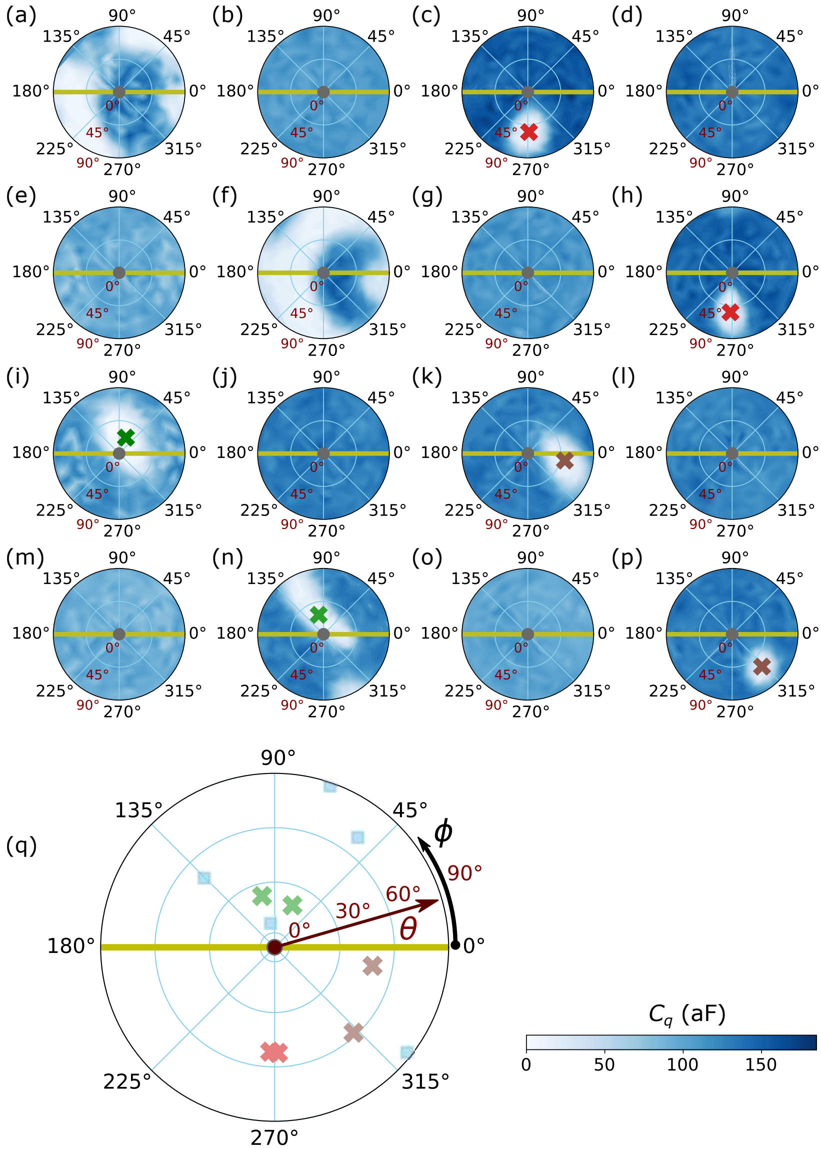

5

Figure 5.5: (a-p) The external magnetic field angle map of $C_{q,max}$ ($0^\circ \leq \theta \leq 90^\circ$, with $|\vec{B}| = 50$ mT) for 16 neighboring ICTs, with their extracted $\vec{B}_{SO}$ directions marked by colored crosses. These ICTs are labeled with the corresponding charge occupations (n'_L, n'_R) with respect to even charge numbers (N'_L, N'_R). (q) Summary of the extracted $\vec{B}_{SO}$ directions for the even-occupied ICTs under study. Crosses in the same color correspond to the ICT pairs with the same valence orbital. Squares mark the ICTs when the other ICT from a pair is not measured.

for $0° \leq \theta \leq 90°$ are performed.

The markers in Fig. 5.5(q) show no preferred direction among the complete set of measured $\vec{B}_{SO}$ orientations. Notably, for a pair of ICTs corresponding to the same valence orbital, their $\vec{B}_{SO}$ orientations are much closer to each other than to other random pairs. This thereby support the hypothesis that the random orientation of $\vec{B}_{SO}$ arises from the complex shape of the electronic orbitals and the hard-to-predict local $\vec{E}$. Imperfect alignment of the $\vec{B}_{SO}$ orientations within a pair of ICTs might be a consequence of a slight distortion of the confining potential, when the gates are tuning the dot occupancies. The irregular shape of the $C_{q,max}$ suppression regions for some of the ICTs (e.g. Fig. 5.5(a,f,n)) demonstrates that the description of SOI in terms of effective $\vec{B}_{SO}$ and isotropic g-factors is incomplete.

In Ref. [49], Scheübl et al. discuss a topological nature of Weyl points between the lowest singlet and triplet states, which is equivalently manifested by the suppression of C_q in our experiment. They show that the number of such Weyl points is not restricted to be 2 (like in Fig. 5.3(d-e)), but may be 6 or even larger for rare cases. The presence of more than 2 Weyl points might explain the highly irregular regions of $C_{q,max}$ suppression for some ICTs. The $C_{q,max}$ suppression regions in Fig. 5.5(a,f) are too large to fit $\vec{B}_{SO}$ orientations meaningfully, which may be due to a small level spacing to the first excited state.

5

5.6. SUMMARY

In summary, we study $\vec{B}_{SO}$ orientation using DGS in an InSb nanowire-based DQD. At zero magnetic field, DGS can be employed as a charge parity meter, and ICTs with even total parity are identified for further $\vec{B}_{SO}$ characterization. When a finite external field $\vec{B}$ is rotated, the directions in which $C_{q,max}$ is suppressed reveal the $\vec{B}_{SO}$ orientation of even-occupied ICTs. We model the dispersive signal at an even-occupied ICT, and find good agreement with the data for $\vec{B} \perp \vec{B}_{SO}$. However, for $\vec{B} \parallel \vec{B}_{SO}$, our model lacks a description of the suppressed spin relaxation rates due to Pauli blockade. Finally, we find that $\vec{B}_{SO}$ for the ICT pairs with the same valence orbital have similar orientations, while the $\vec{B}_{SO}$ orientation varies enormously between different orbitals. Our work indicates that considerations about $\vec{B}_{SO}$ orientation based purely on device design may often not apply to quantum dot systems. Resolving whether the randomness of $\vec{B}_{SO}$ orientation persists in quantum devices, either based on nanowires or two-dimensional electron gases, is essential to assess the viability of different materials for quantum computing with spins and Majorana zero modes. Moreover, DGS is shown to be an effective tool in characterizing the $\vec{B}_{SO}$ orientation, especially when transport measurements are not applicable. This result also broadens the prospects for systems applying DGS that feature integrated capabilities for qubit characterization and readout, while avoiding increasing the complexity in the chip design [30, 31, 50].

5.7. APPENDIX: MODELING THE DQD

In order to describe the effects observed in the DQD, we construct an effective Hamiltonian $\hat{H}_{tot}$ for the system in the Hund-Mulliken approximation using the second quantization notation [51, 52]. Only one orbital per dot, which can be doubly occupied by electrons, is considered in this approximation. In our model, $\hat{H}_{tot}$ consists of an electrostatic term $\hat{H}_e$, a magnetic Zeeman term $\hat{H}_m$ and a spin-orbit interaction (SOI) term $\hat{H}_{SO}$:

$$\hat{H}_{tot} = \hat{H}_e + \hat{H}_m + \hat{H}_{SO}. \tag{5.3}$$

Formally, SOI mixes the orbital and spin part of the electron wave function, and results in Kramers doublets. They are referred to as the conventional spin doublets: an external magnetic field $\vec{B}$ induces a Zeeman splitting between the spin doublets. The SOI itself is modeled as an effective electron momentum dependent magnetic field $\vec{B}_{SO}$, around which the spin of the tunneling electron precesses[14]. We use a phenomenological interaction Hamiltonian of the form of

$$\hat{H}_{SO} = \vec{B}_{SO}(\hat{p}_x, \hat{p}_y, \hat{p}_z) \cdot \hat{\vec{\sigma}}, \tag{5.4}$$

where $\hat{p}_i$ is the momentum operator in the three Cartesian directions $(i = x, y, z)$, and $\hat{\vec{\sigma}}$ is the Pauli (spin-1/2) operators. In particular, we define the spin basis of the electron such that the spin quantization axis (the projection of the spin on z-axis) aligns with $\vec{B}$. The angle η is defined as the angle associated with the inner product of $\vec{B}$ and $\vec{B}_{SO}$, allowing us to decompose $\vec{B}_{SO}$ into a parallel and perpendicular component with respect to the spin quantization axis. For simplicity, we choose the projection of the spin on the y-axis align with the component of $\vec{B}_{SO}$ that is perpendicular to $\vec{B}$. The SOI Hamiltonian is therefore given as

$$\begin{aligned}\hat{H}_{SO} = i t_p \sum_{\alpha,\beta=\{\uparrow,\downarrow\}} \Big(&\cos(\eta)\, \hat{c}^{\dagger}_{L,\alpha} \sigma_z^{\alpha\beta} \hat{c}_{R,\beta} \\ &+ \sin(\eta)\, \hat{c}^{\dagger}_{L,\alpha} \sigma_y^{\alpha\beta} \hat{c}_{R,\beta} - h.c.\Big),\end{aligned} \tag{5.5}$$

where t_p is the spin precessing tunnel coupling due to SOI, while $\sigma_{y(z)}$ is the spin $\frac{1}{2}$ Pauli y-(z-) matrices. $\hat{c}^{\dagger}_{i,\sigma}$ and $\hat{n}_{i,\sigma}$ are the fermionic creation and number operator for the electrons in dot i with spin σ.

Together with

$$\begin{aligned}\hat{H}_e = &\frac{\epsilon}{2} \sum_{\sigma,\sigma'=\{\uparrow,\downarrow\}} \left(\hat{n}_{L,\sigma} - \hat{n}_{R,\sigma'}\right) \\ &+ t \sum_{\sigma} \left(\hat{c}^{\dagger}_{L,\sigma} \hat{c}_{R,\sigma} + h.c.\right) \\ &+ \sum_{i=\{L,R\}} \left(U_i \hat{n}_{i,\uparrow} \hat{n}_{i,\downarrow}\right),\end{aligned} \tag{5.6}$$

and

$$\begin{aligned}\hat{H}_m = -\frac{\mu_B B}{2} \big(&g_L(\hat{n}_{L,\uparrow} - \hat{n}_{L,\downarrow}) \\ &+ g_R(\hat{n}_{R,\uparrow} - \hat{n}_{R,\downarrow})\big),\end{aligned} \tag{5.7}$$

we obtain the full Hamiltonian of the DQD system. Here, ϵ is the detuning, t is the spin conserving tunnel coupling, and $U_{L(R)}$ is the Coulomb repulsion induced energy cost for placing two electrons on the same left(right) dot. Moreover, μ_B denotes the Bohr magneton, B the external field magnitude and $g_{L(R)}$ the Landé g factor of the left(right) dot.

For ICTs between the $|(2,0)\rangle$ and $|(1,1)\rangle$ charge states, the following even parity states are of relevance:

$$\begin{aligned}
|(2,0)S\rangle &= \hat{c}^\dagger_{L,\uparrow}\hat{c}^\dagger_{L,\downarrow}|0\rangle \\
|(1,1)S\rangle &= \frac{1}{\sqrt{2}}\left(\hat{c}^\dagger_{L,\uparrow}\hat{c}^\dagger_{R,\downarrow} - \hat{c}^\dagger_{L,\downarrow}\hat{c}^\dagger_{R,\uparrow}\right)|0\rangle \\
|T_+\rangle &= \hat{c}^\dagger_{L,\uparrow}\hat{c}^\dagger_{R,\uparrow}|0\rangle \\
|T_0\rangle &= \frac{1}{\sqrt{2}}\left(\hat{c}^\dagger_{L,\uparrow}\hat{c}^\dagger_{R,\downarrow} + \hat{c}^\dagger_{L,\downarrow}\hat{c}^\dagger_{R,\uparrow}\right)|0\rangle \\
|T_-\rangle &= \hat{c}^\dagger_{L,\downarrow}\hat{c}^\dagger_{R,\downarrow}|0\rangle,
\end{aligned} \tag{5.8}$$

with $|0\rangle$ being a vacuum state.

5

For $B = 0$, we can project $\hat{H}_{tot}$ onto this basis and analytically diagonalize the Hamiltonian to find the ground state energy

$$E_g = \frac{1}{2}\left((U_L+\epsilon) - \sqrt{(U_L+\epsilon)^2 + 8(t^2+t_p^2)}\right). \tag{5.9}$$

Note that U_L offsets (the onset of) the avoided crossing along the detuning axis only and can be set to zero by redefining the detuning axis. The C_q value can then be calculated as the curvature of the ground state energy $-(e\alpha')^2\frac{\partial^2 E_g}{\partial\epsilon^2}$, for which we find ($\alpha'$ is the effective lever arm accounted for cross coupling) [34, 35, 53]

$$C_{q,B=0} = \frac{(e\alpha')^2}{2}\frac{8t_{tot}^2}{\left(\epsilon^2+8t_{tot}^2\right)^{\frac{3}{2}}}, \tag{5.10}$$

where e is the elementary charge. In addition, we define $t_{tot} = \sqrt{t^2+t_p^2}$ as the total tunnel coupling set by the barrier gates.

Another special limit is when $\vec{B} \perp \vec{B}_{SO}$, where $\eta = \pi/2$. According to $\hat{H}_{SO}$, the spin flipping due to SOI during tunneling is strongest. When the Zeeman energy E_z is the second largest energy scale ($E_z >> t_{tot}$), we expect that the ground state is solely contributed to by the states $|(2,0)S\rangle$ and $|T_+\rangle$ that are coupled by SOI through the tunneling element t_p. In this case, the ground and first excited state are analytically approximated by projecting $\hat{H}_{tot}$ onto the aforementioned two states. The ground state energy and C_q are found as

$$\begin{aligned}
E_g &= \frac{1}{2}\Bigg[U_L+\epsilon-\frac{\mu_B B}{2}(g_L+g_R) \\
&\quad - \sqrt{\left(U_L+\epsilon+\frac{\mu_B B}{2}(g_L+g_R)\right)^2+4t_p^2}\Bigg]; \\
C_{q,B\perp B_{SO}} &= \frac{2(e\alpha')^2 t_p^2}{\left[(U_L+\epsilon+\frac{\mu_B B(g_L+g_R))^2}{2}+4t_p^2\right]^{\frac{3}{2}}}.
\end{aligned} \tag{5.11}$$

For the more general case, we employ numerical simulations to compute C_q. We project the five spin basis states (in Eq. (5.8)) onto $\hat{H}_{tot}$ and numerically diagonalize it to find the eigenenergies E_n and states Ψ_n. In the limit of relaxation rates being slower than the probing frequency, C_q is calculated as the curvature of the energy bands, or equivalently through $\left(e\alpha'\right)^2 \frac{d\langle n_L\rangle}{d\epsilon}$ [41]. In thermal equilibrium, C_q can be expressed as

$$C_q = \left(e\alpha'\right)^2 \sum_n \frac{e^{-\frac{E_n(\epsilon)}{k_B T}}}{\mathcal{Z}} \left(\frac{d\left\langle \Psi_n|\hat{n}_L|\Psi_n\right\rangle(\epsilon)}{d\epsilon}\right), \tag{5.12}$$

where k_B is the Boltzmann constant, T is the electronic temperature, and $\mathcal{Z} = \mathrm{Tr}\left(e^{-\frac{\hat{H}_{tot}}{k_B T}}\right)$ is the partition function. $\frac{d\langle n|\hat{n}_R|n\rangle(\epsilon)}{d\epsilon}$ itself is numerically computed using the central difference method.

BIBLIOGRAPHY

[1] EI Rashba and Al L Efros. Orbital mechanisms of electron-spin manipulation by an electric field. *Physical review letters*, 91(12):126405, 2003.

[2] Igor Žutić, Jaroslav Fabian, and S Das Sarma. Spintronics: Fundamentals and applications. *Reviews of modern physics*, 76(2):323, 2004.

[3] Vitaly N Golovach, Massoud Borhani, and Daniel Loss. Electric-dipole-induced spin resonance in quantum dots. *Physical Review B*, 74(16):165319, 2006.

[4] Ronald Hanson, Leo P Kouwenhoven, Jason R Petta, Seigo Tarucha, and Lieven MK Vandersypen. Spins in few-electron quantum dots. *Reviews of modern physics*, 79(4):1217, 2007.

[5] S Nadj-Perge, SM Frolov, EPAM Bakkers, and Leo P Kouwenhoven. Spin–orbit qubit in a semiconductor nanowire. *Nature*, 468(7327):1084–1087, 2010.

[6] Karl D Petersson, Louis W McFaul, Michael D Schroer, Minkyung Jung, Jacob M Taylor, Andrew A Houck, and Jason R Petta. Circuit quantum electrodynamics with a spin qubit. *Nature*, 490(7420):380–383, 2012.

[7] Seigo Tarucha, Michihisa Yamamoto, Akira Oiwa, Byung-Soo Choi, and Yasuhiro Tokura. Spin qubits with semiconductor quantum dots. In *Principles and Methods of Quantum Information Technologies*, pages 541–567. Springer, 2016.

[8] Alessandro Crippa, Rami Ezzouch, Agostino Aprá, A Amisse, R Laviéville, L Hutin, B Bertrand, M Vinet, M Urdampilleta, T Meunier, et al. Gate-reflectometry dispersive readout and coherent control of a spin qubit in silicon. *Nature communications*, 10(1):1–6, 2019.

[9] Christoph Kloeffel and Daniel Loss. Prospects for spin-based quantum computing in quantum dots. *Annu. Rev. Condens. Matter Phys.*, 4(1):51–81, 2013.

[10] Anasua Chatterjee, Paul Stevenson, Silvano De Franceschi, Andrea Morello, Nathalie P de Leon, and Ferdinand Kuemmeth. Semiconductor qubits in practice. *Nature Reviews Physics*, 3(3):157–177, 2021.

[11] R Winkler, S Papadakis, E De Poortere, and M Shayegan. *Spin-Orbit Coupling in Two-Dimensional Electron and Hole Systems*, volume 41. Springer, 2003.

[12] Thomas Ihn. *Semiconductor Nanostructures: Quantum states and electronic transport*. OUP Oxford, 2009.

[13] Jakob Kammhuber, Maja C Cassidy, Fei Pei, Michal P Nowak, Adriaan Vuik, Onder Gul, Diane Car, SR Plissard, EPAM Bakkers, M Wimmer, et al. Conductance through a helical state in an indium antimonide nanowire. *Nature communications*, 8(1):1–6, 2017.

[14] S Nadj-Perge, VS Pribiag, JWG Van den Berg, K Zuo, SR Plissard, EPAM Bakkers, SM Frolov, and LP Kouwenhoven. Spectroscopy of spin-orbit quantum bits in indium antimonide nanowires. *Physical review letters*, 108(16):166801, 2012.

[15] Ji-Yin Wang, Guang-Yao Huang, Shaoyun Huang, Jianhong Xue, Dong Pan, Jianhua Zhao, and Hongqi Xu. Anisotropic pauli spin-blockade effect and spin–orbit interaction field in an inas nanowire double quantum dot. *Nano letters*, 18(8):4741–4747, 2018.

[16] S Dorsch, B Dalelkhan, S Fahlvik, and AM Burke. Side-gated, enhancement mode, inas nanowire double quantum dot devices—toward controlling transverse electric fields in spin-transport measurements. *Nanotechnology*, 30(14):144002, 2019.

[17] Roman M Lutchyn, Erik PAM Bakkers, Leo P Kouwenhoven, Peter Krogstrup, Charles M Marcus, and Yuval Oreg. Majorana zero modes in superconductor–semiconductor heterostructures. *Nature Reviews Materials*, 3(5):52–68, 2018.

[18] A Pfund, I Shorubalko, K Ensslin, and R Leturcq. Spin-state mixing in inas double quantum dots. *Physical Review B*, 76(16):161308, 2007.

[19] S Nadj-Perge, SM Frolov, JWW Van Tilburg, J Danon, Yu V Nazarov, R Algra, EPAM Bakkers, and LP Kouwenhoven. Disentangling the effects of spin-orbit and hyperfine interactions on spin blockade. *Physical Review B*, 81(20):201305, 2010.

[20] Alex Bogan, Sergei Studenikin, Marek Korkusinski, Louis Gaudreau, Jason Phoenix, Piotr Zawadzki, Andy Sachrajda, Lisa Tracy, John Reno, and Terry Hargett. Spin-orbit enabled quantum transport channels in a two-hole double quantum dot. *Physical Review B*, 103(23):235310, 2021.

[21] DM Zajac, TM Hazard, Xiao Mi, E Nielsen, and Jason R Petta. Scalable gate architecture for a one-dimensional array of semiconductor spin qubits. *Physical Review Applied*, 6(5):054013, 2016.

[22] Torsten Karzig, Christina Knapp, Roman M Lutchyn, Parsa Bonderson, Matthew B Hastings, Chetan Nayak, Jason Alicea, Karsten Flensberg, Stephan Plugge, Yuval Oreg, et al. Scalable designs for quasiparticle-poisoning-protected topological quantum computation with majorana zero modes. *Physical Review B*, 95(23):235305, 2017.

[23] JI Colless, AC Mahoney, JM Hornibrook, AC Doherty, H Lu, AC Gossard, and DJ Reilly. Dispersive readout of a few-electron double quantum dot with fast rf gate sensors. *Physical review letters*, 110(4):046805, 2013.

[24] Guoji Zheng, Nodar Samkharadze, Marc L Noordam, Nima Kalhor, Delphine Brousse, Amir Sammak, Giordano Scappucci, and Lieven MK Vandersypen. Rapid gate-based spin read-out in silicon using an on-chip resonator. *Nature nanotechnology*, 14(8):742–746, 2019.

[25] Damaz De Jong, Jasper Van Veen, Luca Binci, Amrita Singh, Peter Krogstrup, Leo P Kouwenhoven, Wolfgang Pfaff, and John D Watson. Rapid detection of coherent tunneling in an in as nanowire quantum dot through dispersive gate sensing. *Physical Review Applied*, 11(4):044061, 2019.

[26] Jasper Van Veen, Damaz De Jong, Lin Han, Christian Prosko, Peter Krogstrup, John D Watson, Leo P Kouwenhoven, and Wolfgang Pfaff. Revealing charge-tunneling processes between a quantum dot and a superconducting island through gate sensing. *Physical Review B*, 100(17):174508, 2019.

[27] Deividas Sabonis, Eoin CT O'Farrell, Davydas Razmadze, David MT van Zanten, Judith Suter, Peter Krogstrup, and Charles M Marcus. Dispersive sensing in hybrid inas/al nanowires. *Applied Physics Letters*, 115(10):102601, 2019.

[28] Damaz De Jong, Daan Waardenburg, Nejc Blaznik, Lin Han, Filip Malinowski, Christian Prosko, Jasper Van Veen, Peter Krogstrup, Leo Kouwenhoven, and Wolfgang Pfaff. Dispersive sensing of electron tunneling between quantum dots in proximitized inas nanowires. *Bulletin of the American Physical Society*, 65, 2020.

[29] J Stehlik, Y-Y Liu, CM Quintana, C Eichler, TR Hartke, and Jason R Petta. Fast charge sensing of a cavity-coupled double quantum dot using a josephson parametric amplifier. *Physical Review Applied*, 4(1):014018, 2015.

[30] Stephan Plugge, Asbjørn Rasmussen, Reinhold Egger, and Karsten Flensberg. Majorana box qubits. *New Journal of Physics*, 19(1):012001, 2017.

[31] Thomas B Smith, Maja C Cassidy, David J Reilly, Stephen D Bartlett, and Arne L Grimsmo. Dispersive readout of majorana qubits. *PRX Quantum*, 1(2):020313, 2020.

[32] Ghada Badawy, Sasa Gazibegovic, Francesco Borsoi, Sebastian Heedt, Chien-An Wang, Sebastian Koelling, Marcel A Verheijen, Leo P Kouwenhoven, and Erik PAM Bakkers. High mobility stemless insb nanowires. *Nano letters*, 19(6):3575–3582, 2019.

[33] JM Hornibrook, JI Colless, AC Mahoney, XG Croot, S Blanvillain, H Lu, AC Gossard, and DJ Reilly. Frequency multiplexing for readout of spin qubits. *Applied Physics Letters*, 104(10):103108, 2014.

[34] Tim Duty, Goeran Johansson, Kevin Bladh, David Gunnarsson, Chris Wilson, and Per Delsing. Observation of quantum capacitance in the cooper-pair transistor. *Physical review letters*, 95(20):206807, 2005.

[35] KD Petersson, CG Smith, D Anderson, P Atkinson, GAC Jones, and DA Ritchie. Charge and spin state readout of a double quantum dot coupled to a resonator. *Nano letters*, 10(8):2789–2793, 2010.

[36] Wilfred G Van der Wiel, Silvano De Franceschi, Jeroen M Elzerman, Toshimasa Fujisawa, Seigo Tarucha, and Leo P Kouwenhoven. Electron transport through double quantum dots. *Reviews of Modern Physics*, 75(1):1, 2002.

[37] Audrey Cottet, Christophe Mora, and Takis Kontos. Mesoscopic admittance of a double quantum dot. *Physical Review B*, 83(12):121311, 2011.

[38] MD Schroer, M Jung, KD Petersson, and Jason R Petta. Radio frequency charge parity meter. *Physical review letters*, 109(16):166804, 2012.

[39] MS Khalil, MJA Stoutimore, FC Wellstood, and KD Osborn. An analysis method for asymmetric resonator transmission applied to superconducting devices. *Journal of Applied Physics*, 111(5):054510, 2012.

[40] Filip K Malinowski, Lin Han, Damaz De Jong, Ji-Yin Wang, Christian G Prosko, Ghada Badawy, Sasa Gazibegovic, Yu Liu, Peter Krogstrup, Erik PAM Bakkers, et al. Radio-frequency c-v measurements with subattofarad sensitivity. *Physical Review Applied*, 18(2):024032, 2022.

[41] Ryo Mizuta, RM Otxoa, AC Betz, and M Fernando Gonzalez-Zalba. Quantum and tunneling capacitance in charge and spin qubits. *Physical Review B*, 95(4):045414, 2017.

[42] M Esterli, RM Otxoa, and MF Gonzalez-Zalba. Small-signal equivalent circuit for double quantum dots at low-frequencies. *Applied Physics Letters*, 114(25):253505, 2019.

[43] Andreas Bringer, Sebastian Heedt, and Th Schäpers. Dresselhaus spin-orbit coupling in [111]-oriented semiconductor nanowires. *Physical Review B*, 99(8):085437, 2019.

[44] Paul Ziesche, Olle Gunnarsson, Walter John, and Hans Beck. Two-site hubbard model, the bardeen-cooper-schrieffer model, and the concept of correlation entropy. *Physical Review B*, 55(16):10270, 1997.

[45] Fanming Qu, Jasper van Veen, Folkert K de Vries, Arjan JA Beukman, Michael Wimmer, Wei Yi, Andrey A Kiselev, Binh-Minh Nguyen, Marko Sokolich, Michael J Manfra, et al. Quantized conductance and large g-factor anisotropy in insb quantum point contacts. *Nano letters*, 16(12):7509–7513, 2016.

5

[46] Jingwei Mu, Shaoyun Huang, Ji-Yin Wang, Guang-Yao Huang, Xuming Wang, and HQ Xu. Measurements of anisotropic g-factors for electrons in insb nanowire quantum dots. *Nanotechnology*, 32(2):020002, 2020.

[47] T Fujita, P Stano, G Allison, K Morimoto, Y Sato, M Larsson, J-H Park, A Ludwig, AD Wieck, A Oiwa, et al. Signatures of hyperfine, spin-orbit, and decoherence effects in a pauli spin blockade. *Physical Review Letters*, 117(20):206802, 2016.

[48] Theodor Lundberg, David J Ibberson, Jing Li, Louis Hutin, José C Abadillo-Uriel, Michele Filippone, Benoit Bertrand, Andreas Nunnenkamp, Chang-Min Lee, Nadia Stelmashenko, et al. Non-reciprocal pauli spin blockade in a silicon double quantum dot. *arXiv preprint arXiv:2110.09842*, 2021.

[49] Zoltán Scherübl, András Pályi, György Frank, István Endre Lukács, Gergő Fülöp, Bálint Fülöp, Jesper Nygård, Kenji Watanabe, Takashi Taniguchi, Gergely Zaránd, et al. Observation of spin–orbit coupling induced weyl points in a two-electron double quantum dot. *Communications Physics*, 2(1):1–6, 2019.

[50] Vahid Derakhshan Maman, MF Gonzalez-Zalba, and András Pályi. Charge noise and overdrive errors in dispersive readout of charge, spin, and majorana qubits. *Physical Review Applied*, 14(6):064024, 2020.

[51] Guido Burkard, Daniel Loss, and David P DiVincenzo. Coupled quantum dots as quantum gates. *Physical Review B*, 59(3):2070, 1999.

[52] Dimitrije Stepanenko, Nicholas E Bonesteel, David P DiVincenzo, Guido Burkard, and Daniel Loss. Spin-orbit coupling and time-reversal symmetry in quantum gates. *Physical Review B*, 68(11):115306, 2003.

[53] Matias Urdampilleta, Anasua Chatterjee, Cheuk Chi Lo, Takashi Kobayashi, John Mansir, Sylvain Barraud, Andreas C Betz, Sven Rogge, M Fernando Gonzalez-Zalba, and John JL Morton. Charge dynamics and spin blockade in a hybrid double quantum dot in silicon. *Physical Review X*, 5(3):031024, 2015.

6

RADIO-FREQUENCY C-V MEASUREMENTS WITH SUBATTOFARAD SENSITIVITY

We demonstrate the use of radio-frequency (rf) resonators to measure the capacitance of nano-scale semiconducting devices in field-effect transistor configurations. The rf resonator is attached to the gate or the lead of the device. Consequently, tuning the carrier density in the conducting channel of the device affects the resonance frequency, quantitatively reflecting its capacitance. We test the measurement method on InSb and InAs nanowires at dilution-refrigerator temperatures. The measured capacitances are consistent with those inferred from the periodicity of the Coulomb blockade of quantum dots realized in the same devices. In an implementation of the resonator using an off-chip superconducting spiral inductor we find the measurement sensitivity values reaching down to 75 $\mathrm{zF}/\sqrt{\mathrm{Hz}}$ at 1 kHz measurement bandwidth, and noise down to 0.45 aF at 1 Hz bandwidth. We estimate the sensitivity of the method for a number of other implementations. In particular we predict a typical sensitivity of about 40 $\mathrm{zF}/\sqrt{\mathrm{Hz}}$ at room temperature with a resonator comprised of off-the-shelf components. Of several proposed applications, we demonstrate two: the capacitance measurement of several identical 80 nm-wide gates with a single resonator, and the field-effect mobility measurement of an individual nanowire with the gate capacitance measured in-situ.

This chapter is based on F. K. Malinowski, L. Han, D. de Jong, J. Wang, C. G. Prosko, G. Badawy, S. Gazibegovic, Y. Liu, P. Krogstrup, E. P. Bakkers, L. P. Kouwenhoven and J. V. Koski, Radio-frequency C-V measurements with subattofarad sensitivity, published (2022).

6.1. Introduction

Radio-frequency (rf) resonators are broadly used for readout of solid-state qubits, whether the quantum information is encoded as an excitation of a superconducting circuit [1], a quantum dot's charge, or an electronic spin [2]. This follows from mappings of the equivalent resistance, capacitance or inductance of the quantum system to the transmission or reflection coefficient of the macroscopic rf resonator. Furthermore, resonance frequencies between tens of megahertz and tens of gigahertz enable the use of the near-quantum-limited cryogenic amplifiers, with noise temperatures below 1 K [3, 4]. Seminal work of Schoelkopf et al.[5] demonstrated an orders-of-magnitude improvement in electrometer sensitivity, once the low-frequency measurement of the single-electron transistor is substituted by embedding it in an rf resonator [6].

Concurrently, a number of methods have been developed to measure capacitance of field-effect transistors (FETs), Schottky junctions and various other semiconducting devices[7, 8, 9, 10]. A common feature of these measurement schemes is the use of relatively low excitation frequencies, up to tens of kilohertz, raising a question of whether a scheme similar to Ref. [5] could also improve the sensitivity of capacitance measurements. Such an approach would increase the measurement bandwidth and reduce the influence of the ubiquitous $1/f$ noise by several orders of magnitude. Instead, the measurement would become limited by much smaller Johnson–Nyquist noise, amplifier noise and noise intrinsic to the device.

6

Indeed, the principle of mapping the conductance and resistance, respectively, on the frequency and quality factor of an rf resonator, is widely adopted in studies of gate-defined semiconducting quantum dots[11, 12, 13, 14, 15, 6]. In these cases, the discrete electron charge tunnels between the dots or between the dot and the lead at a well defined gate voltage, giving rise to a relatively large effective capacitance at the charge transition. In a number of works, when the tunneling is spin-dependent, rf capacitance measurement was used to perform high fidelity readout of a spin qubit[16, 17, 18] down to a few-microsecond timescale[19].

We suggest that rf capacitance measurements can be used in studies of micro- and nano-scale semiconducting devices more broadly [6]. In particular, in the absence of a quantum dot enhancing the capacitance at the charge transition, the magnitude of the signal is significantly decreased, requiring much smaller measurement bandwidth. To date, several groups reported the sensitivities in the range from 50 to 100 $\mathrm{zF}/\sqrt{\mathrm{Hz}}$, but these values were benchmarked by measuring the magnitude of a sideband peak under modulation of capacitance [4, 20]. This method compares the magnitude of the signal against the noise background around resonance frequency, which may not straightforwardly translate to equivalent performance for long measurement times.

To explore the performance of radio frequency capacitance measurements in long measurements, we characterize the bulk capacitance of semiconducting nanowire devices in a FET configuration. The resonance frequency is measured as a function of gate voltages, and we demonstrate that the frequency shift quantitatively matches the gate capacitance, extracted independently from the periodicity of Coulomb blockade.

We benchmark the sensitivity of this measurement method for long measurement times, where the relevant noise spectrum is frequency-dependent. We find that while the absolute noise is reduced for bandwidths below 1 kHz, the corresponding sensitivity deteriorates by about an order of magnitude from 70 zF/$\sqrt{\text{Hz}}$ at 1 kHz to 500 zF/$\sqrt{\text{Hz}}$ at 1 Hz. By measuring the noise spectra we attribute the deterioration of sensitivity to an onset of $1/f$ noise and switching of two level systems in the vicinity of the device, illustrating the limitations of the sensitivity as a metric of the measurement precision. Nonetheless, with such performance, moderate integration times (<1 s) are sufficient to measure capacitances of devices with a footprint below 100 nm, as well as quantum contributions to a bulk capacitance of other devices with a typical scale of ∼1 μm [21, 22].

In section 6.2, we introduce the principle of the capacitance measurement with an rf resonator, and discuss its variants and limitations. Section 6.3 presents a validation of the method by comparing the capacitance extracted from the resonator shift with the one extracted from the periodicity of Coulomb blockade in three devices with different gate sizes. In section 6.4 we characterize the sensitivity and the noise of the capacitance measurement, and estimate the performance of the method for several different temperatures, amplifiers, and realizations of rf resonators. Section 6.5 presents the application of the method to measure uniformity of nominally identical gates and to measure field-effect mobility of an individual device. We also discuss several other possible applications and implementations.

6.2. METHOD

The measurement method is based on the elementary fact, that the resonance frequency of an LC circuit depends on its capacitance. Therefore, if the inductance L embedded in the circuit is known, one can infer the capacitance from a measurement of the resonance frequency. To this end, the resonance frequency is extracted from the frequency-dependent reflection or transmission through the resonator. In this section we describe how to apply this principle to measure the capacitance of mesosopic devices. We start by describing the devices used for the validation of the method. Next we outline the experimental procedure. We conclude the section with a discussion of a number of critical factors that need to be taken into account in order for the method to yield valid results.

The nanostructures used for validation and benchmarking of the method are InSb and InAs nanowire single-electron transistors, depicted schematically in Fig. 6.1(a). The nanowires were grown by metalorganic vapour-phase epitaxy (InSb)[23] or molecular beam epitaxy (InAs)[24], and deposited on a highly resistive Si substrate. The devices are bottom-gated in the case of InSb, and top-gated in the case of InAs. The Ti/Au gates for tuning the electron density in the bulk of the nanowire are defined by e-beam lithography and are isolated from the wire by ∼15 nm of ALD AlO_x. Source and drain contacts are made of Ti/Au and deposited with a direct contact to the nanowire. In these devices, we aim to characterize the capacitance C_G between the central gate and the nanowire as a function of the applied voltage V_G. For that purpose, we wire-bond the source or the central gate of each measured device to superconducting NbTiN spiral inductor resonators[25] with inductances between 420 and 730 nH. Together with the parasitic- and self-capacitance (typically 0.3-0.35 pF), these inductors form LC circuits with resonance frequencies between 300 and 500 MHz. The barrier gate voltages, $V_{L/R}$, locally tune the electrostatic potential in order to connect or isolate the bulk of the wire from the contacts, or to form tunnel barriers. The reflection from the resonators is measured using a Rhode&Schwarz ZNB 20 vector network analyzer, with a cryogenic Cosmic

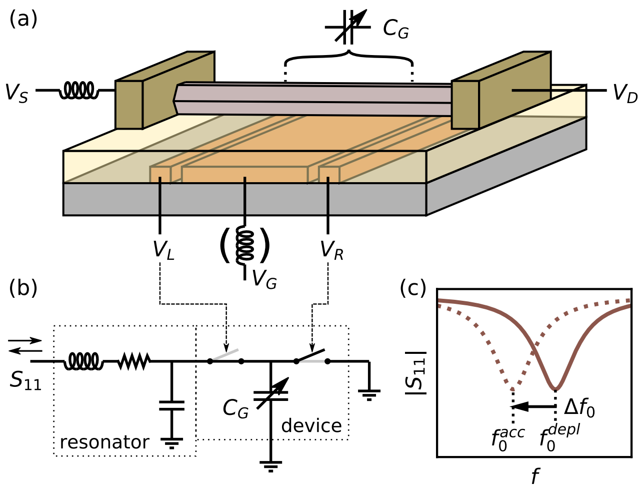

Figure 6.1: **(a)** Schematic of a bottom-gated nanowire device in a FET configuration. A source-drain voltage $V_{SD} = V_S - V_D$ can be applied to measure the conductance of the device. Gate voltages $V_{L/G/R}$ control the electron density in the semiconductor. C_G symbolizes the variable capacitance between the gate and the segment of the nanowire tuned by the gate voltage V_G. Coil symbols indicate contacts that can be connected to an rf resonator to perform capacitance measurements. **(b)** Schematic of the circuit for the capacitance measurement with the resonator attached to the device source contact. A lossy resonator is represented as an RLC circuit. The device is represented as two switches (tuned by gate voltages $V_{L/R}$) and a variable capacitor. For a capacitance measurement the gate voltage V_L is set to accumulate charge carriers, while V_R is set to deplete them. **(c)** Illustration of the resonance frequency shift, measured in reflectometry, resulting from the accumulation of electrons in the nanowire. In the measured nanometer-scale devices the frequency shifts are typically much smaller than the resonance linewidth.

Microwave CITLF2 HEMT amplifier used in the first step of the amplification chain.

Fig. 6.1(b) depicts a schematic of the circuit for the capacitance measurement with the rf resonator connected to the source of the device. Voltage V_L is set to provide a good galvanic connection[1] between the contact and the tuneable bulk of the nanowire. Voltage V_R is such, that the nanowire is locally fully depleted to disconnect the drain contact which would otherwise act as an rf ground. Next, the reflection from the resonator is measured to extract the resonance frequency as a function of the gate voltage V_G. Fig. 6.1(c) illustrates schematically that in the reflection measurement the resonance frequency is reduced when the nanowire is accumulated (dashed line), relative to when the charge carriers are depleted (solid line).

Using the known, designed value of inductance L, and having measured the resonance frequency with the carriers depleted and accumulated $f_0^{\mathrm{depl/acc}}$, the gate capacitance C_G is obtained from a set of two equations:

$$f_0^{\mathrm{depl}} = \frac{1}{2\pi\sqrt{LC}}; \; f_0^{\mathrm{acc}} = \frac{1}{2\pi\sqrt{L(C+C_G)}}, \tag{6.1}$$

[1]Good galvanic connection in this context means that the contact resistance R must be such that $2\pi/RC_G \gg f_0$. For $f_0 = 500$ MHz and $C_G = 1$ fF this implies $R \ll 10$ MΩ.

where C is the capacitance of the resonator, including the self-capacitance of the inductor and parasitic capacitance of the bondwires and the source contact. Equivalently

$$C_G = \frac{1}{(2\pi f_0^{\mathrm{depl}})^2 L} - \frac{1}{(2\pi f_0^{\mathrm{acc}})^2 L} \approx -\frac{\Delta f_0}{2\pi^2 (f_0^{\mathrm{depl}})^3 L}, \tag{6.2}$$

where the last approximation assumes a small resonator shift $\Delta f_0 \ll f_0$.

With the resonator attached to the device gate, the capacitance measurement is performed similarly. In this case, either one or both of the barrier gate voltages $V_{L/R}$ must be set to accumulate electrons to provide a low-impedance shunt to rf ground. The two configurations of connecting the resonator: to the device source or gate, measure slightly different quantities, and are subject to different constraints.

First, the rf resonance frequency is affected by capacitance between the attached contact (source or gate) and any rf ground. This includes e.g. other gates or a conducting substrate. If gating of the active part of the device also influences other relevant parts of the device (e.g. the substrate), the capacitance method becomes unreliable. In the validation experiment we ensure that is not the case by using a highly resistive Si substrate.

Second, the channel tuned by V_G may be coupled capacitatively to multiple gates. Thereby, resonators attached to the device lead or gate will measure different capacitance. If the resonator connected to the tuned gate, it will only detect capacitance changes between the channel and the tuned gate. Meanwhile, a measurement with the resonator connected to the source lead detects capacitance changes between the carriers accumulated in the channel and *all* gates. Depending on the purpose of the measurement, either one or both of these implementations may be desirable.

In particular, if a number of gates is coupled to the same segment of the conducting channel, the resonators attached to the gates can be employed to quantify their relative capacitance. However, we note that in those cases the conducting channel itself often contributes to the screening of the gate. Consequently, the capacitances effectively change depending on e.g. whether the channel is galvanically connected to the leads, depleted, or if the quantum dots are formed. In our devices the capacitance between the channel and the gate dominates over capacitances between the channel and other elements of the device.

Third, attaching the resonator to the device source enables using it for measuring the capacitance of multiple connected devices, since the DC gate voltages can be applied separately, and used to select between the devices. However, if the device yield is low this may be undesirable, as a single faulty device may introduce an rf short to ground and render the resonator unusable.

Finally, in case the resonator is attached to the device source, it can be repurposed for rf conductance measurements [5, 26, 27]. When the source-drain resistance is finite, it introduces dissipation in the resonant circuit, mapping the channel conductance to the internal quality factor of the resonator.

In the validation experiment (Sec. 6.3) we measure the capacitance of three InSb devices: for two of them we attach the resonator to the source contact, and for the last one

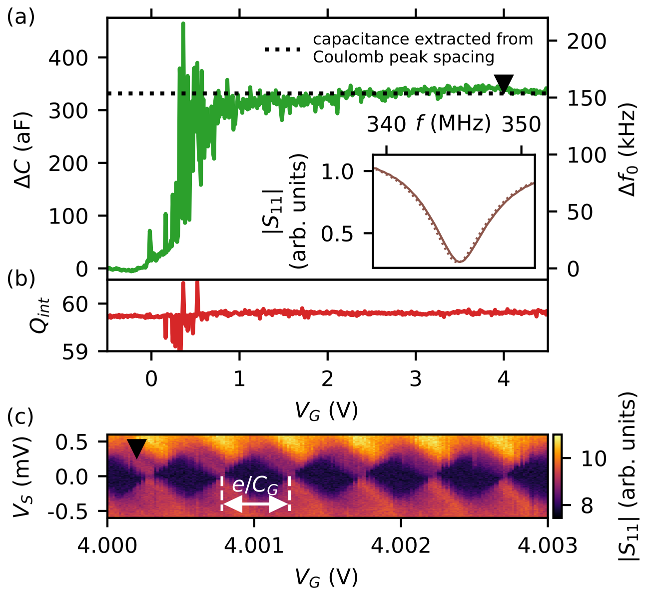

Figure 6.2: (a) Frequency shift, Δf, and a corresponding capacitance change, ΔC, as a function of the plunger gate voltage V_G for 2-μm long InSb device. Dotted line indicates the gate capacitance extracted from Coulomb blockade measurement at $V_G = 4$ V, indicated with a triangular marker. Inset: $|S_{11}|$ versus frequency at $V_G = -0.5$ V (solid line) and 4 V (dotted). (b) Internal quality factor Q_{int} of the resonator. (c) Rf Coulomb diamonds measurement. The periodicity of Coulomb blockade provides an independent measure of the gate capacitance.

– to the gate. In a noise characterization experiment (Sec. 6.4) we measure the resonator attached to the source contact of InAs device.

6.3. VALIDATION

To verify that the rf capacitance measurement provides quantitatively accurate results, we compare the capacitance extracted from the resonator shift and from the periodicity of the Coulomb blockade for InSb devices with 80, 500 and 2000 nm gate widths. An example of such a comparison is shown in Fig. 6.2, for a device with 2 μm-wide bottom gate.

First, we pinch off a section of the nanowire with a gate voltage V_R and accumulate with V_L, thereby connecting the nanowire bulk to the source contact and disconnecting it from the drain. Next, we measure the reflection S_{11} from the rf resonator as a function of drive frequency f and gate voltage V_G. For each V_G, we fit the resonator response (see Appendices 6.7.1, 6.7.2, 6.7.3). The extracted resonance frequency change, Δf_0, capacitance change, ΔC, and resonator internal quality factor, Q_{int}, are plotted in Fig. 6.2(a,b).

The resonance frequency is nearly constant below about $V_G \approx -0.2$ V. The resonator shift gradually increases when increasing V_G from -0.2 to 1 V, and saturates above $V_G \approx$ 1 V. The total shift of about 150 kHz corresponds to an increase in capacitance of $C_G =$ 334.8 ± 1.0 aF, which we identify as a gate-wire capacitance. The range over which the

Table 6.1: Comparison of gate capacitance extracted from Coulomb blockade and resonator shift.

Gate size	Resonator placement	Capacitance (aF) Resonator shift	Capacitance (aF) Coulomb blockade
80 nm	Source	31.7±0.6	27.5±1.7
500 nm	Gate	115.1±0.2	114.4±3.7
2000 nm	Source	334.8±1.0	331.7±7.8

capacitance gradually increases is consistent with the range over which the gate voltage V_G tunes the channel from fully closed to fully open in a lock-in conductance measurement (c.f. Sec.6.5.2 and Fig. 6.5). We attribute the peaks in the intermediate range of V_G to the quantum capacitance of unintentional quantum dots formed in the disordered potential in the wire. Panel (b) demonstrates the change of the resonator internal quality factor Q_{int} as a function of the gate voltage. The inset of Fig. 6.2(a) illustrates a small change of the resonance frequency compared to the resonator linewidth. Except for the random error, we expect the main source of the potential systematic error to be up to about 1.5% due to kinetic inductance of the 200 nm-thick superconducting film forming the superconducting inductor.

To independently measure the gate capacitance with a different method, we form a quantum dot by setting the gate voltages $V_{L,R} \sim 150$ mV to a tunneling regime, and $V_G \approx 4$ V. Coulomb diamonds versus V_G and V_S are measured by means of rf-conductance[5, 26, 27], using the same resonator that was used for the direct capacitance measurement [Fig. 6.2(c)]. The spacing between the Coulomb peaks ΔV_G corresponds to the gate voltage change required to add a single electron to a quantum dot[28], and is related to the gate capacitance via $\Delta V_G = e/C_G$. This measurement yields capacitance $C_G = 331.7 \pm 7.8$ aF, in good agreement with the value extracted from the resonator shift.

The same measurement is repeated for two other InSb nanowire devices, with gate widths of 80 and 500 nm. Table 6.1 lists the capacitances extracted by both methods for all three devices, and supporting data is presented in Appendix 6.7.5. In all cases we find that the two methods are in good agreement.

6.4. SENSITIVITY

Next, we investigate the sensitivity of the capacitance measurement. To maximize the sensitivity it is beneficial to perform the measurement only near the resonance frequency. With an analytical model of the resonator and assuming fixed quality factors, the amplitude and phase measurement at fixed frequency allows us to determine the frequency shift and, therefore, the added capacitance (Appendix 6.7.3, 6.7.4).

We characterize the sensitivity of the capacitance measurement on an InAs nanowire device with a 340 nm wide gate wrapped around the nanowire. The inductor ($L = 730$ nH) is attached to the source lead of the device. The resonator has a resonant frequency $f_0 = 312.81$ MHz, an internal quality factor of $Q_{int} = 488$, and an external quality factor of $Q_{ext} = 134$.

We acquire time traces of the signal reflected from the resonator at a fixed frequency $f = 313.21$ MHz, first with the gate voltage V_G set to fully open, and then to fully closed.

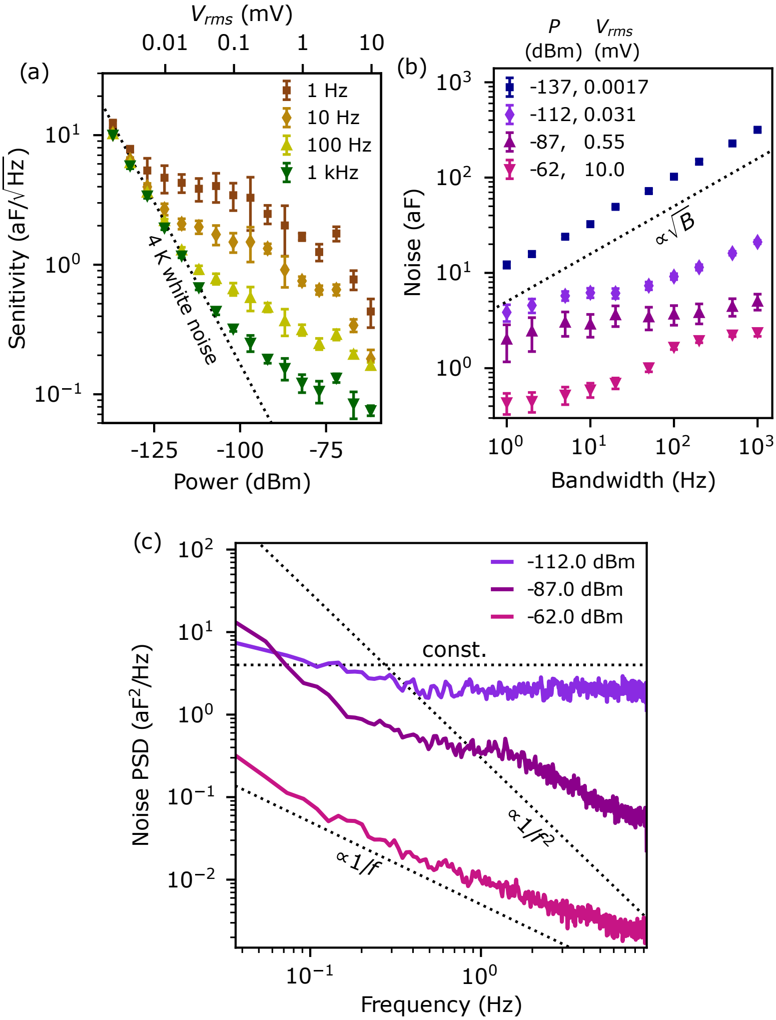

Figure 6.3: (a) The measured sensitivity of the capacitance measurement. The dotted line indicates the sensitivity limit due to the amplifier noise ($T_{\text{noise}} \approx 4$ K). (b) The standard deviation of the gate capacitance measurement vs vector network analyzer bandwidth. The dotted line indicates the scaling of the noise $\propto \sqrt{B}$, expected for white noise such as Johnson-Nyquist noise. (c) The capacitance noise spectrum, for a measurement bandwidth of 50 Hz.

This procedure is repeated for various vector network analyzer bandwidths B and drive powers, while maintaining a fixed total 4.5 min length of the time traces. The fixed duration of several minutes is chosen in order to expose the setup to detrimental influence of the device drift and low-frequency noise, and to obtain fair values of a noise level applicable to real use case. We define the SNR for distinguishing the opened and closed cases as

$$\mathrm{SNR} = \left| \frac{S_{11}^{\text{open}} - S_{11}^{\text{closed}}}{(\sigma_{11}^{\text{open}} + \sigma_{11}^{\text{closed}})/2} \right|. \tag{6.3}$$

where $S_{11}^{\text{open/closed}}$ and $\sigma_{11}^{\text{open/closed}}$ are the mean and standard deviation of the measured complex reflection coefficient for the gate being opened and closed. Based on the SNR we define the noise and the sensitivity of the capacitance measurement as $N = \Delta C/\mathrm{SNR}$ and $s = \Delta C/(\mathrm{SNR} \times \sqrt{B})$, respectively[2].

Fig. 6.3 shows the measured sensitivity and noise for various measurement bandwidths and excitation powers. Panel (a) demonstrates that the measurement sensitivity improves with increased rf excitation power, where the top axis represents the corresponding root-mean-square (rms) voltage V_{rms} on the contact attached to the resonator. The low-power sensitivity is independent from the measurement bandwidth. As power increases, the sensitivity becomes increasingly more bandwidth-dependent with the lowest values corresponding to the highest used bandwidth of 1 kHz. In Fig. 6.3(a) we indicate the sensitivity expected for ~4 K thermal (white) noise (Appendix 6.7.1), which approximates the expected noise level for the used cryogenic amplifier (Cosmic Microwave CITLF2, nominal noise temperature: 1.6 K) mounted at the 4 K plate of the dilution refrigerator (actual temperature: 3.4 K). For 1 kHz bandwidth and below −100 dBm drive power, the measured sensitivity matches the 4 K noise limitation. When the drive power is increased further, the sensitivity falls short of the limit more significantly. As the bandwidth is reduced, the sensitivity exceeds the 4 K limit at lower power – for 1 Hz bandwidth the deviation from amplifier limit occurs already at about −125 dBm. Furthermore, a plateau-like region in sensitivity appears at 1 Hz, between about −110 and −100 dBm.

To gain insight into the absolute precision of the capacitance measurement we plot the absolute noise level in Fig. 6.3(b). At the lowest drive power (−137 dBm) the noise scales as $\sqrt{B}$, indicating that white amplifier and thermal noise are dominating. As the power increases, the noise appears to saturate at a few-attofarad level. At −87 dBm the bandwidth change from 1 kHz to 1 Hz only reduces the noise from 4 to 2 aF. At even higher power (−62 dBm) the noise decreases further, reaching the lowest value of 0.45 aF for 1 Hz bandwidth.

To identify an origin of the plateau-like region in low-bandwidth sensitivity and the apparent saturation of noise at a few-attofarad level we measure the capacitance noise spectra at 50 Hz bandwidth and for −87 dBm power (Fig. 6.3(c)). At low drive power (−112 dBm) we find that the noise is predominantly white, while at the highest power

[2]We note that sensitivity is the most practical measure of measurement performance when the noise spectrum is white, which is explicitly violated here. In case the noise is white, the definition presented here would be equivalent to sensitivity measured using a sideband modulation. For the noise power monotonically decreasing with frequency, the sensitivity is a measure of the best-case performance if the integration time is longer, and worst case performance if the the integration time is shorter.

Table 6.2: Summary of the estimated sensitivities for several realizations of the rf resonant circuits and amplifiers, assuming the performance is limited by Johnson–Nyquist noise. Last entry illustrates the capacitance performance of a low-noise capacitance bridge. The first column lists the resonator types with type 1 – superconducting spiral inductors; type 2 – superconducting co-planar wave guide (CPW) resonator; type 3 – Surface mount (limped-element resonator made of off-the-shelf surface mount compnents), cryogenic; type 4 – Surface mount, room remperature; type 5 – Capacitance bridge. The full names of the abbreviations in the table are HEMT – high-electron-mobility transistor; TWPA – travelling wave parametric amplifier; SQUID – superconducting quantum interference device.

Type	Amplifier	f_0 (GHz)	Z_{char} (Ω)	Q_{int}	Q_{ext}	P (dBm)	V_{rms} (mV)	T_{noise} (K)	S_C (zF/$\sqrt{\text{Hz}}$)	Source
1	4 K HEMT	0.35	1000	500	300	−100	0.14	4	80	this work[a]
2	TWPA	5	50	10^4	10^3	−120	6.7×10^{-3}	0.6	60	Ref. [3]
3	Low-noise SQUID	0.196	275	30	30	−80	0.20	0.6	110	Ref. [4]
4	300 K HEMT	0.26	650	30	150	−40	40	300	40	Appendix 6.7.5[b]
5	n/a	n/a	n/a	n/a	n/a	n/a	20	n/a	2200	Ref. [9]

[a] typical values from among several spiral inductor chips and nanowire devices

[b] self-resonance of a 1 μH surface-mount inductor (Coilcraft, 1008CS-102X_E_)

(−62 dBm) its spectrum is close to $1/f$. The onset of the $1/f$ noise explains why the sensitivity is above the 4 K limit at low bandwidths and high powers. However, for intermediate drive power, the noise exhibits a peculiar spectrum: it is white in range between 0.5 Hz and 1 Hz, and close to $1/f^2$ below and above that range. Direct inspection of time traces used to calculate noise (supplementary Fig. 6.8) reveals that this noise spectrum is due to telegraph noise from two two-level systems, characterized by very different switching rates. Each contributes a Lorentzian component to the noise spectrum.

We speculate that these two level systems are individual impurities in the vicinity of the nanowire device that are activated only at a specific gate voltage. At low drive powers the influence of impurities is not resolvable due to the white noise. At intermediate power their influence is resolvable, leading to the apparent saturation of noise and plateau-like features. For high power the impurities contribute less to the capacitance because charging of the impurity with a fixed charge $Q_{impurity}$ contributes relatively less to the capacitance for larger rms voltage excitation – $\sim Q_{impurity}/V_{rms}$. While we expect the white and $1/f$ noise to be generic to the implementations of the rf capacitance measurements with a resonator, the telegraph noise is specific to the device we used for the sensitivity benchmarking.

Finally, we estimate the expected sensitivity of the capacitance measurements for several implementations of rf resonators and noise temperatures (Table 6.2), assuming the dominant contribution to noise is white noise. The first entry represents a slight improvement that could be expected in a setup identical to ours at moderate drive powers, thanks to an increase of the resonator internal and external quality factors. The second entry shows typical sensitivities that could be achieved using the resonator design (i.e. 50 Ω, superconducting CPW resonator) and the amplification chain widely used for readout of superconducting qubits[1]. The third line indicates the possible performance which can be achieved using the self-resonance of off-the-shelf surface-mount inductors at cryogenic temperatures and state-of-the-art amplification[4]. In the fourth entry, we estimate that similar sensitivity can be achieved at room temperature, with the effective rms voltage on the device contact comparable to the magnitude of the voltage excitation in capacitance bridges. The last row presents, as a reference, the performance of a low-noise capacitance bridge.

We note that these estimates may be expected to be valid only in a limited range of bandwidths. For low bandwidths, the sensitivity estimates may likely break down due to intrinsic properties of the device under study, or $1/f$ noise, as is the case in our experiment. For bandwidths $B \sim f_0 \times Q_{int}$ and higher, the estimates break down because measurement time is comparable to the time for the reflection to reach a steady state.

6.5. EXAMPLES OF APPLICATION

In this section we list several use cases for the capacitance measurement with rf resonators. We demonstrate how a single resonator can be used to measure capacitance of multiple gates (Subsec. 6.5.1), and to supplement conductance measurements in extracting the mobility of an individual nanowire (Subsec. 6.5.2). In Subsec. 6.5.3 we list a few quantum-mechanical phenomena that affect the electronic compressibility, and thereby can be studied with a sufficiently sensitive capacitance measurement. Subsec. 6.5.4 proposes an implementation of the rf resonator on the needle of a microma-

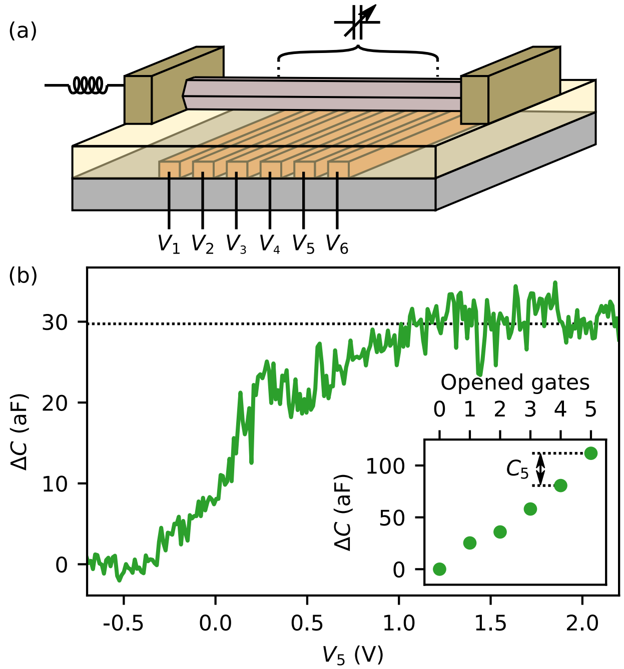

Figure 6.4: (a) A schematic of the InSb nanowire device with six parallel 80-nm-wide bottom gates, spaced by 60 nm. The coil symbol indicates the drain contact connected to a rf resonator. (b) Capacitance added to the circuit as a function of the voltage V_5 on one of the gates. (inset) Values of the added capacitance with 0 to 5 of the bottom gates in the open state. Error bars in the measured capacitance values are smaller than the marker size.

nipulator for rapid capacitance measurements in a probe station.

6.5.1. CAPACITANCE OF MULTIPLE GATES MEASURED WITH ONE RESONATOR

To demonstrate that a single rf resonator attached to a lead can be used to measure multiple gates, we focus on an InSb nanowire device with six 80-nm-wide parallel bottom gates [Fig. 6.4(a)], labeled V_1 through V_6. The rf resonator is only attached to a single lead, and yet we use it to measure the capacitance of gates 1 through 5. We start with all gates at large negative voltages. The gate voltage V_1 is then gradually increased, while measuring the resonance frequency of the resonator. When the measured value of the capacitance saturates we assign the corresponding value to the first gate, and proceed to sweeping the next gate voltage. The measured change of the capacitance in a sweep of a gate voltage V_5 is presented in Fig. 6.4(b). The inset of Fig. 6.4(b) illustrates the saturation values of capacitance with the first N gates opened. In this configuration it is not possible to measure the capacitance of the sixth gate V_6. As soon as it accumulates carriers, the rf circuit becomes terminated with a low impedance of the drain lead and the resonance feature in a reflection measurement vanishes.

We suggest that the capability of measuring capacitance of multiple small gates with

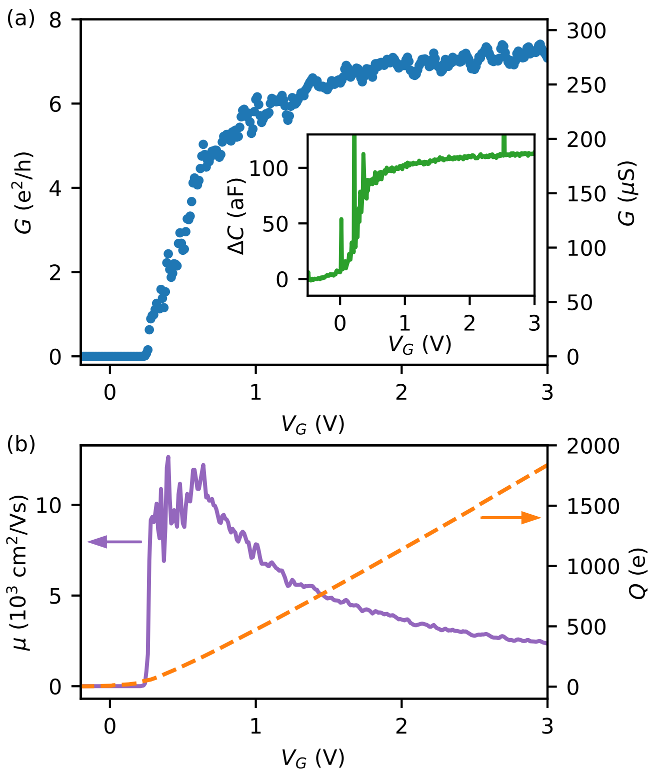

Figure 6.5: (a) Conductance G as a function of gate voltage V_G in an InSb nanowire device with 500-nm-wide bottom gate. (inset) Added capacitance ΔC as a function of gate voltage V_G. (b) Mobility of the nanowire device and charge in the conductive channel versus gate voltage V_G.

a single resonator may be applicable in development and characterization of multi-gate structures, e.g. arrays of quantum dots for spin-qubits [29, 30, 31].

6.5.2. MOBILITY

Next, we demonstrate the possibility of using the rf-resonator-based capacitance measurement to complement DC conductance measurements in determining the mobility of individual sub-micrometer devices. Low-frequency C-V measurements of such devices are very challenging due to the small values of capacitance. This is usually resolved by measuring the capacitance of multiple nominally identical devices connected in parallel, or by relying on finite-element simulations. These approaches may obscure the variation between individual devices or lead to systematic errors.

In our demonstration, we focus on an individual InSb nanowire with a 500-nm-wide bottom gate [cf. Fig. 6.1(a)]. We start by measuring the gate capacitance as described in section 6.2 (inset of Fig. 6.5). Afterwards, we measure the conductance across the device versus gate voltage V_G with all other gates open, using a 2-terminal lock-in measurement with a 3 mVrms excitation voltage, corrected for resistances in the filtered lines of the cryostat [Fig. 6.5(a)].

We integrate numerically the gate capacitance versus V_G to calculate the total charge Q in the conductive channel

$$Q(V_G) = e\int_{-0.5\mathrm{V}}^{V_G} \Delta C(\tilde{V}_G)\mathrm{d}\tilde{V}_G, \tag{6.4}$$

where e is the electron charge, and the lower integration limit of -0.5 V was chosen to be well below the pinch-off voltage. Finally, we calculate the mobility $\mu(V_G) = l^2 G(V_G)/Q(V_G)$, where $l = 500$ nm is the nanowire length and G is the measured conductance. The calculated charge and mobility are plotted in Fig. 6.5(b). We find a peak mobility of $\mu \approx 1.2 \times 10^4$ cm^2/Vs. This value is somewhat lower than other measurements on nanowires grown by the same process [23]. We expect that this is due to the use of the field-effect model[32] to fit the data in Ref. [23], and possibly due to more involved fabrication of the devices for our experiment. The field-effect model assumes gate-independent mobility and saturation of the pinch-off curve to additional in-line (e.g. contact) resistance, yielding higher values of the extracted mobility. Using the field-effect model we extract a mobility of $\mu_{FE} = 2.3 \times 10^4$ cm^2/Vs (Appendix 6.7.5).

6.5.3. ELECTRONIC COMPRESSIBILITY IN MESOSCOPIC DEVICES

6

In multiple solid state physics phenomena, the charging of the mesoscopic system is not only affected by the geometrical capacitance of the device. Properties such as the electronic band structure and electron-electron interaction affect the electronic compressibility, resulting in a non-classical contribution to the device capacitance. To date, measurements of the bulk electronic compressibility were mostly performed by means of capacitance bridges[21, 33] or the electric field penetration technique[34, 35, 36]. Quantum effects of 1-dimensional and mesoscopic devices are at the very limit of what is possible to measure with these methods. With sub-attofarad noise, for the same or smaller excitation amplitudes, a number of phenomena can be further explored.

Electronic compressibility is a hugely informative quantity in topics such as Luttinger liquids[21] and the quantum Hall regime (in all its flavors) [37, 38]. In Ref. [22], Jarratt et al. showed the ability to measure the van Hove singularities in a narrow GaAs quantum point contact using a resonator, demonstrating that compressibility measurements can give insight into the band structure of 1D systems.

Compressibility divergence can indicate closing and reopening of the bulk gap. Compressibility measures the properties of the bulk directly, and does not rely on local probes, making it a uniquely good quantity to investigate topological phase transitions[39], including the case of topological superconducting phase transitions [40].

6.5.4. IMPLEMENTATION ON A PROBE NEEDLE

As quantified in Table 6.2, sub-attofarad sensitivities can be achieved using low-Q rf resonators. In particular, LC resonators constructed from surface-mount components are commonly used for state-of-the-art charge and spin readout[41, 42, 43, 4]. These realizations use the self-resonance of the surface-mount inductor, and supplement it with additional capacitances to adjust the resonance frequency and characteristic impedance.

While the referenced uses are demonstrated at cryogenic temperatures, these resonant circuits perform comparably well at room-temperature (Appendix 6.7.5).

This suggests a possible realization of a rf resonator in the form of a needle probe of a micromanipulator, or a scanning probe microscope. The needle could either make galvanic connection with the contact on the device, or approach the surface of the characterized material[44]. The surrounding environment would affect both the resonance frequency and quality factor as such a probe makes contact with the device, but lack of strict requirements on the resonance frequency and the quality factor render such changes mostly irrelevant in practical use cases. Thereby, the capacitance measurement method is suitable for the purpose of rapid screening of devices on a large scale.

6.6. SUMMARY

To summarize, we validate a method of measuring capacitance of micro- and nano-scale devices by means of rf resonators. The method is characterized by the sensitivity reaching values as low as 75 zF/$\sqrt{\mathrm{Hz}}$ and noise below 1 aF for moderate integration times. It is suitable for applications at both room temperature and cryogenic temperatures, including dilution refrigerators. It is also suitable for measuring multiple gate capacitances with a single resonator, reducing the reliance on finite element simulations for mobility measurements. Finally we propose that the rf capacitance measurements can detect the quantum contribution to bulk capacitance in mesoscopic devices and can be implemented on the needle of a probe station with a micromanipulator.

6

6.7. APPENDIX

6.7.1. BASIC RESONATOR MODEL AND SENSITIVITY ESTIMATE

The starting point for modeling the resonator is series RLC circuit coupled to a $Z_0 = 50\,\Omega$ transmission line[45]. The impedance of such a resonator is

$$Z = R + 2\pi i f L + \frac{1}{2\pi i f C} \overset{\Delta f \ll f_0}{\approx} Q_{ext} Z_0 \left(\frac{1}{Q_{int}} + i \frac{2\Delta f}{f_0} \right) \tag{6.5}$$

where R, L, and C are resistance, inductance and capacitance of the RLC circuit, respectively; $Q_{ext} = Z_{char}/Z_0$ is the external quality factor; $Q_{int} = Z_{char}/R$ is the internal quality factor; $Q = \left(Q_{ext}^{-1} + Q_{int}^{-1}\right)^{-1}$ is the total quality factor; $Z_{char} = \sqrt{L/C}$ is the characteristic impedance of the resonator; $f_0 = 1/(2\pi\sqrt{LC})$ is the resonance frequency; f is the probe frequency and $\Delta f = f - f_0$.

The reflection coefficient of the resonator is thereby

$$S_{11} = \frac{Z - Z_0}{Z + Z_0} = 1 - \frac{2QQ_{ext}^{-1}}{1 + 2iQ\frac{(f-f_0)}{f_0}}. \tag{6.6}$$

Maximum sensitivity to small changes in resonator frequency is achieved by measuring exactly on resonance

$$\left.\frac{dS_{11}}{df_0}\right|_{f=f_0} = -4i\frac{Q^2 Q_{ext}^{-1}}{f_0}. \tag{6.7}$$

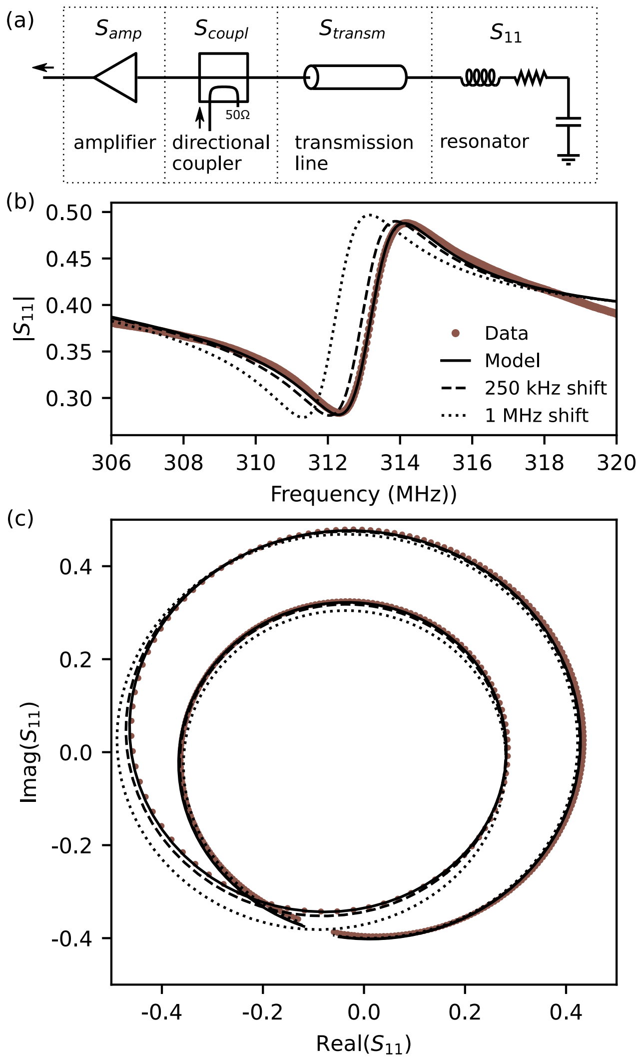

Figure 6.6: (a) Circuit schematics employed to model the resonance assymetry of the resonator used for characterization of the performance in Sec. 6.4. (b) Absolute value of S_{11} and (c) parametric plot of real and complex part. Solid line indicates the fit of Eq. (6.15) to the data. Dashed and dotted line indicate the predicted signal in case the resonance frequency is lowered by 250 kHz and 1 MHz, respectively.

In a lumped-element resonator model this corresponds to a maximum sensitivity to capacitance changes of

$$\left.\frac{dS_{11}}{dC}\right|_{f=f_0} = 4\pi i \frac{Q^2}{Q_{ext}} f_0 Z_{char}. \tag{6.8}$$

For a drive amplitude A and noise voltage variance σ_v^2 per unit of bandwidth, the sensitivity is given by

$$S_C = \frac{\sigma_v}{A}\left|\frac{dS_{11}}{dC}\right|^{-1}. \tag{6.9}$$

6.7.2. ORIGIN OF THE RESONANCE ASYMMETRY

In the study we generally find asymmetric line shapes of the rf resonances [c.f. Fig. 6.6(b)], with the asymmetry typically being more pronounced for high internal quality factors. In the hanger geometry an asymmetry is usually attributed to mismatch between impedance of input and output transmission line [46], however an such interpretation has no physical justification in a reflection measurement. One approach in reflectometry is therefore to neglect the extraction of the frequency shift and quality factor from the data. Another approach is to use additional phenomenological factors to account for asymmetry[47]. The phenomenological approach leads to correct extraction of the resonance frequency, but introduces systematic error in the extraction of the internal and external quality factors. Here, we introduce an approach utilizing a physically motivated model, that captures the resonance asymmetry.

Our model considers a cryogenic circuit depicted in Fig. 6.6(a), consisting of the resonator itself, a directional coupler (characterized by a coupling parameter γ), a connecting transmission line (length l, and microwave propagation speed c) and an amplifier. We describe each of these components using scattering matrices:

$$S_{coupl} = \begin{pmatrix} 0 & \sqrt{1-\gamma^2} & i\gamma & 0 \\ \sqrt{1-\gamma^2} & 0 & 0 & i\gamma \\ i\gamma & 0 & 0 & \sqrt{1-\gamma^2} \\ 0 & i\gamma & \sqrt{1-\gamma^2} & 0 \end{pmatrix} \tag{6.10}$$

$$S_{transm} = \begin{pmatrix} 0 & e^{-2\pi i f l/c} \\ e^{-2\pi i f l/c} & 0 \end{pmatrix} \tag{6.11}$$

$$S_{amp} = \begin{pmatrix} \sqrt{1-\alpha^2}e^{i\phi} & \alpha \\ \alpha & \sqrt{1-\alpha^2}e^{i\phi} \end{pmatrix}, \tag{6.12}$$

where the amplifier is treated as a partially reflective mirror with a transmission coefficient α, that introduces a phase shift ϕ to the reflected signal. The reflection coefficient of the resonator S_{11} is given by Eq. (6.6). Two effective mirrors, the resonator and the amplifier, form a low-Q cavity which modulates the transmission through the circuit from the coupled port of the directional couplet to the output of the amplifier. The modulation leads to the resonance asymmetry, and in some cases can even turn the resonance dip into peak, through the following mechanism.

The cavity formed between the resonator and the amplifier reduces the output signal, except on resonance (i.e. when on the round trip between the amplifier and the resonator the microwaves acquire a phase that is a multiple of 2π). This leads to the oscillating background in the reflection measurement. If the resonator is undercoupled ($Q_{int} > Q_{ext}$), near resonance frequency f_0, the phase of S_{11} rapidly wraps by 2π. Therefore there must exist a frequency, close to f_0, for which the round trip is an exact multiple of 2π, resulting in an increase of the transmission through the cavity formed by an amplifier, and leading to an asymmetry.

Analytically, we solve a set of linear equations

$$\vec{V}_i^{out} = S_i \times \vec{V}_i^{in}, \tag{6.13}$$

given by the scattering matrices S_i (Eqs. (6.6), (6.10), (6.11), (6.12)), relating the microwave amplitude and phase at the inputs ($\vec{V}_i^{in}$) and outputs ($\vec{V}_i^{out}$) of each component of the circuit. In the solution we assume that the microwave drive is applied only to the coupled port of the directional coupler, and the drive is zero on the isolated port and output of the amplifier/mirror. We find the transmission from the coupled input of the directional coupler to the amplifier

$$\tilde{S}_{11} = \frac{i\gamma\alpha\sqrt{1-\gamma^2}e^{-4\pi f li/c+i\phi}S_{11}}{1-\sqrt{1-\alpha^2}(1-\gamma^2)e^{-4\pi f li/c+i\phi}S_{11}}. \tag{6.14}$$

6.7.3. RESONATOR FITTING

In a final fit to the data, we include additional prefactors to modify Eq. (6.14)

$$\tilde{\tilde{S}}_{11} = A\left(1+B\frac{f-f_0}{f_0}\right) \times e^{-i\zeta+i\beta(f-f_0)} \times \tilde{S}_{11}, \tag{6.15}$$

and record the optimal parameters. The term $A\left(1+B\frac{f-f_0}{f_0}\right)$ phenomenologically accounts for a frequency-dependent attenuation and amplification, while $e^{-i\zeta+i\beta(f-f_0)}$ accounts for the phase shift due accumulated during propagation through the transmission lines. A and B parametrize the background amplitude and slope, while ζ and β parametrize the global phase shift and phase winding.

In the fits we fix several of the parameters independently. The coupling coefficient $\gamma = 0.178$ (equivalently: 15 dB) is chosen according to the specification of the used Mini Circuits ZEDC-15-2B[3], and the reflection coefficient $\alpha = 0.398$ corresponds to 8 dB return loss of the Cosmic Microwave CITLF2 HEMT cryogenic amplifier[4]. We set the value of $(2l/c)^{-1} = 111.4$ MHz based on the measurement of the reflection at 4K, with no device mounted in the setup. The remaining parameters are optimized in the nonlinear fit. Fig. 6.6 depicts the fit result for the resonator used to quantify sensitivity in Sec. 6.4.

6.7.4. FREQUENCY SHIFT FROM FIXED-FREQUENCY MEASUREMENT

To maximize the measurement sensitivity it is optimal to perform a fixed-frequency measurement, near the resonance frequency, for which the reflection coefficient responds most strongly. To recover the frequency shift from such a fixed-frequency measurement

[3]https://www.minicircuits.com/WebStore/dashboard.html?model=ZEDC-15-2B

[4]https://www.cosmicmicrowavetechnology.com/citlf2

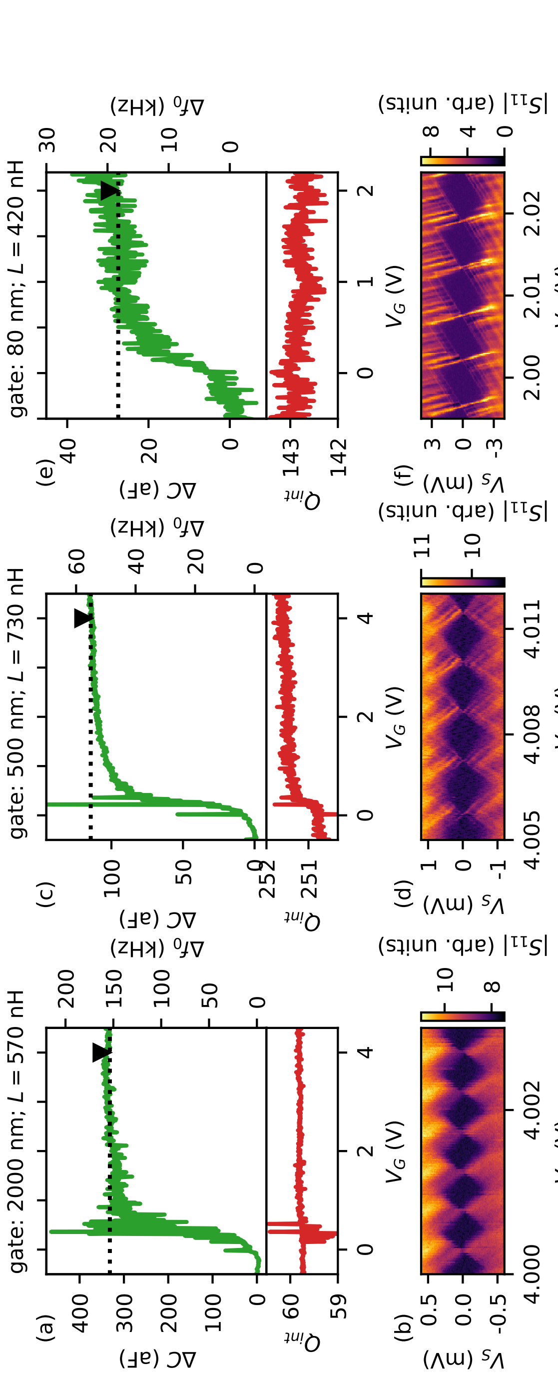

Figure 6.7: (a,c,e) C-V measurements using the rf resonators for the three InSb devices with the gate width of 2000, 500 and 80 nm. Bottom panels present internal quality factors of the resonators as a function of the gate voltage V_G. (b,d,f) Rf-conductance measurements of Coulomb diamonds for quantum dots formed in the nanowire devices.

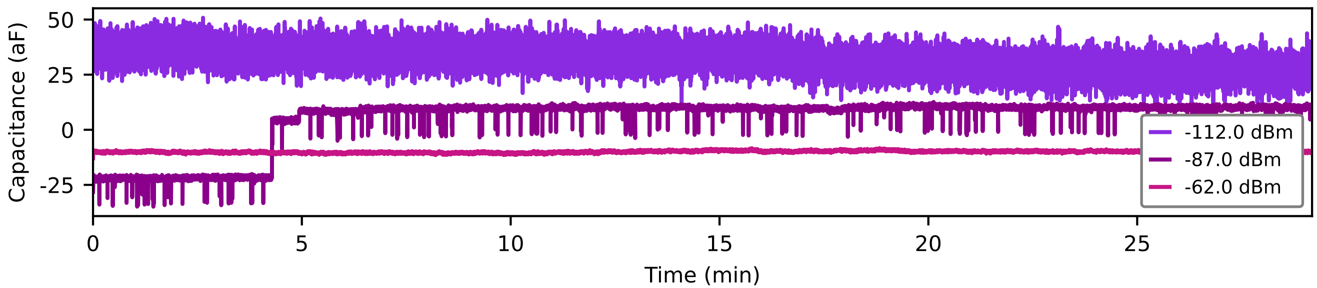

Figure 6.8: Time traces of measured capacitance in for the depleted InAs nanowire device, used to calculate the noise power spectrum density in Fig. 6.3(c). Time traces are offset vertically for clarity.

we perform a calibration resonator measurement (Fig. 6.6) and fit the analytical model (Eq. (6.15)) to the data (Appendix. 6.7.3). We fix all of the parameters of the model, except for the resonance frequency f_0. In this way we are able to predict the expected reflection coefficient for different values of resonance frequency (e.g. dashed and dotted lines in Fig. 6.6).

Next, we measure the reflection at fixed frequency f versus the gate voltage. For each data point we perform numerical optimization to find f_0 which best matches the data, and identify the corresponding value as the resonance frequency at a given gate voltage.

In this work we assume that the internal quality factor Q_{int} of the resonator is not gate-dependent, which is reasonably fulfilled [Fig. 6.2(b)]. We note that since the reflection coefficient is complex-valued it could be used to infer two real-valued parameters simultaneously (f_0 and Q_{int}) via numerical optimization.

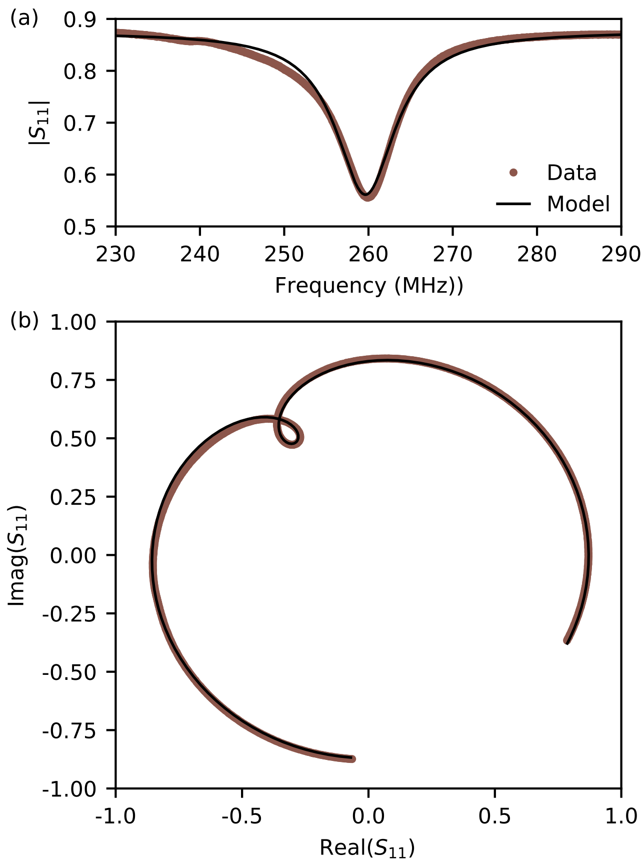

Figure 6.9: (a) Magnitude of the reflection around the self-resonance frequency of the surface mount inductor. (b) Parametric plot of the real and imaginary part of the reflection around the self resonance-frequency. Black lines indicate the fit to the data.

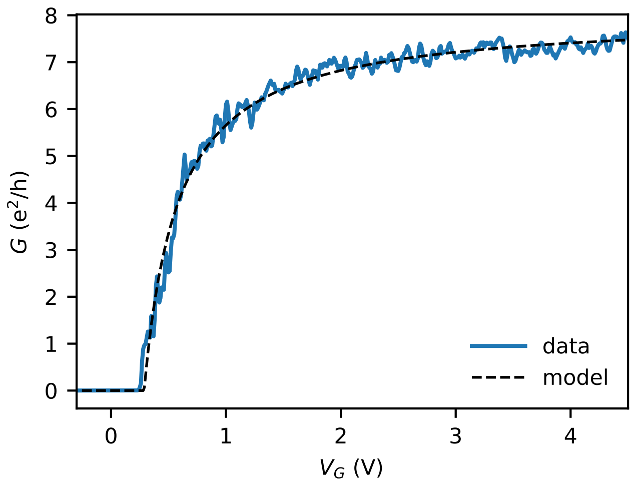

Figure 6.10: Pinch off curve of the 500 nm InSb device, used for extraction of mobility in Fig. 6.5.

6.7.5. ADDITIONAL DATA SETS

6

In this appendix we present additional data sets, backing up the numerical values provided in the main text.

Figure 6.7 presents the CV measurement for three devices listed in Table 6.1. In the top panel of Fig. 6.7 the dashed line indicates the capacitance value extracted from the periodicity of Coulomb blockade, and the triangular marker indicates the gate voltage V_G which was used for tuning the quantum dot.

Figure 6.8 presents time traces of the measured capacitance used to calculate the noise power spectra in Fig. 6.3(c). The dataset for −112 dBm drive power is dominated by white noise with a large magnitude, with a hint of a discrete jump at time stamp ~17 min. For −87 dBm drive power the SNR is sufficiently high to detect discrete changes in charge susceptibility from two level systems in the vicinity of the device. At −62 dBm the large voltage excitation reduces the contribution of the individual impurities causing the telegraph noise.

Figure 6.9 presents the measurement of the self-resonance of the 1 μH surface-mount inductor (Coilcraft, 1008CS-102X_E_), together with a complex fit to the data. In these measurements no directional coupler or cryo-amplifier was used, therefore the data is fited by Eq. 6.6, with the prefactors listed in Appendix 6.7.3. The parameters extracted from the fit were used in the final entry in Table 6.2.

Figure 6.10 shows a fit of the field-effect model [32] to the pinch-off curve from Fig. 6.5. This fit yields the quoted value of mobility $\mu_{FE} = 2.3 \times 10^4$ cm^2/Vs.

BIBLIOGRAPHY

[1] Philip Krantz, Morten Kjaergaard, Fei Yan, Terry P Orlando, Simon Gustavsson, and William D Oliver. A quantum engineer's guide to superconducting qubits. *Applied Physics Reviews*, 6(2):021318, 2019.

[2] Anasua Chatterjee, Paul Stevenson, Silvano De Franceschi, Andrea Morello, Nathalie P de Leon, and Ferdinand Kuemmeth. Semiconductor qubits in practice. *Nature Reviews Physics*, 3:157–177, 2021.

[3] Chris Macklin, K O'Brien, D Hover, ME Schwartz, V Bolkhovsky, X Zhang, WD Oliver, and I Siddiqi. A near–quantum-limited josephson traveling-wave parametric amplifier. *Science*, 350(6258):307–310, 2015.

[4] FJ Schupp, F Vigneau, Yutian Wen, A Mavalankar, J Griffiths, GAC Jones, I Farrer, DA Ritchie, CG Smith, LC Camenzind, et al. Sensitive radiofrequency readout of quantum dots using an ultra-low-noise squid amplifier. *Journal of Applied Physics*, 127(24):244503, 2020.

[5] RJ Schoelkopf, P Wahlgren, AA Kozhevnikov, P Delsing, and DE Prober. The radio-frequency single-electron transistor (rf-set): A fast and ultrasensitive electrometer. *Science*, 280(5367):1238–1242, 1998.

[6] Florian Vigneau, Federico Fedele, Anasua Chatterjee, David Reilly, Ferdinand Kuemmeth, Fernando Gonzalez-Zalba, Edward Laird, and Natalia Ares. Probing quantum devices with radio-frequency reflectometry. *arXiv preprint arXiv:2202.10516*, 2022.

[7] Oki Gunawan, Lidija Sekaric, Amlan Majumdar, Michael Rooks, Joerg Appenzeller, Jeffrey W Sleight, Supratik Guha, and Wilfried Haensch. Measurement of carrier mobility in silicon nanowires. *Nano Letters*, 8(6):1566–1571, 2008.

[8] Erik C Garnett, Yu-Chih Tseng, Devesh R Khanal, Junqiao Wu, Jeffrey Bokor, and Peidong Yang. Dopant profiling and surface analysis of silicon nanowires using capacitance–voltage measurements. *Nature Nanotechnology*, 4(5):311–314, 2009.

[9] Yu-Chih Tseng and Jeffrey Bokor. Characterization of the junction capacitance of metal-semiconductor carbon nanotube schottky contacts. *Applied Physics Letters*, 96(1):013103, 2010.

[10] Z Ji, J Gillbert, JF Zhang, and W Zhang. A new ultra-fast single pulse technique (ufsp) for channel effective mobility evaluation in mosfets. In *2013 IEEE International Conference on Microelectronic Test Structures (ICMTS)*, pages 64–69. IEEE, 2013.

[11] KD Petersson, CG Smith, D Anderson, P Atkinson, GAC Jones, and DA Ritchie. Charge and spin state readout of a double quantum dot coupled to a resonator. *Nano letters*, 10(8):2789–2793, 2010.

[12] JI Colless, AC Mahoney, JM Hornibrook, AC Doherty, H Lu, AC Gossard, and DJ Reilly. Dispersive readout of a few-electron double quantum dot with fast rf gate sensors. *Physical review letters*, 110(4):046805, 2013.

[13] MF Gonzalez-Zalba, S Barraud, AJ Ferguson, and AC Betz. Probing the limits of gate-based charge sensing. *Nature communications*, 6:6084, 2015.

[14] Matias Urdampilleta, Anasua Chatterjee, Cheuk Chi Lo, Takashi Kobayashi, John Mansir, Sylvain Barraud, Andreas C Betz, Sven Rogge, M Fernando Gonzalez-Zalba, and John JL Morton. Charge dynamics and spin blockade in a hybrid double quantum dot in silicon. *Physical Review X*, 5(3):031024, 2015.

[15] Damaz De Jong, Jasper Van Veen, Luca Binci, Amrita Singh, Peter Krogstrup, Leo P Kouwenhoven, Wolfgang Pfaff, and John D Watson. Rapid detection of coherent tunneling in an in as nanowire quantum dot through dispersive gate sensing. *Physical Review Applied*, 11(4):044061, 2019.

[16] P Pakkiam, AV Timofeev, MG House, MR Hogg, T Kobayashi, M Koch, S Rogge, and Michelle Y Simmons. Single-shot single-gate rf spin readout in silicon. *Physical Review X*, 8(4):041032, 2018.

[17] Anderson West, Bas Hensen, Alexis Jouan, Tuomo Tanttu, Chih-Hwan Yang, Alessandro Rossi, M Fernando Gonzalez-Zalba, Fay Hudson, Andrea Morello, David J Reilly, et al. Gate-based single-shot readout of spins in silicon. *Nature nanotechnology*, 14(5):437–441, 2019.

[18] F Borjans, X Mi, and JR Petta. Spin digitizer for high-fidelity readout of a cavity-coupled silicon triple quantum dot. *Physical Review Applied*, 15(4):044052, 2021.

6

[19] Guoji Zheng, Nodar Samkharadze, Marc L Noordam, Nima Kalhor, Delphine Brousse, Amir Sammak, Giordano Scappucci, and Lieven MK Vandersypen. Rapid gate-based spin read-out in silicon using an on-chip resonator. *Nature nanotechnology*, 14(8):742–746, 2019.

[20] P Apostolidis, BJ Villis, JF Chittock-Wood, A Baumgartner, V Vesterinen, S Simbierowicz, J Hassel, and MR Buitelaar. Quantum paraelectric varactors for radiofrequency measurements at mk temperatures. *arXiv preprint arXiv:2007.03588*, 2020.

[21] Shahal Ilani, Luke AK Donev, Mark Kindermann, and Paul L McEuen. Measurement of the quantum capacitance of interacting electrons in carbon nanotubes. *Nature Physics*, 2(10):687–691, 2006.

[22] MC Jarratt, SJ Waddy, A Jouan, AC Mahoney, GC Gardner, S Fallahi, MJ Manfra, and DJ Reilly. Detection of the quantum capacitance of a point contact via dispersive gate sensing. *Physical Review Applied*, 14(6):064021, 2020.

[23] Ghada Badawy, Sasa Gazibegovic, Francesco Borsoi, Sebastian Heedt, Chien-An Wang, Sebastian Koelling, Marcel A Verheijen, Leo P Kouwenhoven, and Erik PAM Bakkers. High mobility stemless insb nanowires. *Nano Letters*, 19(6):3575–3582, 2019.

[24] P Krogstrup, NLB Ziino, W Chang, SM Albrecht, MH Madsen, Erik Johnson, Jesper Nygård, Charles M Marcus, and TS Jespersen. Epitaxy of semiconductor–superconductor nanowires. *Nature Materials*, 14(4):400–406, 2015.

[25] JM Hornibrook, JI Colless, AC Mahoney, XG Croot, S Blanvillain, H Lu, AC Gossard, and DJ Reilly. Frequency multiplexing for readout of spin qubits. *Applied Physics Letters*, 104(10):103108, 2014.

[26] Davydas Razmadze, Deividas Sabonis, Filip K Malinowski, Gerbold C Ménard, Sebastian Pauka, Hung Nguyen, David MT van Zanten, CT Eoin, Judith Suter, Peter Krogstrup, et al. Radio-frequency methods for majorana-based quantum devices: fast charge sensing and phase-diagram mapping. *Physical Review Applied*, 11(6):064011, 2019.

[27] Damaz de Jong, Christian Prosko, Daan Waardenburg, Lin Han, Filip K Malinowski, Peter Krogstrup, Leo P Kouwenhoven, Jonne V Koski, and Wolfgang Pfaff. Rapid microwave-only characterization and readout of quantum dots using multiplexed gigahertz-frequency resonators. *Physical Review Applied*, 16:014007, 2021.

[28] Thomas Ihn. *Semiconductor Nanostructures: Quantum states and electronic transport*. Oxford university press, 2010.

[29] DM Zajac, TM Hazard, Xiao Mi, E Nielsen, and Jason R Petta. Scalable gate architecture for a one-dimensional array of semiconductor spin qubits. *Physical Review Applied*, 6(5):054013, 2016.

[30] M Veldhorst, HGJ Eenink, Chih-Hwan Yang, and Andrew S Dzurak. Silicon cmos architecture for a spin-based quantum computer. *Nature Communications*, 8:1766, 2017.

[31] Emmanuel Chanrion, David J Niegemann, Benoit Bertrand, Cameron Spence, Baptiste Jadot, Jing Li, Pierre-André Mortemousque, Louis Hutin, Romain Maurand, Xavier Jehl, et al. Charge detection in an array of cmos quantum dots. *Physical Review Applied*, 14(2):024066, 2020.

[32] Önder Gül, David J Van Woerkom, Ilse van Weperen, Diana Car, Sébastien R Plissard, Erik PAM Bakkers, and Leo P Kouwenhoven. Towards high mobility insb nanowire devices. *Nanotechnology*, 26(21):215202, 2015.

[33] Spencer Louis Tomarken, Yuan Cao, Ahmet Demir, Kenji Watanabe, Takashi Taniguchi, Pablo Jarillo-Herrero, and RC Ashoori. Electronic compressibility of magic-angle graphene superlattices. *Physical Review Letters*, 123(4):046601, 2019.

[34] JP Eisenstein, LN Pfeiffer, and KW West. Negative compressibility of interacting two-dimensional electron and quasiparticle gases. *Physical Review Letters*, 68(5):674, 1992.

[35] LW Smith, AR Hamilton, KJ Thomas, M Pepper, I Farrer, JP Griffiths, GAC Jones, and DA Ritchie. Compressibility measurements of quasi-one-dimensional quantum wires. *Physical Review Letters*, 107(12):126801, 2011.

[36] AF Young, CR Dean, I Meric, S Sorgenfrei, H Ren, K Watanabe, T Taniguchi, J Hone, KL Shepard, and P Kim. Electronic compressibility of layer-polarized bilayer graphene. *Physical Review B*, 85(23):235458, 2012.

[37] Jens Martin, Benjamin Ezekiel Feldman, R Thomas Weitz, Monica T Allen, and Amir Yacoby. Local compressibility measurements of correlated states in suspended bilayer graphene. *Physical review letters*, 105(25):256806, 2010.

[38] Vivek Venkatachalam, Amir Yacoby, Loren Pfeiffer, and Ken West. Local charge of the ν= 5/2 fractional quantum hall state. *Nature*, 469(7329):185–188, 2011.

[39] XG Wen and A Zee. Compressibility and superfluidity in the fractional-statistics liquid. *Physical Review B*, 41(1):240, 1990.

[40] David Nozadze and Nandini Trivedi. Compressibility as a probe of quantum phase transitions in topological superconductors. *Physical Review B*, 93(6):064512, 2016.

[41] Christian Barthel, Morten Kjærgaard, J Medford, M Stopa, Charles Masamed Marcus, MP Hanson, and Arthur C Gossard. Fast sensing of double-dot charge arrangement and spin state with a radio-frequency sensor quantum dot. *Physical Review B*, 81(16):161308, 2010.

[42] Matias Urdampilleta, David J Niegemann, Emmanuel Chanrion, Baptiste Jadot, Cameron Spence, Pierre-André Mortemousque, Christopher Bäuerle, Louis Hutin, Benoit Bertrand, Sylvain Barraud, et al. Gate-based high fidelity spin readout in a cmos device. *Nature Nanotechnology*, 14(8):737–741, 2019.

[43] D Keith, MG House, MB Donnelly, TF Watson, Bent Weber, and MY Simmons. Single-shot spin readout in semiconductors near the shot-noise sensitivity limit. *Physical Review X*, 9(4):041003, 2019.

[44] Yun-Pil Shim, Rusko Ruskov, Hilary M Hurst, and Charles Tahan. Induced quantum dot probe for material characterization. *Applied Physics Letters*, 114(15):152105, 2019.

[45] David M Pozar. *Microwave engineering*. John wiley & sons, 2011.

[46] MS Khalil, MJA Stoutimore, FC Wellstood, and KD Osborn. An analysis method for asymmetric resonator transmission applied to superconducting devices. *Journal of Applied Physics*, 111(5):054510, 2012.

[47] Jasper Van Veen, Damaz De Jong, Lin Han, Christian Prosko, Peter Krogstrup, John D Watson, Leo P Kouwenhoven, and Wolfgang Pfaff. Revealing charge-tunneling processes between a quantum dot and a superconducting island through gate sensing. *Physical Review B*, 100(17):174508, 2019.

7

DISPERSIVE GATE SENSING OF DIVERSE CHARGE TUNNELLING PROCESSES IN A FLOATING HYBRID TRIPLE QUANTUM DOT

Hybrid semiconductor-superconductor systems are considered as a potential platform for constructing Majorana-based topological qubits. For readout, we typically measure the charge cotunneling strength between two quantum dots via a superconducting island, whose value distinguishes between the two different qubit states. Regarding the readout technique, dispersive gate sensing provides the flexibility to measure charge-conserving systems, even in scalable qubit configurations. However, it remains to be proven that the technology can independently identify and analyze charge tunneling events in such systems. Here we employ dispersive gate sensing to investigate a hybrid system based on an InAs nanowire, where an superconducting island with a hard gap is situated between two normal quantum dots. With the system electrically isolated from external charge reservoirs, we study the elastic cotunneling (ECT) and crossed Andreev reflection (CAR) processes. We observe that the evolution from ECT being dominant to the emergence of CAR is solely driven by reducing the charging energy of the island. When the two energies are equal, both processes coexist and merge to a point in the gate space. The charge tunneling strengths are estimated from the measured quantum capacitance, and the extracted Sisyphus dissipations of different charge transitions indicate the presence of incoherent processes. Our work demonstrates the efficacy of exploring Kitaev chains with superconducting islands and constructing coherent Cooper pair splitters. Both qualitative and quantitative understandings of the sensing signal form the foundation for using dispersive gate sensing in developing topological qubits.

This chapter is based on L. Han, Dispersive gate sensing of diverse charge tunnelling processes in a floating hybrid triple quantum dot, In preparation (2024).

7.1. Introduction

Topological quantum computing is an emerging field with great potential for developing fault-tolerant quantum computation. This approach exploits the intrinsic robustness of topologically protected states against local perturbations. Central to this field are Majorana-based qubits, where the qubit state is encoded in the parity of fermion occupation numbers: even parity corresponds to one qubit state, while odd parity signifies the other [1]. Distinguishing between these parity states involves measuring the charge cotunneling strength between two quantum dots through a topological island, where electrons tunnel via a pair of Majorana modes located at the two ends of the topological island. This principle underscores the importance of studying charge tunneling processes within a dot-island-dot hybrid system, especially for floating [1]hybrid systems to minimize quasiparticle poisoning and facilitate scalability. Recent studies on dot-based Kitaev chains supporting poor man's Majoranas [2] have emphasized the critical roles of both elastic cotunneling (ECT) and cross-Andreev reflection (CAR) as essential charge tunneling processes. There ECT involves the coherent transfer of an electron between two quantum dots via a virtual intermediate state in the superconducting island, while CAR entails Cooper pair splitting and its converse process[2]. So far, investigations into these charge tunneling events have been limited to using grounded superconductors that do not conform to charge conservation.

As standard methods for characterizing devices, transport or charge sensing measurements are commonly used, but have substantial limitations. Transport measurements necessitate the flow of current through the device, which is not ideal for qubits due to the risk of quasiparticle poisonings that can disrupt the computational basis, as well as the slow measurement speed. Charge sensing measurements entail the incorporation of a nearby sensing dot, leading to heightened fabrication complexity. Dispersive gate sensing (DGS), a potent technique for non-invasive charge detection, is suggested for reading out the topological qubits, as it can accurately measure the charge tunneling strengths that convey the parity information regarding the qubit states. However, up to this point, DGS has primarily been employed on normal or hybrid double quantum dot devices that do not exhibit ECTs or CARs. The latest research on a dot-island-dot hybrid system only provides a qualitative demonstration of ECTs and CARs, but was accomplished by creating superconducting islands of varying sizes [3].

In this work, using DGS and RF multiplexing techniques, we measure a floating dot-island-dot device and distinguish diverse charge tunneling processes across different regimes achievable by gate tuning. By adjusting the charging energy of the superconducting island E_C^{SC}, the charge stability diagrams shift from the absence of CARs to their emergence. Simulation using a two-Anderson impurity zero-bandwidth model, which accounts for a subgap state at E_0 near the hard gap of the island, elucidates this evolution by the decrease in E_C^{SC} from being larger to smaller than E_0. Remarkably, the resonators coupled to different hybrid dots exhibit varying sensitivities to the same charge

[1]Floating refers to a system that is charge-conservative. In many instances, floating is achieved by fully pinching off the barrier gates between the system and the metal contacts.

[2]In CAR, two electrons from separate quantum dots adjacent to the superconducting island simultaneously enter a superconductor to form a Cooper pair, or alternatively, a Cooper pair can be split into two electrons that tunnel to different quantum dots.

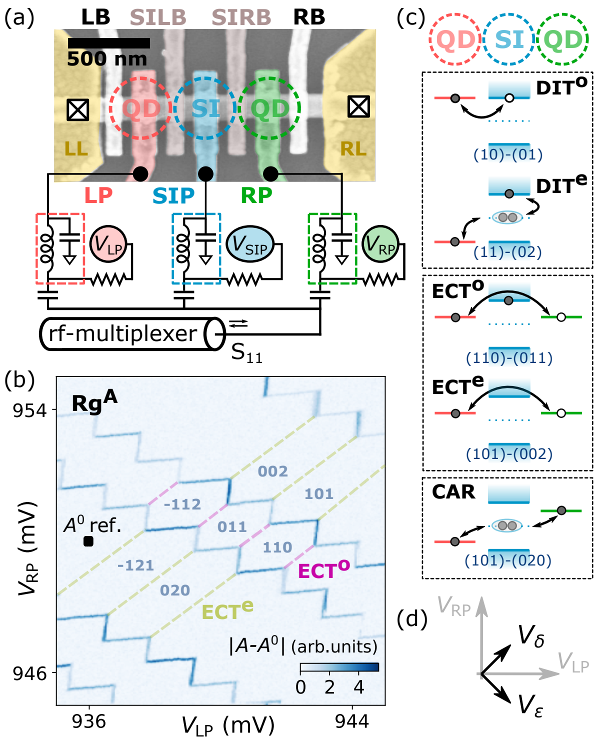

Figure 7.1: **Device and the charge tunneling processes within the hybrid triple dot.** **(a)** A false-colored SEM image of the device with gates labeled. The RF multiplexer concurrently transmits reflected gate sensing signals from resonators linked to each hybrid dot's plunger gate. **(b)** The charge stability diagram of the floating system, measured by the SIP resonator, is depicted in terms of $|A - A^0|$, representing the measured amplitude relative to that in the Coulomb blockade regime (indicated by the black square). The dot-island charge transitions (DIT) are clearly presented, with elastic cotunnelings (ECTs) not directly visible but indicated by dashed lines. The relative charge numbers of each dot n_i (i = L, SC, R) are annotated in the corresponding charge state regions as $n_L n_{SC} n_R$. **(c)** Illustrations of all relevant charge tunneling processes are provided, encompassing the DITs and ECTs with the island occupied by an even or odd number of charges, as well as crossed Andreev reflections (CARs). **(d)** A new set of axis, V_ε and V_δ, is illustrated in relation to the V_{LP} and V_{RP} axis. These axis will be utilized for the subsequent figures.

transitions. The extraction of different tunneling strengths and the Sisyphus dissipation of various charge tunneling processes provide comprehensive insights into the hybrid triple dot system, particularly concerning the detuned virtual states and the coherence of the tunneling process.Our findings not only showcase the potential for tuning Majorana-based qubits using the same readout technique but also pave the way for constructing multi-site floating Kitaev chains and coherent Cooper pair splitters.

7.2. SETUP AND A TYPICAL CHARGE STABILITY DIAGRAM

The device is constructed using an InAs nanowire enclosed by a two-facet Al shell. Through the use of an etching process and the deposition of top-gates, a dot-island-dot structure is formed, creating a hybrid triple dot system as illustrated in Fig. 7.1(a). The dimensions of both quantum dots and the superconducting island are approximately equal, measuring around 250 nm. To ensure charge conservation within the hybrid triple dot system during measurements, the LB and RB barrier gates are set to -2.5 V. The interdot barrier gates SILB and SIRB facilitate various charge transitions within the system, such as ECTs and CARs. The plunger gates LP, SIP, and RP are responsible for regulating the electrochemical potentials of the left quantum dot (occupied by N_{L} charges), the middle superconducting island (occupied by N_{M} charges), and the right quantum dot (occupied by N_{R} charges), respectively. All plunger gates are connected to off-chip resonators with unique spiral inductances, which allows for differentiation based on resonant frequencies. In particular, the resonant frequencies are approximately 374.8 MHz for f_0^{LP}, 648.4 MHz for f_0^{SIP}, and 323.4 MHz for f_0^{RP}. The bottom of Fig. 7.1(a) illustrates the effective RLC circuits of the three principal resonators, with RF multiplexing enabling the concurrent acquisition of gate sensing signals from all three resonators. The sensing signals obtained from the LP, SIP, and RP resonators are displayed in red, blue, and green colormaps, respectively.

When a charge transition occurs, additional parametric capacitance C_{pm} and effective conductance G_{eff} are introduced to the circuit. This results in shifts in the resonance frequency Δf and a reduction in the internal quality factor Q_{int}. The values of Δf and Q_{int} can be determined from the reflectometry signal using an analytical resonator model referenced in Ref. [4]. This analysis assumes that, within the gate region of a charge stability diagram, all other parameters in the model remain constant and can be obtained in advance through a reflectometry test [5, 6]. The measurements are conducted at a base temperature of approximately 30 mK in a dilution refrigerator, with no external magnetic field present.

7

In Fig. 7.1(b), we illustrate a charge stability diagram within the gate space defined by V_{LP} and V_{RP}, denoting it as regime A (Rg^{A}). The diagram is obtained using the SIP resonator and represents the relative amplitude response $|A - A^0|$, where A^0 is the average amplitude response value within the Coulomb blockade (indicated by the black square). The SIP resonator exhibits sensitivity to the left (right) dot-to-island transitions (DITs), resulting in nearly vertical (horizontal) lines. The dashed lines in Fig. 7.1(b) indicate the locations where the elastic cotunneling transitions (ECTs) between the two outer dots may occur. By observing the range of V_{LP} or V_{RP} in the diagram over which the ECTs extend, we can distinguish between ECTs associated with the superconducting island being occupied by an even or odd number of charges. We label these as odd-island ECTs ($\mathrm{ECT}^{\mathrm{o}}$s) and even-island ECTs ($\mathrm{ECT}^{\mathrm{e}}$s). Assuming that the total charge number of the floating triple dot is even (as demonstrated in Appendix. 7.8.4), we assign labels to the relative charge numbers of each charge state ($n_{\mathrm{L}} n_{\mathrm{SC}} n_{\mathrm{R}}$). Here, $n_i = N_i - [N_i]^{\mathrm{even}}$ (i = L, SC, R) with $[N_i]^{\mathrm{even}}$ being the nearest even number that N_i is truncated to.

It is evident that the SIP resonator can clearly detect DITs but not ECTs. This can be attributed to the SIP resonator's heightened sensitivity to charge transitions that involve the island. In the case of ECTs, the island states are solely engaged in an intermediary virtual process, which may not trigger a noticeable response in the SIP resonator, emphasizing its selective detection of DITs in regime Rg^{A}.

Fig. 7.1(c) presents the schematics of all possible tunneling processes included in this hybrid system, such as the DIT with the dot-island occupied by odd and even number of total charges, ECT$^{\text{o}}$, ECT$^{\text{e}}$ and CAR. Subsequently, we redefine the swept gates as depicted in Fig. 7.1(d), with $V_{\delta,\varepsilon} = (V_{\text{LP}} \pm V_{\text{RP}})/\sqrt{2}$. Under this transformation, any conceivable DITs are represented as (anti-)diagonal lines, while the ECTs (CARs) manifest as predominantly horizontal (vertical) lines, as shown in Fig. 7.2.

7.3. From the absence of CAR to its appearance

Starting from the regime depicted in Fig. 7.1 (b), we fine-tune the interdot barrier gates and adjust the electrochemical potentials of the outer dots. Through a series of measurements, we categorize the system into four distinct regimes and present them in a top-to-bottom arrangement in Fig. 7.2. The four regimes are listed in the order of effectively lifting the interdot barriers. They are named from a closed regime (Rg$^{\text{C}}$) to an open regime (Rg$^{\text{O}}$) via an intermediate regime (Rg$^{\text{I}}$) and a transitional regime (Rg$^{\text{T}}$), as labeled from the top to the bottom row on the left side. For each regime, we show the maps of $|A - A^0|$ measured by the resonator coupled to the LP, SIP, and RP gate, respectively. The rightmost panel of each row in Fig. 7.2 then highlights the corresponding charge transitions that are detectable from different resonators with thick colorful lines, and also clarifying the boundaries of different charge states using dotted grey lines.

In the regime Rg$^{\text{C}}$ shown in Fig. 7.2 (a), where the LP (RP) resonator clearly detects the left (right) DITs as well as ECT$^{\text{o}}$s, albeit with a much weaker amplitude. We then observe regime Rg$^{\text{I}}$ in Fig. 7.2 (b), which is analogous to Rg$^{\text{C}}$ but exhibits a more pronounced signal of ECT$^{\text{o}}$s for all three resonators. ECT$^{\text{e}}$s start to emerge in a discontinuous fashion as they fade away around the midpoint of the ECT$^{\text{e}}$s. Next, Fig. 7.2 (c) shows the unique transition regime Rg$^{\text{T}}$ where the ECT$^{\text{o}}$s converge to a single point where the CARs are supposed to emerge. At this specific point, the signal amplitude captured by the SIP resonator exceeds that of the DITs. The ECT$^{\text{e}}$s measured by LP (RP) resonator become continuous, with a signal amplitude comparable to that of the DITs. Fig. 7.2 (d) finally depicts the regime Rg$^{\text{O}}$, where the ECT$^{\text{o}}$s are no longer present due to the emergence of CARs. In this regime, the CARs (shown as vertical signals in the central panel) are the primary contributors to the sensing signals via the SIP resonator, whereas the ECT$^{\text{e}}$s (shown as horizontal signals in the left and right panels) dominate the sensing signals through the LP and RP resonators. The DITs detected by all the resonators are less pronounced, although not entirely absent (as indicated by the small amplitude response observed for the DIT between the two charge states 011 and 101 in the left panel, for instance). The black line segments in Figure 7.2 (d) intersect a CAR identified by all the resonators (results to be displayed in Figure 7.6 (b)).

The evolution from the absence of CARs to their presence, as evidenced by the transition from Rg$^{\text{C}}$ to Rg$^{\text{O}}$ in Fig. 7.2, is observed across multiple measurements when the interbarriers are lowered. In the specific measurements included in Fig. 7.2, the interbarrier gates are not much tuned, instead, the plunger gates are extensively lifted. As a result of the crosstalk between the interbarrier and plunger gates, this adjustment effectively causes a partial opening of the interbarrier gates, leading to a decrease in the charging energy of the superconducting island E_C^{SC}.

In Fig. 7.2, it is evident that the amplitude of sensing signals can effectively capture the tunneling processes occurring within the floating hybrid triple-dot system. As E_C^{SC} decreases, the range of the measured relative amplitude $|A - A^0|$ in the entire charge sta-

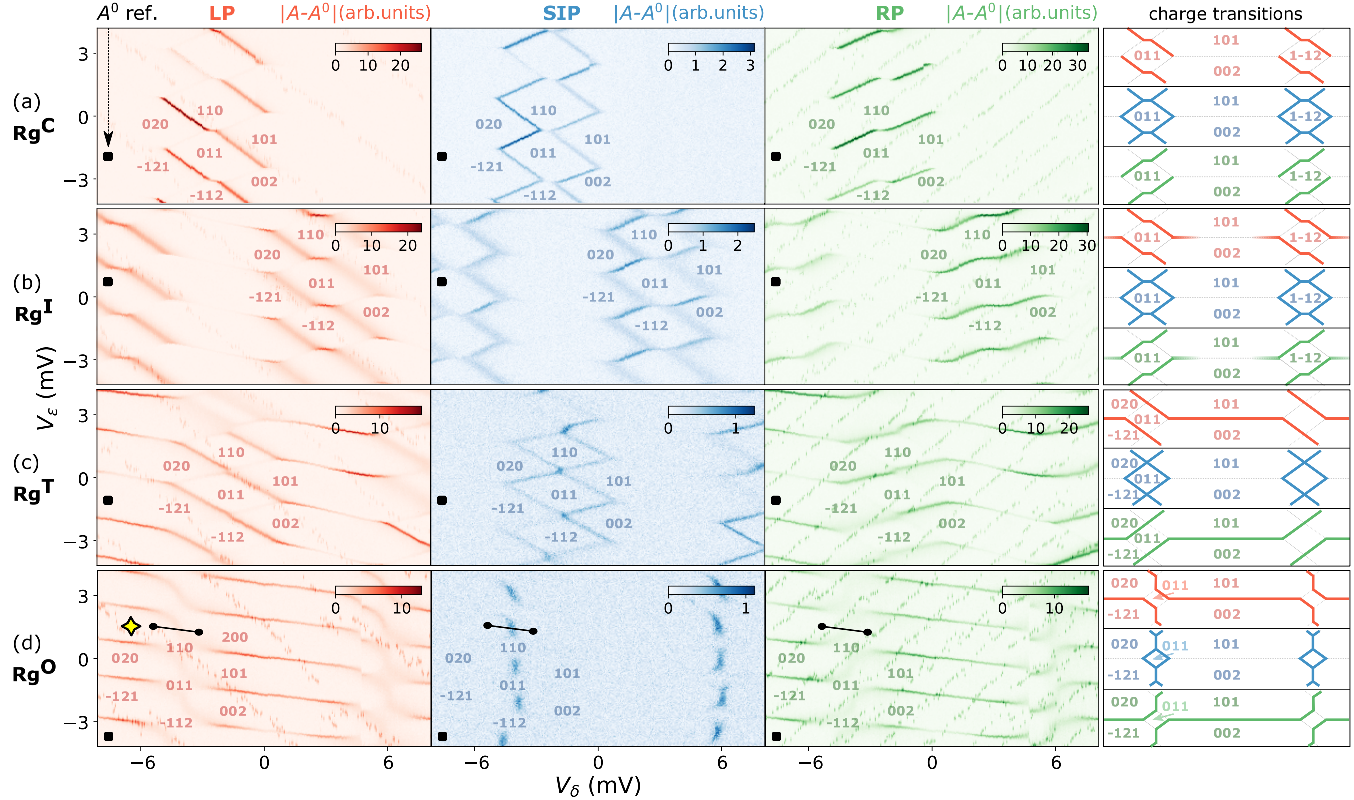

Figure 7.2: **Charge stability diagrams with different sets of gate settings.** The charge stability diagrams are obtained successively from the left to the right column. This is achieved by coupling the resonators to the LP gate (depicted in red maps), SIP gate (blue maps), and RP gate (green maps). The relative charge numbers of each dot are annotated in the corresponding charge state regions just as in Fig. 7.1 (b). The black square in each panel marks the area where A^0 is derived, enabling all the plots to be presented in terms of the relative amplitude $|A - A^0|$ of the sensing signal. **(a)** In the closed regime (Rg^C), only the DITs are clearly captured by all three resonators. The ECT^{o}s are more prominent than in Fig. 7.1(b). **(b)** An intermediate regime (Rg^I), in which the ECT^{o}s become obvious via the outer dot resonators, while the ECT^{e}s are also visible but not continuous. **(c)** The transition spot (Rg^T) where the ECT^{o}s shrink to singular points, where the CARs are also supported. **(d)** In the open regime (Rg^O), ECT^{o}s are no longer prominent, but CARs become the dominant feature. The black line segments correspond to the linecuts shown in Fig. 7.6.

7

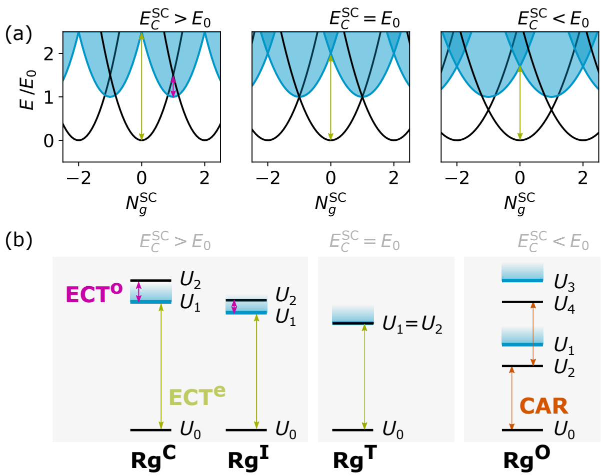

Figure 7.3: **Energy spectra of the superconducting island for three typical scenarios.** **(a)** The energy of the island, denoted as E, are determined as a function of the induced charge N^{SC}. The blue regions represent the continuum of states above the superconducting gap. The parabolas for the electron occupancy number N being even are shown in black. The yellow (pink) arrows depict the addition energy for introducing an extra quasiparticle to the superconducting island, depending on whether the island is occupied by even (odd) charge numbers. **(b)** The relative electrochemical potentials of a few superconducting island states, corresponding to the three scenarios in (a) and the four regimes in Fig. 7.2. The zero potential U_0 is defined in relation to the island being occupied by a even number of charges. The distance between the closest potentials $U_{N+1} - U_N$ (also denoted by arrows) signifies the energy required to add an extra charge to the superconducting island. In the left panel, arrows labeled ECT^e (ECT^o) depict the addition energy needed to reach the virtual state during the ECT process for even (odd) charge occupancies of the island. In the middle panel, the overlap of U_1 and U_2 implies no extra energy has to be paid for ECT^o. In the right panel, with U_2 lower than U_1, CARs become more energetically favorable, as indicated by the arrows.

bility diagrams decreases monotonically. This behavior follows the principle that the relative amplitudes exhibit an inverse relationship with the tunneling strengths as the resonance frequency of the probing resonator shifts, especially when the tunneling strength surpasses a specific threshold $t_{\text{threshold}}$ [7]. In situations where the tunneling strength is extremely low, the resonators remain unresponsive, resulting in no noticeable frequency shift. This implies that the signals corresponding to accessible transitions become less distinct and weaker due to higher tunnel strengths.

Furthermore, the external quantum dot resonators are sensitive to all possible charge transitions, while the superconducting island resonator remains insensitive to ECTs but sensitive to CARs. This can be explained by the fact that ECTs are virtual processes seen from the island, but CARs change the charge occupancy of the island. Having an understanding that the parametric capacitance C_{pm} reflects the adjustment in charge occupancy of the probed system in response to variations in the system's electrostatic potential, the modification in charge occupancy influences capacitance, potentially leading to shifts in the resonance frequency and subsequently affecting the measured amplitude. Consequently, the resonator becomes more sensitive to charge transitions involving direct or sequential tunneling processes rather than virtual tunneling events.

From Fig. 7.2 (a) to (d), the spacing between the ECTs along the V_ε axis decreases, indicating a trend of decreasing charging energies $E_C^{\mathrm{L,SC,R}}$. Fig. 7.3 (a) illustrates the energy spectra for the superconducting island, showing the variation of charging energy E_C^{SC} from being larger to smaller than the ground state energy E_0 of the island. Here E_0 equals the induced superconducting gap, given that the island possesses a hard gap (see Appendix. 7.8.2). The relationship between the gate-induced charge number N_g^{SC} and energy E of the island is described by the formula $E(N_g^{\mathrm{SC}}) = E(N_g^{\mathrm{SC}} - N)^2 + p_N E_0$, where $p_N = 0$ or 1 depending on whether the electron occupancy number N is even or odd, respectively. Fig. 7.3 (b) displays the relative electrochemical potentials of each panel in (a). The arrows marked as ECT$^{\mathrm{e}}$, ECT$^{\mathrm{o}}$, and CAR represent the addition energy required to attain the virtual state in the respective charge tunneling processes. As derived in Appendix. 7.8.3, the value of addition energies can be calculated using the expression $U_{N+1} - U_N = 2(E_C^{\mathrm{SC}} + (-1)^N E_0)$, which alternates between two values. This provides further clarification of the variations in tunneling strengths illustrated in Fig. 7.2, as discussed below.

In Fig. 7.2 (a), the amplitude response of ECT$^{\mathrm{e}}$s in regime Rg$^{\mathrm{C}}$ is negligible, which can be attributed to the substantial detuning of the virtual states involved in assisting ECT$^{\mathrm{e}}$s (as indicated by the large value of $U_1 - U_0$ in the left panel of Fig. 7.3 (b)). Conversely, the amplitude response of ECT$^{\mathrm{o}}$s is noticable. This can be explained by a much less detuned virtual state assisting ECT$^{\mathrm{o}}$s (as indicated by the small value of $U_2 - U_1$ in the left panel of Fig. 7.3 (b)). The amplitude response magnitude of ECT$^{\mathrm{o}}$s is smaller than that of DITs in Rg$^{\mathrm{C}}$, possibly due to weaker tunneling strengths for DITs compared to ECT$^{\mathrm{o}}$s in this regime. We interpret this as a result of the energy levels alignment in the outer dots, while the energy levels of the island remain unaligned.

Tuning from Rg$^{\mathrm{C}}$ to Rg$^{\mathrm{I}}$ shown in Fig. 7.2 (b), both the ECT$^{\mathrm{e}}$s and ECT$^{\mathrm{o}}$s are more significant in amplitude response. Now the missing segment in the middle of the ECT$^{\mathrm{e}}$s can still be attributed to the significant detuning of the virtual states in the superconducting island. The discontinuous segments at the two ends of the ECT$^{\mathrm{e}}$s may be due to a lower detuning $U_1 - U_0$ in Rg$^{\mathrm{I}}$ (shown in Fig. 7.3 (b)). Regarding to ECT$^{\mathrm{o}}$s, we can understand that they become stronger in Rg$^{\mathrm{I}}$, based on their corresponding energy spectra in Fig. 7.3 (b). Comparing with Rg$^{\mathrm{C}}$, the addition energy $U_2 - U_1$ in Rg$^{\mathrm{I}}$ decreases further, making the virtual state assisting ECT$^{\mathrm{o}}$s more energetically accessible. Their amplitude response, however, also get stronger in Rg$^{\mathrm{I}}$ for stronger ECT$^{\mathrm{o}}$s (shown in Fig. 7.2 (b)). This seems contradictory to the principle that the relative amplitudes exhibit an inverse relationship with the tunneling strengths. With the information to be provided in Sec. 7.6 we can explain this apparent discrepancy. Fig. 7.7 (a) implies that ECT$^{\mathrm{o}}$s in Rg$^{\mathrm{C}}$ contribute more tunneling capacitance to the parametric capacitance C_{pm}, leading to additional frequency shifts and thus larger amplitude response that are not solely dependent on the charge tunneling strength. As to the DITs, it is more intuitive that their amplitude response decreases as the strength of these transitions increases with the raising of the interdot barriers.

In Fig. 7.2 (c), Rg$^{\mathrm{T}}$ corresponds to the point where the value of E_C^{SC} equals to E_0. This leads to both the ECT$^{\mathrm{o}}$s and CARs being observed at the same location on the charge stability diagram. The central panel in Fig. 7.3 (a) illustrates that the crossings occur exclusively between even-charge parabolas in the lowest energy parabolas, except at the bottom of the odd-charge parabolas. This implies the emergence of CARs, as charge transfer occurs in units of Cooper pairs. While at the bottom of the odd-charge parabolas, the central panel in Fig. 7.3 (b) demonstrates that the addition energy required to access the virtual state during an ECT$^{\mathrm{o}}$ process is zero, enabling the presence of ECT$^{\mathrm{o}}$s without any additional cost. This implies the coexistance of ECT$^{\mathrm{o}}$s. With a further reduction of $U_1 - U_0$, the virtual state during ECT$^{\mathrm{e}}$s becomes more easily accessible, resulting in continuously visible transitions along the V_δ axis in Fig. 7.2 (c). The amplitude response of ECT$^{\mathrm{e}}$s is lower in magnitude compared to that in Rg$^{\mathrm{I}}$, indicating stronger ECT$^{\mathrm{e}}$s.

In the right panel of Fig. 7.3 (a), Rg$^{\mathrm{O}}$ occurs when E_C^{SC} is less than E_0. This results in the odd-charge parabolas consistently being higher than the even-charge parabolas. Consequently, the ground state of the island does not intersect with cases involving odd charge numbers. Furthermore, as depicted in the right panel of Fig. 7.3 (b), the relative electrochemical potentials $U_1 - U_2 < 0$, which make the CARs energetically more favorable than ECT$^{\mathrm{o}}$s. The higher addition energy needed for $U_1 - U_0$ compared to $U_2 - U_0$ is only warranted for sequential charge tunnelings. For example, this phenomenon is observed in the hybrid system with relative charge numbers transitioning from 101, through 011, to 020.

7.4. SIMULATION OF CHARGE STABILITY DIAGRAMS

We then extract the map of quantum capacitance C_{q} (proved as the primary component of parametric capacitance in Appendix. 7.8.5) for each of the measured charge stability diagrams presented in Fig. 7.2. The evolution, as determined by the relationship between E_C^{SC} and E_0, is effectively captured by a two-Anderson impurity zero-band-width model adopted from Ref. [8], as depicted in Fig. 7.4 (b). In this model, we consider the outer quantum dot states as two Anderson impurities that couple to and through the middle superconducting island. Furthermore, in the absence of subgap states, the lowest energy state in the island is $E_0 = \Delta_{\mathrm{gap}}$, and the total charge number for the floating system is even. To eliminate the side effects arising from the more lifted interbarriers, the tunneling strength of DITs (t_{DIT}) in Rg$^{\mathrm{C}}$, Rg$^{\mathrm{T}}$ and Rg$^{\mathrm{O}}$ is deliberately adjusted to the same value. Rg$^{\mathrm{I}}$ differs from Rg$^{\mathrm{C}}$ only for unequal $t_{\mathrm{L,DIT}}$ and $t_{\mathrm{R,DIT}}$, to give an example of the influence of from larger $t_{\mathrm{L,DIT}}$. The lever arms of the three plunger gates are adjusted manually to ensure that both the simulated range of C_{q} and the size of the corresponding charge states are comparable to those observed in the data (values are recorded in Appendix.7.8.7).

Fig. 7.4 (a) contains information comparable to that in Fig. 7.2, demonstrating that amplitude measurement is sufficient for qualitatively characterizing charge stability diagrams and distinguishing the properties of different tunneling processes. The line segments in Rg$^{\mathrm{C}}$ and Rg$^{\mathrm{O}}$ will be further discussed in Fig. 7.5.

The simulated C_{q} maps in Fig. 7.4 (b) have almost identical features as the data in (a), except for the ECT$^{\mathrm{e}}$ sensed by the outer dot resonators. This discrepancy can be explained by the existing lower threshold for the tunnel strength $t_{\mathrm{threshold}}$ required for dispersive gate sensing. Below this threshold $t_{\mathrm{threshold}}$, the C_{q} values cease to be inversely proportional to the tunneling strength but drop to zero [7]. The sizes and shapes of the simulated charge states in different regimes are in agreement with the data, proving that the evolution from the absence of CARs to their presence is solely attributed to the de-

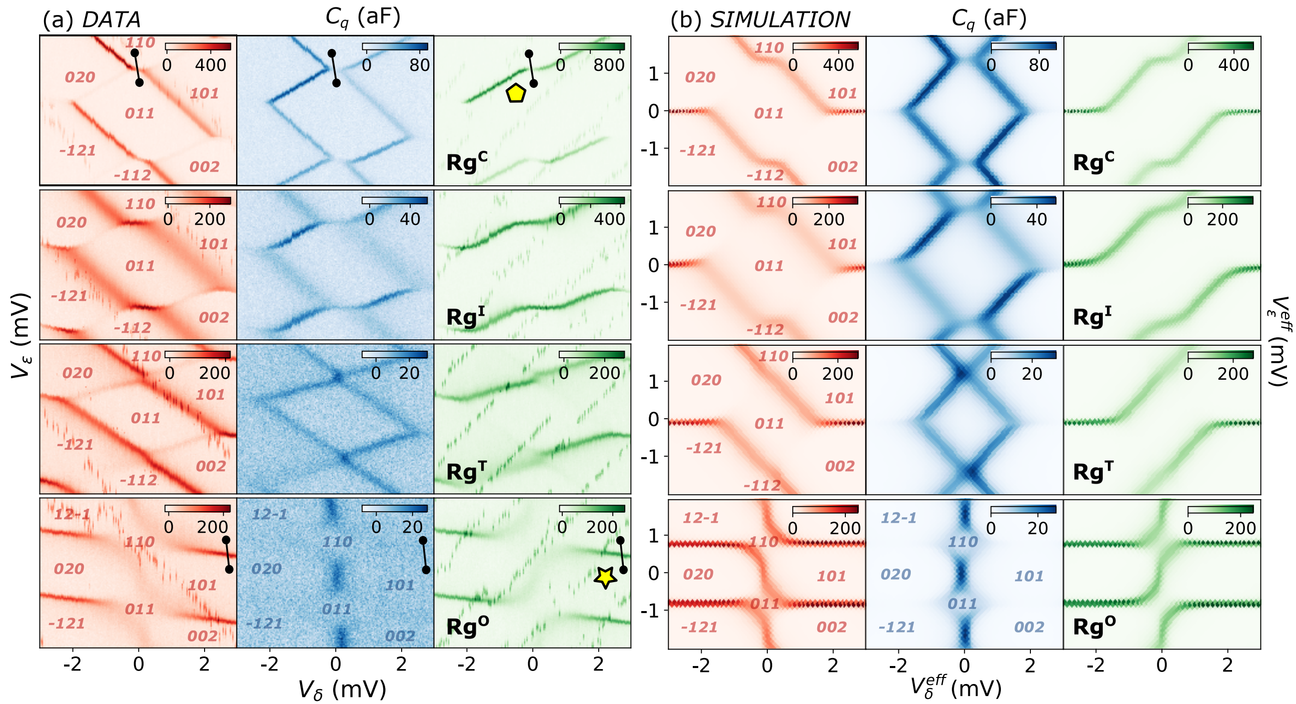

Figure 7.4: **Measured and simulated charge stability diagrams with extracted quantum capacitance.** **(a)** The zoomed-in version of Fig. 7.2 is depicted in quantum capacitances derived from the measurements. The linecuts near the two types of yellow markers are shown in Fig. 7.5. **(b)** The simulation based on two-Anderson impurity model yields similar results compared to the data. Note that except for Rg$^{\mathrm{I}}$, which differs from Rg$^{\mathrm{C}}$ only in the tunneling strength of DITs, the input charging energy of the island E_C^{SC} decreases from Rg$^{\mathrm{C}}$ to Rg$^{\mathrm{T}}$ and Rg$^{\mathrm{O}}$. In Rg$^{\mathrm{T}}$, the ground state energy of the island E_0 is equal to E_C^{SC}.

crease of E_C^{SC} from greater to less than E_0. The evolution also highlights the possibility of tuning the gates instead of altering the length of the island to fulfill the criteria for either forming topological qubits[1] or creating floating Cooper pair splitters[3].

7.5. CHARGE TUNNELING STRENGTHS

The tunneling strength of an ECT, denoted as t_{ECT}, can be determined from the C_q value as a function of the effective detuning voltage $V_\varepsilon^{\mathrm{eff}}$. By treating the middle superconducting island, along with the SILB and SIRB gates, as a unified barrier (as indicated by the grey regions in Fig. 7.5 (a) and (d)) positioned between the two outer normal dots, we can extract the tunneling strength t_{ECT} using a method similar to that used for calculating the interdot tunneling strengths in a normal double dot [6]. The value of t_{ECT} is obtained by fitting the expression

$$C_\mathrm{q} = \frac{(e\alpha)^2}{2} \frac{4p' t_{\mathrm{ECT}}^2}{(2\varepsilon_{\mathrm{eff}}^2 + 4p' t_{\mathrm{ECT}}^2)^{3/2}}, \tag{7.1}$$

with $p' = 1$ for ECT$^\mathrm{o}$ and $p' = 2$ for ECT$^\mathrm{e}$. Here, e is the unit electron charge, α is the lever arm of the plunger gate coupled to the probing resonator, and $\varepsilon_{\mathrm{eff}}$ is the effective detuning of the outer dot states.

When taking into account all the virtual tunneling processes through the two possible charge states (within the grey regions in Fig. 7.5 (a) and (d)), the tunneling strength t_{ECT} can be approximated by the tunneling strength of DITs from the left and right sides (identified as $t_{L(R)1(2)}$) according to the formula:

$$t_{\mathrm{ECT}} = P_1 \frac{t_{L1} t_{R1}}{\delta_{\mathrm{diff}}} + P_2 \frac{t_{L2} t_{R2}}{2p'' E_0 - \delta_{\mathrm{diff}}}, \tag{7.2}$$

where $p'' = -1$, $P_1 = 2$, $P_2 = 1$ for ECT$^\mathrm{o}$ and $p'' = +1$, $P_1 = P_2 = \sqrt{2}$ for ECT$^\mathrm{e}$. δ_{diff} represents the effective energy difference between the virtual and real charge states. We establish that the lowest energy state in the superconducting island E_0 remains in proximity to the superconducting gap represented by Δ_{gap}, with a value of $E_0 = \Delta_{\mathrm{gap}} = 0.25$ meV.

In Fig. 7.5, our attention is directed towards the instances of an ECT$^\mathrm{o}$ from Rg$^\mathrm{C}$ and an ECT$^\mathrm{e}$ from Rg$^\mathrm{O}$, as marked by the linecuts in Fig. 7.4 (a). The curves fitting t_{ECT} using Eq(7.1) through three resonators are depicted in Fig. 7.5 (b) and (e) for ECT$^\mathrm{o}$ and ECT$^\mathrm{e}$, respectively. The sensing signal from the LP resonator, shown as the red curves, yields the values of $t_{\mathrm{ECT}}^\mathrm{o}$ in Rg$^\mathrm{C}$ as 18.1 μeV, and $t_{\mathrm{ECT}}^\mathrm{e}$ in Rg$^\mathrm{O}$ as 8.7 μeV. To estimate the value of t_{DIT}, we rely on hundreds of linecuts near the specific one we highlighted in Fig. 7.4 (a), fitting their t_{ECT} values as a function of V_δ^{eff}. The curves fitted with Eq(7.2) are displayed in Fig. 7.5 (c) and (f), allowing us to estimate the magnitude of t_{DIT}. This estimation is based on the assumption that $t_{L(R)1(2)}$ possesses a similar magnitude. The signals obtained from the RP and LP resonators suggest a magnitude of approximately 34 μeV for t_{DIT} in Rg$^\mathrm{C}$, and 22 μeV in Rg$^\mathrm{O}$. Using the same approach, we ascertain that t_{DIT} amounts to be 41 μeV for ECT$^\mathrm{o}$ in Rg$^\mathrm{I}$, and 18 μeV for ECT$^\mathrm{e}$ in Rg$^\mathrm{T}$.

The extraction of t_{ECT} from C_q in Fig. 7.5 enables both the lever arm and t_{ECT} to be treated as independent variables. The fitting outcomes also indicate a monotonic decrease in the lever arm as E_C^{SC} decreases. This can be explained by the fact that the gates

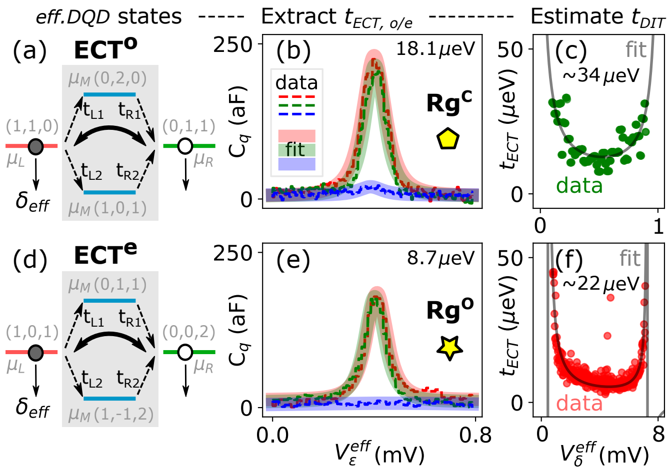

Figure 7.5: **Tunneling strength of ECTs and DITs.** **(a)** Schematic of an odd-island ECT process in Rg$^{\mathrm{C}}$, with all relevant charge states labeled. The associated DIT processes are denoted as $t_{L(R)1(2)}$. The tunneling strength $t^{\mathrm{o}}_{\mathrm{ECT}}$ can be estimated by considering the system as an odd-occupied double quantum dot. **(b)** The data extracted from the linecuts with the pentagon marker in Fig. 7.4 (a). Fitting with the effective double dot interdot transition model in Eq 7.1, we estimate $t^{\mathrm{o}}_{\mathrm{ECT}}$ in Rg$^{\mathrm{C}}$. The raw C_{q} data extracted from the three resonators are shown in dashed curves, while the fitted curves are represented by solid, slightly transparent curves of the same color. **(c)** The set of $t^{\mathrm{o}}_{\mathrm{ECT}}$ values plotted against $V_\varepsilon^{\mathrm{eff}}$, allows us to estimate the magnitude of t_{DIT}. The fitting curve follows Eq 7.2 is shown in grey. **(d)** Schematic of an even-island ECT process in Rg$^{\mathrm{O}}$, similar to (a) but to consider the system as an even-occupied double quantum dot. **(e)** Similar to (b), but this time the data is extracted from the linecuts marked by the pentagram in Fig. 7.4 (a). Here, we estimate $t^{\mathrm{e}}_{\mathrm{ECT}}$ in Rg$^{\mathrm{O}}$. **(f)** Similar to (c), but focusing on fitting $t^{\mathrm{e}}_{\mathrm{ECT}}$ in Rg$^{\mathrm{O}}$.

control a spatially larger wave function for more open regimes. We also quantitatively demonstrate that with a smaller E_C^{SC}, the tunneling strengths of both ECT$^{\mathrm{o}}$s and ECT$^{\mathrm{e}}$s increase. This is because a smaller E_C^{SC} results in a less detuned virtual state that assists ECTs. Additionally, $t^{\mathrm{o}}_{\mathrm{ECT}}$ is typically greater than $t^{\mathrm{e}}_{\mathrm{ECT}}$. This observation supports the idea that, in comparison to ECT$^{\mathrm{e}}$s, significantly less detuned virtual states assist ECT$^{\mathrm{o}}$s, leading to a much larger $t^{\mathrm{o}}_{\mathrm{ECT}}$, as described in Fig. 7.3 (b).

In the case of Rg$^{\mathrm{O}}$, the tunneling strength of CARs detected by LP and RP resonators can be extracted in a similar manner to t_{ECT} using Eq(7.1) with $p' = 2$, as the split Cooper pair can provide either a spin-up or spin-down electron to the outer dot [3] (see Fig. 7.6 (a)). As for the CARs detected by the SIP resonator, we can consider the outer two quantum dots as a single dot that exchanges Cooper pairs with the island. Hence, Eq(7.1) can be utilized to extract t_{CAR} with $p' = 1$, where the unit electron charge is adjusted from $1e$ to $2e$ (see Fig. 7.6 (b)). Taking the CAR near the star marker in Fig. 7.2 (d) as an example, Fig. 7.6 (c) illustrates the respective t_{CAR} values extracted from the LP, SIP and RP resonators using the revised Eq(7.1), resulting in 19.1 μeV, 21.3 μeV, and 24.0 μeV respectively. Note that the lever arm of the SIP gate is currently unknown, but it has been estimated based on the value used in simulations in Sec. 7.4. The t_{CAR} values obtained from the LP and RP resonators can exceed those of t_{ECT}, and are similar to the t_{CAR} values measured from the SIP resonator. This similarity can be explained by the island

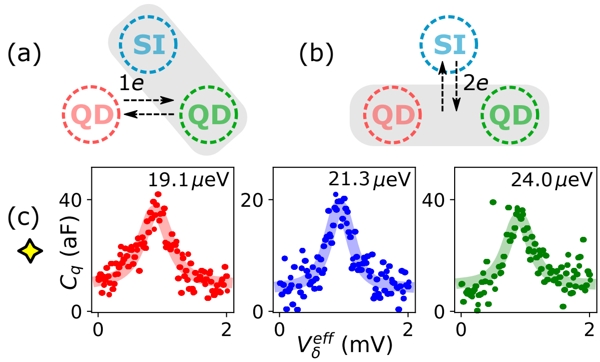

Figure 7.6: **Tunneling strength of CARs. (a)** When using the LP gate for sensing, the hybrid system is analogous to the left quantum dot being connected to an effective quantum dot comprising the middle island and the right quantum dot. The unit of charge transfer is $1e$. **(b)** When using the SIP gate for sensing, the hybrid system is akin to the middle island being linked to an effective quantum dot consisting of the two outer dots. The unit of charge transfer is $2e$. **(c)** The linecuts of a CAR detected by the LP, SIP and RP resonators as marked in Fig. 7.2 (d), with the corresponding estimated t_{CAR} values annotated. The data points depict the raw C_q data, while the solid transparent curves denote the fitting outcomes.

tunneling Cooper pairs to the outer dots at the same rate as the quantum dots receive charges. Meanwhile, we find the fitted lever arms of the LP and RP gates are approximately half of what was observed in Fig. 7.5. The discrepancy is caused by the crosstalk effects between the corresponding quantum dot and the other effective dot (as shown in Fig. 7.6 (a)), which cannot be overlooked.

7.6. EFFECTS ON LOSSES

Apart from the parametric capacitance discussed in relation to the amplitude response, the Sisyphus dissipation, which is inversely proportional to the Sisyphus resistance R_sis, is also finite in our measurements and encompasses valuable additional information that merits attention. In our equivalent circuit, which includes two resistors in parallel to the ground - one representing the losses in the resonator ($1/R_0$) and the other in the hybrid triple-dot system ($1/R_\mathrm{sis}$) - the total conductance is given by $G = 1/Z_\mathrm{ch}Q_\mathrm{int} = 1/R_0 + 1/R_\mathrm{sis}$, where Z_ch denotes the characteristic impedance. The losses intrinsic to the resonator, denoted as $G_0 = 1/R_0$, can be determined by extracting Q_int in Coulomb blockade, enabling us to calculate the effective conductance $G_\mathrm{eff} = G - G_0$. Figure 7.7 illustrates the Sisyphus dissipation at the charge transitions, represented as $G_\mathrm{eff} = 1/R_\mathrm{sis}$ [5].

Among all regimes exhibit in Fig. 7.7, G_eff stands out prominent for certain DITs and ECTs, but not for CARs. The resonators coupled to the outer dots can detect a finite G_eff for ECTs where the ECTs exist, as well as for DITs in the regimes where $E_C^\mathrm{SC} > E_0$. On the other hand, the resonator coupled to the island appears to be sensitive only to the G_eff for DITs in Rg^C, becoming completely noisy in other regimes. We then shift our focus to the detected G_eff by the LP and RP resonators. In Rg^C, the highest values of G_eff are observed for $\mathrm{ECT^o}$s, whereas G_eff values for $\mathrm{ECT^e}$s are nearly zero except near

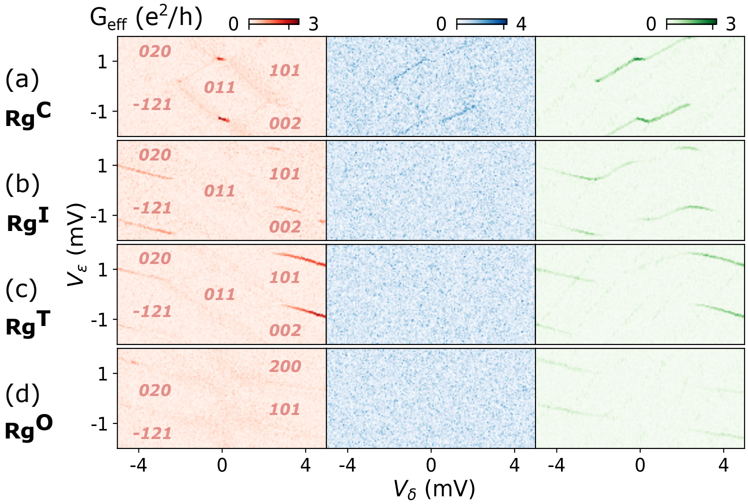

Figure 7.7: **The Sisyphus dissipation of the tunneling processes.** The effective conductance G_{eff} is extracted to show the Sisyphus dissipation on the charge stability diagrams of the four regimes. Larger G_{eff} indicates larger losses for the corresponding charge tunneling process.

intersections of the three nearby charge states. The G_{eff} of the DITs is also finite, albeit with a lower magnitude. It is evident from the RP resonator that the value of G_{eff} for DIT^{e} is greater than that for DIT$^{\text{O}}$, a trend also observed in Rg$^{\text{I}}$. In Rg$^{\text{I}}$, the G_{eff} of the ECT$^{\text{e}}$s becomes dominant, with their magnitude decreasing from the two ends towards the center, just as the amplitude response of those ECT$^{\text{e}}$s in Fig. 7.2 (b). In Rg$^{\text{T}}$ and Rg$^{\text{O}}$, the ECT$^{\text{e}}$s are the only charge transitions that brings about a nonzero G_{eff}. In contrast to the ECT$^{\text{e}}$s in Rg$^{\text{I}}$, the magnitude of G_{eff} for the ECT$^{\text{e}}$s increases from the two ends towards the center. We notice that the value of G_{eff} for these ECT$^{\text{e}}$s drops dramatically from Rg$^{\text{T}}$ to Rg$^{\text{O}}$.

The detectable Sisyphus dissipation for DITs and ECTs suggests that some of those tunneling processes are incoherent attributed to electron-phonon interactions. These interactions lead to unequal phonon absorptions and emissions throughout the charge tunneling process, rendering the charge tunnelings irreversible [9]. For DITs, incoherent signifies that the process of the charge tunneling into (out of) the island from (to) the same quantum dot involves electron-phonon interactions that induce decoherence. While in the context of ECTs, incoherent describes the intermediate process of charge tunneling through the middle superconducting island, which is no longer purely virtual. Instead, some of these cotunneling processes involve sequential DITs between the two outer dots at speed that exceed the measurement rate. The presence of finite Sisyphus dissipation, or the noted incoherence, is consistent with the assumption that $E_0 = \Delta_{\text{gap}}$, indicating that numerous states within the quasiparticle continuum instead of a descrete Andreev bound state below the superconducting gap are supporting the DITs or the virtual process of ECTs. The lower Sisyphus dissipation observed in either larger ECT$^{\text{o}}$s (comparing Fig. 7.7 (a) and (b)) or ECT$^{\text{e}}$s (comparing Fig. 7.7 (c) and (d)) may be attributed to a stronger tunneling effect, leading to reduced cumulative dissipation arising from electron-phonon interactions. Essentially, the heightened tunneling strength decreases the probability of phonon absorptions and emissions taking place during the charge tunneling process. This phenomenon can also account for the enhanced Sisyphus dissipation observed in the middle of ECT^{e}s along the V_δ axis (as seen in Fig. 7.7 (c) and (d)), where smaller t_{ECT} values are prevalent.

Based on our current understanding of CARs, it is believed that they are also facilitated by the lowest energy state $E_0 = \Delta_{gap}$ within the island [10]. In essence, each of the two charges originating from the outer dots is expected to pair up to form a Cooper pair upon entering the middle island. However, before reaching the Cooper pair condensation phase, they must briefly occupy the lowest energy state within the island as part of an intermediate virtual process. If this process lacks coherence, we would anticipate that CARs would exhibit measurable dissipation, similar to the aforementioned ECTs. Nevertheless, the data collected thus far does not seem to support this expectation, as depicted in a manner akin to the presentation in Fig. 7.7 (d). This absence of Sisyphus dissipation for CARs could serve as compelling evidence that CARs are indeed coherent processes.

7.7. Conclusion

To sum up, we have investigated the various charge tunneling processes in an InAs nanowire-based hybrid triple quantum dot system, where a superconducting island is embedded between two normal dots. Using dispersive gate sensing and multiplexed RF techniques, we are able to characterize the charge stability diagrams and estimate the tunneling strength between different charge states, with the system completely isolated from charge resources. Our results highlight the tunability of such a floating system between elastic cotunneling (ECT) and cross-Andreev reflection (CAR), and demonstrate a transition point where both processes coexist in resonance. The agreement of our measurements with the theoretical model underlines that the comparison between the charging energy and the ground state energy of the island leads to this evolution. In addition to the quantum capacitances from which we obtain the corresponding tunneling strength, the extractable Sisyphus dissipation adds another dimension to the understanding of the coherence of different types of charge transitions. With the recent progress in few-site Kitaev chains and their parity readout, we offer a promising avenue for an updated version with superconducting islands [2]. Further work can also be directed towards Cooper pair splitters and topological Kondo effects, where the charge tunneling events are of interest. This work not only advances our approach to the qualitative and quantitative analysis of a floating hybrid quantum dot system with dispersive gate sensing, but also paves the way for the implementation of Majorana-based qubits [1].

7.8. Appendix

7.8.1. Device

The device is fabricated on an InAs nanowire coated with a thin shell of aluminium. After transferring the nanowire onto a Si/SiNx substrate, a positive resist is spin-coated, and electron-beam lithography is employed to define the etching window for removing the aluminium. Subsequently, the etching process using liquid Transene-D results in the nanowire being solely covered by aluminium at the location of the superconducting island. Titanium/gold (Ti/Au) metal contacts are then deposited at the both ends of the nanowire, followed by a thin layer of AlOx as the dielectric, and another layer of Ti/Au metal gates on top. The metal gates SILB and SIRB in Fig. 7.1 (a) are precisely positioned above the edge of the nanowire segment where aluminum is present. This deliberate positioning covers the interface between the normal semiconductor segment and the proximitized superconducting segment.

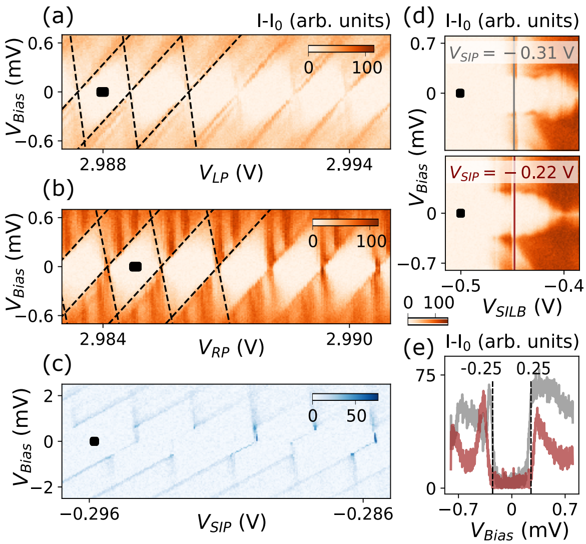

Figure 7.8: **Coulomb diamonds of each hybrid quantum dot and the characterization of the superconducting island. (a)** The Coulomb diamond of the left quantum dot, measured in the relative in-phase values ($|I - I_0|$) via the resonator couple to the left lead. The black square marks where the in-phase value of the Coulomb blockade regime (I_0) is selected and averaged. **(b)** The Coulomb diamond of the right quantum dot, similar to (a) but measured via the resonator couple to the right lead. **(c)** The Coulomb diamond of the middle superconducting island, similar to (a) but measured via the SIP resonator (therefore plotted in blue colormap). **(d)** Tunneling spectroscopy from the left side of the island with V_{SIP} = -0.31 V and -0.22 V, measured by the lead resonator. The vertical cuts with grey and brown colors corresponds to the V_{SILB} gate at -0.448 V. **(e)** The linecuts of (d) when V_{SILB} = -0.448 V, illustrating clearly a hard gap for a relatively large range of V_{SIP}, at least between -0.31 V and -0.22 V. The estimated gap size is slightly over 0.25 meV, as marked by the verticle lines.

7.8.2. Characterization of individual hybrid dots

Each dot in the hybrid system is characterized prior to the measurements in the main text. Fig. 7.8 (a,b) display the Coulomb diamonds of the left quantum dot and right quantum dot, measured using the left and right lead resonators (LL and RL labeled in Fig. 7.1 (a)), respectively. The resonance frequencies of these lead resonators are approximately 529.6 MHz for LL and 433.5 MHz for RL. The charging energy of the two outer dots E_C^{QD} is known to be about 0.33 μeV, and the lever arms of their plunger gates (LP and RP) are about 0.5, providing a reference for the top gates tunability.

The middle superconducting island is characterized by the SIP resonator, as shown in Fig. 7.8(c). The alternation between even and odd Coulomb diamonds along the SIP gate voltage (V_{SIP}) indicates that the lowest state energy (E_0) within the island is smaller than its charging energy (E_C^{SC}). Fig. 7.8(d) illustrates the tunneling spectroscopy of the superconducting island as read from the RL resonator, with V_{SIP} set to -0.31 V (top panel) and -0.22 V (bottom panel). Linecuts with $V_{SILB} = -0.448$ V, as depicted in Fig. 7.8(e), reveal a hard gap within the superconducting island, with the estimated gap size Δ_{gap} slightly above 0.25 meV.

7.8.3. CALCULATION OF ADDITION ENERGIES

As defined in Sec. 7.3, the relationship between the gate-induced charge number N_g^{SC} and energy E of the island is described by $E(N_g^{\mathrm{SC}}) = E(N_g^{\mathrm{SC}} - N)^2 + p_N E_0$, where $p_N = 0$ or 1 depending on whether the electron occupancy number N is even or odd, respectively. The relative electrochemical potentials

$$\begin{aligned} U_N &= E(N) - E(N-1) = -E_C^{\mathrm{SC}}(2N_g^{\mathrm{SC}} - 2N + 1) + E_0(p_N - p_{N-1}) \\ U_{N+1} &= E(N+1) - E(N) = -E_C^{\mathrm{SC}}(2N_g^{\mathrm{SC}} - 2N - 1) + E_0(p_{N+1} - p_N) \end{aligned} \tag{7.3}$$

Then the addition energies for the superconducting island with N charges

$$\begin{aligned} U_{N+1} - U_N &= 2E_C^{\mathrm{SC}} + E_0(p_{N+1} - 2p_N + p_{N-1}) \\ &= 2[E_C^{\mathrm{SC}} + (-1)^N E_0] \end{aligned} \tag{7.4}$$

When $E_C^{\mathrm{SC}} = E_0$, the addition energy becomes zero for an odd-charge superconducting island.

7.8.4. PROOFS OF EVEN TOTAL CHARGE NUMBERS

The analysis in the main text rests on the assumption that the total charge of the hybrid triple dot system is even, rather than odd. We present a supporting simulation to verify this assumption. In the course of measurements across various regimes, a specific regime (labeled as Rg^{P} in Fig. 7.9(a)) reveals the appearance of CARs from the SIP resonator, exhibiting an alternating bending tendency. This behavior aligns with our model's predictions based on an assumption of an even-occupied system (refer to Fig. 7.9(b)), but is absent when assuming an odd-occupied system (refer to Fig. 7.9(c)). Given that the LB and RB gates are intended to be fully closed to uphold charge conservation, the presence of this characteristic serves as additional evidence that measurements for all other regimes in the main text are conducted with an even total charge number.

7.8.5. NEGLIGIBLE TUNNELING CAPACITANCE

The total capacitance contributed to the circuit by the device can be regarded as the sum of two components: the constant geometrical capacitance, and the variable parametric capacitance $C_{\mathrm{pm}} = C_{\mathrm{q}} + C_{\mathrm{t}}$, which includes the quantum capacitance term C_{q} and a tunneling capacitance term C_{t}. Any alteration in C_{pm} causes a frequency shift, resulting in a distinct value for the measurable component of the reflection coefficient S_{11}. The value of C_{pm} can thus be determined through inverse derivations.

In the main text, we opt to graph the charge stability diagrams and examine the charge tunneling processes in C_{q} rather than C_{pm} because we consider the value of C_{t}

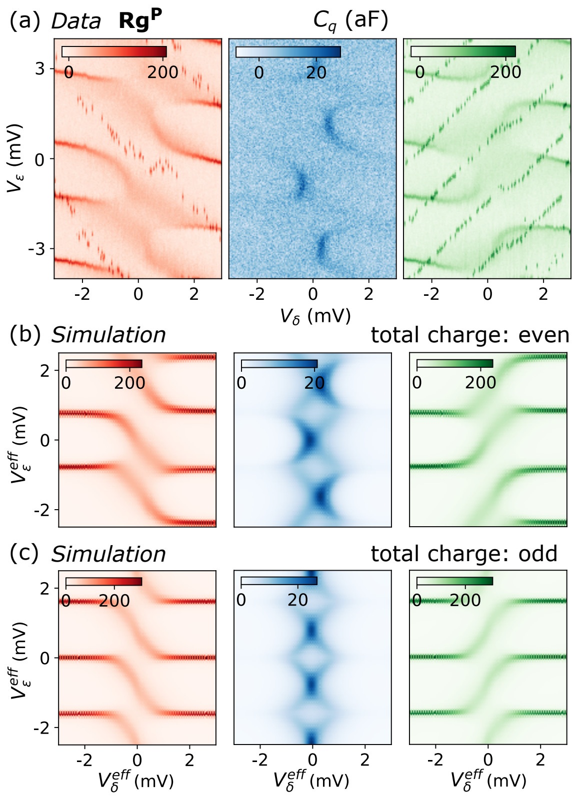

Figure 7.9: **Reasons on assuming even total charge number for the hybrid triple dot. (a)** The charge stability diagram for another measured regime Rg^{P}. **(b)** The simulation result when assuming even-occupied system. The data in (a) show a much closer qualitative resemblance to (b) than to (c), particularly in relation to the signal recorded through the SIP resonator. **(c)** The simulation result when assuming odd-occupied system.

to be relatively insignificant. This decision may be debatable, considering that Fig. 7.7 already illustrates numerous dissipative charge tunneling processes, indicating that C_t is not zero. Furthermore, to extract t_ECT using Eq(7.1), we employ the expression of C_q under the assumption that thermal broadening can be neglected.

Here, in Fig. 7.10, we provide evidence supporting the feasibility of relying solely on C_q to assess the strength of charge tunneling, particularly for dissipative ECTs. The precise C_q and C_t can be written as

$$C_\mathrm{q} = \frac{(e\alpha)^2}{2}\frac{t_\mathrm{ECT}^2}{(\Delta E)^3}\tanh\frac{\Delta E}{2k_B T}, \tag{7.5}$$

$$C_\mathrm{t} = \frac{(e\alpha)^2}{4k_B T}(\frac{\varepsilon_\mathrm{eff}}{\Delta E})^2\frac{\gamma^2}{\omega^2+\gamma^2}\cosh^{-2}(\frac{\Delta E}{2k_B T}), \tag{7.6}$$

where ε_eff is the effective detuning, ΔE is the energy difference between the excited and ground state, and $k_B T$ is the thermal energy [11]. In C_t, γ represents the characteristic relaxation rate of the system, while ω denotes the assumed low relaxation rate. Both

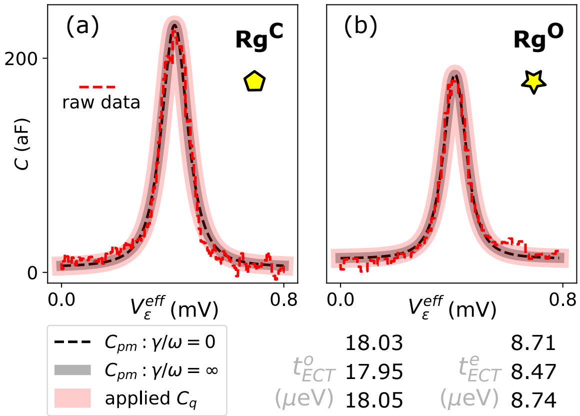

Figure 7.10: **Reasons on using C_q quantity. (a)** The location of the linecut in Rg^O along V_ε^{eff}. **(b)** The measured and fitted capacitances of the linecut. As the parametric capacitance $C_{pm} = C_q + C_t$ brings about negligible difference between the case when the tunneling capacitance C_t term is excluded ($\gamma/\omega = 0$) and included ($\gamma/\omega = \infty$), we conclude that the measured capacitance is dominated by C_q. The applied C_q fitting model marked in thick red curve comes from the simplified expression of C_q where the temperature effects are further ignored. We find that the simplified fitting model fits the data well and gives a reliable tunneling strength t^o_{ECT} within an error of 0.03 μeV.

Fig. 7.10 (a) and (b) show the observed changes in capacitance along the linecut of a lossy ECT^o in RgC and an ECT^e in Rg^O (as indicated in Fig. 7.4 and measured by the LP resonator). The fitting curves for scenarios assuming zero C_t (when $\gamma/\omega = 0$), finite C_t (when $\gamma/\omega = \infty$), and pure C_q without thermal effects (labeled as the applied C_q) closely aligh with each other. Consequently, the extracted value of t_{ECT} from Eq(7.1) is quite precise.

7.8.6. EFFECTIVE TUNNEL COUPLINGS

QUANTUM CAPACITANCES

The effective Hamiltonian of the charge qubit formed by the two outer quantum dots (as shown in Fig. 7.5 (a) and (d)) is given by:

$$H_{\text{eff}} = \begin{bmatrix} \varepsilon'/2 & t_{\text{ECT}} \\ t_{\text{ECT}} & -\varepsilon'/2 \end{bmatrix}, \tag{7.7}$$

providing the ground state energies $E_g = -\sqrt{(\varepsilon'/2)^2 + t^2_{\text{ECT}}}$, with $\varepsilon' = \mu_L - \mu_R = \sqrt{2}\varepsilon_{\text{eff}}$ the detuning and t_{ECT} the cotunneling strength. As per the definition of quantum capaitcance, when the tunneling capacitance is proved to be negligible for estimating the tunneling strengths, we have $C_q = C_{\text{pm}} = (e\alpha'^2)\partial^2 E_g/\partial\varepsilon'^2$, where α' denotes the effective lever arm that incorporates cross-coupling effects.

For the two outer quantum dot system with total charge occupancy being even or odd, we obtain different ground state energy due to the spin degeneracy. That is,

$$C_{\mathrm{q,o}} = \frac{(e\alpha')^2}{2}\frac{4t_{\mathrm{ECT}}^2}{(2\varepsilon_{\mathrm{eff}}^2 + 4t_{\mathrm{ECT}}^2)^{3/2}} \tag{7.8}$$

$$C_{\mathrm{q,e}} = \frac{(e\alpha')^2}{2}\frac{8t_{\mathrm{ECT}}^2}{(2\varepsilon_{\mathrm{eff}}^2 + 8t_{\mathrm{ECT}}^2)^{3/2}}, \tag{7.9}$$

which can be summarized as in Eq. 7.1 [6]. There, we assume the cross-coupling between the LP and RP gates is close to zero and thus allows $\alpha' = \alpha$.

ELASTIC COTUNNELINGS

The Hamiltonian describing the ECT$^{\mathrm{o}}$s can be expressed in the basis $|\psi_1\rangle = |110\rangle$, $|\psi_2\rangle = |011\rangle$, $|\psi_3\rangle = |020\rangle$, $|\psi_4\rangle = |101\rangle$ as:

$$H_{\mathrm{ECT^o}} = \begin{bmatrix} (\mu_L-\mu_R)/2 & 0 & \sqrt{2}t_{L1} & t_{L2} \\ 0 & (\mu_R-\mu_L)/2 & \sqrt{2}t_{R1} & t_{R2} \\ \sqrt{2}t_{L1} & \sqrt{2}t_{R1} & \delta_{\mathrm{eff,o}} & 0 \\ t_{L2} & t_{R2} & 0 & -2E_0-\delta_{\mathrm{eff,o}} \end{bmatrix}, \tag{7.10}$$

with $\mu_{L(R)}$ the chemical potential of the left (right) quantum dot state, $t_{L(R)1(2)}$ the tunneling strength between a superconducting island state and a quantum dot state, as labeled in Fig. 7.5 (a) and (d). The value of $\delta_{\mathrm{eff,o}}$ is defined as $\delta_{\mathrm{eff,o}} = E_C^{\mathrm{SC}} - E_C^{\mathrm{QD}} - E_0 - (\mu_L-\mu_R)/2$. The $\sqrt{2}$ term serves as a spin degeneracy term when the total charge occupancy of the DIT is even [12, 6]. Similarly, the Hamiltonian describing the ECT$^{\mathrm{e}}$s can be expressed in the basis $|\psi_1\rangle = |101\rangle$, $|\psi_2\rangle = |002\rangle$, $|\psi_3\rangle = |011\rangle$, $|\psi_4\rangle = |1{-}12\rangle$ as:

7

$$H_{\mathrm{ECT^e}} = \begin{bmatrix} (\mu_L-\mu_R)/2 & 0 & t_{L1} & t_{L2} \\ 0 & (\mu_R-\mu_L)/2 & \sqrt{2}t_{R1} & \sqrt{2}t_{R2} \\ t_{L1} & \sqrt{2}t_{R1} & \delta_{\mathrm{eff,e}} & 0 \\ t_{L2} & \sqrt{2}t_{R2} & 0 & 2E_0-\delta_{\mathrm{eff,e}} \end{bmatrix}. \tag{7.11}$$

The value of $\delta_{\mathrm{eff,e}}$ is then defined as $\delta_{\mathrm{eff,o}} = E_C^{\mathrm{SC}} - E_C^{\mathrm{QD}} + E_0 - (\mu_L-\mu_R)/2$.

The tunneling strength t_{ECT} between $|\psi_1\rangle$ and $|\psi_2\rangle$ can be calculated as:

$$t_{\mathrm{ECT^o}} = \frac{2t_{L1}t_{R1}}{\delta_{\mathrm{eff}}} + \frac{t_{L2}t_{R2}}{-2E_0-\delta_{\mathrm{eff}}} \tag{7.12}$$

$$t_{\mathrm{ECT^e}} = \frac{\sqrt{2}t_{L1}t_{R1}}{\delta_{\mathrm{eff}}} + \frac{\sqrt{2}t_{L2}t_{R2}}{2E_0-\delta_{\mathrm{eff}}}, \tag{7.13}$$

and can be summarized as in Eq. 7.2 [13].

7.8.7. RELEVANT INPUT PARAMETERS

BIBLIOGRAPHY

[1] Stephan Plugge, Asbjørn Rasmussen, Reinhold Egger, and Karsten Flensberg. Majorana box qubits. *New Journal of Physics*, 19(1):012001, 2017.

regime:	$\mathrm{Rg^A}$	$\mathrm{Rg^C}$	$\mathrm{Rg^I}$	$\mathrm{Rg^T}$	$(\mathrm{Rg^P})$	$\mathrm{Rg^O}$	
LP	0.940	0.155	0.340	0.397	0.391	1.936	
RP	0.950	0.132	0.307	0.406	0.396	2.106	
SIP	-0.30	-0.25	-0.25	-0.25	-0.25	-0.10	unit:
SILB	-0.170	-0.050	-0.100	-0.050	-0.050	-0.055	(V)
SIRB	0.690	1.060	1.260	1.250	1.250	0.880	
LB/RB	-2.50	-2.50	-2.50	-2.50	-2.50	-2.50	

Table 7.1: **Gate setting parameters for all the measured regimes.** From left to right columns, the LP and RP gates typically increase the applied voltages, resulting in a decrease in the charging energy of all hybrid quantum dots. The SIP gate remains constant, except for the $\mathrm{Rg^O}$ regime. SILB and SIRB are not significantly adjusted, while the LB and RB gates are set to -2.5 V to maintain charge conservation within the hybrid triple dot system.

regime:	$\mathrm{Rg^C}$	$\mathrm{Rg^I}$	$\mathrm{Rg^T}$	$\mathrm{Rg^O}$	
$t_{\mathrm{L,DIT}}$	0.05	0.10	0.05	0.05	
$t_{\mathrm{R,DIT}}$	0.05	0.05	0.05	0.05	unit:
E_0	0.25	0.25	0.25	0.25	(meV)
E_C^{QD}	0.42	0.42	0.30	0.18	
E_C^{SC}	0.35	0.35	0.25	0.15	
α_{QD}	0.435	0.405	0.325	0.320	unit:
α_{SC}	0.325	0.245	0.145	0.090	(eV/V)

Table 7.2: **Parameters for simulations.** The ground state of the island is assumed to be the size of the hard gap, specifically $E_0 = \Delta_{\mathrm{gap}} = 0.25$ meV. Except for $\mathrm{Rg^I}$, the t_{DIT} term is fixed at 0.05 meV for both the left and right dot-to-island transitions. The comparison between $\mathrm{Rg^I}$ and $\mathrm{Rg^C}$ shows the impact on the differentiation of $t_{L,DIT}$ and $t_{R,DIT}$. The lever arms are adjusted to align the C_{q} range of the simulation with that of the data, resulting in a reasonable reduction of the lever arms as E_C^{SC} decreases.

7

[2] Tom Dvir, Guanzhong Wang, Nick van Loo, Chun-Xiao Liu, Grzegorz P Mazur, Alberto Bordin, Sebastiaan LD Ten Haaf, Ji-Yin Wang, David van Driel, Francesco Zatelli, et al. Realization of a minimal kitaev chain in coupled quantum dots. *Nature*, 614(7948):445–450, 2023.

[3] Damaz de Jong, Christian G Prosko, Lin Han, Filip K Malinowski, Yu Liu, Leo P Kouwenhoven, and Wolfgang Pfaff. Controllable single cooper pair splitting in hybrid quantum dot systems. *Physical review letters*, 131(15):157001, 2023.

[4] Filip K Malinowski, Lin Han, Damaz De Jong, Ji-Yin Wang, Christian G Prosko, Ghada Badawy, Sasa Gazibegovic, Yu Liu, Peter Krogstrup, Erik PAM Bakkers, et al. Radio-frequency c-v measurements with subattofarad sensitivity. *Physical Review Applied*, 18(2):024032, 2022.

[5] Filip K Malinowski, RK Rupesh, Luka Pavešić, Zoltán Guba, Damaz de Jong, Lin Han, Christian G Prosko, Michael Chan, Yu Liu, Peter Krogstrup, et al. Quantum capacitance of a superconducting subgap state in an electrostatically floating dot-island. *arXiv preprint arXiv:2210.01519*, 2022.

[6] Lin Han, Michael Chan, Damaz De Jong, Christian Prosko, Ghada Badawy, Sasa Gazibegovic, Erik PAM Bakkers, Leo P Kouwenhoven, Filip K Malinowski, and Wolfgang Pfaff. Variable and orbital-dependent spin-orbit field orientations in an insb double quantum dot characterized via dispersive gate sensing. *Physical Review Applied*, 19(1):014063, 2023.

[7] Damaz De Jong, Jasper Van Veen, Luca Binci, Amrita Singh, Peter Krogstrup, Leo P Kouwenhoven, Wolfgang Pfaff, and John D Watson. Rapid detection of coherent tunneling in an in as nanowire quantum dot through dispersive gate sensing. *Physical Review Applied*, 11(4):044061, 2019.

[8] Filip K Malinowski. Two anderson impurities coupled through a superconducting island: charge stability diagrams and double impurity qubit. *arXiv preprint arXiv:2303.14410*, 2023.

[9] M Esterli, RM Otxoa, and MF Gonzalez-Zalba. Small-signal equivalent circuit for double quantum dots at low-frequencies. *Applied Physics Letters*, 114(25), 2019.

[10] Alberto Bordin, Guanzhong Wang, Chun-Xiao Liu, Sebastiaan LD Ten Haaf, Nick Van Loo, Grzegorz P Mazur, Di Xu, David Van Driel, Francesco Zatelli, Sasa Gazibegovic, et al. Tunable crossed andreev reflection and elastic cotunneling in hybrid nanowires. *Physical Review X*, 13(3):031031, 2023.

[11] Florian Vigneau, Federico Fedele, Anasua Chatterjee, David Reilly, Ferdinand Kuemmeth, M Fernando Gonzalez-Zalba, Edward Laird, and Natalia Ares. Probing quantum devices with radio-frequency reflectometry. *Applied Physics Reviews*, 10(2), 2023.

[12] Jasper Van Veen, Damaz De Jong, Lin Han, Christian Prosko, Peter Krogstrup, John D Watson, Leo P Kouwenhoven, and Wolfgang Pfaff. Revealing charge-tunneling processes between a quantum dot and a superconducting island through gate sensing. *Physical Review B*, 100(17):174508, 2019.

[13] Floris R Braakman, Pierre Barthelemy, Christian Reichl, Werner Wegscheider, and Lieven MK Vandersypen. Long-distance coherent coupling in a quantum dot array. *Nature nanotechnology*, 8(6):432–437, 2013.

8

Conclusion and outlooks

The aim of this thesis was to explore the application of dispersive gate sensing on the platform of nanowire-based semiconductor-superconductor hybrid quantum dots, with the aim of characterizing and reading the parity of potential topological qubits, albeit in their simplified form. Through a combination of chip design and fabrication, experimental work, data interpretation and theoretical analysis, several findings have emerged, the key points of which are first summarized in this chapter. The second part of this chapter contains some future topics that can be followed up later.

8.1. CONCLUSION

CHAPTER 4

This work was implemented in parallel to the initial technical characterizations of dispersive gate sensing on top-gated InAs nanowires, as included in Ref. [1]. Instead of measuring normal double quantum dots, the modification we made is to measure a hybrid system, namely a normal dot and a superconducting island in series. The device was fabricated on an InAs nanowire that covered by aluminium shell on two facets, such that the island can be defined by aluminum etching.

By analyzing the resonator response, we detected and characterized the charge tunneling processes between the quantum dot and the superconducting island. Our findings revealed that depending on the dominant energy scales of the hybrid double dot, both single-quasiparticle and Cooper pair tunneling processes can occur. Notably, our data indicated that dispersive gate sensing is a highly effective tool for investigating subgap excitations, even in scenarios where the absence of leads prevents transport measurements.

Comparing with Ref. [1] where Damaz et al. effectively measured the simplest component of a Majorana box qubit that depicted in Fig. 1.1 (e), this work can be regarded as measuring an upgraded version that depicted in Fig. 1.1 (d). The results demonstrated a feasible way to achieve projective parity measurements by coupling a quantum dot to a Majorana zero mode.

CHAPTER 5

Having observed the clear signal from dispersive gate sensing, and enlightened by the advanced fabrication approaches, we tested dispersive gate sensing on a batch of non-superconducting InSb nanowires, deliberately using bottom gates. With many unknown parameters due to the completely different device design, we went back to the double quantum dot geometry and fabricated the device in such a way that was adapted to the shallow-wall technique. Fig. 8.1 gives the schematics of a small- and large-angle deposition of aluminium, to get the nanowire proximitized at a selected area, with the meticulous design of the shallow-wall patterns. Charge sensors were also fabricated and tested, as mentioned in Chapter. 3.

We then studied the spin-orbit field orientations using dispersive gate sensing in the InSb nanowire-based double quantum dot. At zero magnetic field, we realized that the dispersive gate sensing serves as a charge parity meter. By rotating an external magnetic field, the spin-orbit field orientation can be identified by the suppression of the maximum quantum capacitance. We modeled the dispersive signal for even-occupied charge transitions, and found good agreement when the external field is perpendicular

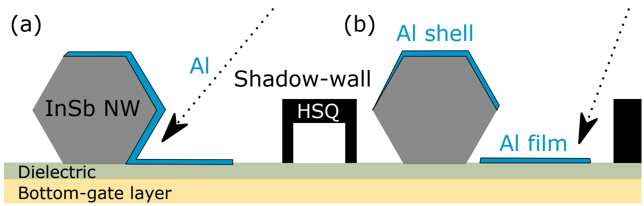

Figure 8.1: **Shadow-wall technique on achieving (un)grounding superconducting segments.** Cross-section of the InSb nanowire with **(a)** a small-angle deposition of aluminium, which allows either the grounding of the superconducting segment or the connections between individual islands along the nanowire. The shadow-wall is fabricated using a hydrogen silsesquioxane (HSQ) bilayer approach, which makes it easier to leave openings while reducing the geometric capacitance. **(b)** a large-angle deposition of aluminium that provides ungrounded islands. Here a single layer of HSQ shadow-wall is utilized.

to the spin-orbit field orientation. Furthermore, the spin-orbit field orientation is consistent within the same valence orbital but varies significantly between different orbitals. Our results suggested that predictions of spin-orbit field orientation based solely on device design may not always be accurate.

Dispersive gate sensing therefore proved to be an effective tool for characterizing spin-orbit field orientation, especially when transport measurements are not feasible or less complex chip design is preferred. We also benefited from the high speed of the measurements to obtain a more complete picture of the spin-orbit field orientations. It is worth noting that we have attempted to obtain superconducting island devices using the advanced fabrication approaches, but all have failed for lack of measurable superconductivity.

CHAPTER 6

In order not to be exclusively associated with topological quantum systems, we have also tried to look at other possible applications of RF reflectometry to the measurement of semiconductor devices, not only limited to dispersive gate sensing, but also to RF conductance. The measured devices are all based on one-dimensional systems, both InAs and InSb nanowires are involved.

We validated a method for measuring the capacitance of micro- and nanoscale devices using RF resonators. This method features sensitivity as low as 75 $\mathrm{zF}/\sqrt{\mathrm{Hz}}$ and noise below 1 aF for moderate integration times. It is suitable for both room temperature and cryogenic applications, including dilution refrigerators. In addition, multiple gate capacitances can be measured with a single resonator, reducing the reliance on finite element simulations for mobility measurements. Finally, we proposed that RF capacitance measurements can detect the quantum contribution to bulk capacitance in mesoscopic devices and can be implemented on the needle of a probe station using a micromanipulator. To quantify the reflectometry signal more accurately, we developed a new fitting model for the measured reflection coefficients that explains the resonance asymmetry.

CHAPTER 7

The latest progress came back to the main pursuit of the Majorana box qubit, but with a further improved version shown in Fig. 1.1 (c). With the explosions of the minimal Kitaev chain experiments and the investigations of the poor man's Majorana [2, 3, 4, 5, 6, 7], our system differs mainly in that the central superconductor is not grounded.

There, we investigated various charge tunneling processes within an InAs nanowire-based hybrid dot-island-dot system. Using dispersive gate sensing and multiplexed RF techniques, we characterized the charge stability diagrams and estimated the tunneling strengths between different charge states, with the system completely isolated from charge resources. Our results highlighted the tunability of such a floating system between elastic cotunneling and cross-Andreev reflection, and demonstrated a transition point where both processes coexist in resonance. The agreement of our measurements with the theoretical model underlines that the comparison between the charging energy and the ground state energy of the island leads to this evolution. In addition to the quantum capacitances from which we obtain the corresponding tunneling strength, the extractable Sisyphus dissipation adds another dimension to understanding the different types of charge transitions. This work advances our approach to the qualitative and quantitative analysis of a floating hybrid quantum dot system with dispersive gate sensing.

The employment of dispersive gate sensing on a floating hybrid system is well verified, and can then be continued with parity readout measurements even with poor man's Majorana. This means that once reliable sets of materials containing robust Majorana zero modes are established, we can build and read the first topological qubit by repeating the work. As our results show the ability to characterize the hybrid system with the same technique for readout, it is possible to remove the need for metal contacts.

8.2. OUTLOOKS

8

We propose below some experiments that can be continued, based on our current achievements and understanding of dispersive gate sensing.

8.2.1. PARITY READOUT

In parallel with our focus on nanowires, experiments on two-dimensional gases (2DEGs) are also progressing in the study of semiconductor-superconductor hybrid systems. More specifically, by early 2024, Microsoft has published a single-shot interferometric measurement of fermion parity in an InAs-Al heterostructure with a gate-defined nanowire [8]. The SEM image of their device is shown in Fig. 8.2 (a). They equivalently achieved the form depicted in Fig. 1.1 (b), although they were unable to distinguish between Majorana zero modes in the topological phase and fine-tuned low-energy Andreev bound states in the trivial phase. A full form of the Majorana box qubit device can be further designed as depicted in Fig. 1.1 (a). All three Pauli operators can be measured by repeating the interferometry measurements between different pairs of the three quantum dots. One of the initial applications of the single Majorana box qubit is the construction of a quantum number generator. In a more distant future, dispersive gate sensing will continue to support scalable topological quantum computation structures [9].

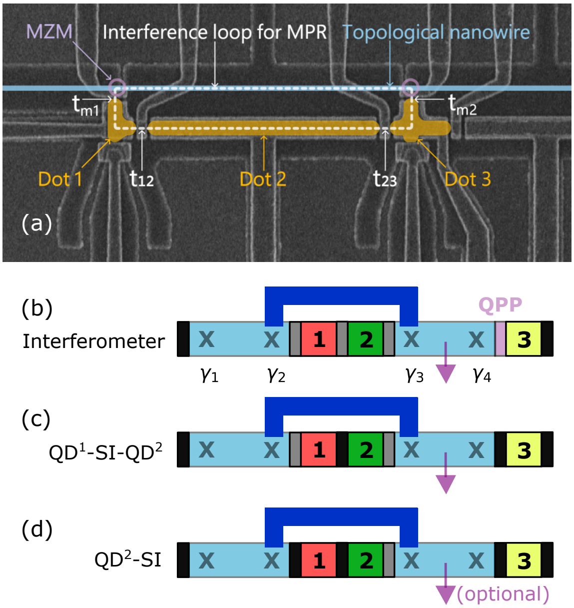

Figure 8.2: **Parity readout measurements.** **(a)** The SEM image of an achieved interferometer for parity readout, adopted from Ref. [8]. **(b-d)** An interferometer geometry for parity readout realized on a single nanowire, with the characterization of each component implemented by closing different barrier gates. The black (grey) barriers indicate that charge transitions are blocked (allowed). The grounding line is optional, depending on the purpose of the experiments. (b) An example of measuring a floating interferometer system based on a nanowire, equivalent to (a) and the schematic in Fig. 1.1 (b). The rightmost quantum dot is used for the purpose of studying quasiparticle poisoning, such that the barrier gate functions as a switch. **(c)** An example for measuring a floating dot-island-dot system. With a grounded superconductor, we obtain a minimal Kitaev chain connects to zero lead. **(d)** An example for measuring a floating dot-island system. When the superconductor is grounded, the quasiparticle poisoning rate can be detected.

8.2.2. PARITY HYBRIDIZATION

The topology of a Majorana box qubit is not achievable with single nanowire platforms. Instead, we propose a more straightforward geometry that can be integrated with the existing nanowire framework, as illustrated in Fig. 8.2 (b-d). This loop geometry shares the same concept as the interferometer in Fig. 8.2 (b). The Majorana box qubit is still there espite the fact that only one basis σ_z can be measured. In such a system, we can examine the hybridization between a pair of Majorana zero modes from the same island. This helps us to rotate the qubit in another basis, σ_x. The Hamiltonian of the system is discribed in the parity basis

$$H_{loop} = (h_{12} + P_{tot} h_{34})\sigma_x + (h_{23} + \delta_z)\sigma_z, \tag{8.1}$$

with h_{ij} being the hybridization coupling between Majorana zero modes γ_i and γ_j. P_{tot} is the overall parity $-\gamma_1\gamma_2\gamma_3\gamma_4$, and δ_z is the dephasing component due to the readout or charge noise. The hybridization of a pair of Majorana zero modes can be suppressed by a factor of $e^{-L/\xi}$, while h_{23} is proportional to tunnel coupling between the dot and the island over the charging energy of the island. Raising tunnel barriers sets the hybridization of $\gamma_2\gamma_3$ to zero, and in that regime the qubit start rotating with a certain frequency $\omega = (h_{12} + P_{tot}h_{34})/\hbar$. Leaving the qubit rotating for time τ_r, the tunnel barriers are subside for a quick measurement that take time τ_m much less than the qubit rotation period. The probability of measuring the same quantum capaictance would be $\cos^2(\omega\tau_r)$. For a given rotation time, the projection measurement provides two possible values. The averaged result after multiple trials suggests the superposition component of two parities. Later on, by varying the rotation time with a great amount of projection measurements, the relation between τ_r and the parity state probability could be resolved. The statistics should show a Rabi oscillation as in a two-level system, being a strong evidence of having a Majorana loop qubit. The overall hybridization energy is thus extracted from the periodicity of the Rabi oscillation. With the superconducting island is grounded, the hybridization of the poor man's Majorana can be similarly tested.

8.2.3. QUASIPARTICLE POISONING

Topological quantum computation is claimed to be error protected, as the large charging energy of the system will conserve parity. However, despite the benefits of the dispersive gate sensing measurement protocol without a conducting lead, the system still has to undergo quasiparticle poisoning, which constrains the qubit lifetime. There are several potential causes for this. First, quasiparticles can quickly fly through the continuum above the gap and then jump out of the island. There is a possibility that the qubit rotation speed will change within a short time scale (P_{tot} may change in a short time). Second, quasiparticles may fly through Majorana zero modes and change the occupancy of a pair of them, which could result in a qubit flip. Third, quasiparticles can be originally excited from the superconducting island itself. The device shown in Fig. 8.2 (b) would be helpful for understanding the quasiparticle poisoning effect on parity readout. In the case where the spontaneous quasiparticle poisoning rate is low, the rightmost quantum dot can be employed as a controllable reservoir for artificial quasiparticle poisoning.

8

To study the spontaneous quasiparticle poisoning rate of the superconductor segment, we close three of the barrier gates and ground the superconductor as in Fig. 8.2 (d). By tuning the system to the sweet spot of a minimal Kitaev chain (the elastic cotunneling rate equals to the rate of crossed Andreev reflection), we can investigate the impact of quasiparticle poisoning on the total charge parity iteration in time domain. This can be achieved by applying dispersive gate sensing to the remaining quantum dot. For a system with an ungrounded superconductor, it would be beneficial to conduct a comprehensive study on the impact of island charging energy on the poisoning rate.

8.2.4. COOPER PAIR SPLITTER

A controllable Cooper pair splitter is also simultaneously formed in Fig. 8.2 (c). So far most Cooper pair splitters are consists of a grounded superconductor, however, with dispersive gate sensing, we are also capable to measure them in floating systems. Both Ref. [10] and Chapter. 7 provide a comprehensive analysis of the Cooper pair splitting process, being the reversed process of crossed Andreev reflection. Based on this, we have determined that when the charging energy of the island is smaller than the gap, we are able to measure coherent Cooper pair splittings. Next steps can be taken to perform a Bell test verifying the spin-singlet entanglement by coupling charge sensors to the two dots [11]. The impact of driving frequency on the resonator coupled to the island is another area worthy of further investigation [12].

BIBLIOGRAPHY

[1] Damaz De Jong, Jasper Van Veen, Luca Binci, Amrita Singh, Peter Krogstrup, Leo P Kouwenhoven, Wolfgang Pfaff, and John D Watson. Rapid detection of coherent tunneling in an in as nanowire quantum dot through dispersive gate sensing. *Physical Review Applied*, 11(4):044061, 2019.

[2] Guanzhong Wang, Tom Dvir, Grzegorz P Mazur, Chun-Xiao Liu, Nick van Loo, Sebastiaan LD Ten Haaf, Alberto Bordin, Sasa Gazibegovic, Ghada Badawy, Erik PAM Bakkers, et al. Singlet and triplet cooper pair splitting in hybrid superconducting nanowires. *Nature*, 612(7940):448–453, 2022.

[3] Tom Dvir, Guanzhong Wang, Nick van Loo, Chun-Xiao Liu, Grzegorz P Mazur, Alberto Bordin, Sebastiaan LD Ten Haaf, Ji-Yin Wang, David van Driel, Francesco Zatelli, et al. Realization of a minimal kitaev chain in coupled quantum dots. *Nature*, 614(7948):445–450, 2023.

[4] Alberto Bordin, Guanzhong Wang, Chun-Xiao Liu, Sebastiaan LD Ten Haaf, Nick Van Loo, Grzegorz P Mazur, Di Xu, David Van Driel, Francesco Zatelli, Sasa Gazibegovic, et al. Tunable crossed andreev reflection and elastic cotunneling in hybrid nanowires. *Physical Review X*, 13(3):031031, 2023.

[5] Rubén Seoane Souto and Ramón Aguado. Subgap states in semiconductor-superconductor devices for quantum technologies: Andreev qubits and minimal majorana chains. *arXiv preprint arXiv:2404.06592*, 2024.

[6] Alberto Bordin, Xiang Li, David Van Driel, Jan Cornelis Wolff, Qingzhen Wang, Sebastiaan LD Ten Haaf, Guanzhong Wang, Nick Van Loo, Leo P Kouwenhoven, and Tom Dvir. Crossed andreev reflection and elastic cotunneling in three quantum dots coupled by superconductors. *Physical review letters*, 132(5):056602, 2024.

[7] Alberto Bordin, Chun-Xiao Liu, Tom Dvir, Francesco Zatelli, Sebastiaan LD ten Haaf, David van Driel, Guanzhong Wang, Nick van Loo, Thomas van Caekenberghe, Jan Cornelis Wolff, et al. Signatures of majorana protection in a three-site kitaev chain. *arXiv preprint arXiv:2402.19382*, 2024.

[8] Morteza Aghaee, Alejandro Alcaraz Ramirez, Zulfi Alam, Rizwan Ali, Mariusz Andrzejczuk, Andrey Antipov, Mikhail Astafev, Amin Barzegar, Bela Bauer, Jonathan Becker, et al. Interferometric single-shot parity measurement in an inas-al hybrid device. *arXiv preprint arXiv:2401.09549*, 2024.

[9] T. Karzig, C. Knapp, R. M. Lutchyn, P. Bonderson, M. B. Hastings, C. Nayak, J. Alicea, K. Flensberg, S. Plugge, Y. Oreg, C. M. Marcus, and M. H. Freedman. Scalable designs for quasiparticle-poisoning-protected topological quantum computation with Majorana zero modes. *Physical Review B*, 95(23):235305, 2017.

[10] Damaz de Jong, Christian G Prosko, Lin Han, Filip K Malinowski, Yu Liu, Leo P Kouwenhoven, and Wolfgang Pfaff. Controllable single cooper pair splitting in hybrid quantum dot systems. *Physical review letters*, 131(15):157001, 2023.

[11] Zoltán Scherübl, András Pályi, and Szabolcs Csonka. Probing individual split cooper pairs using the spin qubit toolkit. *Physical Review B*, 89(20):205439, 2014.

[12] Fredrik Brange, Riya Baruah, and Christian Flindt. Adiabatic cooper pair splitter. *Physical Review B*, 109(8):L081402, 2024.

ACKNOWLEDGEMENTS

The uniqueness of a doctoral journey lies in the fact that it is a period during which one should build upon previous learning experiences to further expand their knowledge, continue their research training, and focus deeply on their studies while eliminating distractions. This phase also coincides with crucial years of mental maturation, allowing one to move beyond their original understanding and shape their perceptions of life and the world. It can be said that this is a key period for brain development. I feel incredibly fortunate to have come to Delft at the right time and place to experience this process. Here, I have access to a world-class research environment and brilliant colleagues, which often makes me feel that a doctoral thesis may never fully capture this wonderful experience, and my insights and gains cannot be adequately described in words. But I'll still give it a try.

First and foremost, I would like to express my gratitude to my promoter **Leo**. Receiving the PhD offer from our group was one of the happiest moments as I completed my master's program. I am continually impressed by the breadth of topics you have explored throughout your career and the talented young researchers you have nurtured across various branches of condensed matter physics. I often reflect on how "my supervisor is a person with a grand vision." I sincerely appreciate your unwavering support in my participation in various academic conferences, your patience in helping me discover my research motivations, and our insightful discussions about career planning before graduation. Your role has been invaluable, serving not only as an academic mentor but also as a guiding figure during one of the most "transformative" periods of my life. And to my copromotor **Srijit**, I am very grateful for your proactive concern for my progress when you learned that I was the only one working on my project. Your help in summarizing and organizing my thoughts has been immensely beneficial. I also thoroughly enjoyed those relaxed conversations over beers during parties, and do hope we had more. I'm also obliged to the collaborators who contributed to the materials development, especially **Erik**'s group at TU Eindhoven and **Peter**'s group at Copenhagen University. Special thanks to the growers **Ghada, Sasa, Yu L., Di X.**, whose efforts were essential to the success of the devices.

I would also like to extend my gratitude to **Michael W.** and **Csilla** for the support during the times I was preoccupied with family matters, as well as for the warm small talks that made me feel a sense of familial comfort. I am also thankful to **Jenny** for the consistent ability to arrange everything so efficiently, to **Jason** for many assistances in our basement labs, to **Olaf** for saving our cool-downs countless times, to **Raymond S.** for the fantastic design of our electrical instruments, and to **Raymond V., Roy, DEMO** for their reliability when I'm trapped by troubleshootings. Additionally, thanks to my committee members, **Yaroslav B., Christian A., Leo D., Jan R.**, for their support of my thesis and for attending my defense.

To my close colleagues, **Wolfgang**, it was wonderful to join your CQ team right when

I started my position. I appreciate the fresh perspective you and **Angela** brought to our more transport-focused research group by introducing high-frequency topics. The initial projects truly excited me as someone who was originally an outsider in the field. **Filips**, my PhD project could not have been completed smoothly without your presence. I have greatly benefited from your vast knowledge and execution skills. When we sit together in front of B1 facing the test signals, you consistently generate brilliant ideas and immediately put them into action. I've often described you as the 'talented composer' type, a quality that I find difficult to replicate and learn from. You truly embody the standards I have for a physicist. **Jonne**, thank you for the numerous pieces of advice when I was struggling with the yield of fabrications. I really appreciate your insights from the CQED perspective. **Michael C.**, it was a pleasure working together with you on the DQD project, and I always enjoy reading the manuscripts you write. It's fantastic that you have gained experience from so many exciting projects at QuTech, please accept my envy! **Jasper**, you are an exceptional cleanroom mentor, and thanks to your guidance, my first sample successfully operated for a year. Your support and thoughtful suggestions were instrumental during my learning phase. **Damaz**, I really miss the sound of you typing on the keyboard at B1 after your graduation, and I love the camera recognition alarm system you developed for the power supply. I'm sure you will have more fun in QBlox! **Christian P.**, it's truly impressive to see you derive complex equations in such a short time, and you always seem to have a great idea for everything. Thanks for all the intellectual contributions! **Daan, Nejc**, it's so nice to have you around, and also in the CQ family portrait I drew in 2020.

And to those talented members of the other subteams and labs, **Jaap**, sharing an office with you has brought me immense joy, especially when we freely discuss physics, careers, society, and our understanding of the world. **Marta**, your speed and quality in completing your PhD thesis made me realize that the template for life is right beside me, great success in IBM! **Arno**, thank you for always sharing a wealth of knowledge whenever we come to you with questions or curiosity. **Tom, Guan**, the collaboration between you two is impressive, and it's wonderful to witness your debates on physics. **Alberto**, it's incredible to see you exploring so many types of Kitaev chains while also nurturing your startup, Olivia! **David**, I really enjoy your presenting style, have more fun in Groove with qubits measurements! **Lukas S.**, having casual chats with you while working in the cleanroom is a cherished memory. Enjoy your research and running sessions in Sweden! **Nick**, I recall many times you shared philosophical insights in little conversations, reminding me of the physicists I imagined as a child, haha! **Greg**, it's a bit of a pity that I didn't seize the opportunity to collaborate with you. Wishing you amazing results soon in Oxford! **Francesco Z.**, it's fantastic to have you as my paranymph, and I'm excited to see your results on the parity readout measurements! **Vukan**, you are the most talented person around me when it comes to being happy, and I'm impressed by how you always know what you want. **Jiyin**, cheers for always making the best choices, whether it's starting the non-local experiment or buying and selling a house at the perfect timing! Also happy to know **Shuang** and your little girl. **Ivan**, hope we gather more in ASML, and best luck to your defense. **Qing**, very glad to see how much you've accomplished in just a few years, hope your new chapter is as vibrant as ever! **Prasanna**, it's really fun to have super no-brainer chat with you. **Chungting**, thank you for sharing your tips on mindset when I was at my lowest point. They were quite helpful. **Figen**, your diligent attitude reminds me of the QuTech-ers when I just joined here, and thank you for being so warm. **Yining**, I am looking forward to your data in 2DEG. Go make some more big news! **Michiel**, I remember many times coming to your desk asking about superconductivity and other concepts. You are always willing to share your notes. **Francesco B.**, it's really impressive to see you being down-to-earth in many things we interact with while consistently achieving results. Wishing you all the best in Copenhagen! **James**, you are such a chill person in the cleanroom, and I've learned a lot about optimization tricks from you. **Daniel**, it's great to still see you around often even after your graduation, what a wonderful journey through the world of qubits! **Willemijn**, I'm so jealous seeing you travel during your gap year! I miss the days we loudly ordered "White Willy" at the bars. I also remember I forgot to deliver the sketch for Leo as promised. I'll practice soon! **Kongyi**, my progress on the InSb projects wouldn't be as quick without your help with the nanowire transfer. **Jie, Lingling**, it's so inspiring to see you both as superwomen in academia in China! Please keep me updated with more news about you! **Xin, Xinxin**, how nice it is to see you both doing research at QuTech, and see **Zhiyuan** learning about EXE right after his first month. **Cecile**, I always feel so positive after chatting with you. It's great to hear that you're settling in well in the Netherlands! **Chunxiao**, I'm happy to learn so many board game strategies with you and **Shuang**. Wishing you all the best in landing your ideal positions! **Xiao**, you can imagine how grateful I am for all the conversations that took unexpected turns. Enjoy Shenzhen with your fridges and **Le**! **Di, Yang**, sharing so many hotpots together and engaging in debates about personal values is one of my fondest memories from my PhD years, and it makes me incredibly curious about what the future holds. Also thanks to **Bas, Jinlun, Chien-An, Bart, Fokko, Delphine, Luca, Vanessa, Amrita, Christina, Mathilde, Lukas G., Gijs, Bernard, John, Christian M., Alex, Jouri, Anton, Chung Kay, Lieuwe, Marina, Pavel, Lydia, Simone, Attila**, and all other **QuTech** and **QN** and **Microsoft Delft** early members who make up this great community.

To my dear friends, I couldn't have made it without those sweet phone calls and the energy you all shared! Thanks you **Shaoxin, Changcai, Lincui, Yu** for always enthusiastically brainstorming with me and for being able to dispel my bizarre assumptions in a timely manner. **Xiaoqing**, it's so hilarious that we both ended up in industry! You are always supportive since we both in colledge, no matter how foolish my decisions may be. I can't wait for the moment you visit me in Eindhoven! **Ruyue**, the amulets you sent from Tokyo are so cute, they made my days! I think I will finally have time to visit you in Japan. **Xinrui, Yu Z.**, I really miss the girl's nights we spent together, let's plan a reunion someday in Beijing! **Ruoyu, Tian, Zhoumuyan, Daniel Y., Roy, Yi, Zichen, Yonghao, Liang, Ying, Gang, Zijin, Qingzhi**, thanks a ton for the long chats and all the great advice on the next steps to take! **Siyu, Ran, Wei, Weining, Yihui, Mengyu, Han, Qing**, it's so heartwarming to be able to occasionally connect with you and share life experiences. Sometimes, those conversations act like a lighthouse, providing a lot of strength.

Finally, I'd thank my **dad** for always being there for me since I was a little girl. I've learned so much from you - from history to philosophy, from architecture to aesthetics. It's both unfortunate and a bit amusing that I've come to realize many of your sources of knowledge are not entirely accurate; yet our conversations have ignited my curiosity about everything. They have often left me confused especially during my PhD years, but they are also the very reason I am here today. And thank you **mum** for being my professional role model. I know you made the best decision to focus on your work from the beginning of your career. Your experience has inspired me during my darkest times, and I hope that one day I can feel as satisfied with my choices and growth as you are.

I am also grateful for the numerous challenges I've faced outside of my PhD research in my twenties, as they provided me the opportunity to establish a stronger self-supporting system. I believe that what I gain from this will far outweigh what I have lost. As one of my favorite writers says, there is no wave that only rises and never falls. To everyone around me facing struggles and applause, there's no need to define overselves by the setbacks or praises we've encountered. Let's expect nothing and take jumps!

CURRICULUM VITÆ

Lin HAN

21-08-1993 Born in Shijiazhuang, Hebei, China.

EDUCATION

2005–2008 Secondary school
Shijiazhuang Foreign Language Education Group (SFLE), China

2008–2011 High School (science and technology)
Shijiazhuang No.2 Middle School, China

2011-2015 Bachelor's degree in Physics
Nankai University, Tianjin, China
Thesis: Nanostructural Engineering of Perovskite Solar Cells via First-Principles Calculation
Promotor: Prof. dr. Lixin Zhang

2015-2017 Master's degree in Physics (Applied and Engineering Physics)
Technische Universität München (TUM), Munich, Germany
Thesis: Towards P-type Modulation Doped GaAs-AlGaAs Core-shell Nanowires
Promotor: Prof. dr. Jonathan J. Finley
Prof. dr. Gregor Koblmüller

2018-2024 PhD. degree in Physics
Delft University of Technology (TU Delft), Delft, the Netherlands
Thesis: Diverse Charge Tunneling in Hybrid Quantum Confined Sysetms
Promotor: Prof. dr. ir. Leo P. Kouwenhoven
Dr. Srijit Goswami

List of Publications

10. **L. Han**, M. Chan, C. G. Prosko, F. K. Malinowski, J. V. Koski, Y. Liu, P. Krogstrup, and L. P. Kouwenhoven, *Dispersive gate sensing of diverse charge tunneling processes in a floating hybrid triple quantum dot*, In preparation.

9. M. Chan, C. G. Prosko, **L. Han**, S. Oosterhout, A. Sammak, G. Scappucci, M. Veldhorst, and F. K. Malinowski, *RF compressibility measurements in Germanium*, In preparation.

8. C. G. Prosko, I. Kulesh, M. Chan, **L. Han**, D. Xiao, C. Thomas, M. Manfra, S. Goswami, and F. K. Malinowski, *Flux-tunable hybridization in a double quantum dot interferometer*, SciPost Physics 17, no. 3 (2024): 074.

7. D. de Jong, C. G. Prosko, **L. Han**, F. K. Malinowski, Y. Liu, L. P. Kouwenhoven, and W. Pfaff, *Controllable single Cooper pair splitting in hybrid quantum dot systems*, Physical Review Letters 131, no. 15 (2023): 157001.

6. **L. Han**, M. Chan, D. de Jong, C. G. Prosko, G. Badawy, S. Gazibegovic, E. P. A. M. Bakkers, L. P. Kouwenhoven, F. K. Malinowski, and W. Pfaff, *Variable and orbital-dependent spin-orbit field orientations in an InSb double quantum dot characterized via dispersive gate sensing*, Physical Review Applied 19, no. 1 (2023): 014063.

5. F. K. Malinowski, R. K. Rupesh, L. Pavešić, Z. Guba, D. de Jong, **L. Han**, C. G. Prosko, M. Chan, Y. Liu, P. Krogstrup, A. Pályi, R. Žitko, and J. V. Koski, *Quantum capacitance of a superconducting subgap state in an electrostatically floating dot-island*, arXiv:2210.01519.

4. F. K. Malinowski, **L. Han**, D. de Jong, J.-Y. Wang, C. G. Prosko, G. Badawy, S. Gazibegovic, Y. Liu, P. Krogstrup, E. P. A. M. Bakkers, L. P. Kouwenhoven and J. V. Koski, *Radio-Frequency - Measurements with Subattofarad Sensitivity*, Physical Review Applied 18, no. 2 (2022): 024032.

3. D. de Jong, C. G. Prosko, D. M. A. Waardenburg, **L. Han**, F. K. Malinowski, P. Krogstrup, L. P. Kouwenhoven, J. V. Koski, and W. Pfaff, *Rapid microwave-only characterization and readout of quantum dots using multiplexed gigahertz-frequency resonators*, Physical Review Applied 16, no. 1 (2021): 014007.

2. **L. Han**, C. G. Prosko, J. van Veen, D. de Jong, F. K. Malinowski, P. Krogstrup, L. P. Kouwenhoven, and W. Pfaff, *Dispersive gate sensing for probing the triviality of superconducting subgap states in a magnetic field*, In preparation.

1. J. van Veen, D. de Jong, **L. Han**, C. Prosko, P. Krogstrup, J. D. Watson, L. P. Kouwenhoven, and W. Pfaff, *Revealing charge-tunneling processes between a quantum dot and a superconducting island through gate sensing*, Physical Review B 100, no. 17 (2019): 174508.